Dissertation zur Erlangung des Doktorgrades
der Fakultät für Chemie und Pharmazie
der Ludwig-Maximilians-Universität München

The Synergy of DNA Nanodevice Engineering and Single-Molecule Fluorescence Technique Development

Von Fiona Lhasa Cole

aus
München, Deutschland

2024

Erklärung

Diese Dissertation wurde im Sinne von § 7 der Promotionsordnung vom 28. November 2011 von Herrn Prof. Dr. Philip Tinnefeld betreut.

Eidesstattliche Versicherung

Diese Dissertation wurde eigenständig und ohne unerlaubte Hilfe erarbeitet.

München, 05.12.2024

Fiona Cole

Dissertation eingereicht am	05.12.2024
1. Gutachter:	*Prof. Dr. Philip Tinnefeld*
2. Gutachterin:	*Prof. Dr. Alena Khmelinskaia*
Mündliche Prüfung am	10.02.2025

SUMMARY

Advancing our understanding of molecular dynamic processes on the nanoscale is essential for unlocking new frontiers in both biology and DNA nanotechnology. Biological systems and artificial nanostructures often rely on complex, dynamic molecular interactions that occur in parallel and on both temporal and spatial scales challenging the resolution limits of conventional fluorescence microscopy techniques. This thesis addresses this challenge by engineering novel DNA-based nanodevices while simultaneously developing imaging techniques that are crucial for studying these dynamic systems.

A central focus of this work is the development of SEPP (Serial Execution of Programmable Processes), a programmable DNA nanorobot capable of autonomously responding to multiple environmental stimuli by performing a sequence of tasks with precise spatial and temporal control. The nanorobot makes use of a modular design based on combining reconfigurable DNA origami arrays with allosteric regulation. It applies insights gained from exploring the platform's energy landscape to engineer the nanorobot's sophisticated functionality based on a hardware-software framework. By strategically tuning (stimulus-responsive) energy barriers, SEPP achieves logic-gating based input processing followed by the controlled conduction of multiple responses, demonstrating the potential for DNA nanotechnology to enable breakthroughs in molecular diagnostics and programmable therapeutics.

To enable such intricate designs, novel single-molecule imaging techniques are developed. The introduction of a double fluorescence resonance energy transfer (FRET) assay enables the simultaneous tracking of two coupled conformational changes, revealing the detailed energy landscape of dynamic DNA nanostructures and guiding their design toward more efficient functionalities. These insights, in turn, provide the basis for engineering SEPP, illustrating how imaging advances drive the evolution of complex nanodevices.

In parallel, this thesis exploits novel DNA origami structures as rationally controllable innovative probes for advancing imaging methods. By integrating FRET into pulsed-interleaved MINFLUX, a nanometer precise super-resolution microscopy technique, precise multilateration of molecular interactions within small assemblies is achieved, while fluorescence lifetime multiplexing enables the super-resolved co-tracking of two molecules also beyond the typical FRET range of 3-12 nm. These techniques not only bridge the spatial precision gap between FRET and co-tracking but also provide new avenues for studying larger biomolecular complexes.

Altogether, this thesis exemplifies a synergistic cycle. Advancements in single-molecule imaging techniques drive the development of sophisticated DNA nanodevices like SEPP, while such novel sophisticated DNA nanodevices again help push the limits of imaging techniques by providing a testbed for their development and validation. This synergy promises to transform the fields of bioimaging, diagnostics and molecular robotics, paving the way for further breakthroughs to come in future.

TABLE OF CONTENTS

1 INTRODUCTION

"The whole is greater than the sum of its parts." – in *Metaphysics*, one of his principle works, *Aristotle* highlights how interconnected systems, by working together, achieve more than the functionalities of their isolated components predict.[1] This principle, commonly referred to as synergy, forms the foundation of life at the molecular level.[2–4] Within cells, proteins, nucleic acids and other molecules form coordinated networks, enabling organisms to react to their environment, repair damage and enable the countless number of processes that make up life.[5–9]

Synergy implies a mechanism that creates interactions between components and results in emergent properties – functionalities that cannot be predicted by studying individual components in isolation. In biology, synergy often is tied to the flow of information between molecular players and necessitates communication.[2] For example, cell signaling pathways process complex environmental stimuli into cellular responses through feedback loops[10,11], crosstalk[12] and allosteric regulation[13,14]. These mechanisms allow the cell to dynamically adapt to changing conditions.

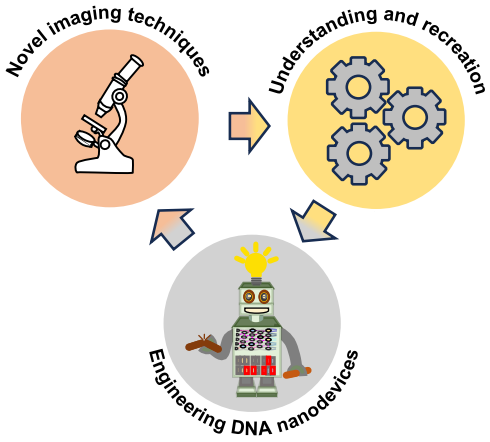

Figure 1: Synergy of DNA nanodevice engineering, understanding and recreation of biological principles and single-molecule fluorescence technique development. Novel imaging techniques aid in understanding naturally occurring synergies which allows their recreation in artificial systems. This lays the basis for exploiting them to create emergent properties in artificial nanodevices which again can serve as a rationally controllable testbed when developing and validating novel imaging techniques.

When aiming to replicate and harness these synergistic biological principles, the challenge lies in designing artificial systems that achieve similar levels of coordination, modularity and adaptability.[15] This thesis tackles the concept of synergy from two directions (see Fig. 1). By recreating emergent synergistic properties in smart nanodevices, this thesis aims to develop systems potentially capable of autonomously operating in biological environments, e.g. for smart therapeutics and molecular

diagnostics. It also addresses the need to observe synergistic interactions as they naturally occur in biological systems by developing novel single-molecule imaging techniques that have the potential to enhance our understanding of complex biomolecular synergies. For this, novel synthetic nanodevices are used as a testbed for development and validation, creating a new synergy between nanodevice engineering and image technique development on a methodological level that promises to synergistically push the limit of both fields further and further in the years to come.

1.1 HARNESSING SYNERGIES FOR ADVANCED NANOTECHNOLOGY

Synergies occurring in nature inspire us not only to understand but also to recreate their complexity by engineering sophisticated nanodevices.[15] The demand for such devices is driven by applications in clinical diagnostics[16,17], smart therapeutics[18–20] but also by sheer scientific curiosity to mimic life[21]. Nanodevices capable of detecting disease biomarkers, delivering drugs to specific locations or conducting complex reactions at the (sub)cellular level could revolutionize medicine and biotechnology.[22]

Among the most promising platforms for creating such devices is the DNA origami technique.[23] By guiding a single-stranded DNA strand into a pre-designed shape exploiting programmable, complementary interactions with shorter staple strands, DNA origami provides nanometer precision and unparalleled programmability.[24,25] This enables the modular assembly of components such as sensing or computation units with a single scaffold.[26–28] Dynamic DNA origami nanostructures extend this capability further by incorporating proximity-induced operations like cargo delivery and signal transduction in response to environmental stimuli.[26,29,30]

Despite their versatility, most current DNA origami devices rely on simple two-state switches – dynamic motifs that change between two conformational states in response to environmental stimuli.[26–28,31,32] While ideal for tasks as biosensing, simple logic gates or single-step drug delivery, these systems lack the interconnectedness needed for more advanced processes.[32] They so far do not have the means to integrate multiple inputs, compute logic-based decisions and execute multi-step output operations on the same system.

An option to advance beyond these limitations exploits the same principles that enable biological synergies, namely modularity and controlled information flow.[15]

1. Modular design: By designing nanodevices to be composed of interchangeable units which are tailored for distinct functionalities such as environmental responsiveness or operational outputs, a plug-and-play approach is realized. This facilitates customizing the nanodevices for specific purposes and thus allows the same platform to be used for different applications with minimal redesign.

2. Controlled information flow: Just as biological systems rely on allostery to connect distant molecular processes,[33–36] nanodevices must incorporate mechanisms that regulate how information is transmitted between their modular components. Allosteric regulation enables not just responsiveness but also logic gating[37,38] and (anti-)cooperativity[39,40] – features essential for creating adaptive and multifunctional systems.

An elegant approach to this concept couples multiple identical two-state switches into a single system. Such a design enables creating a universal framework for modularly encoding distinct functionalities into each of the identical two-state switches. The modularity hereby arises from a shared software framework that describes the design principles of their functionalities, while the interconnected nature of the system – the hardware – governs the flow of information. This analogy mirrors the structure of a computer: the hardware provides the infrastructure for processing, while the software encodes specific tasks.[41] By integrating modularity with controlled information flow, this approach therefore lays the foundation for a rational, universal design strategy to harness synergy in synthetic nanodevices (see Fig. 2).

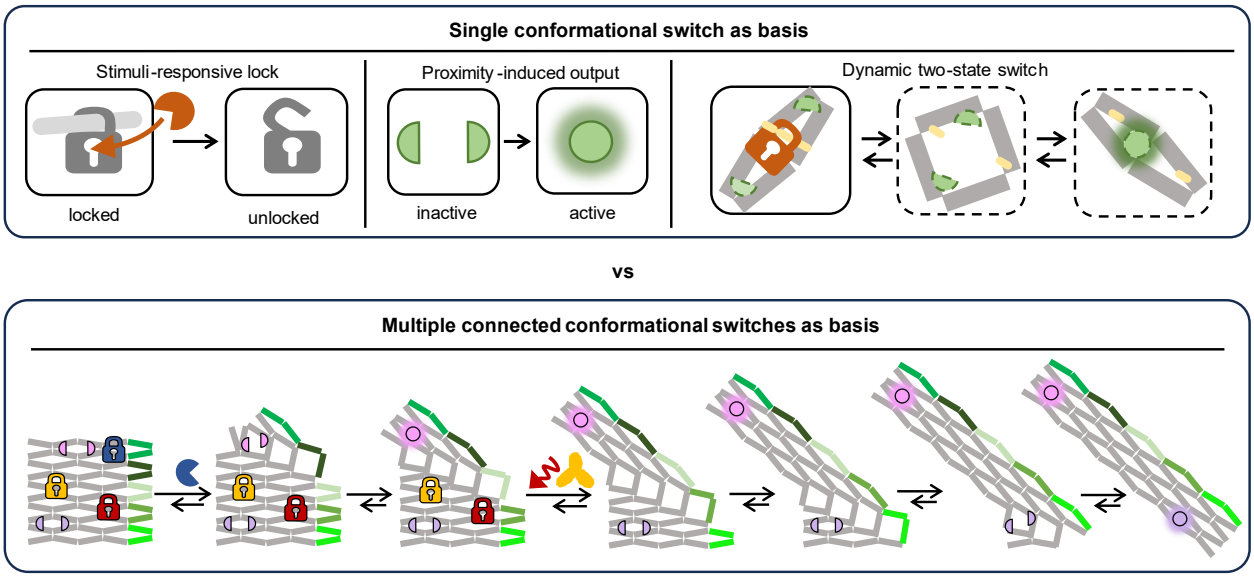

Figure 2: Design concepts in DNA origami nanodevices. Most current DNA nanodevices are based on a structure conducting a single conformational change, exemplarily shown for a single antijunction (upper panel). By including e.g. a stimuli-responsive lock (upper left panel) which locks the structure into the energetically less favorable conformation, environmental responsiveness can be encoded into these structures (upper right panel). Output operations which are conducted in response to the environmental stimuli can additionally be encoded into the structures by placing two parts of an operational unit on distal sites on the structure (upper middle panel). The decrease in distance between these sites then results in a proximity-induced activation of the unit (upper right panel). In contrast, design concepts for advanced DNA nanodevices based on networks of interconnected conformational switches could allow processing multiple inputs and generating multiple proximity-induced outputs in a controlled manner, as conceptually shown for reconfigurable DNA origami arrays (lower panel).

Reconfigurable DNA origami arrays represent a promising platform in this context. They consist of multiple interconnected building blocks, so-called antijunctions, each capable of dynamically switching between two conformations (see Fig. 2). Unlike isolated two-state switches, the conformations of antijunctions in these arrays are coupled, enabling changes in one unit to propagate through the system. This creates a network where information flows in a controlled, cascaded manner, providing a hardware basis.

The first part of this thesis explores methods to engineer the coupling between antijunctions to precisely control and steer the flow of information in the hardware and supplies a software package to encode modular functional units into the individual antijunctions of the hardware. Together, these efforts aim to build a universal framework for designing intelligent nanodevices that go beyond isolated operations to synergistically achieve coordinated functionalities.

1.2 The role of imaging in decoding molecular synergies

Understanding and controlling the flow of information between antijunction units in reconfigurable DNA origami arrays is a prerequisite for unlocking their full potential. Specifically, it necessitates comprehending how the conformational change of one antijunction propagates through the system, influencing distal antijunctions and shaping the overall dynamics of the array. This requires an imaging approach capable of capturing correlative information on the coupled conformational changes of multiple antijunctions simultaneously.

Traditional methods like fluorescence resonance energy transfer (FRET) are a natural starting point for such investigations.[42] FRET is uniquely suited for probing molecular distances in the range of 3–12 nm, making it a valuable tool for studying conformational changes and molecular interactions. By placing fluorescent markers at strategic positions on a biomolecule, FRET can detect changes in their relative distances through shifts in fluorescence intensity. Particularly at the single-molecule level, FRET has provided unparalleled insights into the structural dynamics of proteins,[43–46] nucleic acids,[47–51] and DNA nanostructures.[26,27,52] Its temporal resolution, reaching the microsecond scale,[53] allows us to monitor dynamic processes in real time.

However, the standard two-color FRET approach, which monitors a single distance, is insufficient for capturing the interplay between multiple dynamic components in systems like reconfigurable DNA origami arrays. IN an array where the conformations of multiple antijunctions are coupled, understanding how these conformational changes propagate requires correlative data. Traditional two-color FRET lacks the capacity to provide such multidimensional insights, as it can only track one interaction at a time.[54]

Multi-color FRET extends the capabilities of two-color FRET by incorporating multiple donor and acceptor pairs, allowing the simultaneous monitoring of several distances (see

Fig. 3).[54,55] This approach has been successfully applied to study correlated motions in proteins during folding,[43,56] conformation dependency of ligand binding[57,58] and dynamic processes in artificial DNA nanostructures[59,60]. Despite its promise, multi-color FRET remains limited by the same spatial constraints as two-color FRET. Its working range of ~3–12 nm is insufficient for studying interactions between distant antijunctions in DNA origami arrays, which span over several tens of nanometers.[61,62]

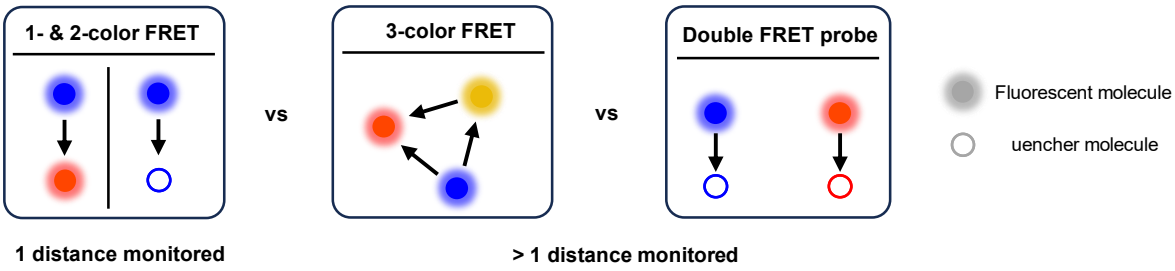

Figure 3: Monitoring multiple distances using FRET. Traditional single-color and two-color FRET typically track a single interaction or distance change, limiting the insight into complex systems. In contrast, multi-color FRET and the double FRET probe developed in this work enable the simultaneous monitoring of multiple interactions, providing information on correlated behaviors and offering a more comprehensive view of dynamic processes.

To overcome these limitations, this thesis introduces a double FRET probe designed to explore coupled dynamics in DNA origami arrays (see Fig. 3). This assay integrates two spectrally separated FRET pairs into the same structure, enabling the simultaneous tracking of two correlated conformational changes. By measuring the timing and sequence of these changes, the double FRET probe provides direct insights into the speed and thus also the strength of allosteric communication between antijunctions. This method also enables quantifying how engineering choices – such as modified DNA sequences or adjusted the coupling strength – affect the propagation of information through the array both between specific antijunctions and globally in the whole array.

Moreover, the development of the double FRET probe exemplifies how the advancement of imaging techniques and DNA nanodevices can drive each other forward. While the probe was specifically designed to study reconfigurable DNA origami arrays, its potential extends far beyond these systems. It can be adapted for investigating allosteric processes in biological systems, such as the conformational changes in multi-protein complexes[50] or signal transduction pathways[63–65] where similar challenges of distance and coordination arise.

1.3 The role of DNA nanodevices in the development of novel single-molecule imaging techniques

Similarly, as single-molecule probes tailored for exploring artificial DNA origami structures can uncover biological dynamics, DNA nanostructures also serve as ideal platforms for developing and validating novel imaging techniques designed to probe biological processes on the nanoscale. Applying principles of information flow in nanotechnology necessitates a deep understanding of how such flow occurs in biological systems. Since information flow is inherently tied to interactions between molecules, studying these interactions requires tools capable of directly observing them in their native environments, on the nanometer scale and in real time.

The double FRET probe developed in this work enables detailed insights into coupled conformational changes within DNA nanostructures, shedding light on the kinetics and timing of interactions. However, its applications remain restricted by the working range of FRET of ~3–12 nm for individual interactions and its inability to provide absolute positional information. Extending beyond these spatial and functional constraints necessitates other approaches.

In fluorescence microscopy, single-particle tracking addresses some of these limitations by following the absolute positions of individual particles over time, generating spatiotemporal trajectories that reveal their interactions with their environment.[66,67] This method has provided invaluable insights into the dynamics of biomolecules as they interact with each other, form multi-component complexes and interact with their biological environment.[66,68–70] However, for more complex mechanisms involving multiple interacting particles or components, a more direct and simultaneous visualization of multiple processes becomes critical.

A promising direction in this regard is the combined application of single-particle tracking and FRET (see Fig. 4). This approach combines the strengths of both techniques, providing precise localizations from single-particle tracking along with environmental insights gained through FRET measurements. As such, it can e.g. link characteristics of the diffusive behavior of proteins to their proximity to other players as recently demonstrated by the *Piehler* group.[71]

Fully merging single-particle tracking with FRET would mean attaining molecular scale resolution both in proximity determination and tracking. This can only be realized with a super-resolution method which resolves distances in the FRET regime with high temporal resolutions. MINFLUX is a recently developed super-resolution technique with one of the best spatiotemporal resolutions to date.[72] As such, MINFLUX resolves single-digit nanometer distances even at one millisecond temporal resolution, making it ideal for precise tracking applications.[73,74] This has – amongst others – been demonstrated on dynamic DNA origami[73] and the motor proteins kinesin[74,75] and dynein[76], for which MINFLUX provided the first direct observation of their stepping mechanism in live cells.

However, similar to less precise methods, also when using MINFLUX in tracking applications, environmental information is lacking. To this end, an approach combining MINFLUX tracking with FRET is introduced. MINFLUX was originally developed as a purely fluorescence intensity-based technique, but our group recently introduced pMINFLUX[77] as a simplified implementation of MINFLUX which additionally allows access to another property of the fluorescence response of the studied molecules known as the fluorescence lifetime. The fluorescence lifetime reports on how long a molecule fluoresces after it is excited and – in contrast to the fluorescence intensity – as an intrinsic property also directly depends on the environment of an imaged molecule and thus can be a measure for the occurrence of FRET. In a combined pMINFLUX-FRET approach, this is used to assign each tracked MINFLUX localization of a FRET donor its distance to a FRET acceptor in its proximity. Using a DNA origami nanostructure, it is demonstrated how this approach enables determining the FRET acceptor's position through multilateration, without directly localizing it. This provides detailed insights into the dynamic behavior of the DNA nanostructure, significantly enhancing our understanding of the system and the processes occurring on it.

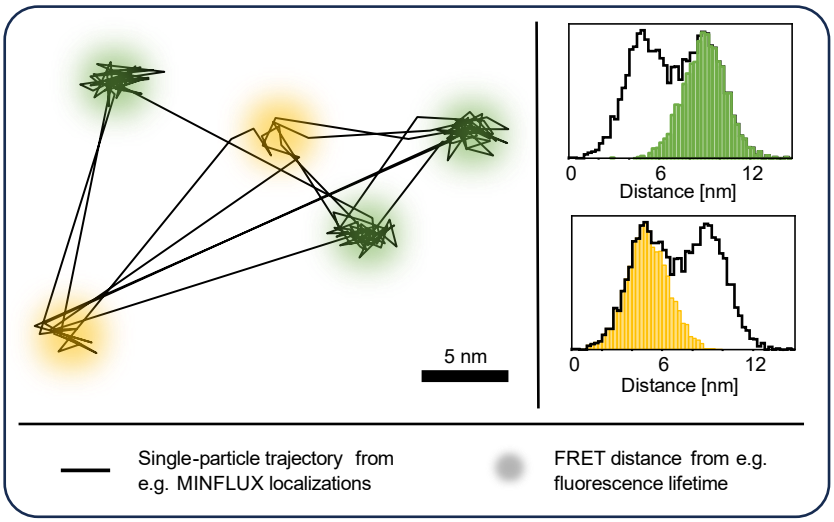

Figure 4: Synergy between single-particle tracking and FRET. Combined single-particle tracking/ FRET measurements enable correlating positional information with FRET information.

While combining single-particle tracking and FRET measurements has proven effective in studying interactions with MINFLUX *within* the FRET range, challenges arise when extending *beyond* this distance. Here, dual-color tracking enables the simultaneous localization of two molecules, allowing the observation of their interactions in real time.[67]

For the simultaneous localization of two molecules within a diffraction limited spot, their individual fluorescence responses to excitation must be separated. This can principally be achieved using any optically distinguishable property of the molecules.[78] The conceptually simplest approach separates the fluorescence response of different

molecules based on their spectral properties.[79] This is realized using different excitation wavelengths to excite the studied molecules and/ or detect their fluorescence. Especially the use of multiple excitation laser wavelengths however adds significant complexity to optical setups, limiting the implementation of these approaches in more complex techniques as e.g. MINFLUX. As such, while excitation multiplexing has been successfully demonstrated in various single-particle tracking techniques including orbital tracking,[80] wide-field tracking[71,81] and TSUNAMI,[82] nanometer spatial resolution at high temporal resolutions still is challenging to attain in multiplexed tracking.

Other optical characteristics of molecules besides their spectral properties suitable for separating their fluorescence response include polarization and fluorescence lifetime.[83–85] Although polarization-based fluorescence separation has already been demonstrated in 2000,[84] achieving the necessary high level of control over the polarization state of the studied molecules remains an ongoing challenge, with current methods still under development.[86–88] In contrast, distinguishing different molecules based on their fluorescence lifetimes is well established in fluorescence lifetime imaging microscopy (FLIM).[89] This approach has the advantage that molecules exhibiting similar absorption and emission spectra, but differing fluorescence lifetimes can be excited and detected by the same wavelengths and on the same detector, keeping the need for modifications to instrumental setups minimal.

The fluorescent signals of two molecules cannot only be differentiated by their distinct fluorescence lifetimes when occurring separately as in imaging. Exploiting the distinct temporal profiles of their fluorescence responses to excitation, they can also be separated when occurring simultaneously within the same diffraction limited spot. For static samples, this has been demonstrated to resolve distances down to 25 nm using FLIM,[83] indicating a strong potential of this approach also for applications in tracking.

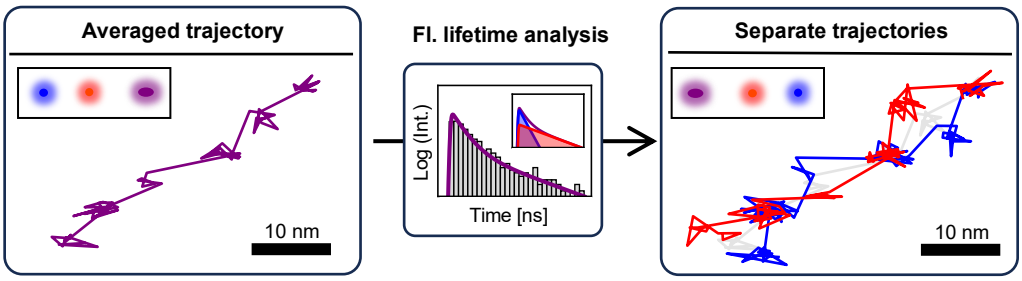

Figure 5: Concept of fluorescence lifetime multiplexing for tracking applications. When two fluorescent molecules within a diffraction limited spot are simultaneously excited by the same wavelength, their average position is recorded during single-particle tracking, resulting in a combined trajectory (left panel). However, if the molecules have different fluorescence lifetimes, analyzing their nanosecond-scale fluorescence decay (middle panel and inset) allows separating their individual signals. This enables the extraction of individual trajectories for each molecule (right panel). For reference, the combined, averaged trajectory is displayed as a light grey line in the right panel.

Consequently, this thesis makes use of this approach to implement fluorescence lifetime-based multiplexing for tracking applications in pMINFLUX (see Fig. 5). Combined with a novel phasor/microtime gating technique for multiplexing in the FRET range, this enables, for the first time, the simultaneous tracking of two molecules at distances between 4 nm and 100 nm with nanometer precision. Additionally, it offers high temporal resolution and does not require any modifications to the optical setup, making it easy to implement on existing setups. The possibilities provided by this approach are demonstrated on DNA origami nanostructures by studying various biorecognition elements incorporated on them. By studying monitoring the hybridization of two DNA strands to different targets within such systems, visualizing antibody binding sites on DNA origami and separating translational and rotational motion of DNA origami on lipid bilayers, our understanding of how DNA origami dynamically interact with different biomolecules on the molecular scale is broadened. This opens the door for rebuilding further biological concepts on DNA nanostructures in future, allowing for further advancement in nanotechnology.

2 THEORETICAL BACKGROUND

2.1 FLUORESCENCE MICROSCOPY

Fluorescence microscopy has established itself as a key method in biological imaging. The optical opacity of biological material paired with the non-invasive nature of visible light make fluorescence microscopy ideally suited for studying DNA nanostructures as well as all other subcellular structures and processes. By marking compounds of interest with a fluorescent tag and illuminating them with laser light of a suitable wavelength, they light up (fluoresce) against an otherwise (ideally) black background, making their precise localization possible.[90]

Besides solely probing the location of molecules, fluorescence microscopy also allows characterizing their immediate environment. The fluorescence response of a molecule to illumination depends on the environment it is placed in. If e.g. other fluorescent molecules or certain chemicals are in close proximity to the studied molecule, properties of its fluorescence response change. Studying these properties, i.e. fluorescence intensities and fluorescence lifetimes, thus allows drawing conclusions on the interplay between multiple molecules.[91] This however necessitates a profound understanding of what fluorescence is and which processes influence it.

2.1.1 FLUORESCENCE AND COMPETING PROCESSES

Fluorescence describes a photophysical process during which a photon is spontaneously emitted from an excited molecule. A molecule generally has multiple distinct electronic states it can occupy. These electronic states are further subdivided into different vibronic levels (see Figure 6a). For fluorescent molecules – commonly referred to as fluorophores – the energetic difference between their electronic ground state S_0 and the first excited state S_1 falls in the range of ~1-8 eV, corresponding to the energy of photons with wavelengths in the UV-vis range.[92]

Under ambient conditions, fluorophores reside in their electronic ground state. If illuminated with light of a suitable energy, photon absorption can promote them to a vibronic level of an excited singlet state S_n with $n \geq 1$. Following this near instantaneous process, fluorophores rapidly relax to the lowest vibronic level of their first excited singlet state, the S_1 state, in the non-radiative processes of internal conversion and vibrational relaxation. These processes occur within femto- to picoseconds, preventing the much slower process of fluorescence (nanoseconds timescale) from taking place. Only from the lowest vibronic level of the S_1 state, fluorescence occurs.[93] In the process of

fluorescence, the molecule returns to its S_0 state under emission of a photon. Due to the preceding non-radiative relaxation, this photon has less energy compared to the initially absorbed photon. As a result, the fluorescence emission spectrum is red shifted to the absorption spectrum (see Figure 6b). This red-shift, known as the *Stokes* shift,[94] allows separating fluorescent photons from scattered excitation photons by applying spectral filters and thus lays the foundation for fluorescence microscopy.[92,95]

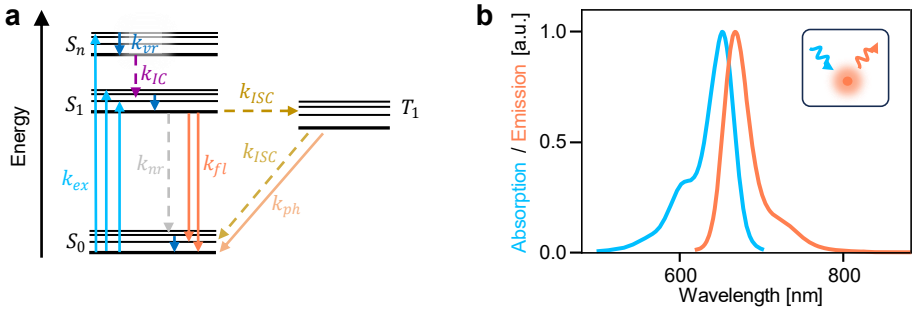

Figure 6: Fluorescence and related processes. (a) *Jablonski* diagram depicting electronic (bold lines) and vibronic (lines) states of a fluorophore as well as transitions between them, namely absorption (k_{ex}), fluorescence (k_{fl}), phosphorescence (k_{ph}), vibrational relaxation (k_{vr}), internal conversion (k_{IC}), non-radiative decay pathways from the S_1 state (k_{nr}) and intersystem crossing (k_{ISC}). Transitions occurring under absorption or emission of a photon are marked with a straight arrow, non-radiative transitions with a dashed arrow. (b) Absorption (blue) and emission (orange) spectrum of the fluorophore AlexaFluor647 highlighting the *Stokes* shift between their maxima and their mirrored curves.

Fluorescence however is not the only possible depopulation pathway of the S_1 state. Next to fluorescence also other non-radiative decay pathways to the S_0 state such as internal conversion as well as intersystem crossing to the triplet state T_1 occur. From the T_1 state, molecules relax to the ground state either non-radiatively via intersystem crossing or under photon emission in a process known as phosphorescence. Depending on the chemical environment of the fluorophore, fluorescence quenching may open another alternative depopulation pathway of the S_1 state.[92,95]

All these processes occur with a certain probability. This probability depends on their kinetic rate constants k_{fl}, k_{nr}, k_{isc} and k_q for fluorescence, non-radiative decay processes, intersystem crossing and environment-dependent quenching, respectively. The likelihood of an excited state fluorophore to relax via fluorescence is described by the fluorescence quantum yield Φ. Φ is defined as the ratio of the number of photons emitted via fluorescence n_{fl} to the total number of photons absorbed during excitation n_{abs}. It is calculated as the fraction the fluorescence rate constant contributes to the sum of the rate constants of all processes depopulating the S_1 state.

$$\Phi = \frac{n_{fl}}{n_{abs}} = \frac{k_{fl}}{k_{fl} + k_{nr} + k_{isc} + k_q} \tag{1}$$

As it depends on k_q, changes in of the fluorescence quantum yield theoretically can be used to report on changes in the environment of a fluorophore. In praxis, the direct experimental determination of fluorescence quantum yields however is challenging.[96] Instead, often another – more directly measurable – intrinsic property of the fluorescence response is used: the fluorescence lifetime τ. τ describes the average time a fluorophore spends in its S_1 state following its excitation. Assuming first order kinetics for all possible relaxation pathways, it is given by the inverse of the sum of all processes depopulating the S_1 state.[91]

$$\tau = \frac{1}{k_{fl} + k_{nr} + k_{isc} + k_q} \tag{2}$$

Fluorescence lifetimes can be directly calculated from fluorescence intensity decay profiles. The number of fluorophores in their S_1 state at a certain time t after excitation is directly proportional to the number of photons emitted via fluorescence at this time $I(t)$. With first order kinetics, the fluorescence intensity decay thus is described by an exponential decay[91]

$$I(t) = I_0 \cdot \exp -\frac{t}{\tau} \tag{3}$$

where I_0 is the fluorescence intensity at the time $t = 0$. Fluorescence lifetimes can then be calculated e.g. by fitting experimental data with an exponential decay[83] or using phasor analysis[97,98].

2.1.2 Fluorescence Resonance Energy Transfer

A popular concept used to study biomolecular interactions occurring in distances of twelve nanometers and below is FRET.[42] FRET is a non-radiative resonance energy transfer from one molecule (FRET donor) to another (FRET acceptor) occurring via dipole-dipole interactions. With its efficiency being inversely proportional to the sixth power of the distance between the interacting molecules, FRET is highly sensitive to small changes in the distance between them. This allows characterizing the interplay between different biomolecules of interest or conformational changes occurring in a single biomolecule by marking them (or positions on them) with FRET donors and acceptors.

Upon FRET donor excitation, FRET opens up an additional depopulation pathway of the S_1 state of the donor by elevating a second (acceptor) molecule which is in close proximity to the donor from the S_0 state to the S_1 state (see Figure 7a). The FRET acceptor, typically also a fluorophore, then relaxes partially via fluorescence. FRET donor excitation thus results in a lowered FRET donor fluorescence intensity in combination with the onset of FRET acceptor fluorescence if FRET occurs. If the FRET acceptor is non-fluorescing, the

acceptor relaxes non-radiatively and only a decrease in FRET donor fluorescence intensity is noted.

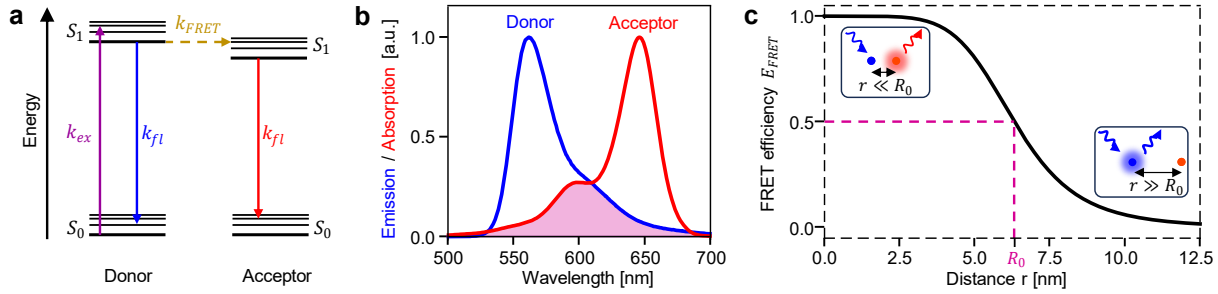

Figure 7: Fluorescence resonance energy transfer. (a) Simplified *Jablonski* diagram illustrating FRET between a donor and an acceptor fluorophore. After donor excitation (k_{ex}), FRET (k_{FRET}) serves as an additional relaxation pathway of the S_1 state of the donor molecule if an acceptor fluorophore is in close proximity. As a result, fluorescence (k_{fl}) cannot only occur from the donor but also from the acceptor fluorophore. (b) Emission (blue) and absorption (red) spectrum of the donor and acceptor fluorophore of the FRET pair ATTO542/ ATTO647N, respectively. The spectral overlap necessary for the occurrence of FRET between both fluorophores is highlighted in purple. (c) Distance dependency of the FRET efficiency of the FRET pair ATTO542/ ATTO647N. The Förster-radius R_0 (purple) marks the inter-fluorophore distance at which a FRET efficiency of 50% occurs.

The occurrence of FRET not only necessitates a small distance between donor and acceptor molecule. The emission spectrum of the FRET donor must also overlap with the absorption spectrum of the FRET acceptor (see Figure 7b). If both these prerequisites are fulfilled, the extent to which FRET occurs between two molecules is then given by the FRET efficiency E_{FRET}. E_{FRET} is defined similar to the fluorescence quantum yield. It describes the fraction the rate constant of FRET k_{FRET} contributes to the sum of the rate constants k of all processes depopulating the S_1 state of the FRET donor.

$$E_{FRET} = \frac{k_{FRET}}{k_{FRET} + k_{fl} + k_{nr} + k_{isc} + k_q} \tag{4}$$

The rate constant k_{FRET} in turn depends on the distance between FRET donor and acceptor r, the quantum yield Φ_D and the fluorescence lifetime τ_D of the donor in absence of the acceptor, the spectral overlap integral between the emission spectrum of the donor and the absorption spectrum of the acceptor $J(\lambda)$, the relative orientation of the donor and acceptor transition dipoles κ^2 and the refractive index of the medium the molecules are placed in n.

$$k_{FRET}(r) = r^{-6}\,\tau_D^{-1}\,\frac{9000\ln 10\,\Phi_D\kappa^2}{128\pi^5 n^4 N_A}\,J(\lambda) \tag{5}$$

where N_A is the *Avogadro's* number. For the refractive index typically a value of $n = 1.4$ is used for biomolecules in aqueous solutions. In most cases, also free rotation of the

donor and acceptor molecules is assumed. As rotation mostly occurs on timescales much faster than fluorescence, FRET then is averaged over all possible donor and acceptor orientations. This results in a constant value of $\kappa^2 = 2/3$ for the orientation of the transition dipoles. Except for the distance r, all other parameters used to calculate k_{FRET} solely depend on the chosen FRET donor and acceptor. They thus can be summarized in the so-called *Förster* radius R_0 to form a single constant specific for the FRET donor-acceptor pair chosen. This simplifies the equation for k_{FRET} as follows.

$$k_{FRET}(r) = \tau_D^{-1} \left(\frac{R_0}{r}\right)^6 \tag{6}$$

Using equation 2, E_{FRET} then can be rewritten to only depend on r and R_0.

$$E_{FRET} = \frac{R_0^6}{R_0^6 + r^6} \tag{7}$$

As such, R_0 describes the distance at which a FRET efficiency of 50% occurs (see Figure 7c). For commonly used organic fluorophore pairs, R_0 has values between ~4-8 nm. The r^{-6} distance dependency thus limits the dynamic range of FRET at which distances can be reliably determined to values between ~2-12 nm.[42,92]

Experimentally, E_{FRET} is determined by comparing either the fluorescence lifetimes or the corrected fluorescence intensities of the FRET donor in absence (τ_D and I_D) and presence (τ_{DA} and I_{DA}) of the FRET acceptor.

$$E_{FRET} = 1 - \frac{\tau_{DA}}{\tau_D} = 1 - \frac{I_{DA}}{I_D} \tag{8}$$

Measurements of either fluorescence intensities or fluorescence lifetimes thus provide a mean to study (changing) distances between FRET donors and acceptors in biological systems.

2.1.3 Photostabilization of Fluorescent molecules

Upon illumination, fluorescent molecules do not emit light indefinitely. At some point, they stop fluorescing. This is caused by photobleaching, a process in which the chemical structure of fluorescent molecules undergoes irreversible changes due to repeated light exposure, rendering them non-fluorescent.[99]

Photobleaching typically originates from the excited states of a molecule, which are more prone to these destructive reactions. Among these, the T_1 triplet state, though rarely accessed, poses the biggest problem. While the S_1 singlet state usually has a lifetime in the nanosecond range, the triplet state can persist for micro- to milliseconds.[92] Not only

does this longer lifetime lead to blinking – a temporary stop in fluorescence, but it also provides a much larger window for harmful reactions to occur.

One key factor in this context is molecular oxygen which exists in a triplet ground state. When a fluorescent molecule enters its T_1 state, it can interact with triplet oxygen, leading to the formation of reactive oxygen species such as singlet oxygen, which further contribute to photobleaching.[99,100] To reduce the likelihood of photobleaching and improve photostability, enzymatic oxygen scavenger systems like glucose oxidase/ catalase or protocatechuate-3,4-dioxygenase are commonly used in fluorescence microscopy to remove oxygen from the surrounding solution.[101] However, since oxygen also quenches the triplet state, its removal extends the triplet lifetime, increasing blinking and even the likelihood of photodamage.[100]

For long-term imaging, it is therefore crucial to combine oxygen removal with an alternative mechanism to quench the T_1 state of fluorescent molecules. Reducing and oxidizing systems (ROXS) are commonly employed for this purpose (see Fig. 8).[100] These systems effectively quench both the triplet state and any reactive oxygen species formed. Fluorescent molecules in their triplet state can be rapidly reduced or oxidized by ROXS agents, forming radical anions or cations. These intermediates are then neutralized by complementary oxidizing or reducing agents, and the fluorescent molecule returns to its ground state. If this reduction and oxidation cycle occurs sufficiently fast, the triplet lifetime is significantly shortened, effectively minimizing the risk of photobleaching. Typically employed ROXS systems include the combination Trolox/ Trolox quinone,[100] along with additives such as ascorbic acid,[101] methyl viologen[102] or beta-mercaptoethanol[103].

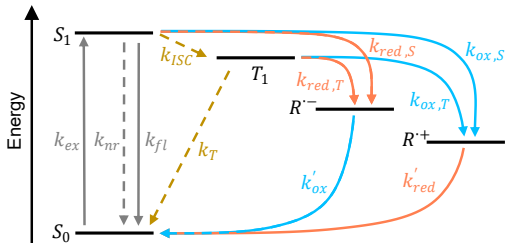

Figure 8: Photostabilization by a reducing and oxidizing system. Simplified Jablonski diagram depicting transitions between the short-lived singlet states S_0 and S_1 and the longer-lived triplet state T_1 as well as the radical states $R^{\cdot-}$and $R^{\cdot+}$. In the presence of both reducing and oxidizing agents, especially the otherwise long-lived T_1 state is rapidly depopulated in reduction (orange arrows, $k_{red,T}$) or oxidation (blue arrows, $k_{ox,T}$) reactions forming cationic or anionic radical states, respectively. By subsequent oxidation (k'_{ox}) or reduction (k'_{red}) of the radical states by ROXS, the electronic ground state S_0 is restored.

2.1.4 Single-Molecule Fluorescence Microscopy

Among the most widely used techniques in single-molecule fluorescence experiments are confocal microscopy and total internal reflection fluorescence (TIRF) microscopy.[92] Both methods offer distinct advantages, making them suitable for different experimental needs.

Confocal microscopy provides detailed insights into the intrinsic properties of fluorescent molecules by detecting the arrival times of individual photons emitted after excitation on the sub-nanosecond scale. Besides enabling high temporal resolutions, this time-resolved detection also enables the determination of fluorescence lifetimes, offering valuable insights into dynamic molecular processes such as energy transfer or interactions with the local environment. By capturing fluorescence lifetimes, confocal microscopy offers a comprehensive view of these processes, unaffected by external factors such as excitation power or detection efficiency. However, this information comes with certain trade-offs: confocal microscopy setups are relatively complex and data acquisition is limited to one molecule at a time, making it comparably slow.[92,95,104]

On the other hand, TIRF microscopy observes many molecules simultaneously. While it does not measure fluorescence lifetimes, its strength lies in fast, parallel data acquisition which makes it ideal for experiments requiring high statistical accuracy. However, compared to confocal microscopy, temporal resolutions typically are lower.[104]

In confocal microscopy, a laser beam is focused into a diffraction limited volume, typically in the femtoliter range, by a high numerical aperture (NA) objective lens. Both the emitted fluorescence and backscattered laser light are then collected by the same objective before being separated by a dichroic mirror. The fluorescence is directed through a pinhole, which spatially rejects out-of-focus light, creating a diffraction limited detection volume. For photon detection, avalanche photodiodes (APD) are commonly used due to their high collection efficiency, fast response, and low dark count rates. APDs coupled with time-correlated single-photon counting electronics enable precise fluorescence lifetime measurements, making confocal microscopy highly versatile for studying both freely diffusing and surface-immobilized molecules. For surface-based measurements, a good control over the position of the sample relative to the laser beam is crucial, often achieved using piezoelectric stages (see Fig. 9a).[104]

In contrast, TIRF microscopy illuminates a much larger area, typically several tens of microns in diameter, using an evanescent field. This evanescent field is generated at the interface between the glass coverslip and the sample when the laser beam is directed at an angle greater than the critical angle for total internal reflection. The resulting evanescent field selectively excites fluorophores located near the surface, making TIRF microscopy especially suited for studying surface-bound molecules. There are two common TIRF configurations: prism-based and objective-based. In prism-based TIRF, the excitation beam is directed through a prism placed above the coverslip, while in objective-based TIRF, the laser beam passes through the edge of a high-NA objective lens. In both cases, the evanescent field decays exponentially with distance from the

surface, limiting excitation to molecules within ~100-200 nm of the interface. The emitted fluorescence is then filtered using a dichroic mirror, and the full illuminated area is captured by highly sensitive cameras, such as EMCCD or CMOS cameras (see Fig. 9b).[104]

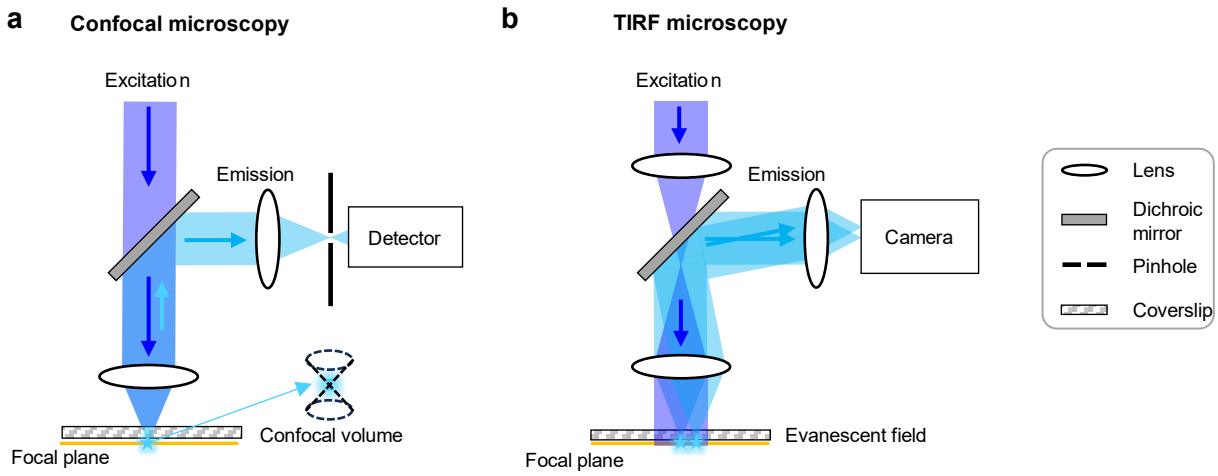

Figure 9: Confocal and TIRF fluorescence microscopy. (a) Confocal microscopy. In confocal microscopy, the excitation beam is focused by an objective lens onto a small diffraction-limited spot within the sample. The fluorescence emitted by molecules in this focal volume is separated from the excitation light using a dichroic mirror. To reduce background signals from out-of-focus light, the fluorescence is directed through a pinhole that blocks out-of-focus light before reaching the detector, typically a photomultiplier tube or an avalanche photodiode, enhancing spatial resolution. (b) Objective-type TIRF microscopy. In TIRF microscopy, an evanescent field is generated at the interface between the glass coverslip and the sample. This field selectively excites fluorophores within approximately 100-200 nm of the surface. The excitation beam is focused onto the back focal plane of the objective lens and angled beyond the critical angle, creating total internal reflection at the glass/sample interface. Fluorescence from molecules excited by this evanescent field is separated from the excitation light using a dichroic mirror and then focused onto a camera, typically an EMCCD or CMOS camera, allowing for imaging of surface-associated processes.

2.1.5 Diffraction Limit

While fluorescence microscopy offers many advantages, it is inherently limited by one fundamental drawback: the diffraction limit of light. This limitation arises from the wave-like nature of light which restricts the resolution of conventional optical microscopes. When two fluorescent molecules move closer towards each other, their fluorescence emission profiles begin to overlap. As a result, below a certain critical distance their fluorescence combines into a single, broader intensity profile with only one discernible peak, making it impossible to resolve the individual positions of the molecules (see Fig. 10a). The distance at which this begins to happen is known as the diffraction limit or also the *Abbe* limit d,[105] named after physicist *Ernst Abbe*, who first described it. It can be calculated from the wavelength of the emitted light λ and the numerical aperture (NA) of

the microscope's objective, which gives a measure for the ability of the objective of a microscope to gather light from different angles.[104]

$$d = \frac{\lambda}{2\,\mathrm{NA}} \tag{9}$$

With modern fluorescence microscopy objectives achieving numerical apertures between 1.3 and 1.5,[104] and the wavelengths of visible light ranging from around 480 nm to 650 nm, the resulting diffraction limit of fluorescence microscopy typically falls between 160 nm and 250 nm. This leaves proteins which range from two to ten nanometers in size, as well as DNA origami nanostructures which span several tens to hundreds of nanometers beyond the reach of conventional fluorescence microscopy. To study these nanoscale structures, overcoming the diffraction limit therefore is essential.

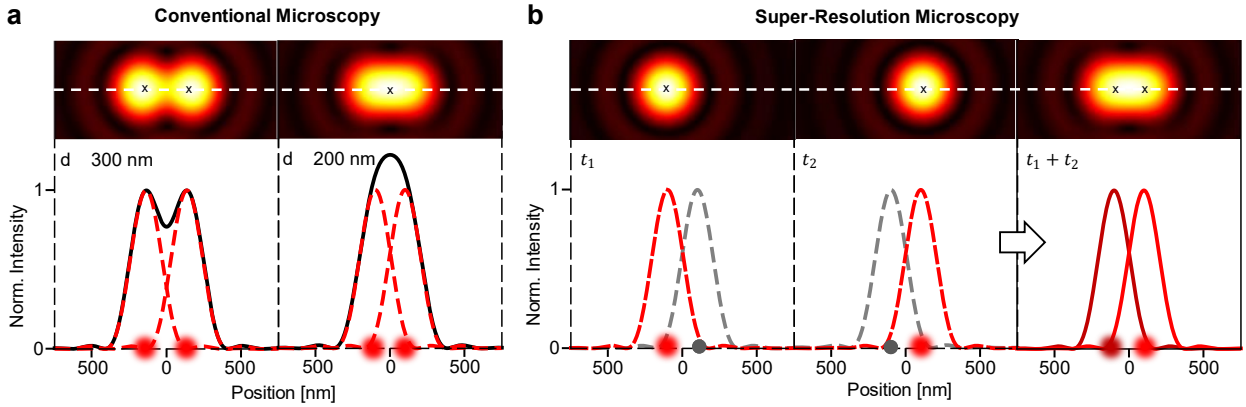

Figure 10: Diffraction limit of light in conventional fluorescence microscopy and super-resolution microscopy. Calculated 2D profiles (upper row) and 1D cross-sections (dashed white line, lower row) of the emission profiles of two fluorophores. (a) Emission profiles of two fluorophores in distances above the diffraction limit (300 nm, left) and below it (200 nm, right) in conventional fluorescence microscopy. The merged intensity profile (black curve) of the emissions of the individual fluorophores (dashed red curves) features two maxima above the diffraction limit and only one below it. This makes the positions of the individual fluorophores below the diffraction limit not discernable with conventional fluorescence microscopy. (b) In super-resolution microscopy, fluorophores in distances below the diffraction limit (200 nm) are temporally switched between a fluorescent (red circle, red curve) and a non-fluorescent dark state (black circle, dashed grey curve). This makes their fluorescent response to illumination discernable, allowing their separate localization (left and middle panel). The full image then is reconstructed by overlaying the individual localizations (right panel).

Super-resolution microscopy represents a major breakthrough in this regard, breaking past the diffraction barrier and enabling the visualization of structures with far greater detail than previously possible. These techniques use time as a distinguishing criterion and localize individual molecules by separating their fluorescence signals temporally. Unlike conventional microscopy in which all fluorescent molecules within a diffraction limited spot are excited and fluoresce simultaneously, super-resolution methods employ

strategies that allow only a subset of fluorescent molecules to fluoresce at any given time point. This reduces the overlap in the emission profiles of the studied molecules, making their localization far below the diffraction limit possible. By sequentially switching fluorescent molecules between a fluorescent and a non-fluorescent state in a controlled manner, the position of each individual molecule is recorded over time, building a highly detailed image (see Fig. 10b).[90]

2.1.6 Super-Resolution Microscopy Techniques

Depending on how they control the fluorescence of molecules, super-resolution microscopy techniques principally can be divided into the categories of coordinate-targeted and stochastic-switching methods.

In coordinate-targeted super-resolution techniques, fluorescent molecules are actively switched between fluorescent and non-fluorescent states in a spatially defined manner. The most well-known example of this approach is stimulated emission depletion (STED) microscopy.[106,107] STED relies on a confocal setup for which the effective volume of the focused excitation laser beam is reduced. As the beam scans over the sample, this enables resolving structures well below the diffraction limit. This is achieved using two laser beams: an excitation beam that illuminates a diffraction limited area of the sample and a superimposed depletion beam with a vortex-shaped intensity profile featuring a zero-intensity minimum at its center. The depletion beam quenches fluorescence everywhere except in the central region of the excitation beam, narrowing the fluorescent spot size and improving resolution. As such, the resolution in STED microscopy is directly linked to the intensity of the depletion beam. Higher intensities further reduce the effective fluorescent spot size, yielding typical resolutions of 20 nm to 30 nm.[108] However, intensities beyond a certain threshold risk photodamaging the sample which limits improving the spatial resolution of STED indefinitely. Other examples of coordinate-targeted techniques include ground state depletion microscopy[109,110] and saturated structured illumination microscopy[111], both of which also achieve sub-diffraction resolution by manipulating the fluorescent state of molecules within spatially defined regions.

In contrast to coordinate-targeted techniques, stochastic-switching techniques control the overall fraction of molecules in their fluorescent state rather than targeting specific areas. These methods typically operate on a widefield setup, allowing large fields of view to be imaged simultaneously by a camera. Using specific buffer conditions or photoactivation, molecules are stochastically switched between their fluorescent and non-fluorescent state. The conditions are tuned such that, at any given time point, only a small subset of molecules is in its fluorescent state, ensuring that the emission profiles of the molecules do not overlap. During imaging, multiple frames are acquired, each capturing the emission of different subsets of molecules. The location of each at the time fluorescent molecule is

determined in every frame and, by combining these localizations, a super-resolved image is reconstructed. The resolution of this image depends on the precision of the individual localizations which, scaling with $\sqrt{N}$, improves with the number of detected photons N. Some of the most commonly employed techniques in the field of stochastic-switching super-resolution microscopy include stochastic optical reconstruction microscopy,[112,113] photoactivated localization microscopy,[114,115] blink microscopy[116,117] and DNA points accumulation for imaging in nanoscale topography (PAINT)[118,119] which uses transient binding of fluorescently labelled DNA strands to achieve stochastic blinking. While recent developments, especially in DNA PAINT, have pushed the resolution of coordinate-targeted techniques to the sub-nanometer scale,[120] their need for stochastic blinking greatly reduces temporal resolution.

Generally, both coordinate-targeted and stochastic-switching super-resolution techniques rely on high photon fluxes to achieve high spatiotemporal resolutions. However, as photon flux increases, so does the likelihood of photobleaching which imposes a practical limit on the attainable resolution. While advances such as the development of brighter fluorescent molecules[121,122] and the application of ROXS[100] reduce photobleaching and extend fluorescence duration, thereby pushing this limit, these measures do not overcome it. As such, this limit prevents achieving arbitrarily high spatiotemporal resolution. To effectively image fast dynamic processes, new photon-efficient techniques are necessary that reduce the trade-off between temporal and spatial resolution.

2.1.7 MINFLUX

MINFLUX is a recently developed concept that addresses the limitation of high photon fluxes in super-resolution microscopy by combining features of both coordinate-targeted and stochastic-switching techniques.[72] This enables nanometer resolution with significantly fewer photons (MINimal photon FLUXes). Unlike conventional approaches that localize fluorescent molecules with an excitation maximum, MINFLUX uses the zero-intensity minimum of a vortex-shaped excitation beam (see Fig. 11). This allows localizations to be based on the absence of photons rather than their presence, making MINFLUX very photon-efficient and reducing the risk of photobleaching.

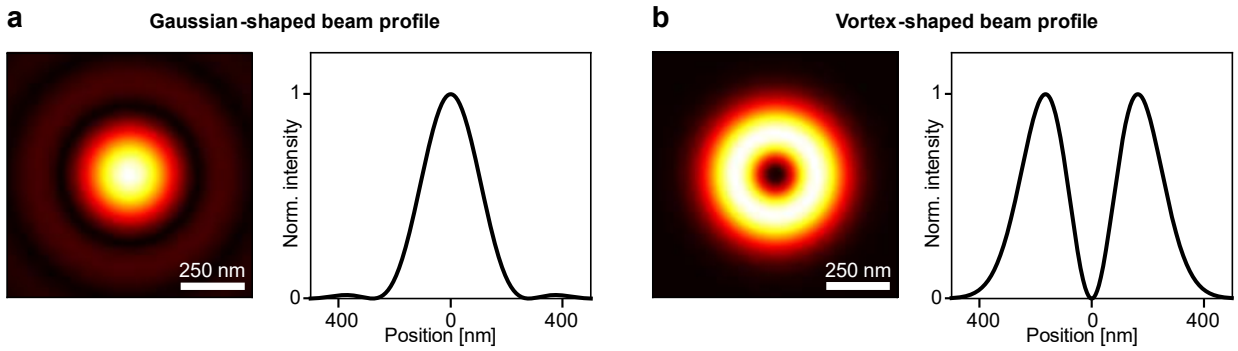

Figure 11: Excitation beam profiles in super-resolution microscopy. (a) Gaussian-shaped beam profile featuring an intensity maximum at its center, conventionally used in super-resolution microscopy to excite fluorescent molecules. (b) Vortex-shaped beam profile featuring an intensity minimum at its center, used to excite fluorescence molecules in MINFLUX. The left image shows calculated two-dimensional beam profiles and the right image the 1D cross-sections through their center.

To achieve this, MINFLUX applies stochastic-switching techniques to ensure that only one molecule is fluorescent within a diffraction limited spot at any given time. It then adopts a coordinate-targeted approach, probing the fluorescence of the molecule at four predefined beam positions arranged in a pattern around it, known as the excitation beam pattern (EBP) which has a diameter L. By comparing the fluorescence intensities recorded at these four positions to the known profile of the vortex-shaped excitation beam, the position of the molecule is determined through triangulation. This is illustrated for the simplified one-dimensional case in Fig. 12.

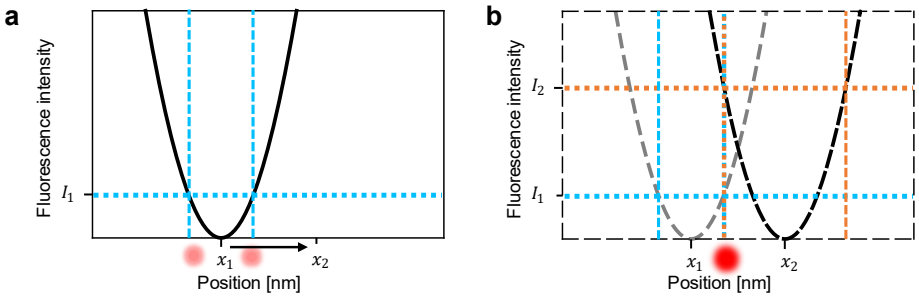

Figure 12: Principle of MINFLUX in one dimension. (a) A single fluorescent molecule is first excited with a parabolic intensity profile (black curve) with its intensity minimum at position $\boldsymbol{x_1}$. By measuring the fluorescence intensity at this position ($\boldsymbol{I_1}$, dotted blue line) and comparing it to the known shape of the excitation profile, the position of the fluorescent molecule can be narrowed down to two possible locations (blue lines, light red circles). (b) The parabolic excitation profile is displaced to a second position $\boldsymbol{x_2}$ (black line). By measuring the corresponding fluorescence intensities of the molecule at this new position ($\boldsymbol{I_2}$, dotted orange line), the fluorescent molecule is precisely localized (bright red spot) by combining the information of both measurements (dotted blue and orange line). The excitation beam profile at its original position is additionally shown as a dashed grey line.

The excellent photon efficiency of MINFLUX arises from two main factors. First, much of the positional information is already encoded in the structured excitation beam whose shape is pre-characterized on a reference structure before experiments. This pre-characterization preserves the limited photon budget of the molecules being localized. Also, since excitation takes place near the intensity minimum of the beam, the contrast in fluorescence between the different positions is maximized even though the total number of emitted photons remains low, significantly reducing the number of photons required for localizations. This effect is amplified by decreasing the size of the EBP (L). Then, the intensity minima at the beam positions move closer to the molecule, further reducing the number of emitted photons and increasing the information content of each photon. As a result, L becomes an adjustable parameter, in addition to the photon count N, for optimizing the localization precision σ and with this also the resolution of MINFLUX.[72]

$$\sigma \propto \frac{L}{\sqrt{N}} \tag{10}$$

The more precise positioning of fluorescent molecules in smaller EBPs needed for smaller L values is commonly achieved in an iterative approach. By centering molecules within the EBP after a localization cycle, the size of the EBP can gradually be decreased, leading to an enhanced precision with each iterative step.[123] Thanks to these principles, MINFLUX achieves precisions of around 2 nm in just 400 microseconds,[73] vastly improving both spatial and temporal performance compared to other super-resolution techniques. MINFLUX can also be extended to three-dimensional imaging by using a 3D tophat beam profile and incorporating axial displacements in the excitation profile,[123] further broadening its range of applications.

2.1.8 Pulsed-Interleaved MINFLUX

Conventional MINFLUX uses a single vortex beam for excitation which is sequentially shifted to the four positions forming the EBP during measurements (see Fig. 13a). This beam displacement is achieved on the microsecond timescale using electro-optical deflectors, introducing additional technical complexity to MINFLUX setups.

pMINFLUX is a novel implementation of MINFLUX that simplifies its experimental setup by eliminating the need for active beam displacement.[77] Instead, each position in the EBP is illuminated by an individual pulsed vortex beam which emits light in short picoseconds bursts. Making use of the concept of pulsed-interleaved excitation (PIE),[124] these spatially displaced beams are interleaved on the nanosecond timescale (see Fig. 13b), replacing the sequential beam movement required in conventional MINFLUX. As such, combining MINFLUX with PIE not only reduces technical complexity but also – and possibly even more important – provides access to fluorescence lifetime information of the localized molecules – something not possible in conventional MINFLUX which typically relies on constant, unmodulated continuous-wave beams. The fluorescence

lifetime information can be used to e.g. provide insights into the local environment of the localized molecules or distinguish between different molecule types in multicolor experiments.[77] By exploiting the reduction in fluorescence lifetime due to graphene energy transfer, it also becomes possible to determine the axial position of molecules based on their distance to a graphene surface, extending localizations in pMINFLUX to three dimensions without any modifications to the experimental setup needed.[125] This makes pMINFLUX a powerful tool for both localizations with high spatiotemporal resolutions and the extraction of fluorescence lifetime-based information, offering new pathways for advanced imaging in super-resolution microscopy.

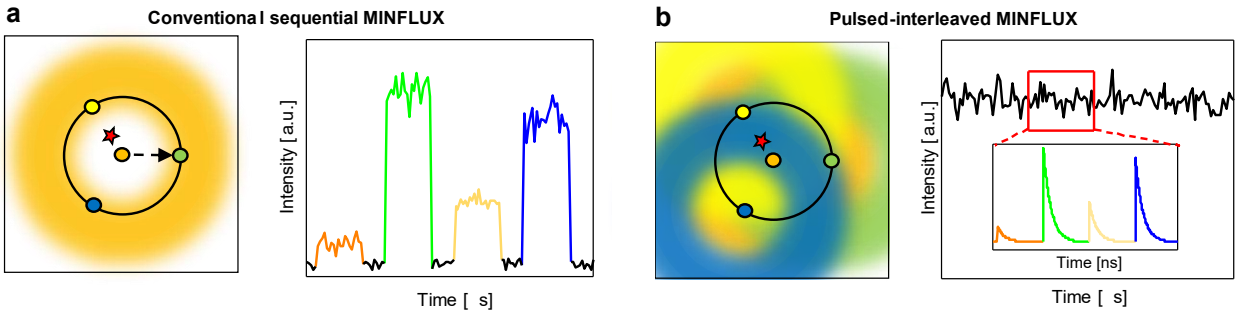

Figure 13: Excitation sequence in conventional MINFLUX and pMINFLUX. (a) Conventional sequential MINFLUX. For localizing a molecule, a single vortex-shaped excitation beam is sequentially displaced to four positions forming the EBP (colored circles) around the target molecule (red star) on the microseconds timescale (left). Fluorescence of an excitation cycle is consequently collected at each position on the microsecond timescale. (b) pMINFLUX. Four spatially displaced pulsed beams forming the EBP, are pulsed-interleaved to separate them temporally on the nanosecond timescale. Fluorescence from each position is extracted from the corresponding nanoscale intervals in the microtime histogram.

Experimentally, the temporal and spatial displacement in pMINFLUX is implemented with beam splitters and optical fibers. A pulsed laser is split into four beams of equal power which are then coupled into optical fibers of different lengths to introduce temporal delays. These delays ensure that the pulses of the beams are separated in time by a quarter of the pulse interval of the laser. The temporally displaced beams are recombined into a single optical path and passed through a vortex phase plate, creating the vortex shape elemental to MINFLUX in all four beams. In this recombination, the beams are spatially displaced to form the EBP on the sample surface.[77]

2.2 DNA ORIGAMI

Both the recreation of biological principles in artificial systems and the validation of novel multiplexed tracking techniques with model systems require precise control over spatial organization on the nanometer scale. The DNA origami technique offers a versatile platform for achieving such control, enabling the programmable self-assembly of both

static and dynamic nanostructures.[23,24] Through the precise attachment of modifications such as fluorescent molecules or biorecognition elements, these structures can be engineered to interact with their environment.[24,26,126,127] This adaptability makes DNA origami an ideal platform not only for constructing nanoscale frameworks with spatial precision but also for mimicking biological functions.

2.2.1 Concepts of DNA origami

DNA origami describes the self-assembly process of designing and fabricating two- and three-dimensional nanostructures using DNA as a building material. DNA is a biopolymer composed of four different nucleotide building blocks, each containing one of the four nucleobases adenine (A), thymine (T), cytosine (C) and guanine (G). The nucleobases form complementary base pairs, specifically A-T and C-G, that hold together through hydrogen bonds.[128] Together with base stacking,[129] an additional stabilizing force, this base pairing leads to the hybridization of two complementary single-stranded DNA strands into a helical double strand. The concept of DNA origami utilizes this programmable self-assembly to fold long single-stranded DNA scaffolds (~1500 – 9000 nt) into predesigned shapes (see Fig. 14a). In this process, short single-stranded staple strands (~20 – 50 nt) with sequences complementary to different sections of the scaffold hybridize to the scaffold, thereby joining distal parts of the scaffold and gradually guiding it into its predesigned shape.[23,24]

Modifications to the resulting nanostructures are made with nanometer precision by conjugating molecules of interest to the DNA staple strands protruding from the folded structure at the corresponding positions. This for example enables the placement of fluorescent molecules, enzymes and bioreceptors in defined distances and geometries used when validating super-resolution microscopy methods,[120,130] when studying proximity effects in enzymatic cascade reactions[131] and when studying the effect of multivalency and spatial patterning on binding efficiencies.[132]

DNA origami nanostructures are not limited to static frameworks. They can be designed to incorporate dynamic elements or even undergo conformational changes themselves (see Fig. 14b). Dynamic elements can e.g. be designed to exhibit a controlled, confined motion ideally suited for validating highly precise tracking techniques[77,125,133] or to change their conformation in response to external stimuli,[27,126,134] a feature useful in biosensing applications. Fully dynamic structures are designed to undergo large-scale structural rearrangements themselves, allowing to program more complex behavior. They have e.g. been demonstrated to release a molecular cargo in response to different external stimuli,[28,135] to perform DNA computing[28,126] or to be used to control the responsive concentration window towards external stimuli.[26] As such, these dynamic features open new possibilities for nanoscale devices. They provide a basis for studying

molecular mechanisms, developing responsive systems and even autonomously operating nanomachines.[52,61,62]

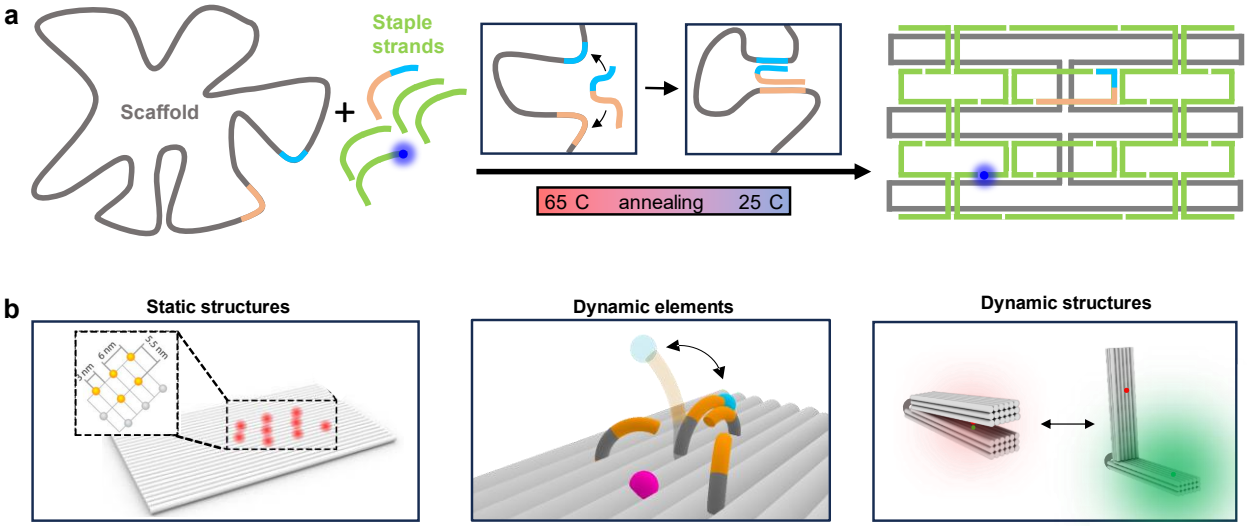

Figure 14: DNA origami nanostructures. (a) DNA origami self-assembly. A long circular single-stranded scaffold DNA strand (grey) is folded into a predefined structure guided by short single-stranded staple strands (green) that bind to different complementary sections of the scaffold (orange, blue) when applying a temperature ramp. By modifying these staple strands, various entities such as fluorescent molecules (blue dot) can be positioned on the resulting DNA origami nanostructures with nanometer precision. (b) Different types of DNA origami nanostructures. The DNA origami technique enables the construction of static frameworks for the precise positioning of entities such as fluorescent molecules (left, adapted from AIP Publishing: APL Materials[136]), of nanostructures hosting dynamic components (middle) as well as entirely dynamic structures (right).

2.2.2 Reconfigurable DNA origami arrays

A special class of fully dynamic DNA origami nanostructures are reconfigurable DNA origami arrays.[61,62,137] Reconfigurable DNA origami arrays are constructed of multiple structurally equivalent building blocks, so called antijunctions, which are interconnected by the scaffold strand of the DNA origami arrays. Antijunctions themselves can be understood as analogues to the more well-known Holliday junctions.

Holliday junctions are branched nucleic acid constructs composed of four double stranded DNA arms joined together in a cross-shaped configuration.[138] They can principally exist in three different conformations, a nearly square, planar (open) form and two stacked forms (see Fig. 15a). In absence of salts, Coulomb repulsion between the negatively charged DNA backbones drives Holliday junctions into their open conformation, maximizing the distance between their individual arms.[139] In contrast, in presence of divalent cations, such as Mg^2 , the positive charge of these ions shields the negative charges of the DNA backbone, weakening Coulomb repulsion. This causes the junctions

to adopt one of their stacked conformations where base stacking interactions at the junction core stabilize the structure.[140] Base stacking refers to the stabilizing interactions between adjacent nucleobases along the DNA helix. Together with Watson-Crick base pairing, these interactions – primarily driven by London dispersion forces and electrostatic attractions – help maintain the alignment of nucleobases in the typical DNA double helix form.[141,142] In presence of salts, these stabilizing forces make the stacked conformations of Holliday junctions more favorable and stable than the open conformation.

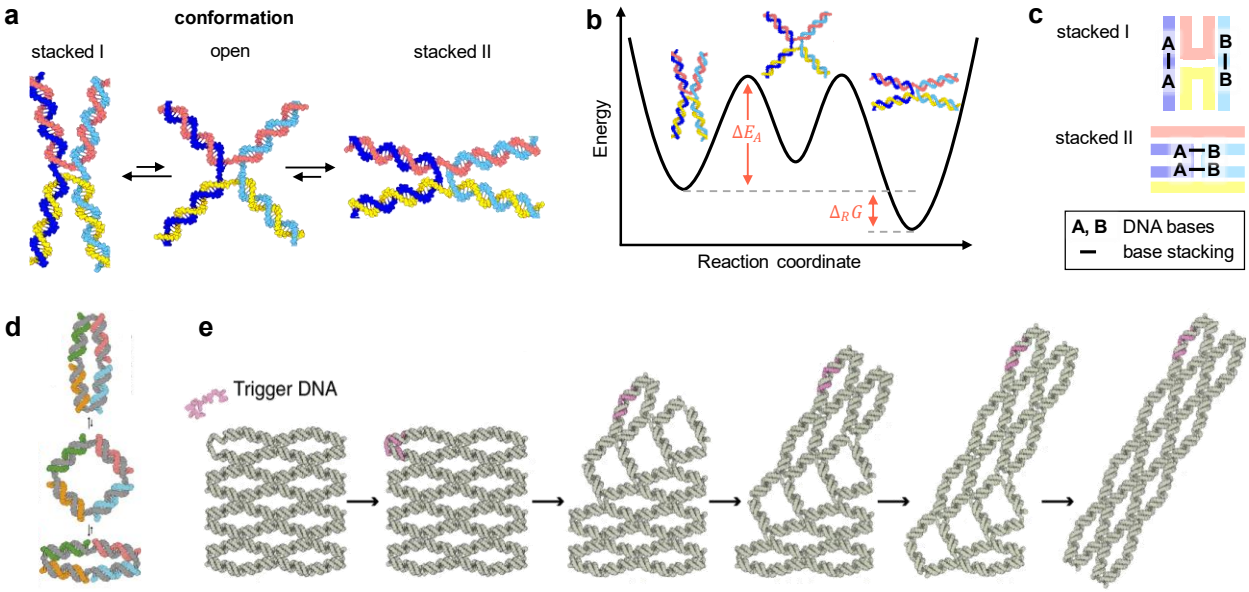

Figure 15: Analogy between Holliday junctions and antijunctions in reconfigurable DNA origami arrays. (a) Conformations of Holliday junctions. In the presence of salts, two stacked conformations stand in equilibrium with each other via an unstable open conformation. (b) Schematic energy landscape of the transition of a Holliday junction between its stacked conformations. (c) Different base stacking pairs forming in the junction's core of different stacked conformations of a Holliday junction. The equilibrium between both conformations is influenced by the difference in base stacking energy between them. As such, $\Delta_r \boldsymbol{G}$ in (b) depends on the DNA sequence of the Holliday junction at its core. (d) Antijunctions as building blocks for reconfigurable DNA origami arrays. Antijunctions transition between two stable stacked conformations analogous to Holliday junctions. (e) Reconfiguration pathway of reconfigurable DNA origami arrays consisting of multiple interconnected antijunctions. Hybridization of a trigger DNA strand (pink) to the left side of the array induces a stepwise conformational change of all antijunctions in the array system. (d,e) Adapted from Springer Nature: Nature Protocols, Copyright 2018.[137]

Holliday junctions then can switch between their two stable stacked conformations. This conformational switching occurs through the unstable open conformation. Equilibrium and kinetics of this dynamic behavior is influenced by various factors such as the concentration of divalent cations and the DNA sequence of the junction.[140,143] Higher Mg^2 concentrations for example increase the stability of the stacked conformations in comparison to the open concentration, increasing the activation energy barrier for the transition between the two stacked forms and slowing down the switching kinetics. The

equilibrium between the two stacked forms, in contrast, primarily depends on the sequence-dependent base stacking interactions, with some sequences biasing the junction towards one conformation over the other (see Fig. 15b,c).[140]

Antijunctions are characterized by an analogue dynamic behavior as Holliday junctions and can also switch between two stable stacked conformations via an unstable open form (see Fig. 15d). Interconnecting them in a reconfigurable DNA origami array forces them to all adapt the same conformation to minimize the presence of their unstable open conformation within the structure. By inducing a conformational change in antijunctions at the edge of the structure – typically through the hybridization of DNA strands – reconfigurable DNA origami arrays undergo a stepwise change in their global conformation. In this process, the antijunction at the edge relays the information of its changed conformational state to neighboring antijunctions, triggering them to change their conformation themselves. In a cascading reaction, this process repeats until all antijunctions in the array have switched their conformation (see Fig. 15e). This global reconfiguration, as visualized using atomic force microscopy, occurs in a diagonal manner to minimize the number of unstable open antijunctions at any given time.[61] It cannot only be triggered by hybridization of DNA strands but also has been shown to be initiated by enzymatic activity of DNA polymerase, exonuclease and ligase as well as by the presence of K^+ ions.[126,127] Besides this, the reconfiguration of the full array has also been demonstrated to activate proximity-induced operations, such as starting catalytic activity,[29] performing pattern-based operations like writing, erasing, and shifting[30] or generating optical output signals[126]. This broad versatility in application promises a good basis when attempting to recreate biological concepts in artificial systems.

3 PUBLICATIONS

3.1 MODULATION OF TRANSFORMATION OF DNA ORIGAMI NANOARRAY VIA SEQUENCE DESIGN

Dongfang Wang[1], **Fiona Cole**[1], Martina Pfeiffer[1], Tim Schröder, Philip Tinnefeld[*] and Yonggang Ke[*]

([1] These authors contributed equally, [*] Correspondence)

Submitted to Nature Communications

Holliday junctions play a key role in homologous recombination and DNA repair, facilitating the exchange of genetic material during cell division. Their typical symmetric design in nature makes them mobile. In a process known as branch migration, their arms slide along the participating DNA helix, moving the crossover position of the Holliday junction. However, to make use of their structural properties in DNA nanotechnology, immobile versions of Holliday junctions have been developed. By introducing asymmetric sequences that prevent branch migration, these immobile four-way junctions have since become one of the most essential structural motifs in DNA nanotechnology. They create connections between DNA strands, enabling the formation of complex constructs on the nanoscale.

Associated publication P1 explores whether the thermodynamic and kinetic properties observed in Holliday junctions can be transferred to synthetic DNA systems. Specifically, it investigates whether the principle of base stacking, which – depending on the DNA sequence at the junction's crossover region – stabilizes a certain conformation over the other in Holliday junctions also applies to DNA origami nanostructures. To explore this, reconfigurable DNA origami arrays where every incorporated junction shares an identical sequence at its core are designed, allowing to systematically study how these sequences influence the reconfiguration process. Using AFM imaging and FRET measurements both in ensemble and at the single-molecule level, both the thermodynamics and the kinetic of the switching behavior of these DNA arrays is investigated. This approach not only confirms that base-stacking principles also apply to larger artificial structures but also serves as a testbed for a dual FRET assay designed to monitor two dynamic processes simultaneously in associated publication P2. By probing different sequences, mismatches and free bases at the junction's core as well as environmental factors such as ion concentration, invaluable insights into the control of DNA origami systems are gained.

Ultimately, this study highlights the potential of DNA origami arrays as model systems for understanding and manipulating the dynamic behavior of DNA junctions, offering new strategies for precise control in nanotechnology.

3.2 Controlled mechanochemical coupling of antijunctions in DNA origami arrays

Fiona Cole[1], Martina Pfeiffer[1], Dongfang Wang[1], Tim Schröder, Yonggang Ke[*] and Philip Tinnefeld[*]

([1] These authors contributed equally, [*] Correspondence)

Nature Communications, volume 15, article number 7894 (**2024**)

DOI: 10.1038/s41467-024-51721-y

Similar to base stacking, allostery is a hallmark of cellular function and important in every biological system. It enables signal transduction and amplification as well as logic gating and (anti-)cooperativity. However, we are only starting to mimic allostery in the laboratory. Reconfigurable DNA origami arrays already carry intrinsic allosteric properties. Upon addition of DNA strands, these structures undergo a conformational change, carrying the input information from one side of the structure to the other. During this conformational change consisting of multiple sub-steps, the binding energy of DNA to the structure is converted to mechanical energy which propagates through the whole structure.

With the goal to introduce and understand allostery in artificial systems, associated publication P2 establishes a double FRET single molecule fluorescence assay and studies kinetics and thermodynamics not only of the whole reconfiguration process but also of different sub-steps in between. The assay reveals that many of the steps are strongly coupled and occur simultaneously – even in distances over tens of nanometers. From these findings, an energy landscape of the whole process, including activation barriers between intermediates, is derived. Using the double FRET assay, it then is shown how – by rational design – the height of these activation barriers can be engineered individually, resulting in a weakened coupling between previously simultaneously occurring steps and an alterable time delay between them. In a last step, it is illustrated how these findings can contribute to building artificial allosteric networks on the nanoscale. A cargo DNA strand is released from the structure under both temporal and spatial control, applying the principle of allosteric inhibition to dehybridize the cargo DNA strand from the structure – tens of nanometers away from the initial activation site. This shows how the recreation of biological concepts in artificial systems can be the direct consequence of the development of novel multiplexed imaging tools such as the double FRET assay, as effectively demonstrated in this work.

3.3 Spring-loaded DNA origami arrays as energy-supplied hardware for modular nanorobots

Martina Pfeiffer[1], **Fiona Cole[1]**, Dongfang Wang[1], Yonggang Ke[*] and Philip Tinnefeld[*]

([1] These authors contributed equally, [*] Correspondence)

Submission pending

The in-depth characterization of the reconfiguration process in associated publication P2 holds immense potential in context of the development of biocompatible nanomachines. For applications in clinical diagnostics, targeted therapeutics and synthetic biology, the capability of autonomously responding to complex environmental stimuli is highly sought-after. In recent years, DNA nanotechnology – particularly DNA origami– has made significant progress toward this goal. However, most existing DNA origami-based systems rely on a single stimulus to trigger a conformational change that produces a corresponding output. While functional for simpler tasks, this approach limits the scalability of these systems, making it difficult to integrate multiple stimuli and autonomously perform a series of controlled responses. Until now, a general framework for building modular nanomachines capable of handling these more complex operations has yet to be realized.

Associated publication P3 presents a novel approach to develop a modular, programmable nanorobot. It introduces a dynamic DNA origami-based hardware-software framework that integrates a pre-loaded energy source, allowing the nanorobot to autonomously perform operations on demand. This marks the first implementation of a generalizable platform that combines programmable control over input response ranges, biocomputing and multiple coordinated outputs.

The reconfigurable DNA origami array introduced in associated publication P2 serves as the scaffold for a series of functional two-state units which are selectively activated or inhibited based on their positioning within the array and the inputs they receive. The energy landscape of the reconfiguration process thereby governs how inputs propagate and are processed across the nanorobot. For activation of the reconfiguration process, the structure is pre-loaded with mechanical energy through fuel DNA hybridization, creating a spring-loaded system capable of storing and releasing energy to drive downstream processes. These include output operations such as fluorescence on/off switching or cargo release, both of which can be triggered in combination with logic gating-based decision making. By functionalizing the array with input-responsive units sensitive to ssDNA, light, enzymes and antibodies, it is demonstrated how the DNA origami array serves as a reconfigurable hardware platform. Inputs trigger or inhibit the

nanorobot's functions and can be combined to perform complex Boolean logic operations, allowing the system to process multiple signals in parallel and execute predefined output actions. Additionally, the responsive concentration window of these inputs can be finely tuned, shifting the effective concentration range by over 3000-fold, thus providing precise control over activation thresholds. The combination of a spring-loaded DNA origami hardware system with a modular software framework provides a powerful foundation for building multifunctional nanomachines capable of operating autonomously in biological environments with potential applications in targeted therapeutics and smart diagnostics.

3.4 Super-resolved FRET and co-tracking in pMINFLUX

Fiona Cole[1], Jonas Zähringer[1], Johann Bohlen, Tim Schröder, Florian Steiner, Martina Pfeiffer, Patrick Schüler, Fernando D. Stefani and Philip Tinnefeld[*]

([1] These authors contributed equally, [*] Correspondence)

Nature Photonics, volume 18, pages 478-484 (**2024**)

DOI: 10.1038/s41566-024-01384-4

Alongside of FRET that is applied in assays to monitor DNA origami array reconfiguration in associated publications P1-P3, pMINFLUX super-resolution microscopy provides an alternative approach for visualizing nanoscale changes, such as the shift in position of the arms of antijunctions during DNA origami reconfiguration. Capable of achieving spatial resolutions of around 2 nm within millisecond timeframes, pMINFLUX is particularly suited for tracking fast molecular events at the nanoscale. Despite these advantages, expanding pMINFLUX to multiple colors remains a major challenge, especially when it comes to the multiplexed co-tracking of multiple interacting molecules.

Associated publication P4 demonstrates the simultaneous tracking of two emitters with nanometer precision both in the FRET range and beyond with pulsed-interleaved MINFLUX (pMINFLUX). It demonstrates how pMINFLUX with its intrinsic fluorescence lifetime information not only allows combining FRET with super-resolved tracking but also enables fluorescence lifetime-based multiplexing without photoswitching, closing the resolution gap between single-molecule FRET and co-tracking.

The simultaneous visualizations are made possible by separating the emission of two emitters with similar spectral properties by their distinct fluorescence lifetimes. In combination with a novel combined phasor microtime gating approach for co-localization in the FRET range, this enables the co-localized tracking of two emitters in distances between 4 nm and 100 nm with nanometer precision. Both this novel multiplexing approach and applications of super-resolved FRET are demonstrated in simulation and experiment by tracking emitters as they transition between different positions on DNA origami model nanostructures, visualizing the binding sites of bivalent antibodies and separating translational and rotational motion of a DNA origami raft on a lipid bilayer. Both the multiplexing approach as well as the approach for super-resolved FRET are simple in their experimental implementation and also extendible to other super-resolution microscopy methods. This makes them invaluable tools for visualizing and understanding the complex interplay of multiple biological components on the nanoscale.

4 CONCLUSION AND OUTLOOK

The work presented in this thesis explores different strategies for advancing the field of nanotechnology and fluorescence microscopy with a focus on the development of novel methods for multiplexed tracking and understanding and engineering dynamic molecular processes. These studies contribute to both the design of artificial systems such as dynamic DNA origami nanostructures and the understanding of biological systems through the recreation of their fundamental principles in synthetic environments.

Associated publication P2 introduces a double FRET assay to map out the energy landscape of the reconfiguration process of DNA origami arrays. By using two distinct FRET pairs – each consisting of a fluorophore and a quencher – this assay enables the simultaneous tracking of multiple conformational changes within the same structure, revealing how energy barriers and intermediates govern the reconfiguration process. This precise characterization provides insights into the kinetics and thermodynamics between intermediates of the system, allowing to fine-tune the activation barriers at different steps. For reconfigurable DNA origami arrays, this deeper understanding translates to improved control over the stepwise reconfiguration process, paving the way for more efficient design strategies and allowing better control over dynamic nanostructures, as highlighted in associated publication P3.

While the double FRET assay is primarily used for qualitative insights in this work, fitting the resulting time difference distributions with (convolved) exponential functions can provide a more quantitative view of the energy landscape. Also, potential applications of the double FRET assay are not limited to artificial nanostructures like DNA origami arrays. The assay can also be extended to biological systems, where it holds promise for mapping energy landscapes of protein complexes or large biomolecular assemblies. For instance, it could reveal protein folding pathways[44,144] (see Fig. 16) or track allosteric regulation in systems like the ribosome complex[145,146]. Future enhancements, such as integrating the assay with plasmonic signal amplification strategies,[53] could further improve its temporal resolution by increasing intensity of its fluorescence response, enabling the study of more rapid interactions.

Besides keeping track of different conformational changes, another promising direction is the recent development of a sensor for measuring cellular loading rates introduced by the *Ha* lab this year, based on a similar double FRET design.[147] Here, the FRET pairs report on when a specified bond in a protein complex is under specific tension. By extracting the time difference between two distinct tension points, allows quantifying the rate at which cellular forces are built up, a critical factor in understanding processes such as mechanotransduction in cell adhesion. This illustrates the flexibility of the double FRET

assay beyond studying molecular conformations, extending its applications into areas such as force sensing and the mechanobiology of cells.

Despite the broad applicability of the double FRET assay, certain challenges remain, particularly in biological systems. One major limitation is the degree of labeling achievable in protein complexes, where the quantitative attachment of multiple fluorescent molecules is often difficult.[148] Recent advances in protein labeling techniques, however, offer potential solutions.[149–151] By overcoming this limitation, the double FRET assay could become a powerful tool for studying complex biomolecular processes in living systems, providing insights into the network of conformational changes that underlie biological function.

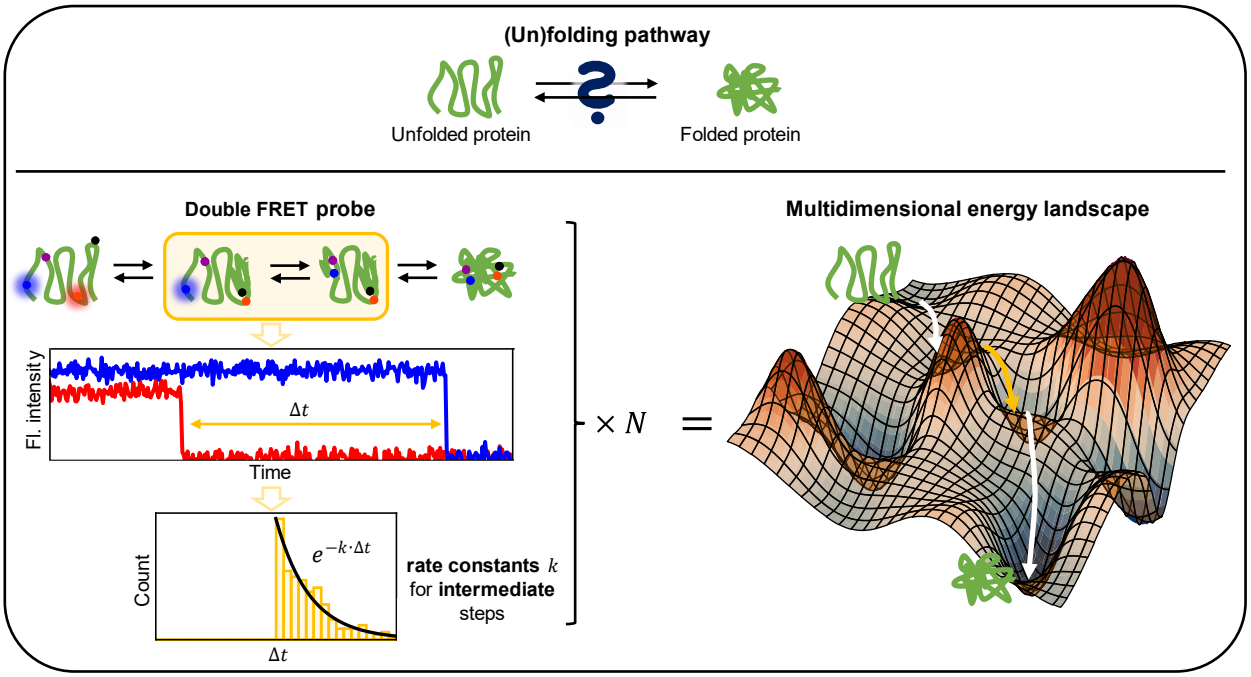

Figure 16: Concept of applying the double FRET assay to map the energy landscape of protein folding. Strategic placement of two FRET probes within an unfolded protein (upper left sketch) enables real-time monitoring of intermediate steps in the protein folding pathway (highlighted in yellow). When measuring the time intervals between folding events (middle left sketch) for multiple structures, analyzing the resulting distributions (lower left sketch) allows determining the rate constants for these steps. Repeating this process with FRET probes at different positions provides deeper insight into the underlying energy landscape of the protein (right sketch).

Associated publication P3 combines pMINFLUX with FRET measurements. In this approach, pMINFLUX is used to localize the FRET donor molecule and the fluorescence lifetimes corresponding to each localization are converted into donor-acceptor distances based on the known Förster radius of the FRET pair. By determining at least three FRET

donor positions and their corresponding lifetimes, multilateration then enables the accurate localization of the (static) FRET acceptor.

The multilateration approach is not just limited to the localization of fluorescent FRET acceptors as demonstrated in associated publication P3. Just as black holes in astrophysics are detected and studied through their gravitational interactions with surrounding celestial bodies,[152] this method could also be applied to locate and study fluorescence quenchers – molecules that do not emit light themselves – by exploiting their effects on neighboring fluorescent molecules. By measuring the impact of quenchers on the fluorescence of nearby localized donor molecules, this method allows for indirect localization of the quenchers even though they remain non-emissive themselves.

Taking this further, if more than three donor molecules are positioned near a static FRET acceptor, the Förster radius can be treated as a free fit parameter in the multilateration approach. This not only enables precise localization of the acceptor but also allows for the direct measurement of the Förster radius itself. Current experimental methods for determining Förster radii typically rely on pre-defined distances between fluorescent molecules, requiring multiple calibration structures with known FRET pair separations.[153] By contrast, this new approach could streamline the process by eliminating the need for such calibrations, enabling a more direct method for determining Förster radii.

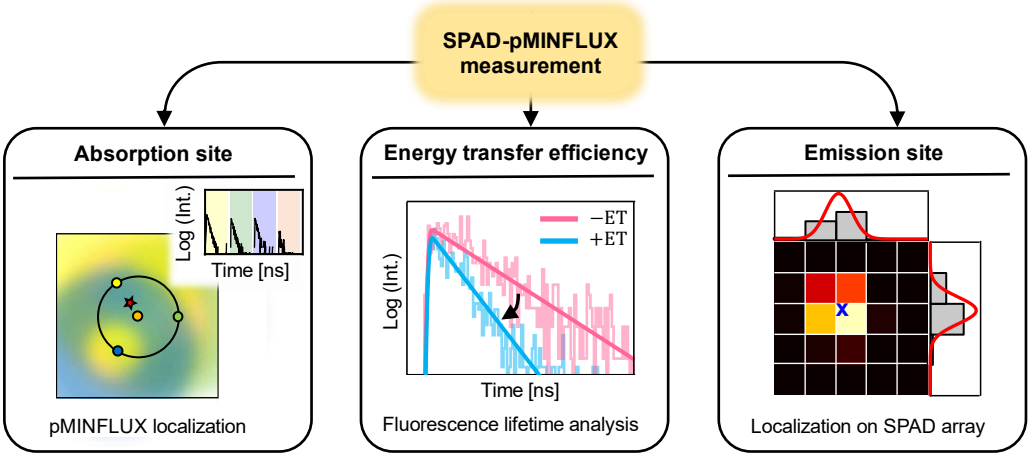

Figure 17: Potential of SPAD array detectors in pMINFLUX for characterizing energy transfer processes. Implementing a SPAD array in the detection system of pMINFLUX allows simultaneously probing both the absorption site (left panel) and the emission site (right panel) of a fluorescent molecule, while also measuring the corresponding energy transfer efficiency (middle panel). The absorption site is localized with pMINFLUX, the energy transfer efficiency is calculated from the reduced fluorescence lifetime and the emission site is determined by localization on the pixelated SPAD array. In combination, this has the potential to offer a detailed picture of energy transfer dynamics.

To study energy transfer processes like FRET in greater detail, integrating an array of single-photon avalanche diodes (SPAD array) into the detection system of MINFLUX could enable simultaneous mapping of both absorption and emission sites (see Fig. 17).

MINFLUX, with its spatial information derived from the controlled excitation beam positions, localizes the absorption sites of fluorescent molecules. In contrast, camera-based techniques determine molecular positions by fitting Gaussian distributions to their emission profiles. SPAD arrays, functioning as pixelated detectors, allow separate photon detection at each pixel, thereby creating an intensity-based image akin to a camera while also providing the information necessary for MINFLUX localizations.[154] Incorporating SPAD arrays into a MINFLUX system could thus combine absorption site localizations through MINFLUX with emission site localizations through the SPAD array. In most cases, these two sites will coincide. However, in instances of energy transfer, absorption and emission may occur at different locations. While energy transfer between two individual molecules are well understood, applying this dual-way detection approach could provide significant insights into the photophysical properties of more complex environments, such as conjugated polymers.[155] These materials find applications in optoelectronic devices like OLEDs and polymer photovoltaic cells and often exhibit energy transfer along their polymer chains.[156–159] Gaining access to both absorption and emission sites on these chains could deepen our understanding of the structure-function relationships governing the performance of conjugated polymers in electronics applications, potentially improving both their efficiency and their functionality.

In terms of multiplexed co-tracking with pMINFLUX, associated publication P4 explores the use of fluorescence lifetime information to enable the nanometer precise co-localization of fluorescent molecules, both inside and beyond the FRET range, without relying on photo-switching. Outside the FRET range, a multi-exponential fit is used to assign detected photons to their respective emitters, achieving the simultaneous localization of two fluorescent molecule within the same diffraction limited spot with a precision of better than 2 nm. Inside the FRET range, a novel microtime-gating phasor approach complements pMINFLUX multiplexing, also enabling precise co-localization. Together, these techniques close the resolution gap between single-molecule FRET and co-tracking.

Building on this, future advancements could involve combining the multi-exponential fitting approach with phasor-based microtime gating also outside the FRET range, making the localization algorithm more robust and potentially extending pMINFLUX multiplexing to simultaneously localize three or more fluorescent molecules. However, increasing the number of localized molecules requires fluorescent molecules with sufficiently distinct fluorescence lifetimes to maintain localization precision. Without this fluorescence lifetime contrast, localization precision could deteriorate as the fluorescence lifetimes become too similar. This challenge is especially pronounced in biological samples where variable background contributions further complicate photon assignment. While it may be technically feasible to extend multiplexing to three fluorophores or more, biological environments pose significant hurdles that may limit the practicality of this approach.

To overcome these limitations, a more promising strategy might be to combine pMINFLUX multiplexing with other orthogonal multiplexing methods. Recent advances, such as two-color excitation MINFLUX developed by the *Hell* and *Balzarotti* groups, use excitation beams with different wavelengths to distinguish between fluorescent molecules with distinct spectral properties.[160,161] Another innovative technique involves a deconvolution-based method that can localize and track two spectrally identical fluorophores as close as 8 nm apart.[162] Since these methods separate fluorophores based on different properties than pMINFLUX multiplexing, they can be integrated without compromising overall precision beyond the convolution of their individual losses in precision. In theory, combining these approaches could enable the simultaneous tracking of up to eight molecules, providing unprecedented detail for studying dynamic molecular processes at the nanoscale.

Such multiplexing capabilities in MINFLUX hold immense potential for advancing scientific understanding. For example, two-color MINFLUX has already shed light on the debated walking mechanism of the motor protein kinesin.[160] Multiplexed MINFLUX could further help explore phenomena such as transport through nuclear pore complexes[163] or DNA repair mechanisms[164] by visualizing how repair proteins interact with damaged DNA sites. Beyond these applications, protein complexes and their dynamic behaviors could also be studied in real-time.[145] The potential of multiplexed MINFLUX is further enhanced by recent adaptations enabling MINFLUX to perform deep-tissue imaging up to 80 micrometers beneath the surface,[165] opening the door to even more exciting developments in the years to come.

Publication P3 presents a modular DNA nanorobot framework, SEPP (Serial Execution of Programmable Processes), which introduces a universal design strategy for nanomachines based on reconfigurable DNA origami arrays. SEPP interprets the individual antijunctions in the arrays as two-state systems into which proximity-dependent functionalities can be included. In DNA origami arrays, these two-state systems are coupled into a network, enabling the resulting nanorobot to process multiple stimuli using multi-level Boolean logics and execute operations in response to them. Through the rational incorporation of various input units such as enzymes, light, and antibodies, SEPP autonomously responds to stimuli with precise control over output operations like cargo release and fluorescence signals. This platform promises a significant leap forward in the development of DNA nanorobots. By integrating both allosteric regulation and programmable energy landscapes into nanodevices, it offers potential applications in diagnostics, targeted drug delivery and synthetic biology.

One of the key challenges for SEPP, particularly in sensing and therapeutic applications, lies in expanding the range of stimuli to which it is responsive to. Currently, the inputs used in most stimuli-responsive dynamic DNA origami systems, including SEPP, are of limited relevance to real-world disease diagnostics and treatments. To broaden the scope

of inputs, the incorporation of aptamers offers a promising solution.[166,167] Aptamers are short, single-stranded nucleic acid sequences that bind specifically to target molecules such as proteins, peptides, small molecules or even whole cells and tissues.[168,169] SOMAmers (Slow Off-rate Modified Aptamers) which include non-native hydrophobic side groups to enhance stability and protein interactions, further extend the design possibilities.[170] For both aptamers and SOMAmers, extensive libraries against diagnostically relevant targets exist, opening new avenues for disease-related inputs in DNA nanotechnology. SEPP could be modified to include aptamer-based inputs in an analogous manner to single-stranded DNA inputs where target molecule binding opens a DNA lock – in this case including the aptamer sequence, triggering or inhibiting reconfiguration. The approach of such DNA locks has already been demonstrated in DNA origami systems,[27] suggesting its potential for reconfigurable arrays. Similarly, aptamers could be employed as output units for drug delivery, enabling precise control over the uptake or release of therapeutic molecules. With a collection of SOMAmers targeting over 11,000 human proteins already available[171] and the emergence of machine learning as a powerful tool for efficient screening,[172] this strategy – if fully realized – holds significant promise for expanding the range of therapeutically relevant targets in reconfigurable DNA origami arrays in the near future.

Another major challenge is the stability of DNA origami nanostructures under physiological conditions. While they show good stability in buffered environments, biological matrices such as blood or saliva degrade these structures quickly due to the presence of e.g. DNases. Recent developments, including polymer coatings[173,174] and self-repair strategies[175], offer ways to protect DNA origami. However, these methods also tend to stiffen the structures, which could affect dynamic systems like SEPP. Protruding DNA strands that provide functional outputs could benefit from stabilization using e.g. bridged nucleic acids[176,177] or hydrophobic modifications, as seen in SOMAmers[170].

Also, dissipative approaches as developed in the *Ricci* group[178,179] could be employed to reset these systems, allowing SEPP to autonomously restore its initial state for repeated operation, an essential feature for some real-world applications. Without this, systems may need manual resetting by actively removing the environmental stimuli from solution, limiting their long-term usability.

A notable advantage of the antijunction motif in SEPP is its symmetry during reconfiguration. While some distances between domains increase, others decrease by the same extent. This feature allows the same design motif to be used for both activation and inhibition as shown in associated publication P3. However, this symmetry could also enable more advanced behaviors, such as creating biphasic dose-response curves where the system is activated at low stimulus concentrations but inhibited at higher levels. Such a response is mathematically described by the product of activation and inhibition curves and can be achieved by incorporating two double-stranded DNA locks: one stabilizing the reconfigured state and the other stabilizing the non-reconfigured state. By designing overlapping locks which share a single-stranded DNA part of the lock and have different

strand displacement thresholds, the reconfiguration can be activated at low stimulus levels and inhibited at higher concentrations, recreating the biphasic response commonly seen in biology in artificial systems (see Figs. 18, 19).

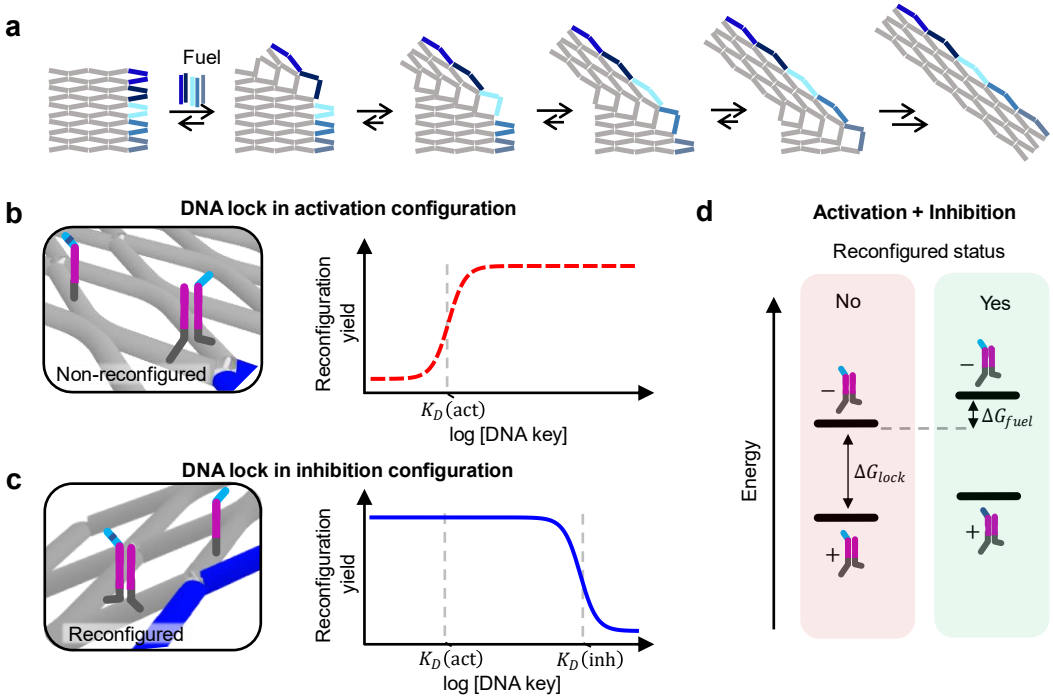

Figure 18: Design strategy for biphasic dose-response curves in SEPP. (a) Reconfiguration of the DNA origami array forming the basis for SEPP. (b) A DNA lock stabilizing the non-reconfigured state (activation lock) is combined (c) with a DNA lock stabilizing the reconfigured state (inhibition lock) of the same antijunction. When triggered by a single-stranded DNA key, the locks are opened, controlling the reconfiguration process: (b) opening of the activation lock promotes reconfiguration, while (c) opening of the inhibition lock suppresses reconfiguration. A higher K_D of the inhibition lock is engineered by reducing the DNA key's affinity for the lock, e.g., via mismatches in the single-stranded overhang of the inhibition lock. Both locks share a common DNA strand, ensuring that only one lock can be closed at a time, enabling biphasic dose-response behavior. (d) Energy landscape for various lock configurations, with four possible states depending on whether the activation or inhibition locks are closed ( ) or opened (-). The added fuel DNA strands (ΔG_{fuel}) result in an energetic favoring of the non-reconfigured state in the absence of any closed locks, while closing a lock stabilizes the corresponding conformation by ΔG_{lock}. The landscape is asymmetrically organized, with each lock's closure favoring its respective state, enabling the design of biphasic dose-response curves.

Biphasic responses, such as hormesis, are prevalent in biology and describe situations where low doses of a stimulus elicit a beneficial response, while higher doses cause inhibition or toxicity.[180] This principle is seen in e.g. oxygen levels where low amounts are necessary for respiration, but excess oxygen becomes harmful.[181] Hormesis is similarly important in fields like toxicology and pharmacology, where dosage defines whether a substance is therapeutic or toxic. Implementing biphasic dose-response systems in artificial constructs like SEPP could advance our understanding of such biological behaviors by recreating them in rationally designed systems. If combined with

e.g. proximity-induced DNAzyme activity,[29,182] these designs could pave the way for more controllable, responsive therapeutic platforms.

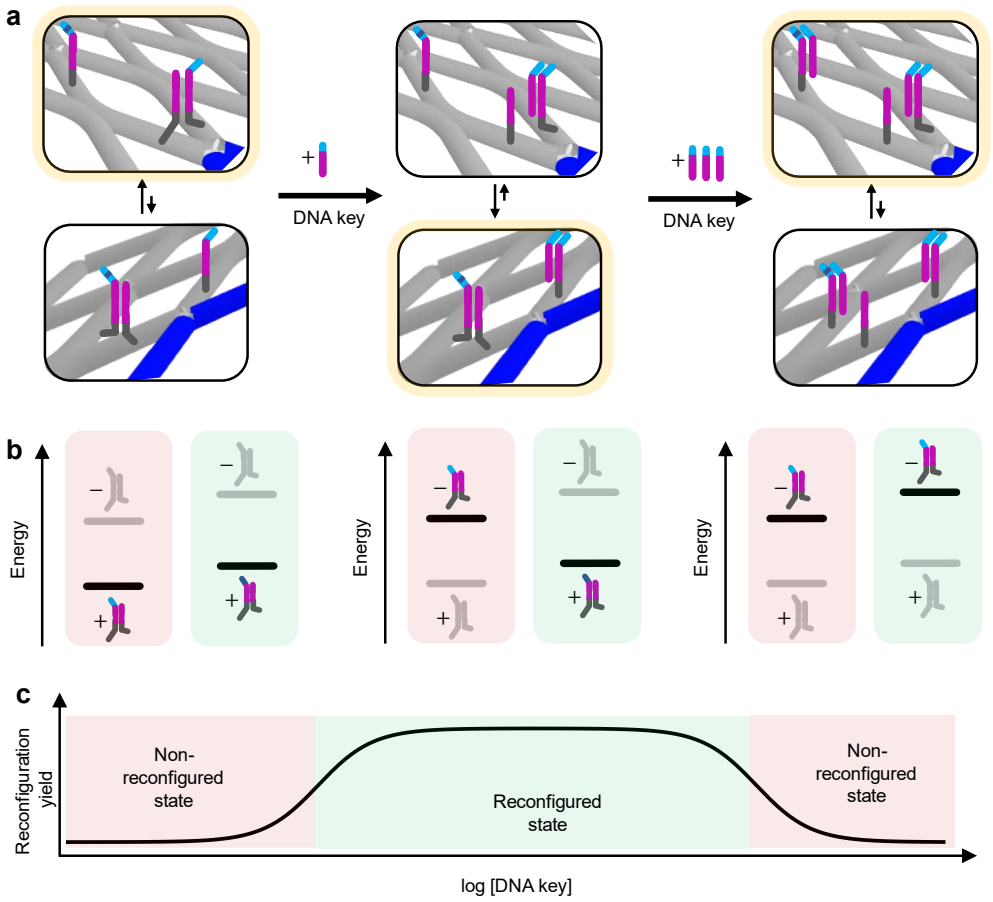

Figure 19: Working principle of prospective SEPP systems with biphasic dose-responses. Potential states of an antijunction configured for biphasic dose-response behavior, as described in Fig. 11. The upper row represents the non-reconfigured conformation, and the lower row represents the reconfigured conformation, both dependent on the concentration of DNA key. Energetically favored states are highlighted with a yellow border. In the absence of DNA key, both locks (activation and inhibition) can remain closed. Due to the energy tilt introduced by fuel DNA strands, the non-reconfigured conformation is energetically preferred. At low DNA key concentrations, the lock stabilizing the non-reconfigured conformation opens first, as designed through differing binding affinities of the DNA key to both locks. This causes competition between the non-reconfigured state without a closed lock and the reconfigured state with a closed lock, energetically biasing the system towards the reconfigured conformation. At higher DNA key concentrations, the lock stabilizing the reconfigured state also opens, and neither state is stabilized by a lock. The tilt in the energy landscape caused by the fuel strands once again favors the non-reconfigured conformation. (b) Scheme of the energy landscape at varying DNA key concentrations. The lowest-energy states of both non-reconfigured (red, left) and reconfigured (green, right) conformations as highlighted in (a) are marked in color. (c) Biphasic dose-response curve potentially enabled by this design.

And with this, I would like to end the thesis with the same quote it started. *“The whole is greater than the sum of its parts.”* In this thesis, I tried to create synergies following Aristotle’s quote on three different levels: by implementing synergies in synthetic nanodevices, by highlighting the how advances in nanodevices engineering and single-molecule imaging techniques create synergies on a methodological level and finally, but no less important by breaking these findings down to simple and easily understandable language in the last 42 pages, hopefully providing a basis for collaborative synergies between researchers, helping to share knowledge to drive new advancements in the years to come.

5 ACKNOWLEDGEMENTS

Pursuing a PhD is a journey. A journey in which you learn to navigate the landscape of scientific research, push your own intellectual limits and – possibly most important – create lasting memories. And as on all journeys, you do not reach your destination purely through your own work but only through the help and contribution of others. And with this, I would like to thank a multitude of different people.

First of all, thank you Philip Tinnefeld. Thank you for serving as a mentor throughout my PhD journey. Thank you for your invaluable contributions of time and insight and for giving me the freedom to explore and develop my own research ideas. Your guidance has been essential for this thesis.

I also would like to thank Prof. Dr. Alena Khmelinskaia for being the second evaluator of this thesis and Prof. Dr. Achim Hartschuh, PD Dr. Jan Vogelsang, Prof. Dr. Thomas M. Klapötke and Prof. Dr. Silvija Markic for joining my thesis committee.

Thank you, Jonas Zähringer. Thank you for taking me on as a Forschungs-Praktikant with no knowledge on single-molecule methods and optics whatsoever and only very limited knowledge on fluorescence altogether. Thank you for continuing to supervise me throughout my Master thesis and also for providing guidance especially at the start of my PhD. Thank you for all the long (and sometimes also very exasperating) days we had aligning the pMINFLUX setup together and all the successful (and even more unsuccessful) measurements we performed. A lot of this work would not have been possible without you. Thank you also Giovanni Ferrari for a really cool graphene measurement we performed together towards the end of my PhD.

In this context also thank you, Florian Steiner. Thank you for introducing me to the world of optics and always being open to discussing and helping with any MINFLUX-related problems. Thank you also Johann Bohlen for designing the clock origami which became some sort of reference system when (re)aligning the MINFLUX and being very helpful with any DNA origami design related questions in general.

Thank you Tim Schröder. Thanks for handing over the reconfiguration origami project to Martina and me towards the end of your PhD. This project accompanied me throughout my whole PhD. Thank you for being so helpful with any questions whether it was concerning the reconfiguration origami, photophysics or anything else. Thank you also Prof. Dongfang Wang and Prof. Yonggang Ke for the very fruitful collaboration on reconfigurable DNA origami arrays and all the long Zoom meetings we had discussing results together.

Thank you, Martina Pfeiffer. Thank you for introducing me to the lab, thank you for the projects we had together, thank you for the near endless measurement series we

performed together, all your advice and generally all the fun times we had together. Same as for Jonas, a lot of this work would not have been possible without you!

A big thank you also goes to all my office members Sarah, Katya, Andres, Patrick, Merve, Giovanni and Martina for providing such a great atmosphere and many fruitful scientific and also very fruitful non-scientific office discussions. Thank you also for putting up with the nearly uncountable number of plants Martina and me grew in our office.

Thanks also to the students, Pauline and Stella, I had the pleasure of supervising. You really helped pushing the projects you worked on forward. Thank you, Angelika, for all the work you are doing in the lab and also for always having an open ear for PhD students. Thank you also Herr Ehrl, for so readily taking on a >3 m Korkeiche on your 60th birthday. Thank you also Herr Ehrl, Frau Steger, Frau Lipfert and Kalys for helping in administrative and organizational matters.

In general, thanks a to all current and former members of the Tinnefeld group. I learnt a lot from really all of you.

And last, but no less important: Although it is not easy to thank dogs, thank you Xaverl, Charly and Luna for all the support you provided throughout experiment design, measurements, data analysis and writing. Without you, none of this would have been possible!

6 OVERVIEW PUBLICATIONS

[1] These authors contributed equally, [*] Correspondence

Peer-Reviewed Publications

1. **Fiona Cole**[1], Martina Pfeiffer[1], Dongfang Wang[1], Tim Schröder, Yonggang Ke[*] and Philip Tinnefeld[*]. Controlled mechanochemical coupling of anti-junctions in DNA origami arrays. *Nat. Commun.* **2024**, *15*, 7894.

2. Julian Bauer, **Fiona Cole**, Renukka Yaadav, Jonas Zähringer, Tim Schröder and Philip Tinnefeld[*]. Ultra-specific detection of nucleic acids by intramolecular referencing, *SPIE* **2024**, 17-20.

3. **Fiona Cole**[1], Jonas Zähringer[1], Johann Bohlen, Tim Schröder, Florian Steiner, Martina Pfeiffer, Patrick Schüler, Fernando D. Stefani and Philip Tinnefeld[*]. Super-resolved FRET and co-tracking in pMINFLUX, *Nat. Photonics* **2024**, *18*, 478-484.

4. Jonas Zähringer, **Fiona Cole**, Johann Bohlen, Florian Steiner, Izabela Kamińska and Philip Tinnefeld*. Combining pMINLFUX, graphene energy transfer and DNA-PAINT for nanometer precise 3D super-resolution microscopy, *Light Sci. Appl.* **2023**, *12*, 70.

5. Martina Pfeiffer[1], Kateryna Trofymchuk[1], Simona Ranallo, Francesco Ricci, Florian Steiner, **Fiona Cole**, Viktorija Glembockyte[*] and Philip Tinnefeld[*]. Single Antibody Detection in a DNA Origami Nanoantenna, *iScience* **2021**, *24*, 103072.

6. Luciano A. Masullo[1], Florian Steiner[1], Jonas Zähringer, Lucia F. Lopez, Johann Bohlen, Lars Richter, **Fiona Cole**, Philip Tinnefeld* and Fernando D. Stefani*. Pulsed interleaved MINFLUX, *Nano Lett.* **2021**, *21*, 840-846.

Manuscripts in preparation

7. Dongfang Wang[1], **Fiona Cole**[1], Martina Pfeiffer[1], Tim Schröder, Philip Tinnefeld[*] and Yonggang Ke[*]. Modulation of transformation of DNA origami nanoarray via sequence design. Submitted to *Nat. Commun*.

8. Martina Pfeiffer[1], **Fiona Cole**[1], Dongfang Wang[1], Yonggang Ke[*] and Philip Tinnefeld[*]. Spring-loaded DNA origami arrays as energy-supplied hardware for modular nanorobots. bioRxiv, Submitted to *Sci. Robot.*

9. Pooyeh Asadiatouei, Johann Bohlen, **Fiona Cole**, Fabio Morella, Philip Tinnefeld, Evelyn Ploetz and Don C. Lamb[*]. Distance and kinetic tunability of

dynamic DNA origami structures examined at the single-molecule level. Submission pending.

10. Tim Schröder[1], Julian Bauer[1], Patrick Schüler[1], Jonas Zähringer, **Fiona Cole**, Johann Bohlen, Giovanni Ferrari, Laura Barnard, Karen Nachname, Gereon Brüggenthies and Philip Tinnefeld[*]. Brownian DNA Computing. Submission pending.

11. Michael Scheckenbach, Cindy Close, Alan Szalai, Julian Bauer, Lennart Grabenhorst, **Fiona Cole**, Lei Zhang, Thorben Cordes, Philip Tinnefeld and Viktorija Glembockyte[*]. Minimally Invasive DNA-Mediated Photostabilization for Extended Single-Molecule and Super-resolution Imaging. Submission pending.

Patent applications

12. Philip Tinnefeld, Jonas Zähringer, Johann Bohlen and **Fiona Cole**. Binding hierarchies for accelerated superresolution, European patent application AF4294 EP S5.

7 BIBLIOGRAPHY

[1] S. M. Cohen, C. D. C. Reeve, *Aristotle's Metaphysics* **2000**.
[2] P. A. Corning, *The synergism hypothesis: A theory of progressive evolution*, McGraw-Hill, New York **1983**.
[3] Z. Bozoky, S. Ahmadi, T. Milman, T. H. Kim, K. Du, M. Di Paola, S. Pasyk, R. Pekhletski, J. P. Keller, C. E. Bear, J. D. Forman-Kay, *Proceedings of the National Academy of Sciences of the United States of America* **2017**, *114*, E2086-E2095.
[4] J. M. Pérez-Pérez, H. Candela, J. L. Micol, *Trends in Genetics* **2009**, *25*, 368.
[5] S. Joshi, T. Wang, T. L. S. Araujo, S. Sharma, J. L. Brodsky, G. Chiosis, *Nat Rev Cancer* **2018**, *18*, 562.
[6] M. Stucki, I. Stagljar, Z. O. Jonsson, U. Hübscher, in *Progress in Nucleic Acid Research and Molecular Biology*, Vol. 65, Academic Press **2000**, p. 261.
[7] C. G. Kalodimos, N. Biris, Alexandre M. J. J. Bonvin, M. M. Levandoski, M. Guennuegues, R. Boelens, R. Kaptein, *American Association for the Advancement of Science* **2004**, https://www-science-org.emedien.ub.uni-muenchen.de/doi/full/10.1126/science.1097064.
[8] T. J. Begley, L. D. Samson, *DNA Repair* **2004**, *3*, 1123.
[9] R. B. Freedman, P. Klappa, L. W. Ruddock, *EMBO reports* **2002**, *3*, 136.
[10] S. L. Harris, A. J. Levine, *Oncogene* **2005**, *24*, 2899.
[11] R. Avraham, Y. Yarden, *Nat Rev Mol Cell Biol* **2011**, *12*, 104.
[12] M. Saxena, S. Williams, K. Taskén, T. Mustelin, *Nature cell biology* **1999**, *1*, 305.
[13] R. Nussinov, C.-J. Tsai, J. Liu, *J. Am. Chem. Soc.* **2014**, *136*, 17692.
[14] R. Nussinov, C.-J. Tsai, B. Ma, *Annual Review of Biophysics* **2013**, *42*, 169.
[15] J.-Y. Trosset, P. Carbonell, *Frontiers in bioengineering and biotechnology* **2013**, *1*, 11.
[16] J. Pilas, Y. Yazici, T. Selmer, M. Keusgen, M. J. Schöning, *Sensors* **2018**, *18*, 1470.
[17] E. Katz, J. Wang, M. Privman, J. Halámek, *Analytical chemistry* **2012**, *84*, 5463.
[18] C. Alvarez-Lorenzo, A. Concheiro, *Chem. Commun.* **2014**, *50*, 7743.
[19] R. Sarup, N. Singh, in *Nanomedicine in Translational Research* (Eds.: C. P. Sharma, K. Kaladhar), Academic Press **2025**, p. 271.
[20] D. Liu, F. Yang, F. Xiong, N. Gu, *Theranostics* **2016**, *6*, 1306.
[21] Y.-C. Lee, J.-Y. Moon, in *Introduction to Bionanotechnology*, Springer, Singapore **2020**, p. 93.
[22] V. Wagner, A. Dullaart, A.-K. Bock, A. Zweck, *Nat Biotechnol* **2006**, *24*, 1211.
[23] P. W. K. Rothemund, *Nature* **2006**, *440*, 297.
[24] K. F. Wagenbauer, F. A. S. Engelhardt, E. Stahl, V. K. Hechtl, P. Stömmer, F. Seebacher, L. Meregalli, P. Ketterer, T. Gerling, H. Dietz, *Chembiochem a European journal of chemical biology* **2017**, *18*, 1873.
[25] J. J. Schmied, M. Raab, C. Forthmann, E. Pibiri, B. Wünsch, T. Dammeyer, P. Tinnefeld, *Nat Protoc* **2014**, *9*, 1367.

[26] L. Grabenhorst, M. Pfeiffer, T. Schinkel, M. Kümmerlin, J. B. Maglic, G. A. Brüggenthies, F. Selbach, A. T. Murr, P. Tinnefeld, V. Glembockyte, *Engineering Modular and Tunable Single Molecule Sensors by Decoupling Sensing from Signal Output* **2023**.
[27] M. S. L. Tang, S. C.-C. Shiu, M. Godonoga, Y.-W. Cheung, S. Liang, R. M. Dirkzwager, A. B. Kinghorn, L. A. Fraser, J. G. Heddle, J. A. Tanner, *Nanomedicine nanotechnology, biology, and medicine* **2018**, *14*, 1161.
[28] S. M. Douglas, I. Bachelet, G. M. Church, *Science (New York, N.Y.)* **2012**, *335*, 831.
[29] S. Fan, B. Ji, Y. Liu, K. Zou, Z. Tian, B. Dai, D. Cui, P. Zhang, Y. Ke, J. Song, *Angewandte Chemie International Edition* **2022**, *61*, e202116324.
[30] S. Fan, J. Cheng, Y. Liu, D. Wang, T. Luo, B. Dai, C. Zhang, D. Cui, Y. Ke, J. Song, *Journal of the American Chemical Society* **2020**, *142*, 14566.
[31] I. Domljanovic, M. Loretan, S. Kempter, G. P. Acuna, S. Kocabey, C. Ruegg, *Nanoscale* **2022**, *14*, 15432.
[32] D. Wang, L. Yu, C.-M. Huang, G. Arya, S. Chang, Y. Ke, *Journal of the American Chemical Society* **2021**, *143*, 2256.
[33] J. MONOD, J. P. CHANGEUX, F. JACOB, *Journal of Molecular Biology* **1963**, *6*, 306.
[34] J. MONOD, F. JACOB, *Cold Spring Harbor symposia on quantitative biology* **1961**, *26*, 389.
[35] D. E. Koshland, G. Némethy, D. Filmer, *Biochemistry* **1966**, *5*, 365.
[36] J. MONOD, J. WYMAN, J. P. CHANGEUX, *Journal of Molecular Biology* **1965**, *12*, 88.
[37] W. A. Lim, *Current Opinion in Structural Biology* **2002**, *12*, 61.
[38] V. Galstyan, L. Funk, T. Einav, R. Phillips, *The journal of physical chemistry. B* **2019**, *123*, 2792.
[39] R. Gruber, A. Horovitz, *Chemical reviews* **2016**, *116*, 6588.
[40] Y. Yuan, M. F. Tam, V. Simplaceanu, C. Ho, *Chemical reviews* **2015**, *115*, 1702.
[41] U. Alon, *Science (New York, N.Y.)* **2003**, *301*, 1866.
[42] R. Roy, S. Hohng, T. Ha, *Nat Methods* **2008**, *5*, 507.
[43] Y. Gambin, A. A. Deniz, *Molecular BioSystems* **2010**, *6*, 1540.
[44] B. Schuler, W. A. Eaton, *Current Opinion in Structural Biology* **2008**, *18*, 16.
[45] D. K. Sasmal, L. E. Pulido, S. Kasal, J. Huang, *Nanoscale* **2016**, *8*, 19928.
[46] T. R. Weikl, F. Paul, *Protein Science* **2014**, *23*, 1508.
[47] A. Robinson, A. M. van Oijen, *Nat Rev Microbiol* **2013**, *11*, 303.
[48] M. Stracy, S. Uphoff, F. Garza de Leon, A. N. Kapanidis, *FEBS letters* **2014**, *588*, 3585.
[49] Y. Alhadid, S. Chung, E. Lerner, D. J. Taatjes, S. Borukhov, S. Weiss, *Protein Science* **2017**, *26*, 1278.
[50] S. C. Blanchard, *Current Opinion in Structural Biology* **2009**, *19*, 103.
[51] J. B. Munro, A. Vaiana, K. Y. Sanbonmatsu, S. C. Blanchard, *Biopolymers* **2008**, *89*, 565.

[52] M. Centola, E. Poppleton, S. Ray, M. Centola, R. Welty, J. Valero, N. G. Walter, P. Šulc, M. Famulok, *Nat. Nanotechnol.* **2024**, *19*, 226.
[53] L. Grabenhorst, F. Sturzenegger, M. Hasler, B. Schuler, P. Tinnefeld, *Journal of the American Chemical Society* **2024**, *146*, 3539.
[54] M. Götz, P. Wortmann, S. Schmid, T. Hugel, *Journal of visualized experiments JoVE* **2018**.
[55] S. Hohng, C. Joo, T. Ha, *Biophysical Journal* **2004**, *87*, 1328.
[56] J. Yoo, J.-Y. Kim, J. M. Louis, I. V. Gopich, H. S. Chung, *Nat Commun* **2020**, *11*, 3336.
[57] E. Kim, S. Lee, A. Jeon, J. M. Choi, H.-S. Lee, S. Hohng, H.-S. Kim, *Nat Chem Biol* **2013**, *9*, 313.
[58] C. Ratzke, B. Hellenkamp, T. Hugel, *Nat Commun* **2014**, *5*, 4192.
[59] S. Wanninger, P. Asadiatouei, J. Bohlen, C.-B. Salem, P. Tinnefeld, E. Ploetz, D. C. Lamb, *Nat Commun* **2023**, *14*, 6564.
[60] E. Kopperger, J. List, S. Madhira, F. Rothfischer, D. C. Lamb, F. C. Simmel, *Science (New York, N.Y.)* **2018**, *359*, 296.
[61] J. Song, Z. Li, P. Wang, T. Meyer, C. Mao, Y. Ke, *Science (New York, N.Y.)* **2017**, *357*.
[62] Y. Cui, R. Chen, M. Kai, Y. Wang, Y. Mi, B. Wei, *ACS nano* **2017**, *11*, 8199.
[63] S. R. Adams, A. T. Harootunian, Y. J. Buechler, S. S. Taylor, R. Y. Tsien, *Nature* **1991**, *349*, 694.
[64] C. Hoffmann, G. Gaietta, M. Bünemann, S. R. Adams, S. Oberdorff-Maass, B. Behr, J.-P. Vilardaga, R. Y. Tsien, M. H. Ellisman, M. J. Lohse, *Nat Methods* **2005**, *2*, 171.
[65] B. Tenner, S. Mehta, J. Zhang, *Current Opinion in Structural Biology* **2016**, *41*, 203.
[66] F. Simon, L. E. Weiss, S. van Teeffelen, *Nat Rev Methods Primers* **2024**, *4*, 1.
[67] C. Manzo, M. F. Garcia-Parajo, *Reports on progress in physics. Physical Society (Great Britain)* **2015**, *78*, 124601.
[68] F. Laurent, C. Floderer, C. Favard, D. Muriaux, J.-B. Masson, C. L. Vestergaard, *Physical biology* **2019**, *17*, 15003.
[69] H. H. Tuson, J. S. Biteen, *Analytical chemistry* **2015**, *87*, 42.
[70] A. N. Kapanidis, S. Uphoff, M. Stracy, *Journal of Molecular Biology* **2018**, *430*, 4443.
[71] J. Sotolongo Bellón, O. Birkholz, C. P. Richter, F. Eull, H. Kenneweg, S. Wilmes, U. Rothbauer, C. You, M. R. Walter, R. Kurre, J. Piehler, *Cell Reports Methods* **2022**, *2*, 100165.
[72] F. Balzarotti, Y. Eilers, K. C. Gwosch, A. H. Gynnå, V. Westphal, F. D. Stefani, J. Elf, S. W. Hell, *Science (New York, N.Y.)* **2017**, *355*, 606.
[73] Y. Eilers, H. Ta, K. C. Gwosch, F. Balzarotti, S. W. Hell, *Proceedings of the National Academy of Sciences of the United States of America* **2018**, *115*, 6117.
[74] T. Deguchi, M. K. Iwanski, E.-M. Schentarra, C. Heidebrecht, L. Schmidt, J. Heck, T. Weihs, S. Schnorrenberg, P. Hoess, S. Liu, V. Chevyreva, K.-M. Noh, L. C. Kapitein, J. Ries, *Science (New York, N.Y.)* **2023**, *379*, 1010.
[75] J. O. Wirth, L. Scheiderer, T. Engelhardt, J. Engelhardt, J. Matthias, S. W. Hell, *Science (New York, N.Y.)* **2023**, *379*, 1004.

[76] J. M. Schleske, J. Hubrich, J. O. Wirth, E. D'Este, J. Engelhardt, S. W. Hell, *Proceedings of the National Academy of Sciences of the United States of America* **2024**, *121*, e2412241121.
[77] L. A. Masullo, F. Steiner, J. Zähringer, L. F. Lopez, J. Bohlen, L. Richter, F. Cole, P. Tinnefeld, F. D. Stefani, *Nano letters* **2021**, *21*, 840.
[78] E. Betzig, *Optics letters* **1995**, *20*, 237.
[79] S. Liu, P. Hoess, J. Ries, *Annual Review of Biophysics* **2022**, *51*, 301.
[80] F. Mieskes, E. Ploetz, F. Wehnekamp, V. Rat, D. C. Lamb, *Small* **2023**, *19*, e2204726.
[81] C. Niederauer, C. Nguyen, M. Wang-Henderson, J. Stein, S. Strauss, A. Cumberworth, F. Stehr, R. Jungmann, P. Schwille, K. A. Ganzinger, *Nat Commun* **2023**, *14*, 4345.
[82] Y.-L. Liu, E. P. Perillo, P. Ang, M. Kim, D. T. Nguyen, K. Blocher, Y.-A. Chen, C. Liu, A. M. Hassan, H. T. Vu, Y.-I. Chen, A. K. Dunn, H.-C. Yeh, *ACS nano* **2020**, *14*, 7927.
[83] M. Heilemann, D. P. Herten, R. Heintzmann, C. Cremer, C. Muller, P. Tinnefeld, K. D. Weston, J. Wolfrum, M. Sauer, *Analytical chemistry* **2002**, *74*, 3511.
[84] L. Cognet, G. S. Harms, G. A. Blab, P. H. M. Lommerse, T. Schmidt, *Appl. Phys. Lett.* **2000**, *77*, 4052.
[85] J. Bückers, D. Wildanger, G. Vicidomini, L. Kastrup, S. W. Hell, *Opt. Express, OE* **2011**, *19*, 3130.
[86] K. Hübner, H. Joshi, A. Aksimentiev, F. D. Stefani, P. Tinnefeld, G. P. Acuna, *ACS nano* **2021**, *15*, 5109.
[87] A. K. Adamczyk, F. Zhu, D. Schaeafer, Y. Kanehira, S. Kogikoski, JR, I. Bald, S. Schluecker, K. Kolataj, F. D. Stefani, G. P. Acuna, *Coupling single-molecules to DNA-based optical antennas with position and orientation control* **2024**.
[88] A. K. Adamczyk, Huijben, Teun A. P. M., K. Kolataj, F. Zhu, R. Marie, F. D. Stefani, G. P. Acuna, *Towards full control of molecular exciton energy transfer via FRET in DNA origami assemblies* **2024**.
[89] R. Datta, T. M. Heaster, J. T. Sharick, A. A. Gillette, M. C. Skala, *Journal of biomedical optics* **2020**, *25*, 1.
[90] S. W. Hell, *American Association for the Advancement of Science* **2007**, https://www-science-org.emedien.ub.uni-muenchen.de/doi/10.1126/science.1137395.
[91] M. Y. Berezin, S. Achilefu, *Chemical reviews* **2010**, *110*, 2641.
[92] J. R. Lakowicz, *Principles of fluorescence spectroscopy*, Springer, New York **2006**.
[93] M. Kasha, *Discuss. Faraday Soc.* **1950**, *9*, 14.
[94] G. G. Stokes, *Philosophical Transactions of the Royal Society of London* **1852**, *142*, 463.
[95] U. Kubitscheck, *Fluorescence microscopy: From principles to biological applications*, Wiley-Blackwell, Weinheim **2013**.
[96] C. Würth, M. Grabolle, J. Pauli, M. Spieles, U. Resch-Genger, *Nat Protoc* **2013**, *8*, 1535.
[97] M. A. Digman, V. R. Caiolfa, M. Zamai, E. Gratton, *Biophysical Journal* **2008**, *94*, L14-6.

[98] W. Chen, E. Avezov, S. C. Schlachter, F. Gielen, R. F. Laine, H. P. Harding, F. Hollfelder, D. Ron, C. F. Kaminski, *Biophysical Journal* **2015**, *108*, 999.
[99] A. P. Demchenko, *Methods Appl. Fluoresc.* **2020**, *8*, 22001.
[100] J. Vogelsang, R. Kasper, C. Steinhauer, B. Person, M. Heilemann, M. Sauer, P. Tinnefeld, *Angewandte Chemie International Edition* **2008**, *47*, 5465.
[101] C. E. Aitken, R. A. Marshall, J. D. Puglisi, *Biophysical Journal* **2008**, *94*, 1826.
[102] T. Cordes, A. Maiser, C. Steinhauer, L. Schermelleh, P. Tinnefeld, *Phys. Chem. Chem. Phys.* **2011**, *13*, 6699.
[103] P. Holzmeister, A. Gietl, P. Tinnefeld, *Angewandte Chemie International Edition* **2014**, *53*, 5685.
[104] C. A. Combs, H. Shroff, *Current protocols in neuroscience* **2017**, *79*, 2.1.1-2.1.25.
[105] E. Abbe, *Archiv f. mikrosk. Anatomie* **1873**, *9*, 413.
[106] T. A. Klar, S. W. Hell, *Optics letters* **1999**, *24*, 954.
[107] T. A. Klar, S. Jakobs, M. Dyba, A. Egner, S. W. Hell, *Proceedings of the National Academy of Sciences of the United States of America* **2000**, *97*, 8206.
[108] G. Donnert, J. Keller, R. Medda, M. A. Andrei, S. O. Rizzoli, R. Lührmann, R. Jahn, C. Eggeling, S. W. Hell, *Proceedings of the National Academy of Sciences of the United States of America* **2006**, *103*, 11440.
[109] S. Bretschneider, C. Eggeling, S. W. Hell, *Phys. Rev. Lett.* **2007**, *98*, 218103.
[110] S. W. Hell, M. Kroug, *Appl Phys B* **1995**, *60*, 495.
[111] M. G. L. Gustafsson, *Proceedings of the National Academy of Sciences of the United States of America* **2005**, *102*, 13081.
[112] M. Heilemann, S. van de Linde, M. Schüttpelz, R. Kasper, B. Seefeldt, A. Mukherjee, P. Tinnefeld, M. Sauer, *Angewandte Chemie (International ed. in English)* **2008**, *47*, 6172.
[113] M. J. Rust, M. Bates, X. Zhuang, *Nat Methods* **2006**, *3*, 793.
[114] E. Betzig, G. H. Patterson, R. Sougrat, O. W. Lindwasser, S. Olenych, J. S. Bonifacino, M. W. Davidson, J. Lippincott-Schwartz, H. F. Hess, *Science (New York, N.Y.)* **2006**, *313*, 1642.
[115] S. T. Hess, T. P. K. Girirajan, M. D. Mason, *Biophysical Journal* **2006**, *91*, 4258.
[116] C. Steinhauer, C. Forthmann, J. Vogelsang, P. Tinnefeld, *Journal of the American Chemical Society* **2008**, *130*, 16840.
[117] J. Vogelsang, C. Steinhauer, C. Forthmann, I. H. Stein, B. Person-Skegro, T. Cordes, P. Tinnefeld, *ChemPhysChem* **2010**, *11*, 2475.
[118] R. Jungmann, M. S. Avendaño, J. B. Woehrstein, M. Dai, W. M. Shih, P. Yin, *Nat Methods* **2014**, *11*, 313.
[119] A. Sharonov, R. M. Hochstrasser, *Proceedings of the National Academy of Sciences of the United States of America* **2006**, *103*, 18911.
[120] S. C. M. Reinhardt, L. A. Masullo, I. Baudrexel, P. R. Steen, R. Kowalewski, A. S. Eklund, S. Strauss, E. M. Unterauer, T. Schlichthaerle, M. T. Strauss, C. Klein, R. Jungmann, *Nature* **2023**, *617*, 711.

[121] J. B. Grimm, B. P. English, J. Chen, J. P. Slaughter, Z. Zhang, A. Revyakin, R. Patel, J. J. Macklin, D. Normanno, R. H. Singer, T. Lionnet, L. D. Lavis, *Nat Methods* **2015**, *12*, 244-50, 3 p following 250.
[122] L. Wang, M. S. Frei, A. Salim, K. Johnsson, *Journal of the American Chemical Society* **2019**, *141*, 2770.
[123] K. C. Gwosch, J. K. Pape, F. Balzarotti, P. Hoess, J. Ellenberg, J. Ries, S. W. Hell, *Nat Methods* **2020**, *17*, 217.
[124] B. K. Müller, E. Zaychikov, C. Bräuchle, D. C. Lamb, *Biophysical Journal* **2005**, *89*, 3508.
[125] J. Zähringer, F. Cole, J. Bohlen, F. Steiner, I. Kamińska, P. Tinnefeld, *Light Sci Appl* **2023**, *12*, 70.
[126] Y. Liu, H. Ge, Y. Wang, L. Tang, Y. Pei, S. Fan, Y. Song, C. Zhang, J. Song, *Small Structures* **2022**, https://onlinelibrary.wiley.com/doi/full/10.1002/sstr.202200167.
[127] . Yan, Y. Wang, J. Shi, B. Wei, *Nucleic Acids Res* **2020**, *48*, 7595.
[128] J. D. WATSON, F. H. CRICK, *Nature* **1953**, *171*, 737.
[129] P. Yakovchuk, E. Protozanova, M. D. Frank-Kamenetskii, *Nucleic Acids Res* **2006**, *34*, 564.
[130] M. Raab, I. Jusuk, J. Molle, E. Buhr, B. Bodermann, D. Bergmann, H. Bosse, P. Tinnefeld, *Sci Rep* **2018**, *8*, 1780.
[131] J. Fu, M. Liu, Y. Liu, N. W. Woodbury, H. Yan, *Journal of the American Chemical Society* **2012**, *134*, 5516.
[132] K. Paloja, J. Weiden, J. Hellmeier, A. S. Eklund, S. C. M. Reinhardt, I. A. Parish, R. Jungmann, M. M. C. Bastings, *ACS nano* **2024**, *18*, 1381.
[133] F. Cole, J. Zähringer, J. Bohlen, T. Schröder, F. Steiner, M. Pfeiffer, P. Schüler, F. D. Stefani, P. Tinnefeld, *Nat. Photon.* **2024**, https://www.nature.com/articles/s41566-024-01384-4.
[134] M. Pfeiffer, K. Trofymchuk, S. Ranallo, F. Ricci, F. Steiner, F. Cole, V. Glembockyte, P. Tinnefeld, *iScience* **2021**, *24*, 103072.
[135] K. E. Bujold, J. C. C. Hsu, H. F. Sleiman, *Journal of the American Chemical Society* **2016**, *138*, 14030.
[136] M. Scheckenbach, J. Bauer, J. Zähringer, F. Selbach, P. Tinnefeld, *APL Materials* **2020**, *8*.
[137] D. Wang, J. Song, P. Wang, V. Pan, Y. Zhang, D. Cui, Y. Ke, *Nature protocols* **2018**, *13*, 2312.
[138] R. Holliday, *Genetics Research* **1964**, *5*, 282.
[139] R. M. Clegg, A. I. Murchie, D. M. Lilley, *Biophysical Journal* **1994**, *66*, 99.
[140] S. A. McKinney, A.-C. Déclais, D. M. J. Lilley, T. Ha, *Nat Struct Mol Biol* **2003**, *10*, 93.
[141] J. ?poner, J. Leszczynski, P. Hobza, *Biopolymers* **2001**, *61*, 3.
[142] A. Hesselmann, G. Jansen, M. Schütz, *J. Am. Chem. Soc.* **2006**, *128*, 11730.

[143] A. R. Mount, C. P. Mountford, S. A. G. Evans, T.-J. Su, A. H. Buck, P. Dickinson, C. J. Campbell, L. M. Keane, J. G. Terry, J. S. Beattie, A. J. Walton, P. Ghazal, J. Crain, *Biophysical Chemistry* **2006**, *124*, 214.
[144] H. S. Chung, W. A. Eaton, *Current Opinion in Structural Biology* **2018**, *48*, 30.
[145] L. Wang, A. Pulk, M. R. Wasserman, M. B. Feldman, R. B. Altman, J. H. D. Cate, S. C. Blanchard, *Nat Struct Mol Biol* **2012**, *19*, 957.
[146] S. C. Blanchard, *Current Opinion in Structural Biology* **2009**, *19*, 103.
[147] M. H. Jo, P. Meneses, O. Yang, C. C. Carcamo, S. Pangeni, T. Ha, *American Association for the Advancement of Science* **2024**, https://www-science-org.emedien.ub.uni-muenchen.de/doi/10.1126/science.adk6921.
[148] E. Lerner, T. Cordes, A. Ingargiola, Y. Alhadid, S. Chung, X. Michalet, S. Weiss, *Science (New York, N.Y.)* **2018**, *359*.
[149] C. M. Haney, R. F. Wissner, E. J. Petersson, *Current opinion in chemical biology* **2015**, *28*, 123.
[150] J. Yin, A. J. Lin, D. E. Golan, C. T. Walsh, *Nat Protoc* **2006**, *1*, 280.
[151] C. S. Theile, M. D. Witte, A. E. M. Blom, L. Kundrat, H. L. Ploegh, C. P. Guimaraes, *Nat Protoc* **2013**, *8*, 1800.
[152] K. Akiyama, A. Alberdi, W. Alef, K. Asada *et al.*, *ApJL* **2019**, *875*, L1.
[153] F. Weihs, J. Wang, K. D. G. Pfleger, H. Dacres, *Analytica Chimica Acta: X* **2020**, *6*, 100059.
[154] E. Slenders, S. Patil, M. O. Held, A. Zunino, G. Vicidomini, *bioRxiv* **2024**, https://www.biorxiv.org/content/10.1101/2024.07.08.602588v1.full#ref-14.
[155] S. Pujals, N. Feiner-Gracia, P. Delcanale, I. Voets, L. Albertazzi, *Nat Rev Chem* **2019**, *3*, 68.
[156] S. Habuchi, S. Onda, M. Vacha, *Phys. Chem. Chem. Phys.* **2011**, *13*, 1743.
[157] A. Merdasa, Á. J. Jiménez, R. Camacho, M. Meyer, F. Würthner, I. G. Scheblykin, *Nano letters* **2014**, *14*, 6774.
[158] S. Habuchi, S. Onda, M. Vacha, *Chem. Commun.* **2009**, https://pubs-rsc-org.emedien.ub.uni-muenchen.de/en/content/articlelanding/2009/cc/b907882g.
[159] H. Park, D. T. Hoang, K. Paeng, L. J. Kaufman, *ACS nano* **2015**, *9*, 3151.
[160] L. Scheiderer, J. O. Wirth, M. Tarnawski, S. W. Hell, *Dual-color MINFLUX: Kinesin-1 takes Chassé-Inchworm steps* **2024**.
[161] M. K. Geismann, A. Gomez-Segalas, A. Passera, M. Shirzadian, F. Balzarotti, *A Fast Interferometric Beam Shaper for Multi-Emitter 3D MINFLUX* **2023**.
[162] T. A. Hensel, J. O. Wirth, S. W. Hell, *Diffraction minima resolve point scatterers at tiny fractions (1/80) of the wavelength* **2024**.
[163] R. Chowdhury, A. Sau, S. M. Musser, *Nature cell biology* **2022**, *24*, 112.
[164] S. P. Jackson, J. Bartek, *Nature* **2009**, *461*, 1071.
[165] T. Moosmayer, K. A. Kiszka, V. Westphal, J. K. Pape, M. Leutenegger, H. Steffens, S. G. N. Grant, S. J. Sahl, S. W. Hell, *MINFLUX fluorescence nanoscopy in biological tissue* **2024**.
[166] C. Tuerk, L. Gold, *Science (New York, N.Y.)* **1990**, *249*, 505.

[167] A. D. Ellington, J. W. Szostak, *Nature* **1990**, *346*, 818.
[168] S. M. Shamah, J. M. Healy, S. T. Cload, *Accounts of chemical research* **2008**, *41*, 130.
[169] M. Blind, M. Blank, *Molecular Therapy - Nucleic Acids* **2015**, *4*, e223.
[170] J. C. Rohloff, A. D. Gelinas, T. C. Jarvis, U. A. Ochsner, D. J. Schneider, L. Gold, N. Janjic, *Molecular Therapy - Nucleic Acids* **2014**, *3*, e201.
[171] SomaLogic, *SomaScan 11K Assay* **2024**, https://somalogic.com/somascan-11k-assay/.
[172] A. Bashir, . Yang, J. Wang, S. Hoyer, W. Chou, C. McLean, G. Davis, . Gong, Z. Armstrong, J. Jang, H. Kang, A. Pawlosky, A. Scott, G. E. Dahl, M. Berndl, M. Dimon, B. S. Ferguson, *Nat Commun* **2021**, *12*, 2366.
[173] A. R. Chandrasekaran, *Nat Rev Chem* **2021**, *5*, 225.
[174] L. M. Wassermann, M. Scheckenbach, A. V. Baptist, V. Glembockyte, A. Heuer-Jungemann, *Advanced materials (Deerfield Beach, Fla.)* **2023**, *35*, e2212024.
[175] M. Scheckenbach, T. Schubert, C. Forthmann, V. Glembockyte, P. Tinnefeld, *Angewandte Chemie International Edition* **2021**, *60*, 4931.
[176] J. Kurreck, E. Wyszko, C. Gillen, V. A. Erdmann, *Nucleic Acids Res* **2002**, *30*, 1911.
[177] M. Frieden, H. F. Hansen, T. Koch, *Nucleosides, nucleotides & nucleic acids* **2003**, *22*, 1041.
[178] E. Del Grosso, E. Franco, L. J. Prins, F. Ricci, *Nat. Chem.* **2022**, *14*, 600.
[179] E. Del Grosso, A. Amodio, G. Ragazzon, L. J. Prins, F. Ricci, *Angewandte Chemie International Edition* **2018**, *57*, 10489.
[180] E. J. Calabrese, *Microbial Cell* **2014**, *1*, 145.
[181] L. Thomson, J. Paton, *Paediatric Respiratory Reviews* **2014**, *15*, 120.
[182] S. K. Silverman, *Trends in Biochemical Sciences* **2016**, *41*, 595.

8 APPENDIX

8.1 ASSOCIATED PUBLICATION P1

Modulation of transformation of DNA origami nanoarray via sequence design

by

Dongfang Wang[1], **Fiona Cole**[1], Martina Pfeiffer[1], Tim Schröder, Philip Tinnefeld[*] and Yonggang Ke[*]

([1] These authors contributed equally, [*] Correspondence)

Submitted to Nature Communications

Author contributions:
The initial idea of the project was proposed by my collaboration partners Yonggang Ke and Dongfang Wang. Dongfang Wang designed the DNA origami array structures and synthesized the corresponding scaffolds. He performed and analyzed the AFM measurements of this work. Tim Schröder performed preliminary fluorescence measurements. I performed and analyzed the ensemble fluorescence measurements and helped with the single-molecule fluorescence measurements and their analysis. Martina Pfeiffer designed, performed and analyzed the single-molecule fluorescence measurements and helped with the ensemble fluorescence measurements and their analysis. I wrote parts of the manuscript. Philip Tinnefeld and Yonggang Ke supervised the project.

Modulation of transformation of DNA origami nanoarray via sequence design

Dongfang Wang[#1,2], Fiona Cole[#3], Martina Pfeiffer[#3], Tim Schröder[3], Philip Tinnefeld[3*] and Yonggang Ke[4*]

[1]School of Biomedical Engineering, University of Science and Technology of China, Hefei 230026, China

[2]Suzhou Institute for Advanced Research, University of Science and Technology of China, Suzhou 215123, China

[3]Department of Chemistry and Center for NanoScience, Ludwig-Maximilians-Universität München, Butenandtstr. 5-13, 81377 München, Germany

[4]Wallace H. Coulter Department of Biomedical Engineering, Emory University and Georgia Institute of Technology, Atlanta, GA 30322, USA

# These authors contributed equally

Emails: yonggang.ke@emory.edu, philip.tinnefeld@cup.uni-muenchen.de

Abstract

DNA nanotechnology has created a rich repository of dynamic, molecular nanomachines with various functions and applications. The four-way DNA junction is the arguably earliest but most prevalent structural motif. Recently, a reconfigurable DNA nanoarray (domino array) was created with this basic motif to realize intricate, stepwise transformation by the information relay between neighboring four-way junction units. Comparing the initial state and the completely transformed state of a DNA nanoarray, every four-way DNA junction in the nanoarray is converted from one stable configuration to another. Because this transformation is driven by only a reorganization of base stacking in all four-way junctions, the reconfigurable DNA origami provides an excellent platform for studying how DNA origami assembly and reconfiguration is influenced by the sequence design of four-way junctions. By regulating the energy difference and thus the conversion between the two configurations of four-way junctions, we showed the transformation of DNA nanoarray can be modulated in a designable manner. More specifically, by using custom-designed DNA scaffolds, we generated a DNA domino array with same sequences at every junction, and used it as a platform to study how the design of DNA bases at junctions influences the kinetics and thermodynamics of transformation of four-way junctions in reconfigurable DNA nanoarrays. The coordinated transformation of four-way junctions in the DNA domino array enabled a detailed investigation

on array transformation by using Atomic Force Microscopy (AFM) imaging and single-molecule Förster resonance energy transfer (FRET) microscopy.

Introduction

In past decades, DNA self-assembly was utilized to construct custom-designed, intricate nanoobjects. Various approaches were developed, including DNA tiles[1,2,3] , DNA bricks[4-6] and DNA origami[7,8]. These versatile methods were used to fabricate not only increasingly more complex DNA nanostructures[6,8-14], but also sophisticated nanomachines that are capable of performing prescribed motions[15-17] and carrying out designated tasks[18]. Interestingly, many of the state-of-the-art nanostructures are still largely constructed by using a structural motif called immobile four-way junction (an adaptation from Holliday Junction[19]), which was invented by Seeman at the dawn of DNA nanotechnology[20]. Since its conception, immobile DNA four-way junctions, as well as its variants (e.g., 3, 5, or 6-way junctions), have been extensively used in DNA tiles, including the double-crossover DNA tiles[2], used for the assembly of the first two-dimensional DNA nanoarrays[21], and later the powerful, versatile DNA origami[7,8].

Natural Holliday junction participates in the gene recombination process and can slide along DNA strands due to the symmetrical sequences at the junction, and plenty theoretical and experimental studies have characterized the structure and dynamics of Holliday junction, including immobilized Holliday Junction. For example, it has been shown that magnesium concentration[22] and sequence near the junction position[23-25] could affect the ratio of two stacked conformational isomers. Other factors were reported to the contribution of the observed isomer ratios, such as the geometric constraints imposed at the junction core[26], and the sequence-dependent electrostatic potential[27] on junction stacking preferences. MD simulations of J1 and J24 junction sequence demonstrated that stacking and geometric factors contributed to their structural changes[28]. Besides, the dynamics of individual Holliday junction has been studied using single-molecule fluorescence methodology[22,29-31].

It is understood that a Holliday junction exhibits a one-helix-over-the-other-helix, X-shaped

conformation (**Figure 1a**) with an inter-helix angle of ~60° [32]. However, the conformation of a four-way junction in a DNA nanostructure is generally different. In most cases (e.g., in a typical DNA origami nanoarray), the conformation of four-way junctions is restricted by the surrounding DNA helices, leading to the four arms being forced into a plane (**Figure 1b**), as observed in microscopy imaging[7,33]. Therefore, although it is certain that the sequence design of four-way junctions influences the stability and dynamics of DNA nanostructures, elucidating this sequence effect needs to be done in DNA nanostructures *in situ*. To this end, it was recently shown that the sequences of Holliday junctions had strong impact on DNA crystal formation[34], and on the thermodynamics of DNA origami[35]. However, it remains challenging to design experiments to explore the effect of junction sequences on the reconfiguration processes of dynamic DNA origami in detail.

We previously established a DNA Origami Domino Array (DODA) which comprises many reconfigurable four-way Junctions (RJ) [33,36,37]. Under normal assembly conditions, a DODA predominately adapts a conformation in which the scaffold DNA strand goes back and forth along each DNA double helix in a raster pattern. This conformation of DODA contains a few unpaired DNA scaffold loops that can bind to complementary trigger DNA strands to initiate a cascading transformation of individual RJs (**Figure 1c and 1d**). When the reaction reaches completion, the DODA is converted to its final conformation, in which every RJ is transformed (**Figure 1e**). In this study, the initial conformation and the final conformation are referred to as conformation I and II, and their corresponding RJ configurations are referred as configuration i and ii, respectively. Since we can consider RJs as the basic structural units of a DODA, it was believed that the assembly and reconfiguration of DODA can be regulated via designing sequences of RJs, particularly the eight basepairs at the junction (**Figure 1e**). However, previous DODAs used M13 viral DNA as the scaffold, preventing any de novo design on RJ sequences. Recent development in custom DNA scaffold engineering[38-40], particularly the pscaf method[38], provides new tools for constructing DODAs with fully designable RJ sequences. Here, we designed a DODA that contains four columns (5, 4, 5, 4 junctions in each column) of RJs (**Figure 1c**) for systematic study of sequence effects on DODAs. Unlike the

M13-scaffolded DODA, every RJ in a DODA were designed to contain identical eight basepairs at the junction by using custom-designed pscaf. Such a design strategy effectively amplifies the effect of sequences, and enabled our investigation on sequence effect in RJs and DODAs with Atomic Force Microscopy (AFM) imaging and single-molecule fluorescence imaging. The knowledge generated via this study can be used not only for programming transformation of DODAs, but also for design custom-scaffolded DNA origami with staple junction sequence design.

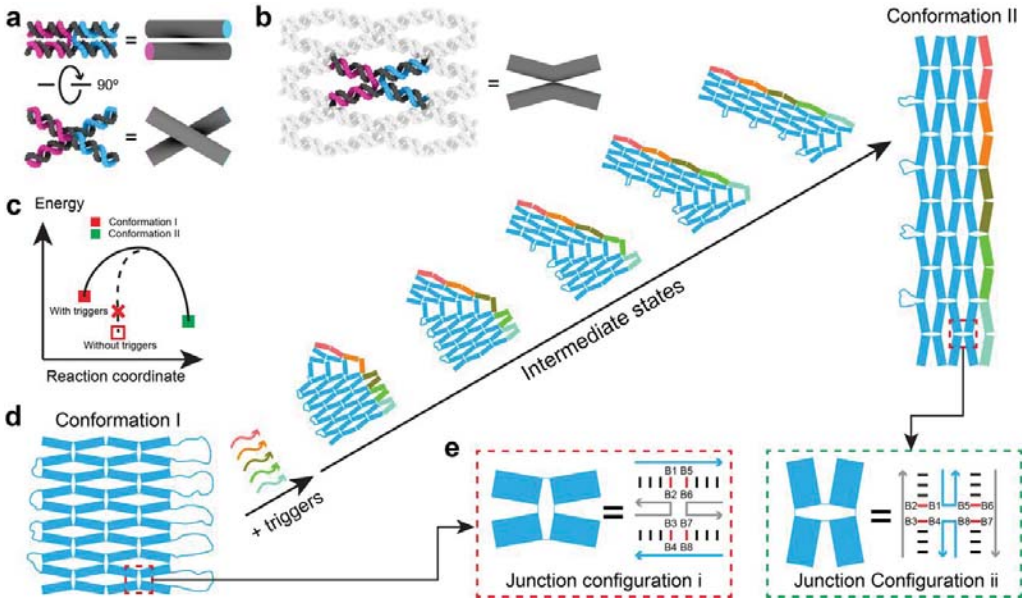

Figure 1. Modulating transformation of DODA via junction sequence design. **a**. Top and side view of a free-stranding Holliday junction, which exhibits the X-shaped conformation with an inter-helix angle of ~60°. **b.** Generally, the four arms of a junction are confined into a plane by the surrounding DNA helices in a DNA nanostructure. **c.** Simplified energy model for DODA transformation. **d.** Schematics showing the step-by-step transformation of the DODA used in this work. **e** Detailed view of a junction in the DODA under conformation I and II. The blue strands and grey strands represent scaffold DNA and staple DNA respectively. The four basepair at the junction are highlighted to illustrate the different stacking patterns in junction configuration i and configuration ii.

Results

There are 64 possible combinations for the four basepairs at the junction (**Supplementary Figure S1**). We estimated the free energy (ΔG) of configuration i and configuration ii based on previous published results[41] (**Supplementary Figure S2**). It is worth pointing out that the ΔGs of configuration i and configuration ii are expected to be substantially different from ΔGs of

free-standing Holliday junctions, due to the fact that the RJs in DODA are confined by surrounding DNA (**Figure 1b**; the four-way junction has a flat X-shape, which probably leads to weakened base stacking at the junction position). Nonetheless, we expect the estimated ΔGs provide a foundation for design DODAs with different assembly and transformation behaviors. Instead of exhaustively testing every combination, we selected three sets of sequence design (**Figure 2a**). G junction consists of four DNA basepairs that has largest ΔG_i-ΔG_{ii} and therefore should favor junction configuration ii. The sequence of R junction is effectively the reverse of the G junction, and should favor junction configuration i. N junction is designed to contain a set of "symmetric" sequence, so that its configuration i and configuration ii have exactly the same arrangement of four basepairs at the junction and presumable the same ΔGs. The DODAs with custom-designed junctions were designed in cadnano[42] (**Supplementary Figure S3**), and custom-design scaffolds for different junction designs were produced by using reported method[38] (**Supplementary Figures S4-S6, Supplementary Table S1**).

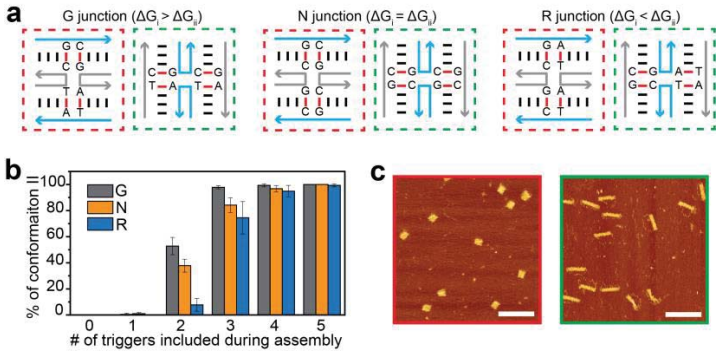

Figure 2. Modulating DODA assembly via junction sequence design. **a.** Three representative junction designs used in this study with different sequences for the eight basepairs at the junction position. Based the analysis on basestacking, G junction favors configuration ii and R junction favors i, while N junction favors neither. The DODAs made with these three junction designs have identical sequences across the structures, except for the basepairs at the 22 junctions. **b.** Percentages of conformation II in one-pot assembly of DODAs with different number of triggers. The percentages of conformation II for G-DODA with 0-5 triggers were 0%, 0.5±0.9%, 53.4±6.0%, 97.9±1.2%, 99.3±1.1% and 100%, respectively. The percentages of conformation II for N-DODA with 0-5 triggers were 0%, 1.0±0.9%, 37.8±5.0%, 84.1±5.7%, 96.8±2.4% and 100%, respectively. The percentages of conformation II for R-DODA with 0-5 triggers were 0%, 0%, 7.8±4.8%, 74.5±12.3%, 94.9±4.4% and 99.3±1.1%, respectively. **c.** Representative AFM images of conformation I and II for G-DODA. Scale bars: 200nm.

The one-pot assembly of three DODAs that contains purely G junction (G-DODA), N junction (N-DODA), and R junction (R-DODA) respectively, was investigated via agarose gel electrophoresis and AFM imaging (**Supplementary Figures S7-S13**). Without triggers, all three DODAs produced only conformation I, suggesting the origami design (scaffold routing) strongly favors conformation I and is sufficient to overcome energy difference induced by the junction sequence design. However, when trigger strands were included in the samples, the three DODAs exhibited different behaviors. The addition of all five trigger strands resulted in almost complete transformation to conformation II for the three DODAs. The reduction of the number of triggers to 4, 3, 2, and 1 clearly revealed the junction sequence design has changed the assembly of DODAs in a way that largely matches with our prediction (**Figure 2b**). Percentages of conformation I and conformation II are calculated by analysis of AFM images in this work. Two examples of conformation I (R-DODA without trigger) and conformation II (G-DODA with all five triggers) are shown in **Figure 2c**. In all cases, the percentages of conformation II follow a trend of G-DODA>N-DODA>R-DODA. For example, G-DODA, N-DODA, and R-DODA assembled with three triggers generated 97.9±1.2%, 84.2±5.7%, and 74.5±12.4% of DODA in conformation II. The percentages of conformation II decreased when fewer triggers were added, which is in good agreement with the model in **Figure 1c**. In absence of trigger DNA strands, the free energy of conformation I is significantly lower than the free energy of conformation II. The addition of each trigger DNA strand increases the free energy of conformation I until it eventually becomes higher than that of the conformation II.

Because the only design variant between the G-, R-, N-DODAs are their junction sequences, we believe the differences in terms of the percentages of conformation II for these DODAs are the direct result of thermodynamic properties of individual junctions. Therefore, this design of DODAs provide a system for understanding single junctions by studying DNA arrays: Because the assembly and transformation behavior of a DODA represent the collective behavior of all junctions (with same junction sequences), studying DODA enables us to understand the single junctions by means (e.g., AFM) that cannot be directly applied on the small units.

We then extended our study to understanding transformation of DODAs with different junction sequences and various numbers of triggers. Three DODAs were incubated with different number of triggers at 50° C overnight. The agarose gel-purified samples were imaged under AFM for counting the fraction of conformation II in the samples. The transformation results were overall consistent with the one-pot assembly (**Supplementary Figures S14-S17**). For each DODA design, the conformation II ratios increased with the addition of more triggers. With the same number of triggers added (2-5 triggers), G-DODA had higher transformation yield than N-DODA, followed by R-DODA.

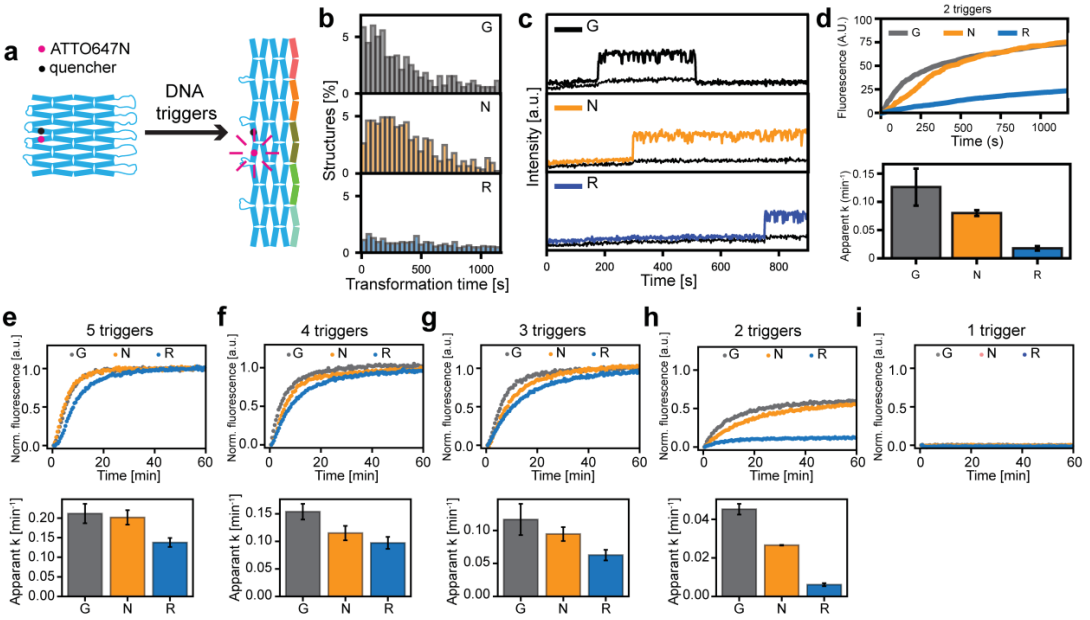

Figure 3. Investigating kinetics of DODA transformation via single-molecule fluorescence imaging and real-time PCR. **a.** Design of DODA for fluorescence experiments. An ATTO647N and a quencher were labeled on the DNA strands on the left side of DNA origami arrays. Before transformation, fluorescence was quenched due to the close proximity with the quencher. After transformation, the fluorescence was enhanced due to the increased distance between ATTO647N and quencher. **b.** Histograms showing percentages of transformed DODAs with two triggers at different time points via single-molecule fluorescence measurement repeated three times. **c.** Representative fluorescence traces for single structure transformation of three DODAs. The black line represented the background signals. **d.** Top: accumulative fluorescence signals from single-molecule fluorescence measurement showing the overall transformation kinetics of three DODAs with two triggers. The experiments were performed three times at 37° C. Below: Apparent transformation rate constant k obtained from the kinetics data 0.126±0.040 min^{-1}, 0.080±0.006 min^{-1} and 0.018±0.005 min^{-1} for G-, N-, R-DODAs, respectively. Error bars represent the standard deviation of the three experiments. **e** to **i**. Kinetics study on ensemble samples by using real-time PCR. Top: ensemble fluorescence for the transformation of three DODAs with different number of triggers. The experiments were performed for three times at 30° C. Below: The apparent rate constant k for three DODAs with different number of trigger input during the transformation. The k for G-, N-, R-DODAs with five

triggers are 0.211±0.030/min, 0.202±0.023/min and 0.138±0.014/min, respectively. The k for G-, N-, R-DODAs with four triggers are 0.154±0.017/min, 0.115±0.016/min and 0.097±0.013/min, respectively. The k for G-, N-, R-DODAs with three triggers are 0.117±0.029/min, 0.095±0.013/min and 0.063±0.010/min, respectively. The k for G-, N-, R-DODAs with two triggers are 0.045±0.003/min, 0.027±0.000/min and 0.06±0.001/min, respectively.

Next, the transformation was studied with single-molecule experiments by using TIRF microscopy. A FRET array was designed for investigating transformation kinetics: A FRET pair composed of a red ATTO647N donor and an IowaBlack@RQ quencher was placed on the DODA nanoarray[43] (**Figure 3a and Supplementary Figure S18a**). Under the initial conformation I, the donor and quencher are in proximity and thus the fluorescence of ATTO647N is quenched. After transformation to conformation II, the distance between the dye and quencher increases (from ~3nm to 6.8nm), resulting in enhanced fluorescence. The DODA was also modified with a biotinylated DNA strand that binds to the unused scaffold, allowing capturing of the DODA on BSA-biotin-NeutrAvidin coated glass coverslips. A green ATTO542 dye label DNA strands was also incorporated in the DODA for identification of the array on surface for single-molecule fluorescence analysis on array transformation. We recorded fluorescence images of the DNA origami array structures before and after overnight incubation with and without different numbers of DNA staples at 37 °C on a total internal reflection fluorescence (TIRF) microscope and quantified the transformation yield of the DNA origami array structures from them. Consistent with the results observed in AFM assay (**Figure 2b**), we observed the highest transformation yields for the G structure followed by both the N and the R structure (**Supplementary Figure S18b**).

We then carried out real-time single-molecule imaging (time lapse imaging with a 100 ms frame every 2 s, in order to guaranty single molecule trajectories for up to 20 minutes) on the FRET DODA in presence of various numbers of trigger strands (**Figure 3b to 3i**). For instance, upon addition of two trigger strands at 37°C, G-, N- and R-DODA exhibited distinctly different behaviors in terms of the transformation time, which was defined as the time from the addition of the DNA triggers to the signal jump (See **Figure 3b and 3c** for single molecule data and example of real time fluorescence trace of individual DODA). Transformation kinetics of G-, N-

and R-DODA were calculated on the basis of percentages of transformed DODAs over time (**Figure 3d, see more discussion about DODA transformation in Supplementary Section multi-step kinetics**): G-DODA showed the fastest apparent rate constant of 0.126±0.040 min^{-1}, while N-DODA showed an apparent rate constant of 0.080 ± 0.006 min^{-1} and R-DODA transformed under the slowest apparent rate constant of 0.018 ± 0.005 min^{-1}.

Next, the real-time ensemble FRET assay was applied for studying transformations of G-, N-, R-DODA with 5, 4, 3, 2, or 1 trigger(s) to understand the transformation kinetics in detail (**Figure 3e to 3i**). The samples were monitored at 30°C for 60 min. We noted a significantly faster increase in fluorescence intensity for all three structures upon incubation with five trigger DNA staples. Notably, for the G and N structure, the transformation occurred quasi-simultaneously upon incubation with all five trigger strands (0.211±0.030 min^{-1} and 0.202±0.023 min^{-1}). In contrast, a time delay between the transformation in the R and the G and N structure was noticed upon incubation with all five trigger DNA strands (0.138±0.014 min^{-1}). The transition kinetics was slowed down gradually when the number of trigger DNA strands was reduced. Notably, when adding only the upper four trigger DNA strands, we notified a difference in the transformation kinetics of the G and the N structure (0.154±0.017 min^{-1} and 0.115±0.016 min^{-1}). Further reduction of the number of trigger DNA strands to three or two slowed down the ensemble kinetics but could still differentiate their kinetics, while the transformation process was not initiated at all upon incubation with no trigger or only 1 DNA trigger. In combination, this set of data shows that the DODA transformation kinetics can be finely tuned by changing trigger strands, temperature, buffers, in addition to junction sequences. It is worth pointing out that the kinetics of these transformations were approximated with a single exponential decay function, which should give us an estimate of the average transformation speed, while the actual reactions are likely more complex, considering the multistep nature of the transformation of the DODAs. For example, when 5 triggers were added to G-, N-, R-DODA, the transformation took various times to reach maximum reaction rates (**Supplementary Figure S19**). Particularly, the G-DODA not only exhibited overall faster

reaction rate, but also is fastest in the first stage of reaction, likely due to the fact that the G-DODA averagely requires fewer triggers (thus shorter time) to initiate the transformation.

We then studied DODA transformation under various concentrations of Mg^{2+} and Na^{+}, because it is expected monovalent or divalent cation would have strong influence on the transformation kinetics. Since it is known that higher Mg^{2+} can enhance base-stacking,[39] as anticipated, we observed faster transformations for R-DODA when the Mg^{2+} concentration was changed from 6 mM to 2 mM and 500 mM NaCl was added (**Supplementary Figures S20**), suggesting the weakening of base-stacking under lower Mg^{2+} allows the transformation to take place faster.

The kinetics of DODA transformations observed experimentally can be qualitatively explained by the difference in activation energy (E_a) associated with the breaking of base-stacking at junctions (**Supplementary Figure S21a**; Note only a single junction was shown). However, since a DODA is a collection of junctions with identical junction sequences, the E_a of three sets junction sequences (G, N, R) can be calculated by the sum of the free energy of four base-pair stacking (**Supplementary Figure S21c to S21e**)[41]. Among them, G junction indeed has the lowest E_a and R junction has the highest E_a, consistent with the observed kinetics in both single-molecule and ensemble assays.

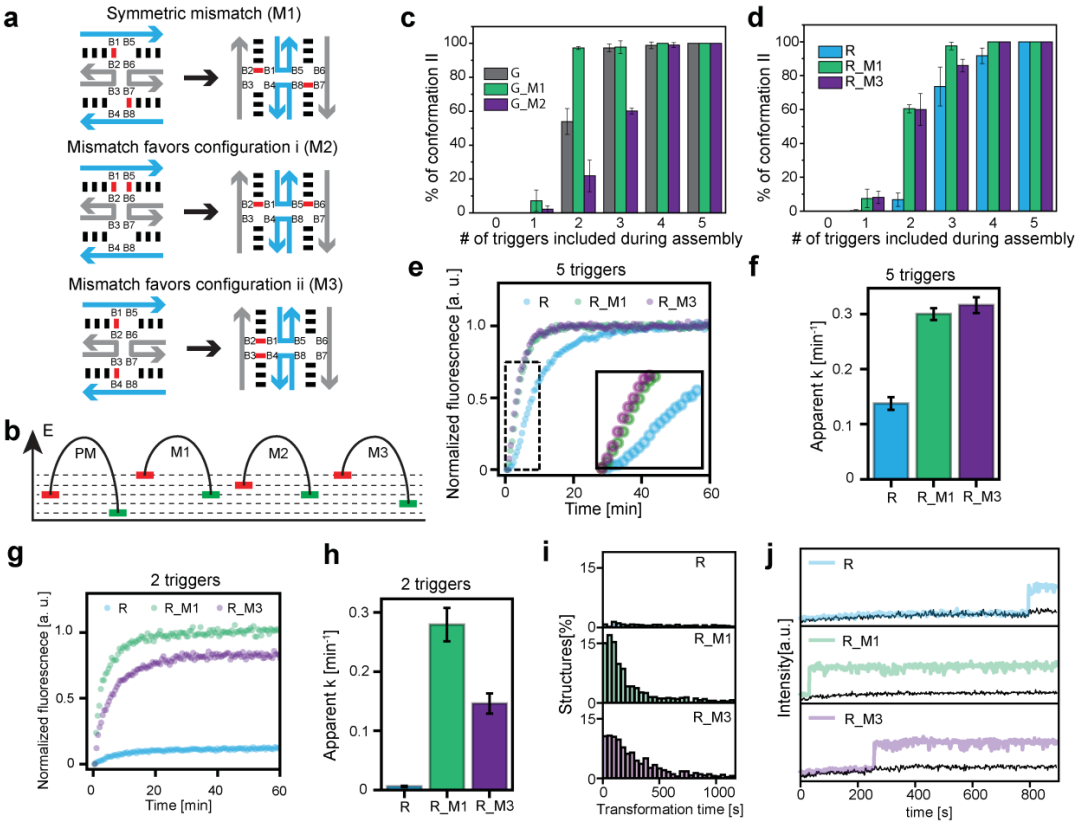

Figure 4. Modulating DODA transformation via sequence mismatch. **a.** Schematics of three designs of mismatches at the junction. **b.** Simple free energy model corresponding to DODAs with three types of mismatches. **c.** Percentages of conformation II for the G-DODA and its mismatched variants in one-pot assembly, in presence of various numbers of triggers. The percentages for G-DODA with 0-5 triggers are 0%, 0%, 54.0±7.7%, 97.4±23.0%, 98.9±1.9% and 100%, respectively. The percentages for G_M1 with 0-5 triggers are 0%, 0%, 7.1±6.3%, 97.3±0.8%, 97.8±3.7% and 100%, respectively. The percentages for G_M2 with 1-5 triggers are 0%, 2.2±2.1%, 21.9±9.3%, 60.1±1.7%, 99.3±1.1% and 100%, respectively. **d.** Percentages of conformation II for the R-DODA and its mismatched variants. The percentages for R-DODA with 0-5 triggers are 0%, 0.4±0.7%, 6.8±3.9%, 73.5±11.5%, 91.7±4.6% and 100%, respectively. The percentages for R_M1 with 0-5 triggers are 0%, 0%, 7.6±5.4%, 60.4±2.3%, 97.5±2.2% and 100%, respectively. The percentages for R_M3 with 0-5 triggers are 0%, 8.2±3.7%, 60.0±9.4%, 86.0±3.7%, 100% and 100%, respectively. **e.** Ensemble fluorescence experiments for transformation of R-DODA and its M1 and M3 variants, after addition of five triggers. **f.** The apparent rate constant k obtained from data in **e** (0.14±0.01 min^{-1}, 0.30±0.01 min^{-1} and 0.32±0.02 min^{-1} for R-DODA, R_M1 and R_M3, respectively. The experiments were performed for three times at 30° C. **g to j.** Single-molecule fluorescence measurement on the transformation of R-DODA, R_M1 and R_M3 after addition of two triggers. **g.** Accumulative fluorescence signals from single-molecule fluorescence measurement showing the overall transformation kinetics. **h.** The apparent rate constant k obtained from data in **g (**0.006±0.001 min^{-1}, 0.279±0.034 min^{-1} and 0.146±0.021 min^{-1} for R_DODA, R_M1 and R_M3, respectively. The experiments were performed for three times at 37° C. **i.** Histograms showing percentages of transformed DODAs with two triggers at different time points via single-molecule fluorescence measurement. **j.** Representative single-molecule fluorescence traces corresponding to the transformation of individual R-DODA, R_M1 and R_M3. The black line represented the background signals.

After gaining a clear understanding on how junction sequences and base-stacking at junctions regulate the kinetic and thermodynamic properties of DODAs, we aimed to explore other options to module the junctions and thus regulate DODA transformation. First, we incorporated mismatches at the junctions and the base-stacking is expected to be eliminated or significantly weakened due to the mismatches. To explore this, we designed and tested three types of mismatches at junction (**Figure 4a**): (1) M1 is a "symmetric" design that contains mismatches on the positions B5/B6 and B3/B4 in the configuration i. (2) M2 contains mismatches on B3/B4 and B7/B8 in configuration i, and is expected to favor configuration i. (3) M3 is a reversed design to M2, and it is expected to favor configuration ii. Based on our understanding in the DODA transformation, we hypothesized simple transformation energy models corresponding to the Incorporation of different mismatches (**Figure 4b**).

To examine how mismatches affect assembly and transformation of DNA origami arrays, we designed DODA variants G_M1 and G_M2 based on G-DODA, R_M1 and R_M3 for R-DODA (**Supplementary Figure S22**). After assembly of DODAs with and without mismatches, the percentages of conformation II were obtained by analyzing AFM images (**Figure 4c and 4d, Supplementary Figures S23 to S34**). The fraction of conformation II structures increased with the number of added trigger DNA strands, being in good agreement with previous results. Interestingly, the mismatches showed different thermodynamic effect on the G- and R-DODA. For the G-DODA, a higher fraction of transformed structures was obtained in the presence of the mismatch G_M1 while the implementation of the mismatch G_M2 resulted in a lower yield. In the presence of either R_M1 or R_M3, an increased yield of transformed structures was obtained for the R structure. Although introducing mismatches results in an increase of the energy of the conformation I and II, the extent of increase for both conformations is different for the two structures. This leads to the uncertainty of the free energy differences between I and II and this difference may vary depending on each specific mismatch. Although quantitative calculation of mismatch effect on the thermodynamics of junction is lacking, our method

presents an experimental strategy to verify the mismatch effect on the thermodynamics of DNA origami arrays.

Next, the mismatch effect on the transition kinetics of DNA origami arrays was investigated. The R origami array as well as its mismatched structures R_M1 and R_M3 were measured with transformation kinetics using single-molecule fluorescence assay and ensemble fluorescence method. In the ensemble fluorescence assay with five triggers (**Figure 4e and 4f**), both mismatched structures R_M1 and R_M2 showed increased kinetics compared with R structure and had similar apparent rate constants. We further reduced the trigger number from five to two to differentiate the kinetics of R_M1 and R_M3 (**Figure 4g and 4h**). The reduced trigger number slowed down the overall kinetics of three structures. Noticeably, R_M1 and R_M2 presented significant kinetic differences. This phenomenon was further verified using the single-molecule fluorescence assay (**Figure 4i to 4j**). We additionally studied the kinetics of G structure and its mismatched structures G_M1 and G_M2 and found the two mismatched structures also had higher apparent rate constant than G structure (**Supplementary Figures S35 and S36**). We reason that the increased transition kinetics in mismatched structures is due to the increased free energy of conformation I, which reduces the activated energy for the transformation.

Besides mismatching, there are other options to change the junction design in a (quasi-) predictable manner. For example, we engineered a junction design that includes two unpaired “free bases” by inserting an “A” on the top scaffold strand of the junction and a base “T” on the bottom scaffold strand, as illustrated in **Supplementary Figure S37a**. Because the base-stacking at junction would be disrupted in conformation I but remain intact in conformation II, we expect this design would greatly favor the latter. Experimental results substantiated this hypothesis, as the DODA assembled into conformation II even without any trigger (**Supplementary Figure S37b to S37d**). This example of incorporating free bases to tune the DODA assembly and transformation showed that there is a wider design space to be explored.

Conclusion

We developed methods to study the effects of junction sequences on thermodynamics and transition kinetics of a reconfigurable DNA nanoarray. This model translates the thermodynamics and transition kinetics of individual junctions into the collective behaviors of a DNA origami array composed of the same junction sequence. The origami array amplifies the thermodynamic and kinetic differences between junctions with varying sequences, enabling the ensemble kinetic characterization of these differences for the first time. Experimental results demonstrated that the collective behaviors of DNA origami arrays are consistent with the energy model for single junctions.

This approach not only enhances the understanding of how junction sequences influence assembled DNA nanostructures but also offers new methods to tune the transformation kinetics of the DNA origami array. This serves as a complementary approach to previously reported methods, such as altering external factors (e.g., temperature or formamide) or structural design. We demonstrated two strategies to adjust the global transformation kinetics of the origami array: modifying the junction sequences in every junction within the array and adjusting the environmental magnesium concentration. Additionally, it is possible to program local transformation kinetics by engineering heterogeneous junction sequences in specific regions of the array.

This approach also provides a model for investigating the thermodynamics and transition kinetics of junctions influenced by various factors. The origami array reflects the properties of individual junctions and offers a straightforward way to reveal subtle changes in thermodynamics and kinetics due to sequence effects. Although this work focuses on the effect of the junction core sequence, the model is applicable for studying other factors affecting junctions. Structurally, sequences near the junction core or even distant junction arm sequences can be investigated using this model. It can also be used to explore mechanical constraints, sequence-dependent electrostatic potentials, nicks, or other structural effects. Environmentally, besides magnesium concentration, other buffer conditions or chemical reagents may affect the junction's preferences. In general, this model can be utilized to study a wide range of structural and environmental effects on junctions. A comprehensive

understanding of junction preferences and their impact on assembled structures can ultimately advance the field of DNA nanotechnology.

Acknowledgements.

This work is supported by Department of Energy grant DE-SC0020996, the National Science Foundation grants CCF-2227399 and ECCS-2328217, and the National Institute of Health grants 1R35GM153472 and 1RM1GM145394 to Y.K. The AFM images of DNA origami were collected on an atomic force microscope supported by Grants GM084070 and 3R01GM084070-07S1. D.W. acknowledges the support by the start-up funding from the University of Science and Technology of China, the Leading Talents of Innovation and Entrepreneurship of Gusu District (ZXL2023197), and the National Science Foundation of Jiangsu Province (SBK2024024218). P.T. gratefully acknowledges financial support from the Federal Ministry of Education and Research (BMBF) and the Free State of Bavaria under the Excellence Strategy of the Federal Government and the Länder through the ONE MUNICH Project 'Munich Multiscale Biofabrication' and the BMBF in the framework of the Cluster4Future program (Cluster for Nucleic Acid Therapeutics Munich, CNATM) (Project ID: 03ZU1201AA).

References:

1 Fu, T. J. & Seeman, N. C. DNA double-crossover molecules. *Biochemistry* **32**, 3211-3220 (1993). https://doi.org:10.1021/bi00064a003

2 Li, X., Yang, X., Qi, J. & Seeman, N. C. Antiparallel DNA Double Crossover Molecules As Components for Nanoconstruction. *J. Am. Chem. Soc.* **118**, 6131-6140 (1996). https://doi.org:10.1021/ja960162o

3 Yin, P., Hariadi, R. F., Sahu, S., Choi, H. M. T., Park, S. H., LaBean, T. H. & Reif, J. H. Programming DNA Tube Circumferences. *Science* **321**, 824-826 (2008). https://doi.org:10.1126/science.1157312

4 Wei, B., Dai, M. & Yin, P. Complex shapes self-assembled from single-stranded DNA tiles. *Nature* **485**, 623-626 (2012). https://doi.org:10.1038/nature11075

5 Ke, Y., Ong Luvena, L., Shih William, M. & Yin, P. Three-Dimensional Structures Self-Assembled from DNA Bricks. *Science* **338**, 1177-1183 (2012). https://doi.org:10.1126/science.1227268

6 Ong, L. L., Hanikel, N., Yaghi, O. K., Grun, C., Strauss, M. T., Bron, P., Lai-Kee-Him, J., Schueder, F., Wang, B., Wang, P., Kishi, J. Y., Myhrvold, C., Zhu, A., Jungmann, R., Bellot, G., Ke, Y. & Yin, P. Programmable self-assembly of three-dimensional

nanostructures from 10,000 unique components. *Nature* **552**, 72-77 (2017). https://doi.org:10.1038/nature24648
7 Rothemund, P. W. K. Folding DNA to create nanoscale shapes and patterns. *Nature* **440**, 297-302 (2006). https://doi.org:10.1038/nature04586
8 Douglas, S. M., Dietz, H., Liedl, T., Högberg, B., Graf, F. & Shih, W. M. Self-assembly of DNA into nanoscale three-dimensional shapes. *Nature* **459**, 414-418 (2009). https://doi.org:10.1038/nature08016
9 Yao, G., Zhang, F., Wang, F., Peng, T., Liu, H., Poppleton, E., Šulc, P., Jiang, S., Liu, L., Gong, C., Jing, X., Liu, X., Wang, L., Liu, Y., Fan, C. & Yan, H. Meta-DNA structures. *Nat. Chem.* **12**, 1067-1075 (2020). https://doi.org:10.1038/s41557-020-0539-8
10 Tikhomirov, G., Petersen, P. & Qian, L. Fractal assembly of micrometre-scale DNA origami arrays with arbitrary patterns. *Nature* **552**, 67-71 (2017). https://doi.org:10.1038/nature24655
11 Wagenbauer, K. F., Sigl, C. & Dietz, H. Gigadalton-scale shape-programmable DNA assemblies. *Nature* **552**, 78-83 (2017). https://doi.org:10.1038/nature24651
12 Dietz, H., Douglas, S. M. & Shih, W. M. Folding DNA into Twisted and Curved Nanoscale Shapes. *Science* **325**, 725-730 (2009). https://doi.org:10.1126/science.1174251
13 Han, D., Pal, S., Nangreave, J., Deng, Z., Liu, Y. & Yan, H. DNA Origami with Complex Curvatures in Three-Dimensional Space. *Science* **332**, 342-346 (2011). https://doi.org:10.1126/science.1202998
14 Han, D., Pal, S., Yang, Y., Jiang, S., Nangreave, J., Liu, Y. & Yan, H. DNA Gridiron Nanostructures Based on Four-Arm Junctions. *Science* **339**, 1412-1415 (2013). https://doi.org:10.1126/science.1232252
15 Thubagere Anupama, J., Li, W., Johnson Robert, F., Chen, Z., Doroudi, S., Lee Yae, L., Izatt, G., Wittman, S., Srinivas, N., Woods, D., Winfree, E. & Qian, L. A cargo-sorting DNA robot. *Science* **357**, eaan6558 (2017). https://doi.org:10.1126/science.aan6558
16 Douglas Shawn, M., Bachelet, I. & Church George, M. A Logic-Gated Nanorobot for Targeted Transport of Molecular Payloads. *Science* **335**, 831-834 (2012). https://doi.org:10.1126/science.1214081
17 Gerling, T., Wagenbauer, K. F., Neuner, A. M. & Dietz, H. Dynamic DNA devices and assemblies formed by shape-complementary, non–base pairing 3D components. *Science* **347**, 1446-1452 (2015). https://doi.org:10.1126/science.aaa5372
18 Ke, Y., Meyer, T., Shih, W. M. & Bellot, G. Regulation at a distance of biomolecular interactions using a DNA origami nanoactuator. *Nat. Commun.* **7**, 10935 (2016). https://doi.org:10.1038/ncomms10935
19 Seeman, N. C. Nucleic acid junctions and lattices. *J. Theor. Biol.* **99**, 237-247 (1982). https://doi.org:https://doi.org/10.1016/0022-5193(82)90002-9
20 Seeman, N. C. The design and engineering of nucleic acid nanoscale assemblies. *Curr. Opin. Struct. Biol.* **6**, 519-526 (1996). https://doi.org:https://doi.org/10.1016/S0959-440X(96)80118-7
21 Winfree, E., Liu, F., Wenzler, L. A. & Seeman, N. C. Design and self-assembly of two-dimensional DNA crystals. *Nature* **394**, 539-544 (1998). https://doi.org:10.1038/28998
22 Hyeon, C., Lee, J., Yoon, J., Hohng, S. & Thirumalai, D. Hidden complexity in the isomerization dynamics of Holliday junctions. *Nat. Chem.* **4**, 907-914 (2012). https://doi.org:10.1038/nchem.1463
23 Miick, S. M., Fee, R. S., Millar, D. P. & Chazin, W. J. Crossover isomer bias is the primary sequence-dependent property of immobilized Holliday junctions. *Proc. Natl. Acad. Sci. U. S. A.* **94**, 9080-9084 (1997). https://doi.org:10.1073/pnas.94.17.9080
24 Carlström, G. & Chazin, W. J. Sequence Dependence and Direct Measurement of Crossover Isomer Distribution in Model Holliday Junctions using NMR spectroscopy. *Biochemistry* **35**, 3534-3544 (1996). https://doi.org:10.1021/bi952571n

25 Overmars, F. J. J. & Altona, C. NMR study of the exchange rate between two stacked conformers of a model holliday junction11Edited by I. Tinoco. *J. Mol. Biol.* **273**, 519-524 (1997). https://doi.org:https://doi.org/10.1006/jmbi.1997.1340
26 Lilley, D. M. J. & Clegg, R. M. The Structure of the Four-Way Junction in DNA. *Annu. Rev. Biophys. Biomol. Struct.* **22**, 299-328 (1993). https://doi.org:10.1146/annurev.bb.22.060193.001503
27 Duckett, D. R., Murchie, A. I. & Lilley, D. M. The role of metal ions in the conformation of the four-way DNA junction. *EMBO J.* **9**, 583-590 (1990). https://doi.org:https://doi.org/10.1002/j.1460-2075.1990.tb08146.x
28 Adendorff, M. R., Tang, G. Q., Millar, David P., Bathe, M. & Bricker, William P. Computational investigation of the impact of core sequence on immobile DNA four-way junction structure and dynamics. *Nucleic Acids Res.* **50**, 717-730 (2022). https://doi.org:10.1093/nar/gkab1246
29 McKinney, S. A., Déclais, A.-C., Lilley, D. M. J. & Ha, T. Structural dynamics of individual Holliday junctions. *Nat. Struct. Biol.* **10**, 93-97 (2003). https://doi.org:10.1038/nsb883
30 Karymov, M., Daniel, D., Sankey, O. F. & Lyubchenko, Y. L. Holliday junction dynamics and branch migration: Single-molecule analysis. *Proc. Natl. Acad. Sci. U. S. A.* **102**, 8186-8191 (2005). https://doi.org:10.1073/pnas.0407210102
31 Nickels, P. C., Wünsch, B., Holzmeister, P., Bae, W., Kneer, L. M., Grohmann, D., Tinnefeld, P. & Liedl, T. Molecular force spectroscopy with a DNA origami–based nanoscopic force clamp. *Science* **354**, 305-307 (2016). https://doi.org:10.1126/science.aah5974
32 Zettl, T., Shi, X., Bonilla, S., Sedlak, S. M., Lipfert, J. & Herschlag, D. The structural ensemble of a Holliday junction determined by X-ray scattering interference. *Nucleic Acids Res.* **48**, 8090-8098 (2020). https://doi.org:10.1093/nar/gkaa509
33 Song, J., Li, Z., Wang, P., Meyer, T., Mao, C. & Ke, Y. Reconfiguration of DNA molecular arrays driven by information relay. *Science* **357**, eaan3377 (2017). https://doi.org:10.1126/science.aan3377
34 Simmons, C. R., MacCulloch, T., Krepl, M., Matthies, M., Buchberger, A., Crawford, I., Šponer, J., Šulc, P., Stephanopoulos, N. & Yan, H. The influence of Holliday junction sequence and dynamics on DNA crystal self-assembly. *Nat. Commun.* **13**, 3112 (2022). https://doi.org:10.1038/s41467-022-30779-6
35 Gambietz, S., Stenke, L. J. & Saccà, B. Sequence-dependent folding of monolayered DNA origami domains. *Nanoscale* **15**, 13120-13132 (2023). https://doi.org:10.1039/D3NR02537C
36 Wang, D., Yu, L., Ji, B., Chang, S., Song, J. & Ke, Y. Programming the Curvatures in Reconfigurable DNA Domino Origami by Using Asymmetric Units. *Nano Lett.* **20**, 8236-8241 (2020). https://doi.org:10.1021/acs.nanolett.0c03348
37 Fan, S., Cheng, J., Liu, Y., Wang, D., Luo, T., Dai, B., Zhang, C., Cui, D., Ke, Y. & Song, J. Proximity-Induced Pattern Operations in Reconfigurable DNA Origami Domino Array. *J. Am. Chem. Soc.* **142**, 14566-14573 (2020). https://doi.org:10.1021/jacs.0c06061
38 Nafisi, P. M., Aksel, T. & Douglas, S. M. Construction of a novel phagemid to produce custom DNA origami scaffolds. *Synth. Biol.* **3**, ysy015 (2018). https://doi.org:10.1093/synbio/ysy015
39 Engelhardt, F. A. S., Praetorius, F., Wachauf, C. H., Brüggenthies, G., Kohler, F., Kick, B., Kadletz, K. L., Pham, P. N., Behler, K. L., Gerling, T. & Dietz, H. Custom-Size, Functional, and Durable DNA Origami with Design-Specific Scaffolds. *ACS Nano* **13**, 5015-5027 (2019). https://doi.org:10.1021/acsnano.9b01025
40 Marchi, A. N., Saaem, I., Vogen, B. N., Brown, S. & LaBean, T. H. Toward Larger DNA Origami. *Nano Lett.* **14**, 5740-5747 (2014). https://doi.org:10.1021/nl502626s
41 Friedman, R. A. & Honig, B. A free energy analysis of nucleic acid base stacking in aqueous solution. *Biophys. J.* **69**, 1528-1535 (1995). https://doi.org:10.1016/S0006-3495(95)80023-8

42 Douglas, S. M., Marblestone, A. H., Teerapittayanon, S., Vazquez, A., Church, G. M. & Shih, W. M. Rapid prototyping of 3D DNA-origami shapes with caDNAno. *Nucleic Acids Res.* **37**, 5001-5006 (2009). https://doi.org:10.1093/nar/gkp436
43 Cole, F., Pfeiffer, M., Wang, D., Schröder, T., Ke, Y. & Tinnefeld, P. Controlled mechanochemical coupling of anti-junctions in DNA origami arrays. *Nat. Commun.* **accepted** (2024).

Supporting Information

Modulation of transformation of DNA origami nanoarray via sequence design

Dongfang Wang[#1,2], Fiona Cole[#3], Martina Pfeiffer[#3], Tim Schröder[3], Philip Tinnefeld[3]* and Yonggang Ke[4*]

[1]School of Biomedical Engineering, University of Science and Technology of China, Hefei 230026, China

[2]Suzhou Institute for Advanced Research, University of Science and Technology of China, Suzhou 215123, China

[3]Department of Chemistry and Center for NanoScience, Ludwig-Maximilians-Universität München, Butenandtstr. 5-13, 81377 München, Germany

[4]Wallace H. Coulter Department of Biomedical Engineering, Emory University and Georgia Institute of Technology, Atlanta, GA 30322, USA

# These authors contributed equally

* Correspondence: yonggang.ke@emory.edu, philip.tinnefeld@cup.uni-muenchen.de

Materials Chemically synthesized DNA short strands were purchased from IDT (www.idtdna.com) and were used without further purification. All other reagents were purchased from Sigma-Aldrich or New England Biolabs.

DNA origami design and folding The DNA origami was designed with the software CaDNAno (http://cadnano.org/)[1]. For DNA Origami folding, 10 nM scaffold together with a tenfold excess of each staple strand was mixed in 1×TE (10 mM Tris, 1 mM EDTA; pH 8.0) buffer with 6 mM $MgCl_2$. In the annealing process, the folding mixture was heated at 80°C and slowly cooled down to 25°C at the rate of -1°C/3 min. Afterwards, the folded DNA origami was purified from excess staple strands by agarose gel electrophoresis.

Agarose gel electrophoresis DNA origami samples were subjected to agarose gel electrophoresis at 70 V for 2-3 hours in an ice water bath. Gels were prepared with 0.5 ×TBE buffer containing 10 mM $MgCl_2$ and 0.005% (v/v) Ethidium Bromide. To purify the sample, the gel was illuminated under UV light. The target band was cut and the sample was extracted by squeezing.

AFM imaging 2 µL samples were deposited onto freshly cleaved mica. The sample area was filled with 80 µL 1×TE buffer with 10 mM $MgCl_2$. The samples were imaged on a Multimode VIII system (Bruker) in liquid mode using commercial tips (SNL-10, Bruker). The results were analyzed by the Nanoscope analysis (Bruker) and Image J.

Production of custom DNA scaffold The method follows a published paper[2] to produce custom DNA scaffold. The method uses a pScaf vector, which is commercially available on http://www.addgene.org/111401/. To produce custom DNA scaffold, a pseudogene with prescribed sequence should be designed first. The pseudogene contains the sequence with prescribed sequence and two restriction enzyme-recognition overhangs on both ends. The pScaf vector and pseudogene were first digested by KpnI and BamHI enzymes and purified by agarose gel electrophoresis. Then pScaf vector and pseudogene were mixed with 1:5 ratio and linked by T4 DNA ligase with overnight reaction. The mixtures were transformed into competent DH5α cells. The cells were grown in a LB plate containing 100 µg/ml carbenicillin in 37˚C overnight. Three colonies were selected to collect the plasmids by miniprep. The plasmids were then digested by KpnI and BamHI and verified on the agarose gel electrophoresis. Correct insertion of pseudogene into pScaf would show correct bands in the gel. The recombinant pScaf plasmid and helper plasmid pSB4423 were co-transformed into competent XL1-blue cells and incubated on a LB plate containing 100 µg/ml carbenicillin and 20 µg/ml chloramphenicol in 30˚C for two days. One colony was selected to continue the growth in 2×YT medium for 24h and the custom DNA scaffold was collected following the standard protocol for extracting ssDNA from M13 cells.

Ensemble fluorescence measurements. For ensemble transformation kinetics measurements, DNA origami samples were assembled by mixing 20 nM DNA scaffold, 200 nM DNA staples, 10 nM ATTO647N modified staple and 20 nM quencher modified staple in 1×TE buffer and 6 mM $MgCl_2$. The mixtures were annealed from 80°C to 25°C with the rate of -1°C/3 min. 200 nM triggers were added to the core structures and their fluorescence measured in a real-time PCR machine (Rotor-Gene Q, Qiagen, USA). Fluorescence measurements were carried out at 30 °C over a time of 60 min and a data point was taken every 30 s. All measurements were repeated three times. To normalize the fluorescence measurements to the completely transformed sample, the fluorescence after 60 min of samples to which all five triggers were added and the fluorescence of the untransformed samples were used as reference points for the untransformed and transformed sample, respectively. An additional experiment in which the samples to which all five triggers were added were heated to 50 °C for 1.5 h

directly after the measurement showed no additional increase in fluorescence intensity, indicating that their fluorescence after 60 min measurement time represents the completely transformed sample and can be used for normalization.

Sample preparation for single-molecule fluorescence measurements For chamber preparation, adhesive SecureSealTM Hybridization Chambers (2.6 mm depth, Grace Bio-Labs, USA) were glued on microscope coverslips of 24 mm × 60 mm size and 170 µm thickness (Carl Roth GmbH, Germany). The created wells were incubated with 1 M KOH for 1 h and washed three times with 1×PBS buffer. After surface passivation by incubation with BSA-Biotin (0.5 mg/mL, Sigma Aldrich, USA) for 30 min, the surface was washed with 200 µL 1× PBS buffer. 150 µL neutravidin (0.25 mg/mL, Thermo Fisher, USA) was incubated for 10 min and then washed three times with 150 µL 1× PBS buffer. The solution of biotinylated DNA origami was diluted with 1× TE buffer containing 750 mM NaCl to a concentration of ~10 pM and then immobilized on the biotin-neutravidin surface via biotin-neutravidin interactions. For this, 150 µL of the DNA origami sample solution was added and incubated for 5 min. Residual unbound DNA origami was removed by washing the chambers with 150 µL 1x TE buffer containing 750 mM NaCl. The density of DNA origami on the surface suitable for single-molecule measurements was checked on a TIRF microscope. For acquisition of single-molecule fluorescence images and movies, an oxidizing and reducing buffer system (1x TAE, 6 mM $MgCl_2$, 2 mM Trolox/Troloxquinone) was used in combination with an oxygen scavenging system (12 mM protocatechuic acid, 56 µM protocatechuate 3,4-dioxygenase from pseudomonas sp., 1% glycerol, 1 mM KCl, 2 mM Tris HCl, 20 µM Na_2 EDTA*$2H_2O$) to suppress blinking and photobleaching. Triggers were added at a concentration of 50 nM each. Chambers were sealed directly after addition of the oxygen scavenging system.

Single-molecule wide-field measurements For detection of single-molecule fluorescence, a commercial wide-field/TIRF microscope Nanoimager from Oxford Nanoimaging Ltd. was used. Red excitation at 638 nm was realized with a 1100 mW laser, green excitation at 532 nm with a 1000 mW laser, respectively. The relative laser intensities were set to 9% for green and to 18% for red excitation. The microscope was set to TIRF illumination. For determining transformation yields, dual-color TIRF images of surface immobilized structures were collected. For studying transformation kinetics, dual-color TIRF movies were collected. Here, data acquisition was initialized directly after addition of the DNA triggers by activating the lasers and taking a frame of 100 ms every two seconds separately for both excitation lasers (with a time lag of 1 s between them) over a measurement period of 20 min. Directly after acquiring the movies, TIRF dual-color TIRF images were collected from different areas of the sample to determine the transformation yield after the measurement. Measurements were carried out at 37 °C.

Multi-step kinetics Unlike the single-exponential decay observed in dwell time histograms for the switching kinetics of single Holliday junctions,[1] for the DNA origami arrays, we often obtained nonexponential transformation time distributions that displayed a rising phase followed by a decay in the single-molecule experiments. Analogously, the ensemble measurements showed an initial phase of increasing transformation rates. Such a behavior cannot be described by kinetic laws of single step processes but is characteristic for the convolution of the kinetics of multiple steps. As such, the array transformation most probably consists of multiple consecutive steps, an assumption which is in good agreement with previous studies. They describe the DNA origami transformation as a multi-step process. In each of these steps, different Holliday junctions in the arrays switch their conformation, ultimately resulting in the transformation of the whole structure.

Extracting 'apparent' transformation rate constants from the ensemble measurements To compare the kinetics of the transformation of the different structures, we defined an apparent transformation rate constant k. For determining k, the normalized fluorescence transients were first calculated as described above. These transients describe the change in concentration of the transformed structures over time. By subtracting the normalized fluorescence values from one, the change in concentration of the untransformed structures was depicted. Similar to single-step first order kinetics, the apparent transformation rate constant k was then extracted as the negative slope of linear fits to the logarithmic representation of the plots. For the linear fit, only data points recorded between 2 min and 15 min were considered to exclude both the initial phase of increasing transformation rates and the end point of the transformation reaction.

Extracting transformation yields and 'apparent' transformation rate constants from the single-molecule TIRF measurements To quantify the percentage of transformed structures from single-molecule TIRF measurements, we divided the number of green (ATTO 542) and red (ATTO647N) co-localized spots by the total number of green spots of dual-color TIRF fluorescence images. To account for a labelling efficiency < 100%, the percentage of co-localized spots was normalized by the percentage of co-localized spots of a DNA origami array folded with all five fuel DNA strands to calculate transformation yields. For calculating apparent transformation rate constants, the recorded TIRF movies were drift-corrected and dual-color background corrected fluorescence intensity transients extracted from the spots. These transients were fitted using a Hidden Markov model and the transformation times extracted from the fits as the time a sudden increase in fluorescence intensity occurred and the intensity afterwards remained at a higher level for at least 10 s for the first time. To extract the evolution of the transformation yield over time, these transformation times were cumulatively added up and divided by the total number of transformation times collected. To account for possible transformation yields <100%, the resulting normalized values were multiplied with the final transformation yields extracted from TIRF images recorded directly after movie acquisition. If not stated otherwise, apparent rate constants were then extracted as described for the ensemble measurements and data points recorded between 20 s and 150 s considered for the linear fit.

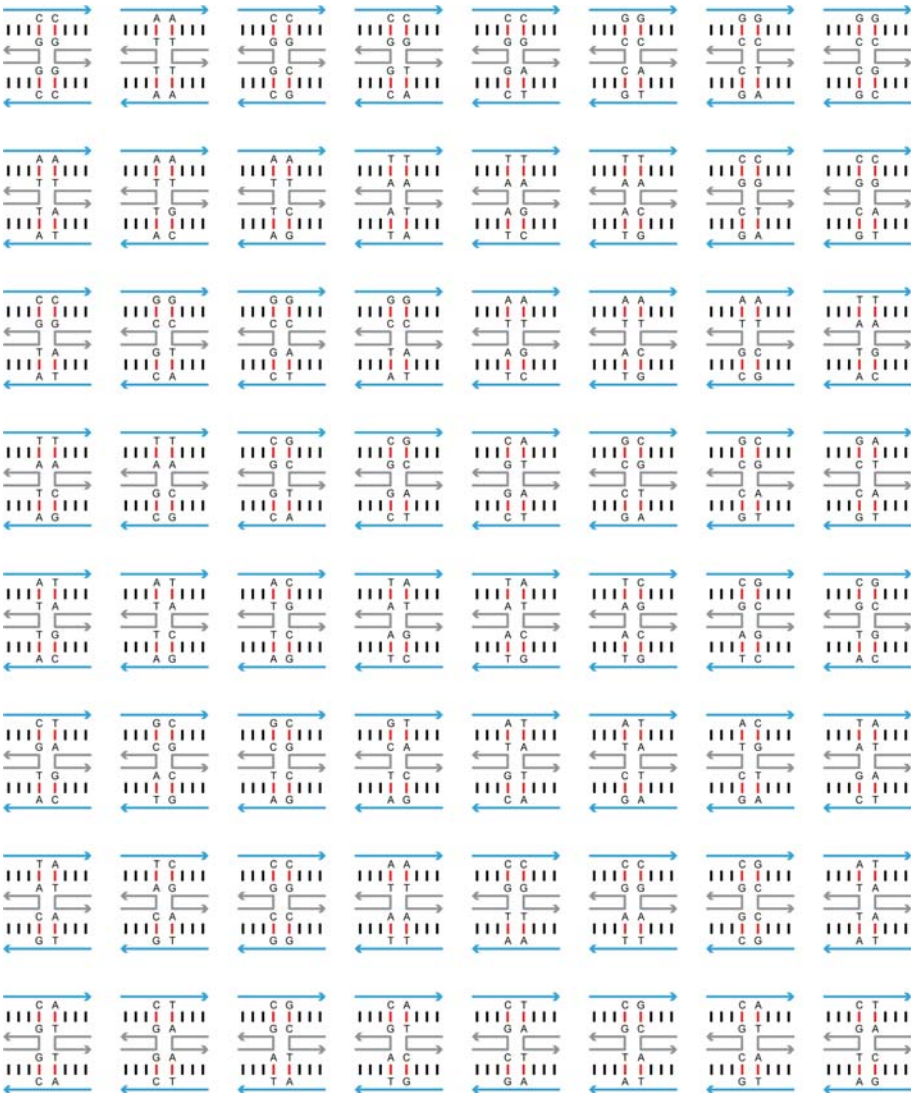

Figure S1. 64 possible basepair combinations at a four-way junction.

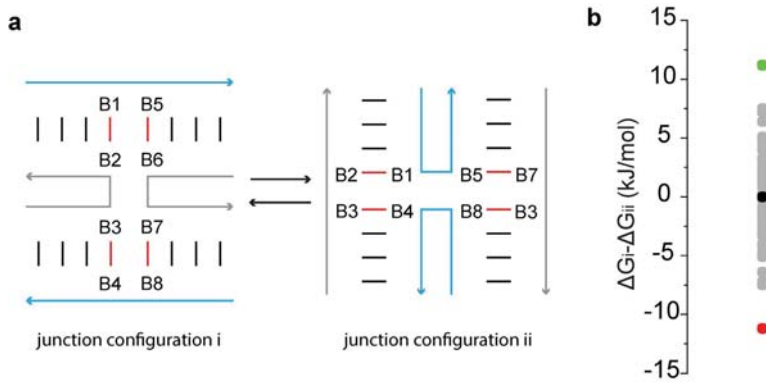

Figure S2. Junction sequence design. **a.** Schematic of the switching of a four-way junction and changing of base stacking. **b.** Plot of free energy differences ($\Delta\Delta G=\Delta G_i-\Delta G_{ii}$) between two stacked junction configurations corresponding to the 64 sequence combinations in Supplementary Figure S1, calculated based on data available in literature[3]. The green dot, black dot, and red dot represent the three sets of sequences used in this work for G junction, N junction, and R junction, respectively.

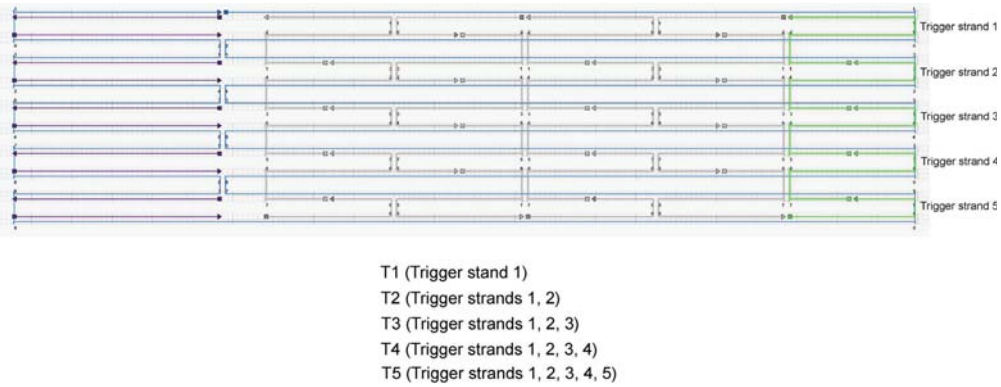

Figure S3. Design of DNA origami domino array in Cadnano.The array contains 22 junctions in four columns (5, 4, 5, 4 junctions in each column). The horizontal distance between two nearest junctions is 26 basepairs. The blue strand represents the DNA scaffold. Grey strands are core strands for assembling the body of DNA origami. Purple strands are used to bind to the extra DNA scaffold. Green strands are triggers used for the transformation of DNA origami array. T1 to T5 indicated the combination of trigger strands used for transformation.

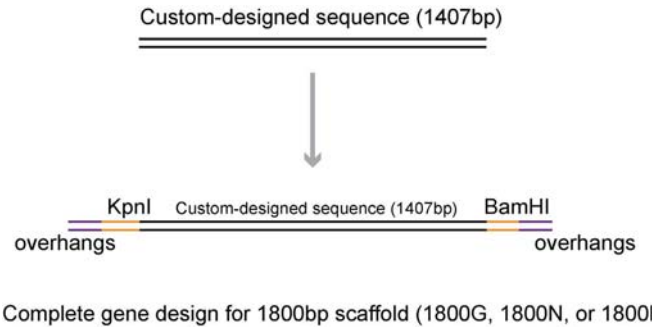

Figure S4. Pseudogene design for producing the three custom-designed DNA scaffolds. First, an initial random sequence (1407 bp) was generated. Then prescribed sequence at the specific positions were assigned at the initial sequence to generate custom pseudogenes. Two restriction enzyme recognition sequences by KpnI and BamHI and 12 bp overhangs were then added on both ends of the pseudogene.

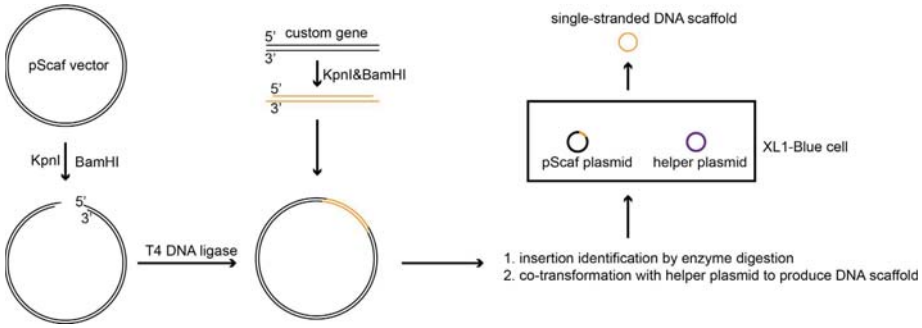

Figure S5. Procedures for producing custom DNA scaffold using pScaf vector. The pScaf vector and custom gene were digested by enzyme KpnI and BamHI. Then the vector and gene were ligated together by the T4 DNA ligase. The recombined plasmid was transformed into competent DH5α cells and successful ligation were verified by enzyme digestion of the new plasmid followed by agarose gel electrophoresis. The recombined plasmid and helper plasmid were co-transformed into competent XL1-Blue cells to produce custom circular ssDNA.

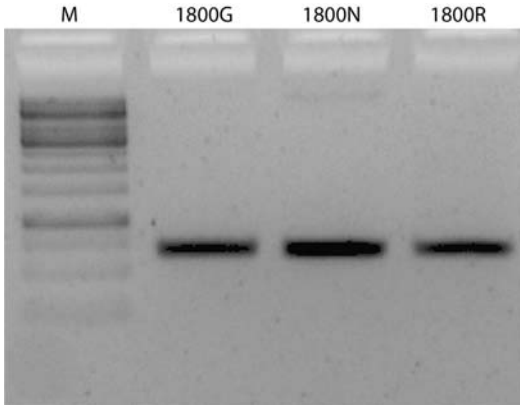

Figure S6. Agarose gel electrophoresis of custom DNA scaffold 1800G, 1800N and 1800R. M: 1kb DNA ladder.

Table S1. Scaffold DNA sequences. The junction sequences are capitalized.

1800G

tacgaagagttccagcagggattccaagaaatgGCcaatgaagattggatcacctttcgcactaagacctacttg
tttgaggagtGCctgatgaattggcacgaccgcctcaggaaagtggaggagcattctgtgatgactgtcaagctc
caatctgaggtggGCaaatataagattgttatccctatcTAgaagtacgtccgcggagaacacctGCcacccg
atcactggctggatctgtTAcgcttgctgggtctgcctcgcggcacatctctggagaaactgctgttcggtgacctgc
tgagagttGCcgataccatcgtggccaaggctgcTAacctgaaagatctgaactcacgcgGCcagggtgaa
gtgaccatccgcgaaTAactcagggaactggatttgtggggcgtgggtgctgtgttcacactgatcgGCtatgag
gactcccagagccgcaccTAgaagctgatcaaggattggaaggaGCtcgtcaaccaggtgggcgacaataT
AtgcctcctgcagtccttgaaggactcaccatactataaaggctttgaagacaaggtcagcatctggGCaagga
aactcgccgaactggacgaTAatttgcagaacctcaaccatattcGCagaaagtgggtttacctcgaaccaTA
ctttggtcgcggagccctgcccaaagagcagaccagattcaacagggtggGCgaagatttccgcagcatcatg
acaTAtatcaagaaggacaatcgcgtcacGCccttgactacccacgcaggcattcTAaactcactgctgacca
tcctggaccaattgcagagatgccagcgcagcctcaacgagttcctggagGCgaagcgcagcgccttccctcg
cttTAacttcatcggagacgatgacctgcGCgagatcttgggccagtcaaccaatTAatccgtgattcagtctca
cctcaagaagctgtttgctggtatcaactctgGCtgtttcgatgagaagtctaagcacTAtactgcaatgaagtcctt
ggagggGCaagttgtgccattcaagaataacgTAcccttgtccaataacgtcgaaacctggctgaacgatctgg
ccctggagatgaagaagaccctggagGCgctgctgaaggagtgcgtgacaacTAgacgcagctctcaggga
gctgtggGCccttctctgttcccatcacagatcTAgtgcttggccgaacagatcaagtttaccgaagatgtggaga
acgcaattaaagatcactccctgcaccagattgagTAacagctggtgaacaaattggagcagtatactaacatc
gacacatcttccgTAgacccaggtaacacagagtccggtattctggagctgaaactgaaagcactgattctcgac
ggatccacgcgccctgtagcggcgcattaagcgcggcgggtgtggtggttacgcgcagcgtgaccgctacacttg
ccagcgccctagcgcccgctcctttcgctttcttcccttcctttctcgccacgttcgccggctttccccgtcaagctctaa
atcgggggctcccttagggttccgatttagtgctttacggcacctcgaccccaaaaaacttgatttgggtgatggttc
acgtagtgggccatcgccctgatagacggtttttcgcccttgacgttggagtccacgttctttAatagtggactcttgtt
ccaaactggaacaacactcaaccctatctcgggctattcttttgatttataagggattttgccgatttcggggtacc

1800N

tacgaagagttccagcagggattccaagaaatgGCcaatgaagattggatcacctttcgcactaagacctacttg
tttgaggagtGCctgatgaattggcacgaccgcctcaggaaagtggaggagcattctgtgatgactgtcaagctc
caatctgaggtggGCaaatataagattgttatccctatcGCgaagtacgtccgcggagaacacctGCcacccg
atcactggctggatctgtGCcgcttgctgggtctgcctcgcggcacatctctggagaaactgctgttcggtgacctgc
tgagagttGCcgataccatcgtggccaaggctgcGCacctgaaagatctgaactcacgcgGCcagggtgaa
gtgaccatccgcgaaGCactcagggaactggatttgtggggcgtgggtgctgtgttcacactgatcgGCtatgag
gactcccagagccgcaccGCgaagctgatcaaggattggaaggaGCtcgtcaaccaggtgggcgacaata
GCtgcctcctgcagtccttgaaggactcaccatactataaaggctttgaagacaaggtcagcatctggGCaagg
aaactcgccgaactggacgaGCatttgcagaacctcaaccatattcGCagaaagtgggtttacctcgaaccaG
CctttggtcgcggagccctgcccaaagagcagaccagattcaacagggtggGCgaagatttccgcagcatcat
gacaGCtatcaagaaggacaatcgcgtcacGCccttgactacccacgcaggcattcGCaactcactgctgac
catcctggaccaattgcagagatgccagcgcagcctcaacgagttcctggagGCgaagcgcagcgccttccct
cgcttGCacttcatcggagacgatgacctgcGCgagatcttgggccagtcaaccaatGCatccgtgattcagtc
tcacctcaagaagctgtttgctggtatcaactctgGCtgtttcgatgagaagtctaagcacGCtactgcaatgaagt
ccttggagggGCaagttgtgccattcaagaataacgGCcccttgtccaataacgtcgaaacctggctgaacgat
ctggccctggagatgaagaagaccctggagGCgctgctgaaggagtgcgtgacaacGCgacgcagctctca
gggagctgtggGCccttctctgttcccatcacagatcGCgtgcttggccgaacagatcaagtttaccgaagatgt
ggagaacgcaattaaagatcactccctgcaccagattgagGCacagctggtgaacaaattggagcagtatact
aacatcgacacatcttccgGCgacccaggtaacacagagtccggtattctggagctgaaactgaaagcactgat
tctcgacggatccacgcgccctgtagcggcgcattaagcgcggcgggtgtggtggttacgcgcagcgtgaccgct
acacttgccagcgccctagcgcccgctcctttcgctttcttcccttcctttctcgccacgttcgccggctttccccgtcaa
gctctaaatcgggggctcccttagggttccgatttagtgctttacggcacctcgaccccaaaaaacttgatttgggtg
atggttcacgtagtgggccatcgccctgatagacggtttttcgcccttgacgttggagtccacgttctttAatagtgga
ctcttgttccaaactggaacaacactcaaccctatctcgggctattcttttgatttataagggattttgccgatttcggggt
acc

1800R

tacgaagagttccagcagggattccaagaaatgGAcaatgaagattggatcacctttcgcactaagacctacttgt
ttgaggagtGActgatgaattggcacgaccgcctcaggaaagtggaggagcattctgtgatgactgtcaagctcc
aatctgaggtggGAaaatataagattgttatccctatcTCgaagtacgtccgcggagaacacctGAcacccgat
cactggctggatctgtTCcgcttgctgggtctgcctcgcggcacatctctggagaaactgctgttcggtgacctgctg
agagttGAcgataccatcgtggccaaggctgcTCacctgaaagatctgaactcacgcgGAcagggtgaagtg
accatccgcgaaTCactcagggaactggatttgtggggcgtgggtgctgtgttcacactgatcgGAtatgaggac
tcccagagccgcaccTCgaagctgatcaaggattggaaggaGAtcgtcaaccaggtgggcgacaataTCtg
cctcctgcagtccttgaaggactcaccatactataaaggctttgaagacaaggtcagcatctggGAaaggaaact
cgccgaactggacgaTCatttgcagaacctcaaccatattcGAagaaagtgggtttacctcgaaccaTCctttg
gtcgcggagccctgcccaaagagcagaccagattcaacagggtggGAgaagatttccgcagcatcatgacaT
CtatcaagaaggacaatcgcgtcacGAccttgactacccacgcaggcattcTCaactcactgctgaccatcctg
gaccaattgcagagatgccagcgcagcctcaacgagttcctggagGAgaagcgcagcgccttccctcgcttTC
acttcatcggagacgatgacctgcGAgagatcttgggccagtcaaccaatTCatccgtgattcagtctcacctca
agaagctgtttgctggtatcaactctgGAtgtttcgatgagaagtctaagcacTCtactgcaatgaagtccttggag
ggGAaagttgtgccattcaagaataacgTCcccttgtccaataacgtcgaaacctggctgaacgatctggccct
ggagatgaagaagaccctggagGAgctgctgaaggagtgcgtgacaacTCgacgcagctctcagggagct
gtggGAccttctctgttcccatcacagatcTCgtgcttggccgaacagatcaagtttaccgaagatgtggagaac
gcaattaaagatcactccctgcaccagattgagTCacagctggtgaacaaattggagcagtatactaacatcga
cacatcttccgTCgacccaggtaacacagagtccggtattctggagctgaaactgaaagcactgattctcgacgg
atccacgcgccctgtagcggcgcattaagcgcggcgggtgtggtggttacgcgcagcgtgaccgctacacttgcc
agcgccctagcgcccgctcctttcgcttcttcccttcctttctcgccacgttcgccggctttccccgtcaagctctaaatc
gggggctccctttagggttccgatttagtgctttacggcacctcgaccccaaaaaacttgatttgggtgatggttcacg
tagtgggccatcgccctgatagacggtttttcgccctttgacgttggagtccacgttctttAatagtggactcttgttcca
aactggaacaacactcaaccctatctcgggctattcttttgatttataagggattttgccgatttcggggtacc

1800RF

tacgaagagttccagcagggattccaagaaatgGCAcaatgaagattggatcacctttcgcTactaagacctac
ttgtttgaggagtGCActgatgaattggcacgaccgcctcaTggaaagtggaggagcattctgtgatgactgtca
agctccaatctgaggtggGCAaaatataagattgttatccctatcTACgaagtacgtccgcggagaacacctG
CAcacccgatcactggctggatctgtTACcgcttgctgggtctgcctcgcggcacatctctggagaaactgctgtt
cggtgacctgctgagagttGCAcgataccatcgtggccaaggctgcTACacctgaaagatctgaactcacgc
gGCAcagggtgaagtgaccatccgcgaaTACactcagggaactggatttgtggggcgtgggtgctgtgttcac
actgatcgGCAtatgaggactcccagagccgcaccTACgaagctgatcaaggattggaaggaGCAtcgtc
aaccaggtgggcgacaataTACtgcctcctgcagtccttgaaggactcaccatactataaaggctttgaagaca
aggtcagcatctggGCAaaggaaactcgccgaactggacgaTACatttgcagaacctcaaccatattcGCA
agaaagtgggtttacctcgaaccaTACctttggtcgcggagccctgcccaaagagcagaccagattcaacagg
gtggGCAgaagatttccgcagcatcatgacaTACtatcaagaaggacaatcgcgtcacGCAccttgactac
ccacgcaggcattcTACaactcactgctgaccatcctggaccaattgcagagatgccagcgcagcctcaacga
gttcctggagGCAgaagcgcagcgccttccctcgcttTACacttcatcggagacgatgacctgcGCAgagat
cttgggccagtcaaccaatTACatccgtgattcagtctcacctcaagaagctgtttgctggtatcaactctgGCAt
gtttcgatgagaagtctaagcacTACtactgcaatgaagtccttggagggGCAaagttgtgccattcaagaata
acgTACcccttgtccaataacgtcgaaacctggctgaacgatctggccctggagatgaagaagaccctggag
GCAgctgctgaaggagtgcgtgacaacTACgacgcagctctcagggagctgtggGCAccttctctgttccca
tcacagatcTACgtgcttggccgaacagatcaagtttaccgaagatgtggagaacgcaattaaTagatcactcc
ctgcaccagattgagTACacagctggtgaacaaattggagcagTtatactaacatcgacacatcttccgTACg
acccaggtaacacagagtccggtattctggagctgaaactgaaagcactgattctcgacggatccacgcgccctg
tagcggcgcattaagcgcggcgggtgtggtggttacgcgcagcgtgaccgctacacttgccagcgccctagcgc
ccgctcctttcgctttcttcccttcctttctcgccacgttcgccggctttccccgtcaagctctaaatcgggggctcccttta
gggttccgatttagtgctttacggcacctcgaccccaaaaaacttgatttgggtgatggttcacgtagtgggccatcg
ccctgatagacggtttttcgccctttgacgttggagtccacgttctttAatagtggactcttgttccaaactggaacaac
actcaaccctatctcgggctattcttttgatttataagggattttgccgatttcggggtacc

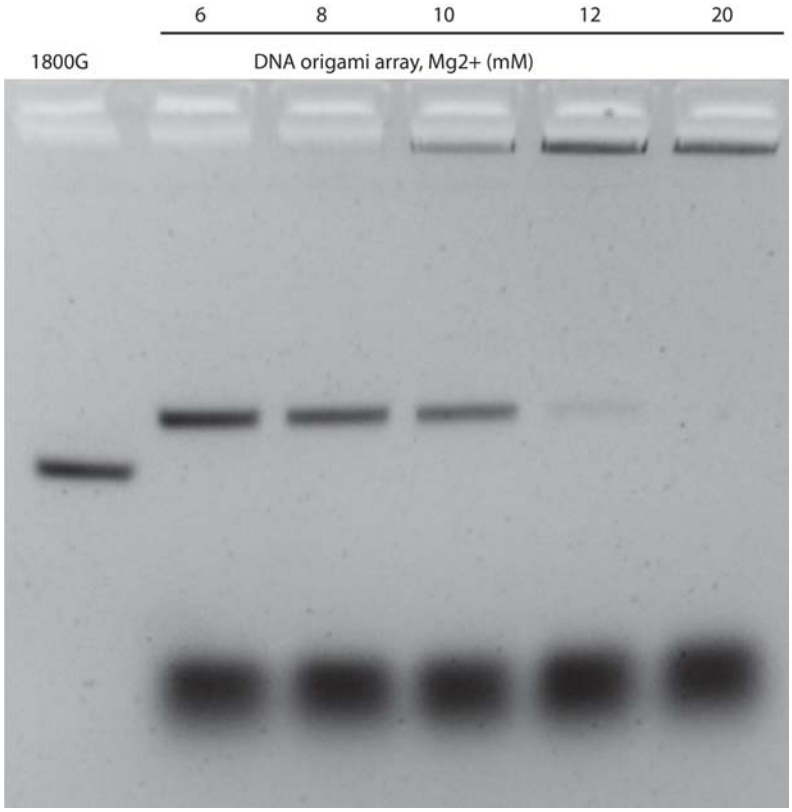

Figure S7. Screening of Mg^{2+} concentration for one-pot assembly of G-DODA.

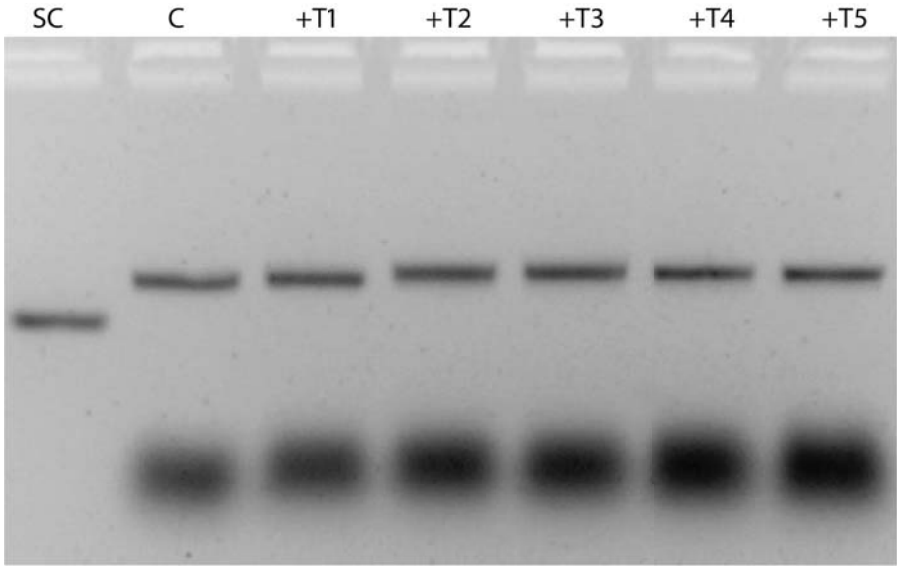

Figure S8. Agarose gel electrophoresis of G-DODA from one-pot assembly with different number of triggers. SC: DNA scaffold 1800G. C: core structure without triggers. T1-T5: assembly with 1, 2, 3, 4, or 5 triggers strands.

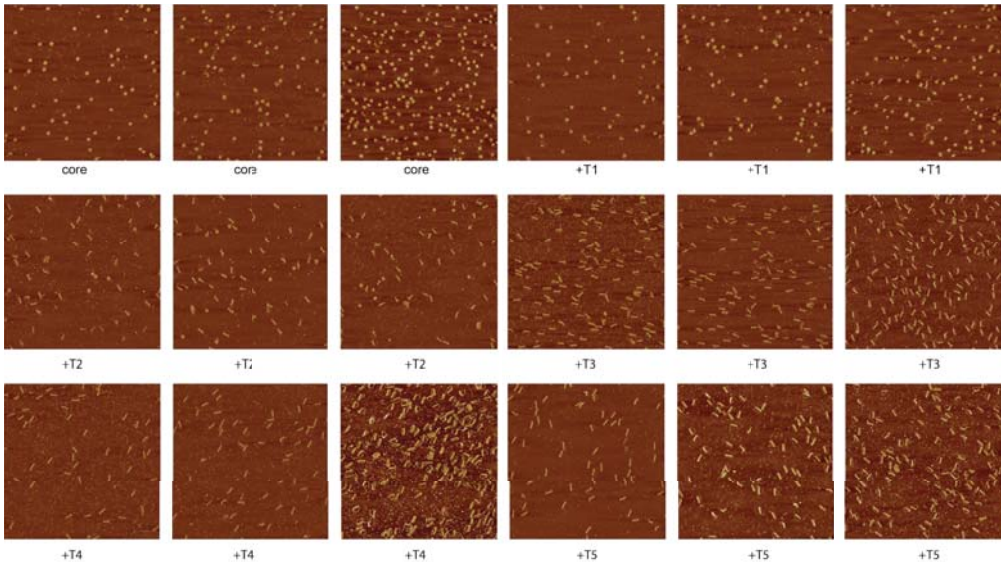

Figure S9. AFM images for G-DODA from one-pot assembly with different number of triggers. Core: assembly of G-DODA without triggers. T1-T5: assembly with 1, 2, 3, 4, or 5 triggers strands. Image size: 2 μm.

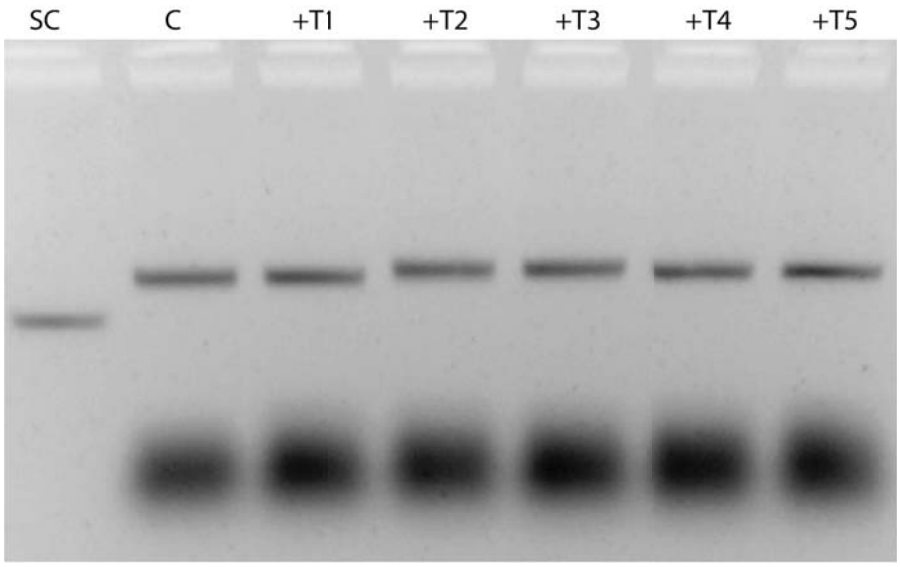

Figure S10. Agarose gel electrophoresis of N-DODA from one-pot assembly with different number of triggers. SC: DNA scaffold 1800N. C: N-DODA without triggers. T1-T5: assembly with 1, 2, 3, 4, or 5 triggers strands.

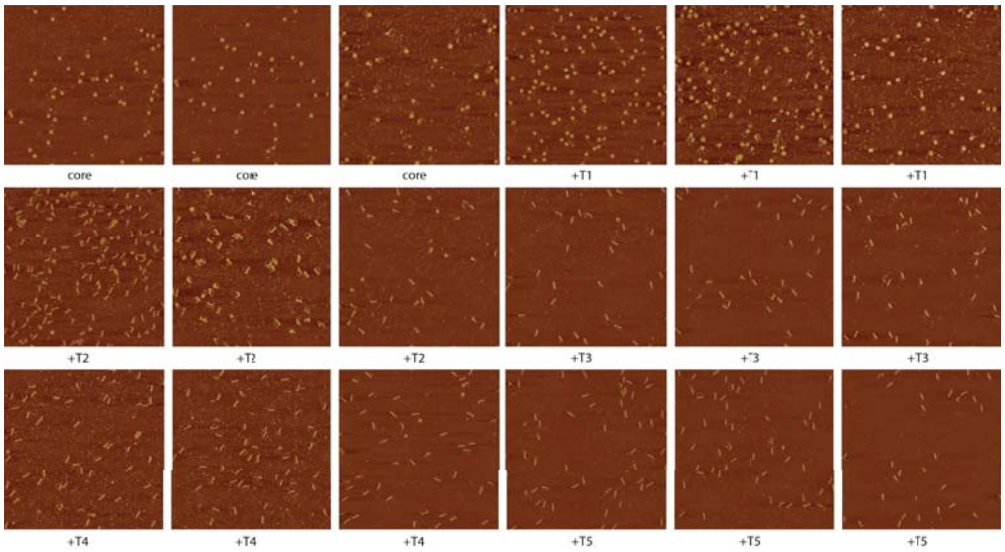

Figure S11. AFM images for N-DODA from one-pot assembly with different number of triggers. Core: assembly of N-DODA without triggers. T1-T5: assembly with 1, 2, 3, 4, or 5 triggers strands. Image size: 2 μm.

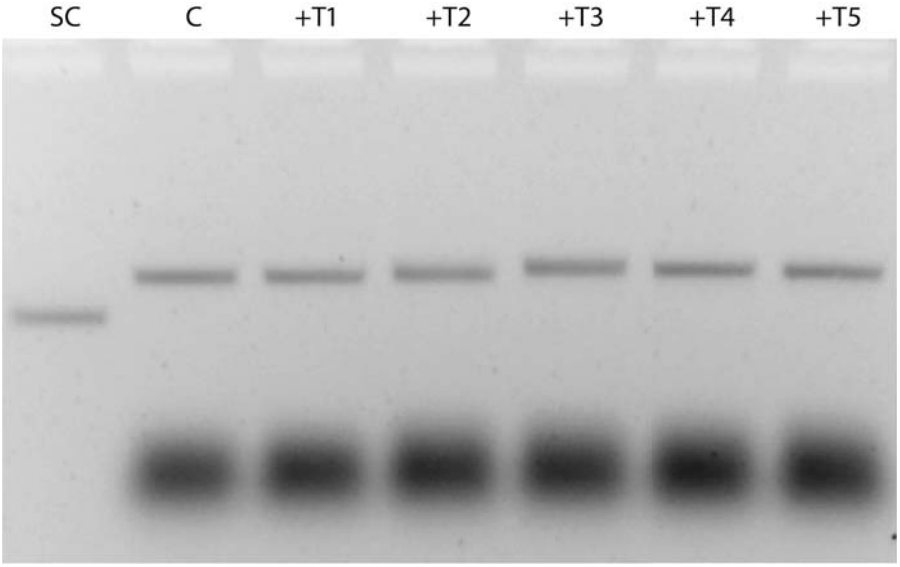

Figure S12. Agarose gel electrophoresis of R-DODA from one-pot assembly with different number of triggers. SC: DNA scaffold 1800R. C: R-DODA without triggers. T1-T5: 1-5 trigger strands.

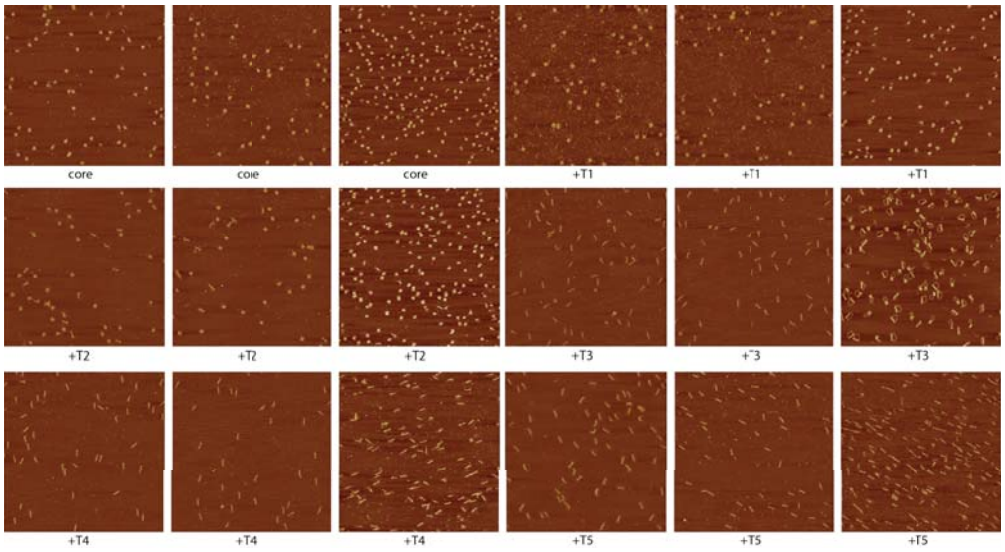

Figure S13. AFM images for R-DODA from one-pot assembly with different number of triggers. core: assembly of R-DODA without triggers. T1-T5: assembly with 1, 2, 3, 4, or 5 triggers strands. Image size: 2 μm.

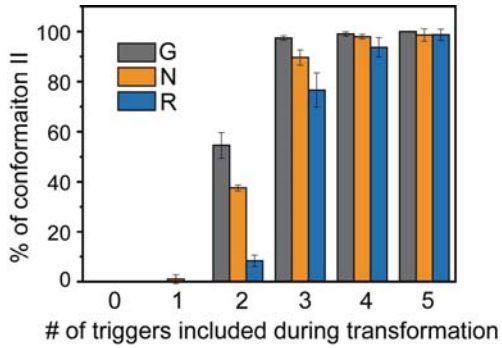

Figure S14. Transformation yields of three DODAs with different number of triggers. Core structures of G-, N- and R-DODAs were incubated with different number of triggers in 6 mM $MgCl_2$ at 50°C for overnight. The samples were purified by agarose gel electrophoresis and imaged under AFM. The conformation II ratios for G-, N- and R-DODAs without triggers were all 0%. The conformation II ratios for G-, N- and R-DODAs without one trigger were 0%, 1.0±1.8% and 0%, respectively. The conformation II ratios for G-, N- and R-DODAs without two triggers were 54.5±5.2%, 37.5±1.2% and 8.4±2.3%, respectively. The conformation II ratios for G-, N- and R-DODAs without three triggers were 97.4±0.9%, 89.7±3.0% and 76.7±6.9%, respectively. The conformation II ratios for G-, N- and R-DODAs without four triggers were 99.0±0.8%, 98.0±0.9% and 93.8±3.8%, respectively. The conformation II ratios for G-, N- and R-DODAs without five triggers were 100%, 98.6±2.4% and 98.7±2.2%, respectively.

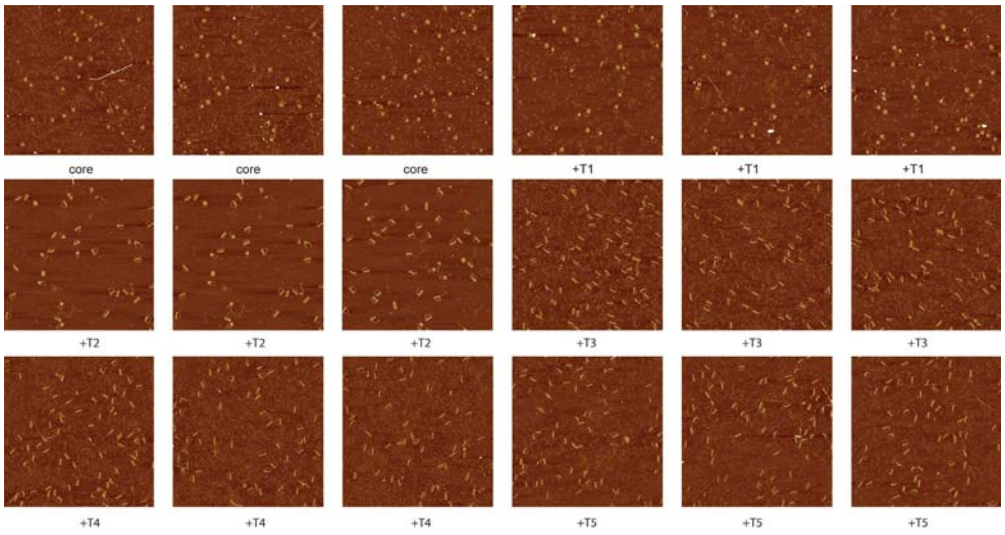

Figure S15. AFM imaging of the transformation of G-DODAs with different number of triggers. Core: the assembled structured without triggers. The core structures of G-DODAs were incubated with different number of triggers in 6 mM $MgCl_2$ at 50°C for overnight. Image size: 2 μm.

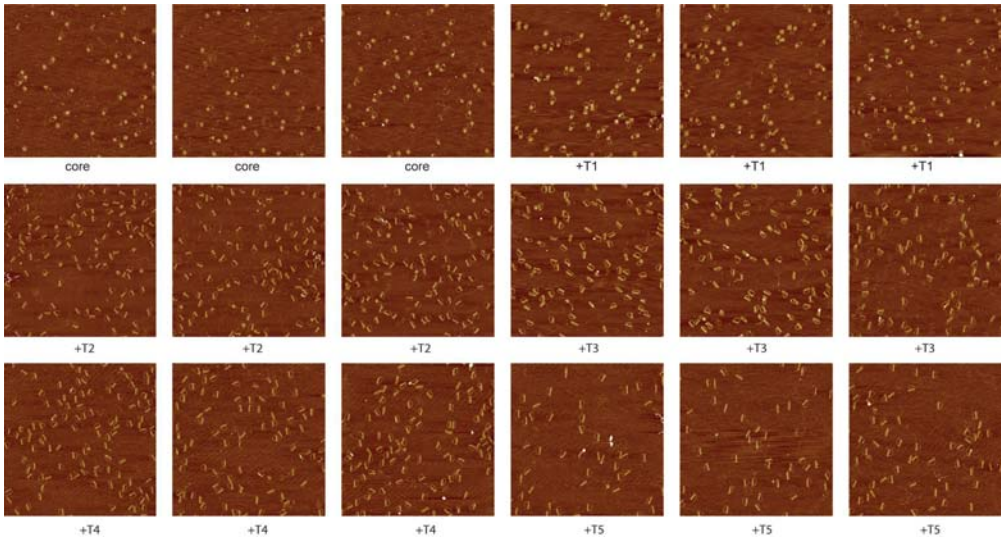

Figure S16. AFM imaging of the transformation of N-DODAs with different number of triggers. Core: the assembled structured without triggers. The core structures of N-DODAs were incubated with different number of triggers in 6 mM $MgCl_2$ at 50°C for overnight. Image size: 2 μm.

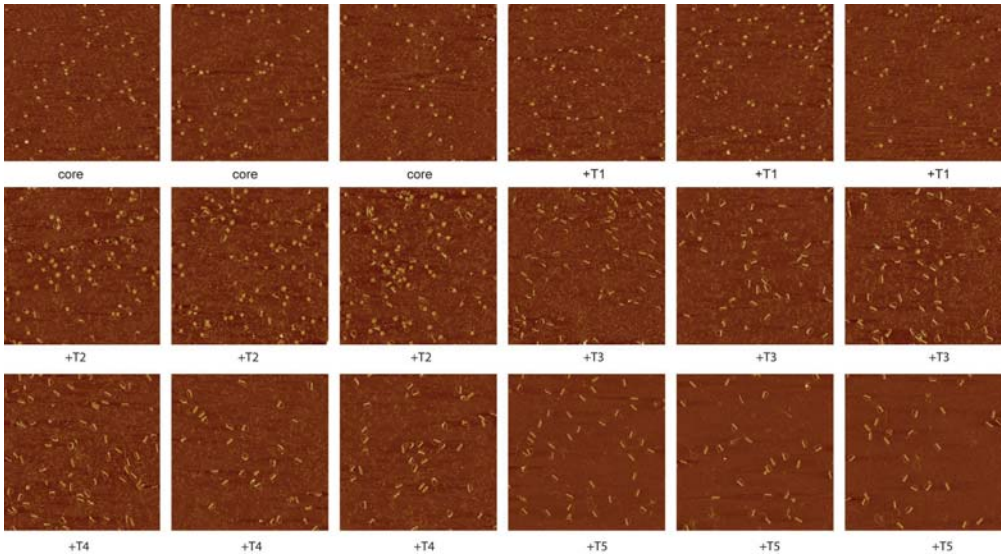

Figure S17. AFM imaging of the transformation of R-DODAs with different number of triggers. Core: the assembled structured without triggers. The core structures of R-DODAs were incubated with different number of triggers in 6 mM $MgCl_2$ at 50°C for overnight. Image size: 2 μm.

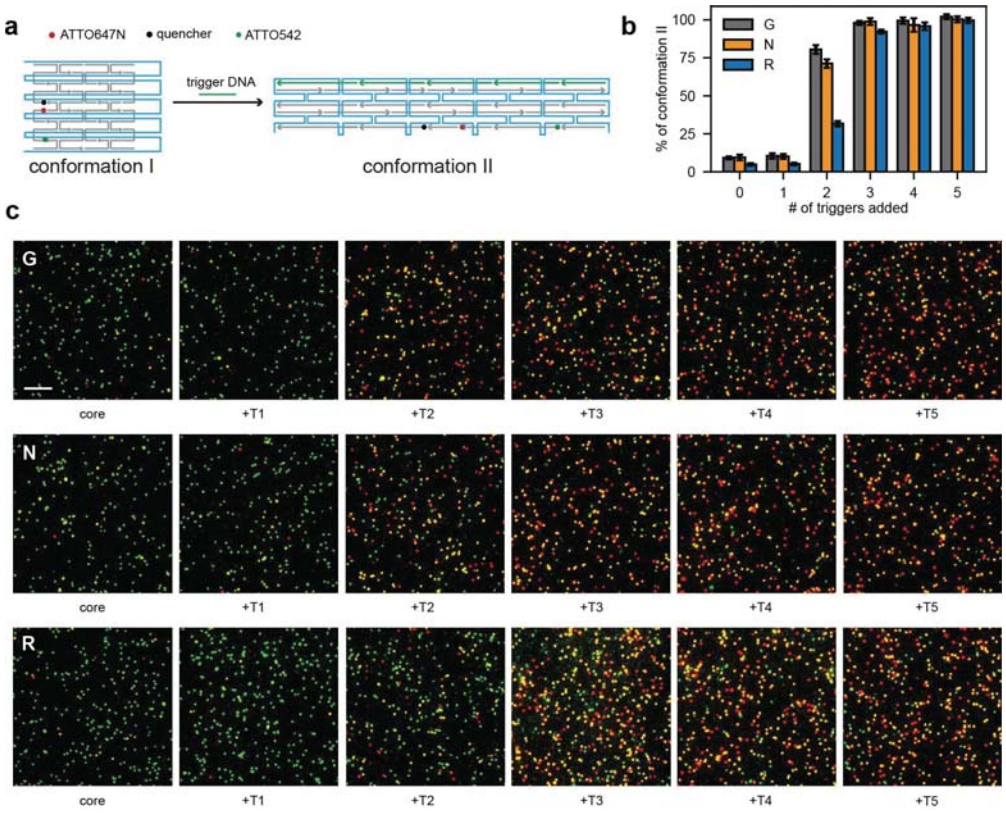

Figure S18. Transformation yields of DNA origami arrays using single-molecule fluorescence method. **a.** fluorescent labelling for the DODAs. ATTO647N and the quencher Iowa Black® RQ were labelled at the left side of the structures. ATTO542 was labelled on the bottom-left postion of structures for the identification of origami structures under TIRF imaging. Before transformation, ATTO647N was quenched and only green fluorescence signal was observed. After transformation, with the increased distance of ATTO647N and Lowa black® RQ, both ATTO647N and ATTO542 were detected. The detection of ATTO647N represented the successful transformation of the array. **b.** transformation yield of G-, N- and R-DODAs under different number of trigger strands. The transformation experiment was performed with 6mM $MgCl_2$ at 37°C for three times. The conformation II ratios for G-, N- and R-DODAs without triggers were 9.1±1.0%, 9.4±1.8% and 4.8±0.9%, respectively. The conformation II ratios for G-, N- and R-DODAs with one trigger were 10.4±1.8%, 10.1±1.6% and 5.1±0.9%, respectively. The conformation II ratios for G-, N- and R-DODAs with two triggers were 80.5±2.9%, 71.2±2.8% and 31.7±1.8%, respectively. The conformation II ratios for G-, N- and R-DODAs with three triggers were 98.0±1.4%, 98.8±2.2% and 95.8±2.5%. The conformation II ratios for G-, N- and R-DODAs with four triggers were 99.5±2.1%, 96.6±4.4% and 95.8±2.5%, respectively. The conformation II ratios for G-, N- and R-DODAs with five triggers were 102.0±1.6%, 100.4±2.0% and 99.6±1.8%. **c.** Example TIRF images for the DODAs before and after triggers input. Each spot represented a single DNA origami structure. The green spots represented DODAs in the conformation I, while red or yellow spots represented the DODAs in the conformation II.

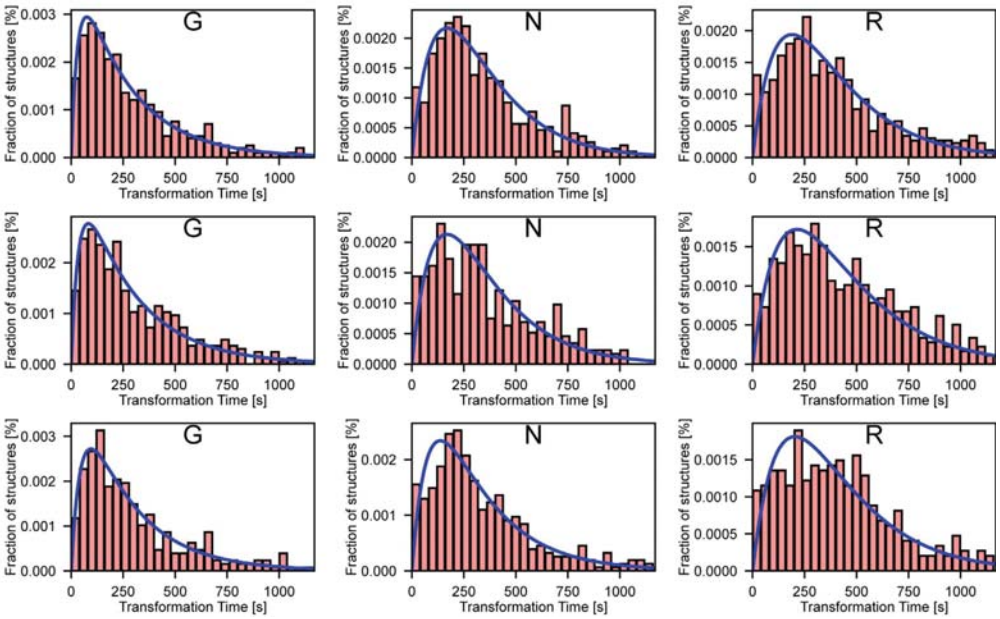

Figure S19. Single-molecule transformation kinetics study of three DODAs with five triggers, which shows a delayed initiation of transformation after addition of triggers. Transformation of each DODA was repeated three times.

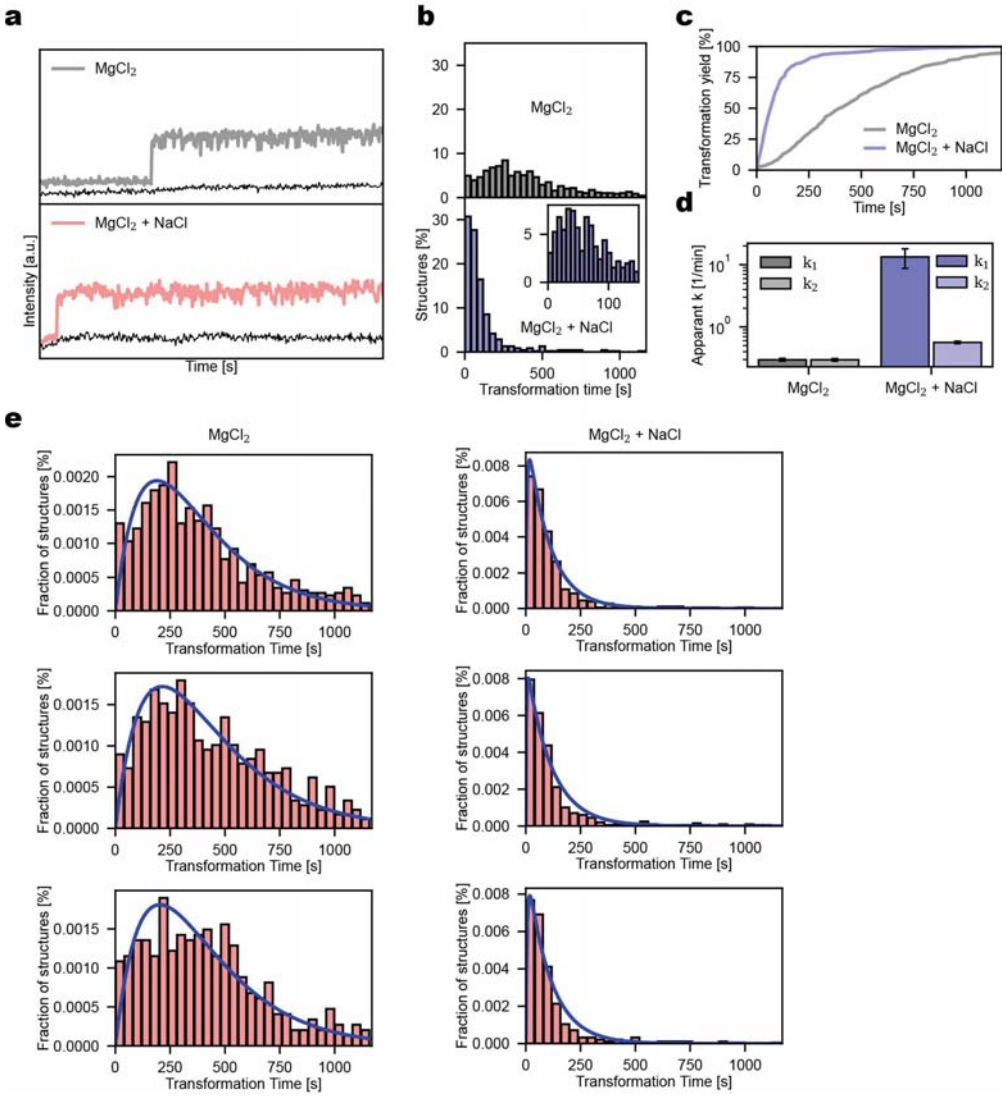

Figure S20. Magnesium concentration effect on the transformation kinetics of R-DODA. **a.** representative fluorescence traces for R-DODA transformation under 12.5 mM $MgCl_2$ and 2 mM $MgCl_2$ and 500 mM NaCl. The black line was the background signal. **b.** The transformation time distributions for R-DODA under 6 mM $MgCl_2$ and 2 mM $MgCl_2$ and 500 mM NaCl. **c.** the transformation yields with time of R-DODA under 6 mM $MgCl_2$ and 2 mM $MgCl_2$ and 500 mM NaCl. **d.** apparent rate constant k obtained from panel (**c)** for R-DODA under different magnesium concentration. The experiments were performed at 37°C for three times. Here, the curves were fitted by convolution of two exponential functions. For the R-DODA transformation under12.5 mM $MgCl_2$, the k1 was 0.297±0.018/min and k2 was 0.297±0.018/min. For the R-DODA transformation under 2 mM $MgCl_2$ and 500 mM NaCl, the k1 was 13.332±5.686/min and k2 was 0.565±0.032/min. **e.** Three batches of transformation time distributions for R-DODA under different magnesium concentrations.

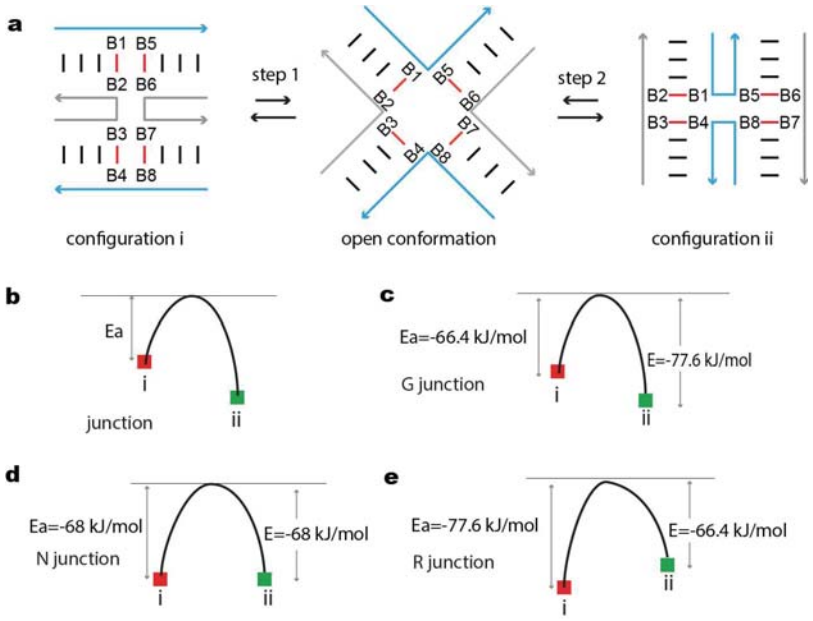

Figure S21. **a.** The switch between two configurations of Holliday junction through an open conformation. B1-8 represents the four DNA bases. **b.** Energy model for the transformation of an individual DNA junction. The junction needs certain activation energy (E_a) to bypass the energy barrier for the transformation. **c, d** and **e**: Simplified free energy model for three four-way junctions.

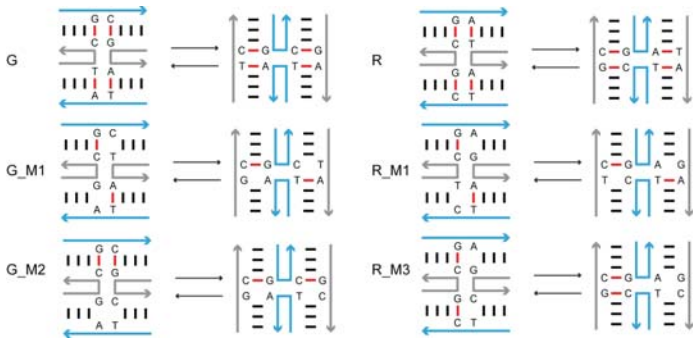

Figure S22. Junction sequences for mismatches of G and R-DODAs.

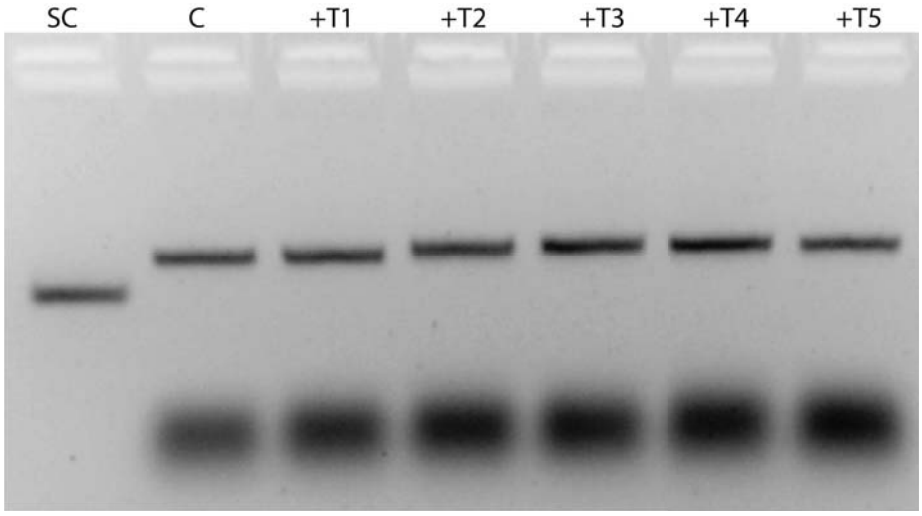

Figure S23. Agarose gel electrophoresis of G-DODA from one-pot assembly with different number of triggers. SC: DNA scaffold 1800G. C: G-DODA without triggers. T1-T5: assembly with 1, 2, 3, 4, or 5 triggers strands.

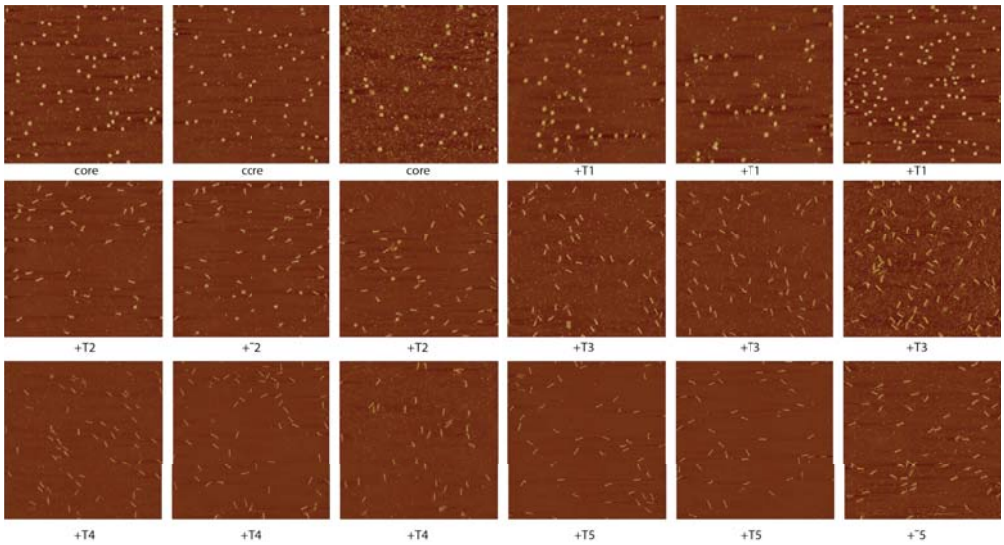

Figure S24. AFM images of G-DODAs from one-pot assembly with different number of triggers. Core: the assembly of G-DODA without triggers. T1-T5: assembly with 1, 2, 3, 4, or 5 triggers strands. Image size: 2 μm.

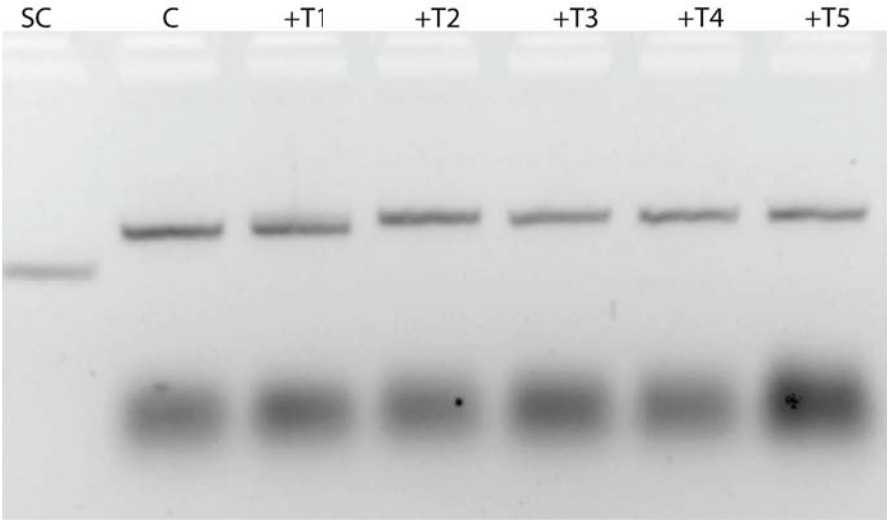

Figure S25. Agarose gel electrophoresis of G_M1 arrays from one-pot assembly with different number of triggers. SC: DNA scaffold 1800G. C: G_M1 DODA without triggers. T1-T5: assembly with 1, 2, 3, 4, or 5 triggers strands.

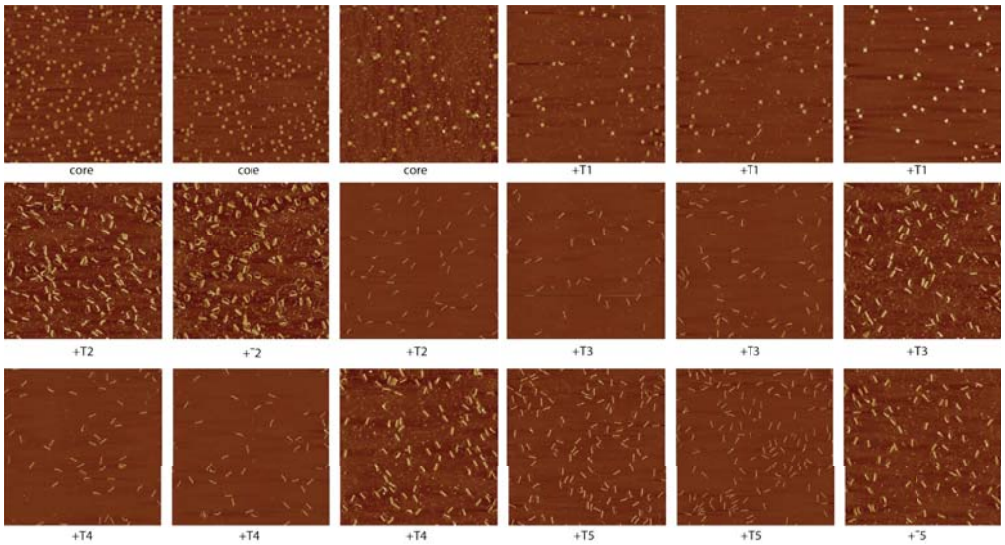

Figure S26. AFM images of G_M1 arrays from one-pot assembly with different number of triggers. Core: the assembly of G_M1 without triggers. T1-T5: assembly with 1, 2, 3, 4, or 5 triggers strands. Image size: 2 μm.

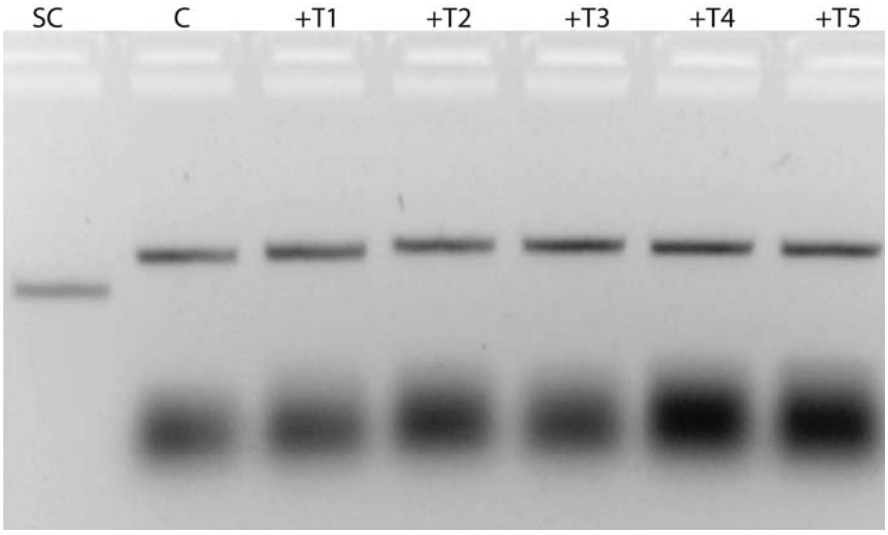

Figure S27. Agarose gel electrophoresis of G_M2 arrays from one-pot assembly with different number of triggers. SC: DNA scaffold 1800G. C: G_M2 DODA without triggers. T1-T5: assembly with 1, 2, 3, 4, or 5 triggers strands.

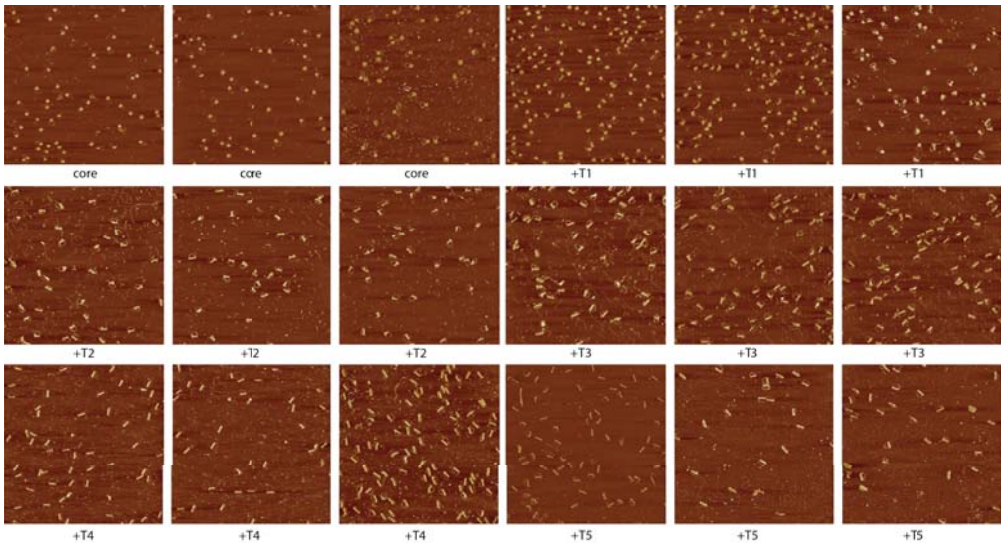

Figure S28. AFM images of G_M2 arrays from one-pot assembly with different number of triggers. Core: the assembly of G_M2 without triggers. T1-T5: assembly with 1, 2, 3, 4, or 5 triggers strands. Image size: 2 μm.

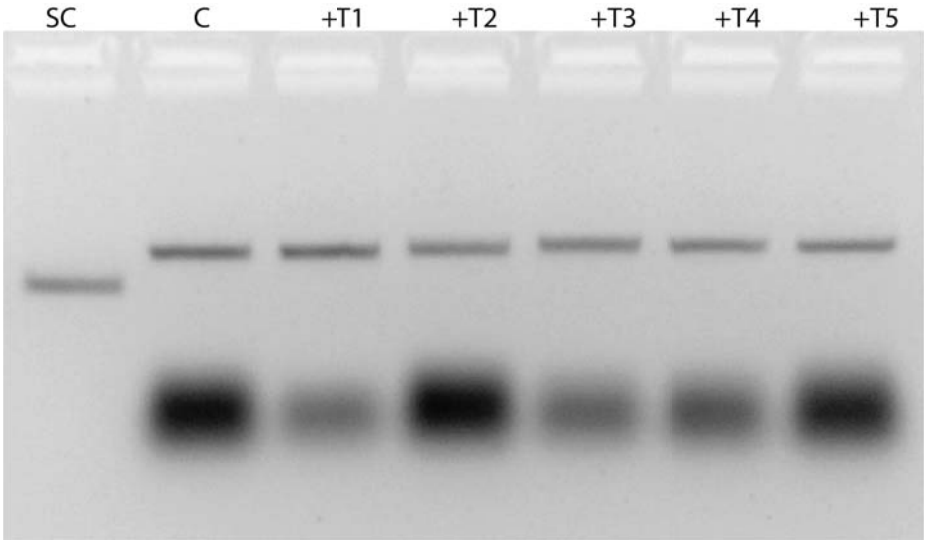

Figure S29. Agarose gel electrophoresis of R-DODAs from one-pot assembly with different number of triggers. SC: DNA scaffold 1800R. C: R-DODA without triggers. T1-T5: assembly with 1, 2, 3, 4, or 5 triggers strands.

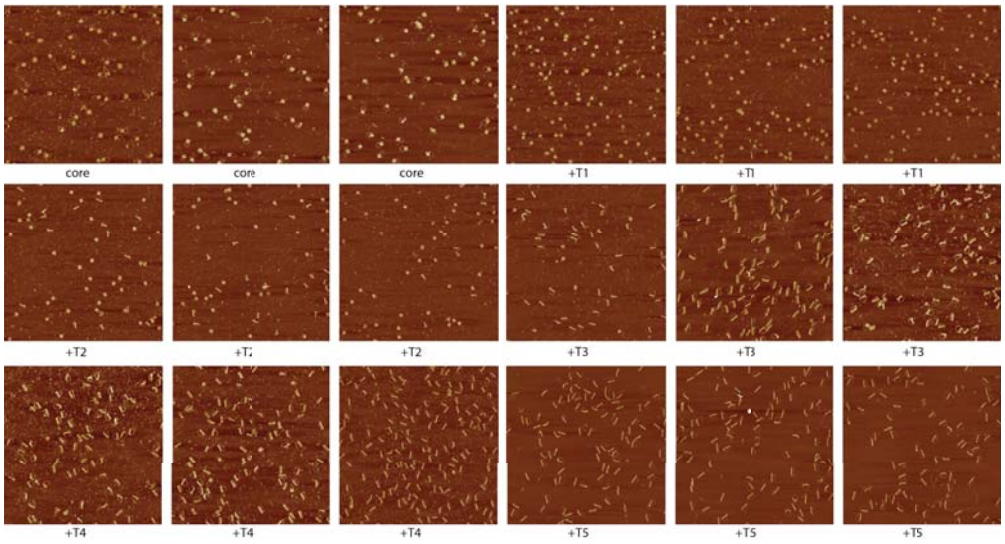

Figure S30. AFM images of R-DODAs from one-pot assembly with different number of triggers. Core: the assembly of R-DODA without triggers. T1-T5: assembly with 1, 2, 3, 4, or 5 triggers strands. Image size: 2 μm.

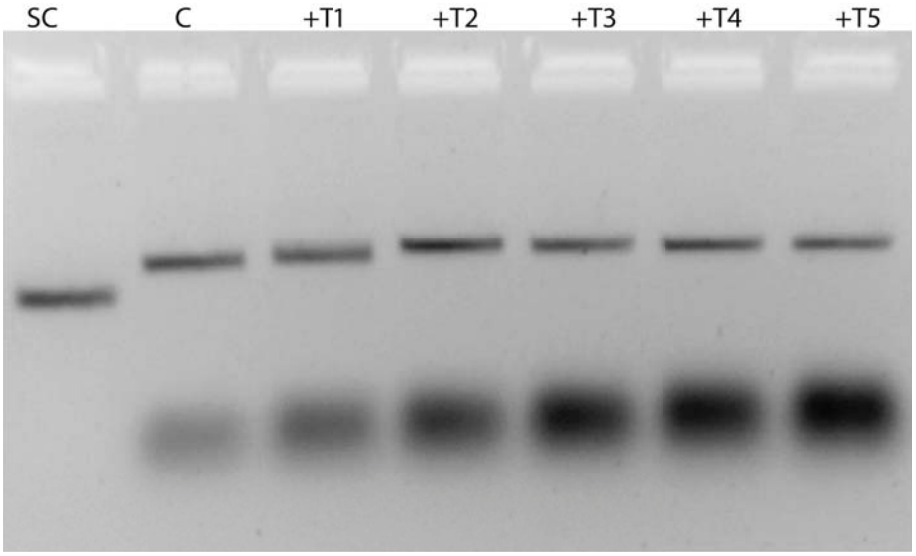

Figure S31. Agarose gel electrophoresis of R_M1 arrays from one-pot assembly with different number of triggers. SC: DNA scaffold 1800R. C: R_M1 DODA without triggers. T1-T5: assembly with 1, 2, 3, 4, or 5 triggers strands.

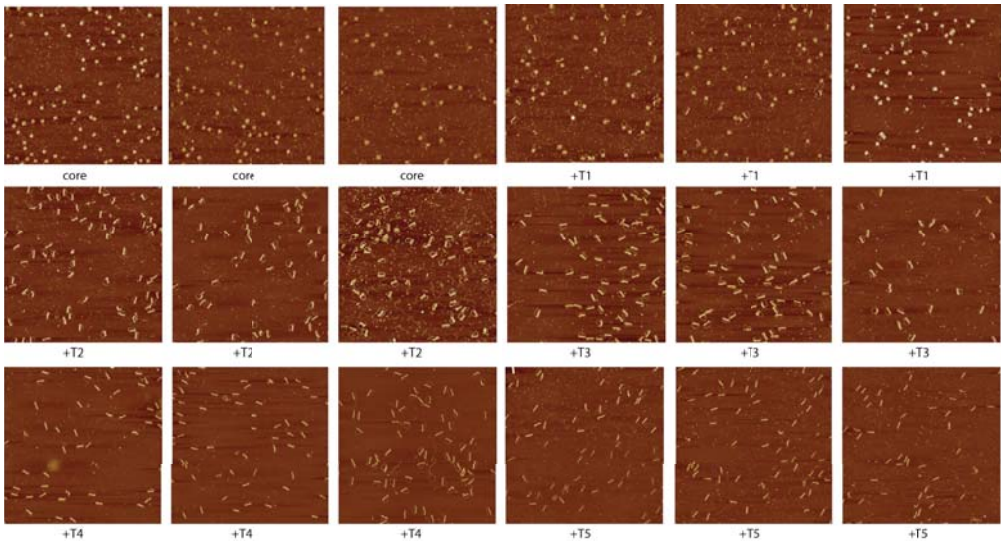

Figure S32. AFM images of R_M1 arrays from one-pot assembly with different number of triggers. Core: the assembly of R_M1 without triggers. T1-T5: assembly with 1, 2, 3, 4, or 5 triggers strands. Image size: 2 μm.

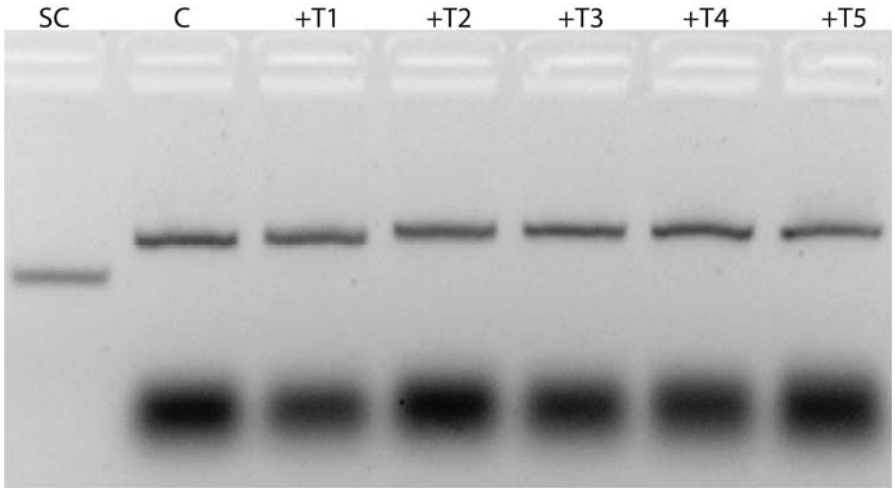

Figure S33. Agarose gel electrophoresis of R_M3 arrays from one-pot assembly with different number of triggers. SC: DNA scaffold 1800R. C: R_M3 DODA without triggers. T1-T5: assembly with 1, 2, 3, 4, or 5 triggers strands.

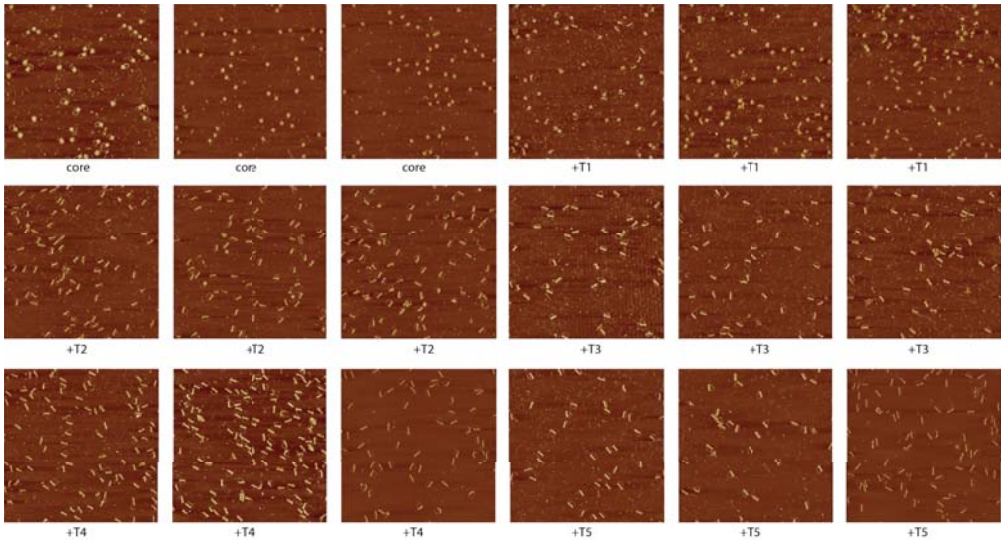

Figure S34. AFM images of R_M3 arrays from one-pot assembly with different number of triggers. Core: the assembly of R_M3 without triggers. T1-T5: assembly with 1, 2, 3, 4, or 5 triggers strands. Image size: 2 μm.

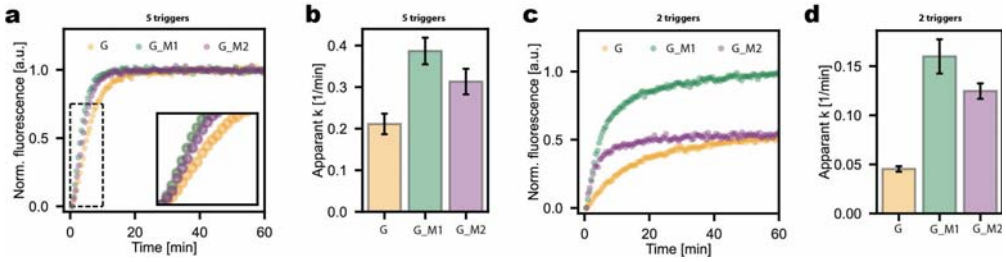

Figure S35. Ensemble kinetics for G-DODA and its mismatched structures. **a.** Ensemble kinetics for G-DODA, G_M1 and G_M2 with five triggers. **b.** The apparent rate constant k obtained from a. The experiments were performed for three times with 6 mM $MgCl_2$ at 30C. The k for G-DODA, G_M1 and G_M2 are 0.211±0.030/min, 0.313±0.038/min and 0.387±0.039/min, respectively. **c.** Ensemble kinetics for G-DODA, G_M1 and G_M2 with two triggers. **d.** The apparent rate constant k obtained from **c.** The experiments were performed for three times with 6 mM MgCl2 at 30C. The k for G-DODA, G_M1 and G_M2 are 0.045±0.003/min, 0.125±0.010/min and 0.160±0.021/min, respectively.

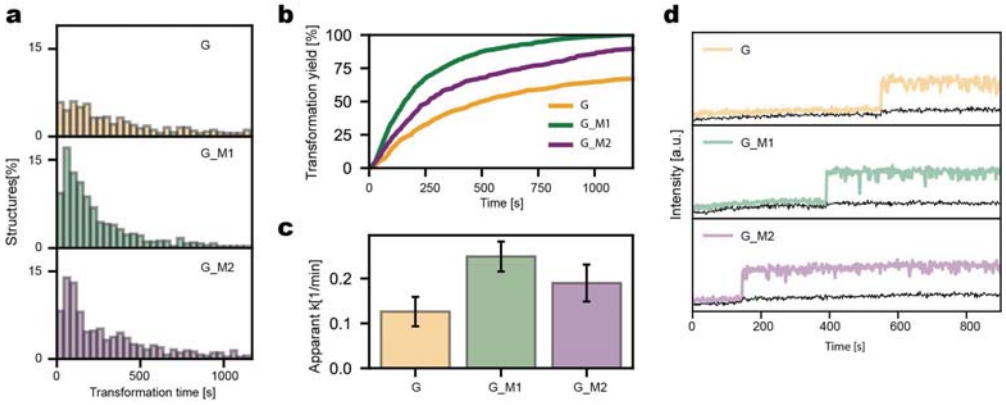

Figure S36. Single-molecule kinetics for G-DODA and its mismatched structures. **a.** Single-molecule transformation time distribution of G-DODA and its mismatched structures. **b.** Single-molecule kinetics of G-DODA and the mismatched structures. **c.** Apparent rate constant for the G-DODA and the mismatched structures in **b.** The experiments were performed for three times with 6 mM $MgCl_2$ at 37C. The k for G-DODA, G_M1 and G_M2 are 0.126±0.040/min, 0.249±0.041/min and 0.190±0.050/min, respectively. **d.** Representative single-molecule transformation fluorescence traces for G-DODA and the mismatched structures.

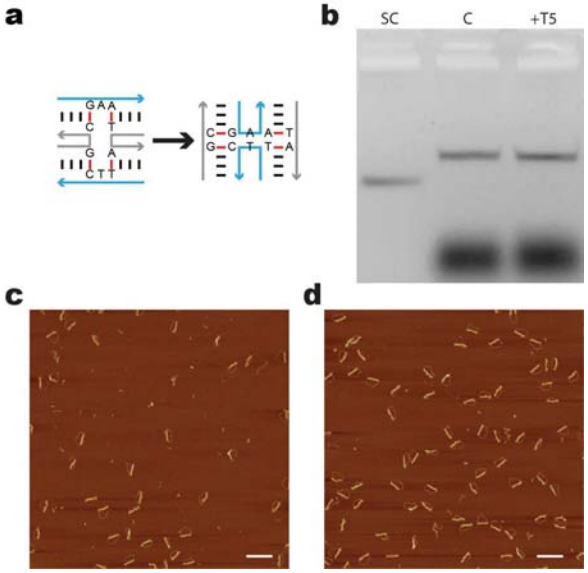

Figure S37. DNA base insertion effect. **a.** Two bases “A” and “T” were inserted into top and bottom strands of the Holliday junction. The strand with blue color represented the scaffold strand when they were integrated in the DNA origami array. **b.** Electrophoresis of agarose gel for the DNA origami structures containing free bases at the junction without and with five trigger strands. Lane SC: DNA scaffold 1800RF. Lane C: core structures without triggers. **c.** and **d.** showed the AFM imaging of samples without and with five triggers, respectively. Scale bars: 200 nm.

Table S2. DNA staple sequences for G-DODA and R_M1.

Start	End	Sequence	Comment
2[194]	0[182]	AGTTCCCTGAGTTCCCACCTCAGATTGGAGCTTGACAGTCATCACAGAATGCTCCTCCACTTTCCTTTTT	trigger strand
4[194]	2[195]	CCGCGACCAAAGTCCGATCAGTGTGAACACAGCACCCACGCCCCACAAATCC	trigger strand
6[194]	4[195]	TGAATCACGGATTCCCACCCTGTTGAATCTGGTCTGCTCTTTGGGCAGGGCT	trigger strand
8[194]	6[195]	TCGGCCAAGCACTCCAGAGTTGATACCAGCAAACAGCTTCTTGAGGTGAGAC	trigger strand
9[182]	8[195]	TTTTTTTAATTGCGTTCTCCACATCTTCGGTAAACTTGATCTGT	trigger strand
0[69]	0[28]	GGTACCCCGAAATCGGCAAAATCCCTTATAAATCAAAAGAAT	loop strand
1[28]	1[69]	AGCCCGAGATAGGGTTGAGTGTTGTTCCAGTTTGGAACAAGA	loop strand
2[69]	2[28]	GTCCACTATTAAAGAACGTGGACTCCAACGTCAAAGGGCGAA	loop strand
3[28]	3[69]	AAACCGTCTATCAGGGCGATGGCCCACTACGTGAACCATCAC	loop strand
4[69]	4[28]	CCAAATCAAGTTTTTTGGGGTCGAGGTGCCGTAAAGCACTAA	loop strand
5[28]	5[69]	ATCGGAACCCTAAAGGGAGCCCCCGATTTAGAGCTTGACGGG	loop strand
6[69]	6[28]	GAAAGCCGGCGAACGTGGCGAGAAAGGAAGGGAAGAAAGCGA	loop strand
7[28]	7[69]	AAGGAGCGGGCGCTAGGGCGCTGGCAAGTGTAGCGGTCACGC	loop strand
8[69]	8[28]	TGCGCGTAACCACCACACCCGCCGCGCTTAATGCGCCGCTAC	loop strand
9[28]	9[69]	AGGGCGCGTGGATCCGTCGAGAATCAGTGCTTTCAGTTTCAG	loop strand
0[129]	1[116]	TTTTTGCGAAAGGTGATCCAATCTTCATTGGAACAGATCCAGCC	core strand
0[181]	1[168]	TTTTTTGAGGCGGTCGTGCCAATTCATCAGGAGATAGGGATAAC	core strand
1[117]	3[116]	AGTGATCGGGTGGAGCAGCCTTGGCCACGATGGTATCGGATATTGTCGCCCA	core strand
1[169]	3[168]	AATCTTATATTTGATTCGCGGATGGTCACTTCACCCTGGAGGTGCGGCTCTG	core strand
2[90]	0[78]	GTCACCGAACAGCTGCCGCGAGGCAGACCCAGCAAGCGTCCATTTCTTGGAATCCCTGCTGGAAC	core strand
2[142]	0[130]	GATCTTTCAGGTTCAGGTGTTCTCCGCGGACGTACTTCTCACTCCTCAAACAAGTAGGTCTTAGTTTTTT	core strand
3[117]	5[116]	CCTGGTTGACGAGATCGTCCAGTTCGGCGAGTTTCCTTGAGAATGCCTGCGT	core strand
3[169]	5[168]	GGAGTCCTCATAGATGGTTCGAGGTAAACCCACTTTCTGATGTCATGATGCT	core strand
4[90]	2[91]	CTTGTCTTCAAAGAGTCCTTCAAGGACTGCAGGAGGCATCAACTCTCAGCAG	core strand
4[142]	2[143]	GGTTCTGCAAATTCTCCTTCCAATCCTTGATCAGCTTCTCCGCGTGAGTTCA	core strand
5[117]	7[116]	GGGTAGTCAAGGGAAAGCGAGGGAAGGCGCTGCGCTTCGACGTTATTCTTGA	core strand
5[169]	7[168]	GCGGAAATCTTCGAATTGGTTGACTGGCCCAAGATCTCGAGTGCTTAGACTT	core strand
6[90]	4[91]	GTTGAGGCTGCGCGGTCCAGGATGGTCAGCAGTGAGTTTCCCAGATGCTGAC	core strand
6[142]	4[143]	CTCCGATGAAGTTCGTGACGCGATTGTCCTTCTTGATATCGAATATGGTTGA	core strand
7[117]	9[129]	ATGGCACAACTTGAGTTGTCACGCACTCCTTCAGCAGCGACGGAAGATGTGTCGATGTTAGTATATTTTT	core strand
7[169]	9[181]	CTCATCGAAACAGAGATCTGTGATGGGAACAGAGAAGGGACTCAATCTGGTGCAGGGAGTGATCTTTTTT	core strand
8[90]	6[91]	CTTCATCTCCAGGAGGTTTCGACGTTATTGGACAAGGGTCCTCCAGGAACTC	core strand
8[142]	6[143]	GAGAGCTGCGTCTCCCCTCCAAGGACTTCATTGCAGTATCGCAGGTCATCGT	core strand
9[78]	8[91]	TACCGGACTCTGTGTTACCTGGGTCTCCTCCAGGGTCTT	core strand
9[130]	8[143]	TTTTTCTGCTCCAATTTGTTCACCAGCTGTTCCCACAGCTCCCT	core strand

Table S3. DNA staple sequences for N-DODA, G_M2 and R_M3.

Start	End	Sequence	Comment
2[194]	0[182]	AGTTCCCTGAGTGCCCACCTCAGATTGGAGCTTGACAGTCATCACAGAATGCTCCTCCACTTTCC	trigger strand
4[194]	2[195]	CCGCGACCAAAGGCCGATCAGTGTGAACACAGCACCCACGCCCCACAAATCC	trigger strand
6[194]	4[195]	TGAATCACGGATGCCCACCCTGTTGAATCTGGTCTGCTCTTTGGGCAGGGCT	trigger strand
8[194]	6[195]	TCGGCCAAGCACGCCAGAGTTGATACCAGCAAACAGCTTCTTGAGGTGAGAC	trigger strand

9[182]	8[195]	TTAATTGCGTTCTCCACATCTTCGGTAAACTTGATCTGT	trigger strand
0[69]	0[28]	GGTACCCCGAAATCGGCAAAATCCCTTATAAATCAAAAGAAT	loop strand
1[28]	1[69]	AGCCCGAGATAGGGTTGAGTGTTGTTCCAGTTTGGAACAAGA	loop strand
2[69]	2[28]	GTCCACTATTAAAGAACGTGGACTCCAACGTCAAAGGGCGAA	loop strand
3[28]	3[69]	AAACCGTCTATCAGGGCGATGGCCCACTACGTGAACCATCAC	loop strand
4[69]	4[28]	CCAAATCAAGTTTTTTGGGGTCGAGGTGCCGTAAAGCACTAA	loop strand
5[28]	5[69]	ATCGGAACCCTAAAGGGAGCCCCCGATTTAGAGCTTGACGGG	loop strand
6[69]	6[28]	GAAAGCCGGCGAACGTGGCGAGAAAGGAAGGGAAGAAAGCGA	loop strand
7[28]	7[69]	AAGGAGCGGGCGCTAGGGCGCTGGCAAGTGTAGCGGTCACGC	loop strand
8[69]	8[28]	TGCGCGTAACCACCACACCCGCCGCGCTTAATGCGCCGCTAC	loop strand
9[28]	9[69]	AGGGCGCGTGGATCCGTCGAGAATCAGTGCTTTCAGTTTCAG	loop strand
0[129]	1[116]	GCGAAAGGTGATCCAATCTTCATTGGCACAGATCCAGCC	core strand
0[181]	1[168]	TGAGGCGGTCGTGCCAATTCATCAGGCGATAGGGATAAC	core strand
1[117]	3[116]	AGTGATCGGGTGGCGCAGCCTTGGCCACGATGGTATCGGCTATTGTCGCCCA	core strand
1[169]	3[168]	AATCTTATATTTGCTTCGCGGATGGTCACTTCACCCTGGCGGTGCGGCTCTG	core strand
2[90]	0[78]	GTCACCGAACAGCTGCCGCGAGGCAGACCCAGCAAGCGGCCATTTCTTGGAATCCCTGCTGGAAC	core strand
2[142]	0[130]	GATCTTTCAGGTGCAGGTGTTCTCCGCGGACGTACTTCGCACTCCTCAAACAAGTAGGTCTTAGT	core strand
3[117]	5[116]	CCTGGTTGACGAGCTCGTCCAGTTCGGCGAGTTTCCTTGCGAATGCCTGCGT	core strand
3[169]	5[168]	GGAGTCCTCATAGCTGGTTCGAGGTAAACCCACTTTCTGCTGTCATGATGCT	core strand
4[90]	2[91]	CTTGTCTTCAAAGAGTCCTTCAAGGACTGCAGGAGGCAGCAACTCTCAGCAG	core strand
4[142]	2[143]	GGTTCTGCAAATGCTCCTTCCAATCCTTGATCAGCTTCGCCGCGTGAGTTCA	core strand
5[117]	7[116]	GGGTAGTCAAGGGCAAGCGAGGGAAGGCGCTGCGCTTCGCCGTTATTCTTGA	core strand
5[169]	7[168]	GCGGAAATCTTCGCATTGGTTGACTGGCCCAAGATCTCGCGTGCTTAGACTT	core strand
6[90]	4[91]	GTTGAGGCTGCGCGGTCCAGGATGGTCAGCAGTGAGTTGCCCAGATGCTGAC	core strand
6[142]	4[143]	CTCCGATGAAGTGCGTGACGCGATTGTCCTTCTTGATAGCGAATATGGTTGA	core strand
7[117]	9[129]	ATGGCACAACTTGCGTTGTCACGCACTCCTTCAGCAGCGCCGGAAGATGTGTCGATGTTAGTATA	core strand
7[169]	9[181]	CTCATCGAAACAGCGATCTGTGATGGGAACAGAGAAGGGCCTCAATCTGGTGCAGGGAGTGATCT	core strand
8[90]	6[91]	CTTCATCTCCAGGAGGTTTCGACGTTATTGGACAAGGGGCCTCCAGGAACTC	core strand
8[142]	6[143]	GAGAGCTGCGTCGCCCCTCCAAGGACTTCATTGCAGTAGCGCAGGTCATCGT	core strand
9[78]	8[91]	TACCGGACTCTGTGTTACCTGGGTCGCCTCCAGGGTCTT	core strand
9[130]	8[143]	CTGCTCCAATTTGTTCACCAGCTGTGCCCACAGCTCCCT	core strand

Table S4. DNA staple sequences for R-DODA, G_M1 and R-DODA with DNA insertions.

Start	End	Sequence	
2[194]	0[182]	AGTTCCCTGAGTGCCCACCTCAGATTGGAGCTTGACAGTCATCACAGAATGCTCCTCCACTTTCC	trigger strand
4[194]	2[195]	CCGCGACCAAAGGCCGATCAGTGTGAACACAGCACCCACGCCCCACAAATCC	trigger strand
6[194]	4[195]	TGAATCACGGATGCCCACCCTGTTGAATCTGGTCTGCTCTTTGGGCAGGGCT	trigger strand
8[194]	6[195]	TCGGCCAAGCACGCCAGAGTTGATACCAGCAAACAGCTTCTTGAGGTGAGAC	trigger strand
9[182]	8[195]	TTAATTGCGTTCTCCACATCTTCGGTAAACTTGATCTGT	trigger strand
0[69]	0[28]	GGTACCCCGAAATCGGCAAAATCCCTTATAAATCAAAAGAAT	loop strand
1[28]	1[69]	AGCCCGAGATAGGGTTGAGTGTTGTTCCAGTTTGGAACAAGA	loop strand
2[69]	2[28]	GTCCACTATTAAAGAACGTGGACTCCAACGTCAAAGGGCGAA	loop strand
3[28]	3[69]	AAACCGTCTATCAGGGCGATGGCCCACTACGTGAACCATCAC	loop strand
4[69]	4[28]	CCAAATCAAGTTTTTTGGGGTCGAGGTGCCGTAAAGCACTAA	loop strand
5[28]	5[69]	ATCGGAACCCTAAAGGGAGCCCCCGATTTAGAGCTTGACGGG	loop strand
6[69]	6[28]	GAAAGCCGGCGAACGTGGCGAGAAAGGAAGGGAAGAAAGCGA	loop strand
7[28]	7[69]	AAGGAGCGGGCGCTAGGGCGCTGGCAAGTGTAGCGGTCACGC	loop strand

8[69]	8[28]	TGCGCGTAACCACCACACCCGCCGCGCTTAATGCGCCGCTAC	loop strand
9[28]	9[69]	AGGGCGCGTGGATCCGTCGAGAATCAGTGCTTTCAGTTTCAG	loop strand
0[129]	1[116]	GCGAAAGGTGATCCAATCTTCATTGTAACAGATCCAGCC	core strand
0[181]	1[168]	TGAGGCGGTCGTGCCAATTCATCAGTAGATAGGGATAAC	core strand
1[117]	3[116]	AGTGATCGGGTGTAGCAGCCTTGGCCACGATGGTATCGTATATTGTCGCCCA	core strand
1[169]	3[168]	AATCTTATATTTTATTCGCGGATGGTCACTTCACCCTGTAGGTGCGGCTCTG	core strand
2[90]	0[78]	GTCACCGAACAGCTGCCGCGAGGCAGACCCAGCAAGCGGCCATTTCTTGGAATCCCTGCTGGAAC	core strand
2[142]	0[130]	GATCTTTCAGGTGCAGGTGTTCTCCGCGGACGTACTTCGCACTCCTCAAACAAGTAGGTCTTAGT	core strand
3[117]	5[116]	CCTGGTTGACGATATCGTCCAGTTCGGCGAGTTTCCTTTAGAATGCCTGCGT	core strand
3[169]	5[168]	GGAGTCCTCATATATGGTTCGAGGTAAACCCACTTTCTTATGTCATGATGCT	core strand
4[90]	2[91]	CTTGTCTTCAAAGAGTCCTTCAAGGACTGCAGGAGGCAGCAACTCTCAGCAG	core strand
4[142]	2[143]	GGTTCTGCAAATGCTCCTTCCAATCCTTGATCAGCTTCGCCGCGTGAGTTCA	core strand
5[117]	7[116]	GGGTAGTCAAGGTAAAGCGAGGGAAGGCGCTGCGCTTCTACGTTATTCTTGA	core strand
5[169]	7[168]	GCGGAAATCTTCTAATTGGTTGACTGGCCCAAGATCTCTAGTGCTTAGACTT	core strand
6[90]	4[91]	GTTGAGGCTGCGCGGTCCAGGATGGTCAGCAGTGAGTTGCCCAGATGCTGAC	core strand
6[142]	4[143]	CTCCGATGAAGTGCGTGACGCGATTGTCCTTCTTGATAGCGAATATGGTTGA	core strand
7[117]	9[129]	ATGGCACAACTTTAGTTGTCACGCACTCCTTCAGCAGCTACGGAAGATGTGTCGATGTTAGTATA	core strand
7[169]	9[181]	CTCATCGAAACATAGATCTGTGATGGGAACAGAGAAGGTACTCAATCTGGTGCAGGGAGTGATCT	core strand
8[90]	6[91]	CTTCATCTCCAGGAGGTTTCGACGTTATTGGACAAGGGGCCTCCAGGAACTC	core strand
8[142]	6[143]	GAGAGCTGCGTCGCCCCTCCAAGGACTTCATTGCAGTAGCGCAGGTCATCGT	core strand
9[78]	8[91]	TACCGGACTCTGTGTTACCTGGGTCGCCTCCAGGGTCTT	core strand
9[130]	8[143]	CTGCTCCAATTTGTTCACCAGCTGTGCCCACAGCTCCCT	core strand

Table S5. DNA staples for replacement and labelling the DNA origami array with biotin, fluorescent dyes and quencher.

Position	DNA sequences	comment
6[69]	Biotin-GAAAGCCGGCGAACGTGGCGAGAAAGGAAGGGAAGAAAGCGA	Biotin labelling
3[91]	CTGCAGGAGGCATCAACTCTCAGCAG	Replacement for G-DODA
4[93]	IowaBlack@RQ-GACCTTGTCTTCAAAGAGTCCTTCAAGGA	IowaBlack@RQ labelling for all structures
5[94]	CAGTGAGTTTCCCAGATGCT	Replacement for G-DODA
6[90]	GTTGAGGCTGCGCGGTCCAGGATGGTCAG-ATTO647N	ATTO647 labelling for all structures
3[91]	CTGCAGGAGGCAGCAACTCTCAGCAG	Replacement for N-and R-DODA
5[94]	CAGTGAGTTGCCCAGATGCT	Replacement for N-and R-DODA
5[166]	ATTO542-GCTGCGGAAATCTTCGAATTGGTTGACTG	ATTO542 labelling

References:

(1) Douglas, S. M.; Marblestone, A. H.; Teerapittayanon, S.; Vazquez, A.; Church, G. M.; Shih, W. M. Rapid prototyping of 3D DNA-origami shapes with caDNAno. *Nucleic Acids Res.* **2009**, *37* (15), 5001-5006.
(2) Nafisi, P. M.; Aksel, T.; Douglas, S. M. Construction of a novel phagemid to produce custom DNA origami scaffolds. *Synth. Biol.* **2018**, *3* (1), ysy015.
(3) Friedman, R. A.; Honig, B. A free energy analysis of nucleic acid base stacking in aqueous solution. *Biophys. J.* **1995**, *69* (4), 1528-1535.

8.2 Associated Publication P2

Controlled mechanochemical coupling of anti-junctions in DNA origami arrays

by

Fiona Cole[1], Martina Pfeiffer[1], Dongfang Wang[1], Tim Schröder, Yonggang Ke[*] and Philip Tinnefeld[*]
([1] These authors contributed equally, [*] Correspondence)

Nature Communications, volume 15, article number 7894 (**2024**)
DOI: 10.1038/s41467-024-51721-y

Author contributions:
The initial idea of the project was proposed by Philip Tinnefeld and my collaboration partner Yonggang Ke. Dongfang Wang designed the DNA origami structure. I designed the FRET probe, performed the corresponding measurements and wrote the analysis software. Martina Pfeiffer designed the cargo release unit and the artificial energy barriers, performed the corresponding measurements and analyzed the data. Tim Schröder performed preliminary measurements on another DNA origami structure and discussed data. I wrote the manuscript together with Martina Pfeiffer and Philip Tinnefeld.

nature communications

Article

https://doi.org/10.1038/s41467-024-51721-y

Controlled mechanochemical coupling of anti-junctions in DNA origami arrays

Received: 20 June 2024

Accepted: 16 August 2024

Published online: 10 September 2024

Check for updates

Fiona Cole[1,2,7], Martina Pfeiffer[1,2,7], Dongfang Wang[3,4,5,6,7], Tim Schröder[1,2], Yonggang Ke[3,4] ✉ & Philip Tinnefeld[1,2] ✉

Allostery is a hallmark of cellular function and important in every biological system. Still, we are only starting to mimic it in the laboratory. Here, we introduce an approach to study aspects of allostery in artificial systems. We use a DNA origami domino array structure which–upon binding of trigger DNA strands–undergoes a stepwise allosteric conformational change. Using two FRET probes placed at specific positions in the DNA origami, we zoom in into single steps of this reaction cascade. Most of the steps are strongly coupled temporally and occur simultaneously. Introduction of activation energy barriers between different intermediate states alters this coupling and induces a time delay. We then apply these approaches to release a cargo DNA strand at a predefined step in the reaction cascade to demonstrate the applicability of this concept in tunable cascades of mechanochemical coupling with both spatial and temporal control.

Allostery is defined as the thermodynamic and mechanochemical coupling of binding reactions to remote conformational changes in molecular systems[1–4]. Nature provides us with a large variety of allosteric systems capable of regulating and modulating biological activity. Allosteric networks enable signal transduction[5,6] and amplification[6–8], logical gating[9,10] and cooperative and anti-cooperative behavior[11,12]. Attaining a similar level of control over these processes in laboratory would allow rationally designing and developing biomolecular networks[13,14]. Building artificial systems capable of mimicking allostery therefore represents a major bioengineering goal[15–19].

Reconfigurable DNA origami array systems have great potential to become a platform to accommodate controlled allosteric cascade reactions over several tens of nanometers (Fig. 1a)[15,17,18]. They consist of multiple equivalent DNA anti-junctions that each exist in two stable conformations between which they can switch through an unstable open conformation (Fig. 1b). Reconfiguration of the whole system is induced by addition of trigger DNA strands that – by hybridization to certain anti-junctions at the edge – stabilize one conformation of the addressed anti-junctions over the other. In a continuous transformation reaction, these anti-junctions relay their conformational information to neighboring anti-junctions causing them to change their conformation. This reaction repeats until all anti-junctions in the array are converted in a diagonal, stepwise, highly coordinated manner. As such, the chemical energy of the trigger DNA strands binding to the structure is first converted to mechanical energy which then propagates through the structure inducing the conformational change.

Our understanding of the cascading transformation in DNA origami arrays has already been greatly improved in previous work where the transformation of DNA structures to different shapes[17,18,20–23], the initiation of proximity induced operations by the transformation process[24,25] and the realization of cascaded reactions[26] were demonstrated. However, the precise nature of the underlying energy landscape and of the transformation kinetics has remained elusive. The lack of knowledge of the mechanism of the transformation at the molecular level prevents us from controlling allosteric behavior in these systems. Therefore, there is a crucial need for new methods to acquire a deeper understanding of the energy landscape and coupling

[1]Department of Chemistry, Ludwig-Maximilians-Universität München, Butenandtstr. 5-13, München, Germany. [2]Center for NanoScience, Ludwig-Maximilians-Universität München, Schellingstraße 4, München, Germany. [3]Wallace H. Coulter Department of Biomedical Engineering, Emory University, Atlanta, GA, USA. [4]Georgia Institute of Technology, Atlanta, GA, USA. [5]School of Biomedical Engineering, University of Science and Technology of China, Suzhou, China. [6]Suzhou Institute for Advanced Research, University of Science and Technology of China, Suzhou, China. [7]These authors contributed equally: Fiona Cole, Martina Pfeiffer, Dongfang Wang. ✉e-mail: yonggang.ke@emory.edu; philip.tinnefeld@cup.uni-muenchen.de

https://doi.org/10.1038/s41467-024-51721-y

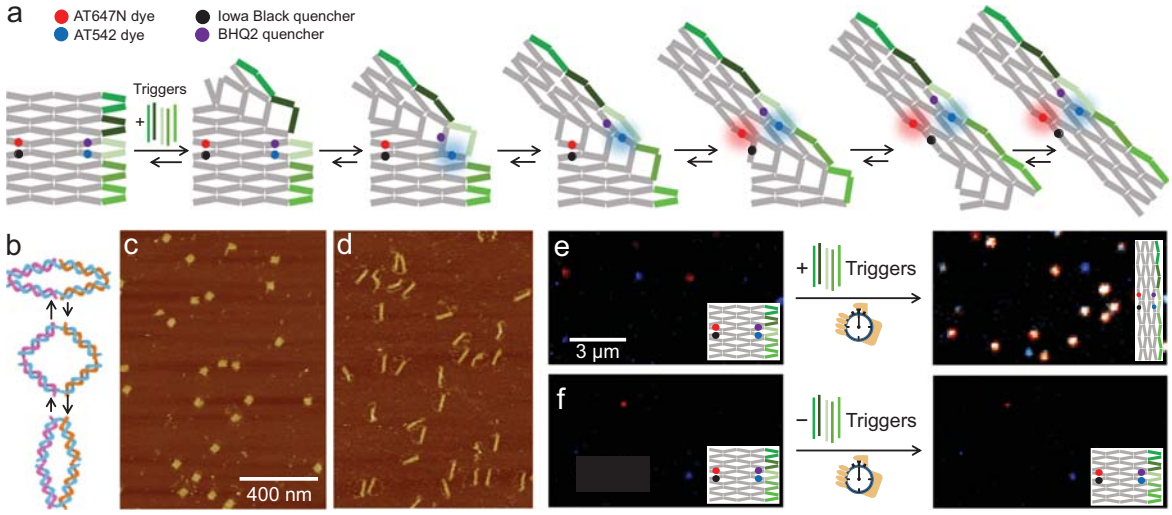

Fig. 1 | Concept for following the transformation reaction of reconfigurable DNA origami array structures on the single-molecule level in real time. **a** Scheme of the DNA origami array model structure transforming upon addition of DNA trigger strands. Red and green FRET probes (ATTO647N-IowaBlack RQ and ATTO542-BHQ2, red/ black and blue/ purple circles) are placed at the positions at which the transformation reaction is studied. The transformation process occurs diagonally, starting either from the top right corner, as shown in the sketch, or from the bottom right corner. **b** Sketch of conformational flipping of a single anti-junction. Blue DNA strands represent sections of the scaffold strand, whereas pink and orange strands represent different staple strands. **c**, **d** AFM images of the DNA origami array (**c**) before and (**d**) after overnight incubation with trigger strands indicate a successful transformation of the structure. **e**, **f** Exemplary TIRF images of the DNA origami array structure before and after incubation with and without trigger strands. Fluorescence of ATTO647N is shown in red, fluorescence of ATTO542 in blue and co-localized fluorescence of both in white.

between individual anti-junctions in the transformation process. Can the coupling be altered and how does it influence the timing of the transformation as well as the possibility to create functional devices from reconfigurable DNA origami array systems?

So far, the transformation process was verified by atomic force microscopy (AFM), gel chromatography and gel chromatography combined with ensemble fluorescence measurements[18,27]. Gel chromatography analyzes only the start and the end point of the transformation process[18,20–22,27], while AFM imaging throughout the transformation process can reveal intermediate states. These states indicate a diagonal transformation pathway that minimizes the number of simultaneously open, unstable conformations of anti-junctions. However, AFM cannot reveal the actual transformation kinetics and pathways, due to the low temporal resolution of AFM and the interference from DNA-mica and DNA-cantilever interactions[18,22].

Here, we establish a fluorescence-based single-molecule assay to measure the time it takes for the transformation to propagate from one specific anti-junction to another non-invasively. To this end, two pairs of FRET probes were placed on two selected anti-junctions in the reconfigurable DNA origami array system. The FRET probes report on the conformation of the anti-junctions they are placed on which allows measuring their transformation times. Comparing the transformation times at different anti-junctions in single structures revealed the propagation process independent of induction (binding), diffusion or experimental synchronization commonly required by classical chemical kinetics measurements. What's more, the free selection of FRET-probe anti-junction combination allowed zooming in into every substep of the transformation process and characterizing it at the single-molecule level additionally providing access to subpopulations and kinetic heterogeneity.

Our double-FRET-probe assay provides access to important aspects of allostery in artificial systems and adds timing as an additional dimension. For a small reconfigurable DNA origami model system, we showed that most steps in the transformation cascade are coupled and how their coupling can be influenced by introducing modifications in the structure. Our understanding of the underlying energy landscape was finally used to release a cargo DNA strand at a predefined step in the transformation cascade to demonstrate the applicability of this concept in tunable allosteric reactions.

Results

DNA origami array structure as a programmable platform for reaction cascades

We designed a small reconfigurable DNA origami array structure as a model system to establish our assay and to study allostery and mechanochemical coupling in the transformation reaction (Fig. 1a, Supplementary Data 1). The model structure is composed of 5 × 2.5 anti-junctions that can be transformed by hybridization of five trigger DNA strands to the right side of the structure. For the trigger DNA strands, an asymmetric design is chosen that energetically favors the initiation of the transformation reaction at the top right corner rather than at the bottom right corner (see Supplementary Fig. 1). This ensures that the transformation reaction always starts from the same corner, facilitating the direct comparison of transformation times of individual anti-junctions.

AFM imaging confirmed the successful formation of the untransformed DNA origami model structure in a square-like shape when assembled without the addition of trigger DNA strands (Fig. 1c). Overnight incubation with 50 nM of the five trigger DNA strands resulted in the quantitative transformation of the structure into its transformed oblong conformation (Fig. 1d).

As the distances between the individual arms of the anti-junctions change during the transformation reaction, we placed two FRET-pairs as signal transduction elements that report on the transformation at specific locations within the DNA origami. In the FRET-pairs, we used photostable, single-molecule optimized fluorophores as donor dyes in the green and red spectral region (ATTO542 and ATTO647N), respectively. Appropriate dark-quenchers (BHQ2 and IowaBlack RQ) as FRET acceptors were placed such that the donor was strongly quenched before the transformation reaction and lighted up in the moment

https://doi.org/10.1038/s41467-024-51721-y

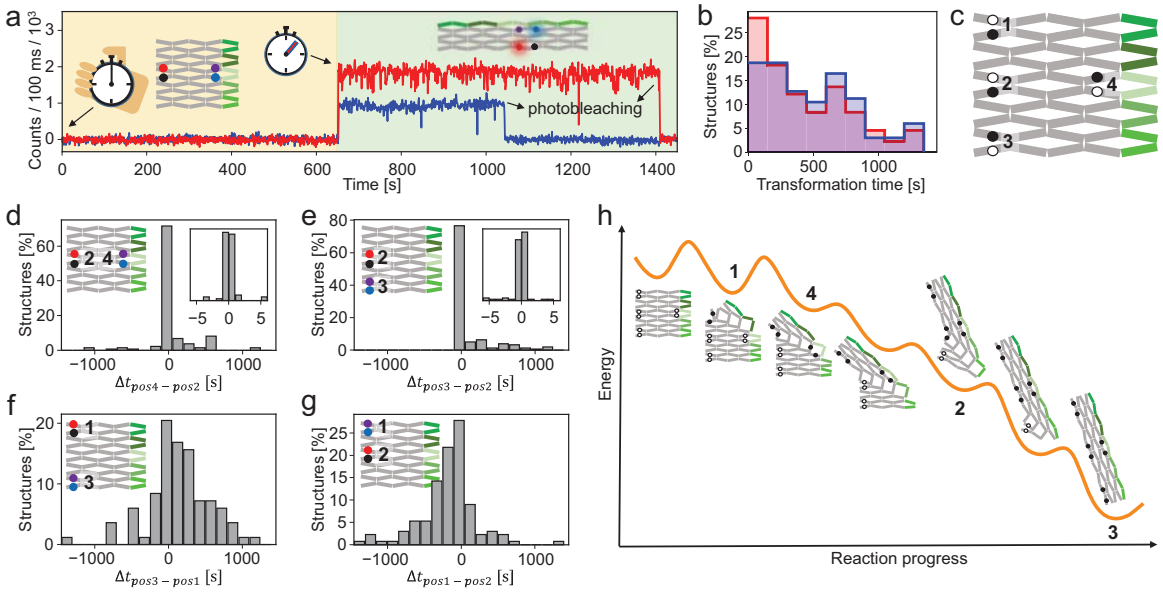

Fig. 2 | Real-time imaging of the transformation reaction of DNA origami arrays. a Representative single-molecule fluorescence intensity transients of DNA origami array with a green and a red FRET probe incorporated after addition of five trigger DNA strands at 0 s. The time the transformation occurs at the red and the green FRET probe positions is marked with an arrow. Fluorescence of ATTO647N and ATTO542 is shown in red and blue, respectively. **b** Transformation time after the addition of five trigger DNA strands at the position of the red FRET probe (red) and the green FRET probe (blue). **c** Scheme of the different positions used for the placement of the FRET probes on DNA origami arrays for tracking the transformation reaction. **d**–**g** Time difference between the transformation occurring at the positions of the green and red FRET probes for different FRET probe positions. **h** Proposed, simplified energy landscape of the transformation reaction. The intermediates at which the studied positions switch their conformation are marked with numbers.

of transformation. This "turn-on" configuration as exemplarily shown in the sketch of Fig. 1a ensured discrimination of transformation events from photobleaching events. Surface-immobilized structures were imaged via total internal reflection fluorescence (TIRF) microscopy using green and red, alternating excitation (see Supplementary Fig. 1 and Methods for experimental details). In the resulting images, blue, red and white spots represent fluorescence of ATTO542, ATTO647N and co-localized fluorescence of both dyes, respectively.

We recorded TIRF images of DNA origami arrays bearing FRET probes (positions of FRET probes as in Fig.1a) before and after 25 min incubation with and without five trigger DNA strands. The corresponding TIRF images are shown in Figs. 1e, f. Before incubation, the fluorescence of both dyes is quenched. Only a small number of spots is visible, which could be attributed to either mislabeled or partially transformed structures (Figs. 1e, f, left images). After incubation with trigger DNA strands, we noted a significant increase of spots of co-localized fluorescence of ATTO542 and ATTO647N which did not occur after incubation without trigger DNA strands (Figs. 1e, f, right images). This demonstrates that the trigger-induced transformation reaction of the DNA origami array structure occurred and that it could be visualized by fluorescence imaging. With a reference dye for localizing DNA origami structures, we determined the transformation yield as studied with the FRET probes to have values of 86% and 93% depending on the position of the FRET probe (Supplementary Fig. 2).

Real time single-molecule observation of the transformation reaction pathway of DNA origami arrays

Next, we explored the dynamics of the transformation reaction upon addition of the five trigger DNA strands. To extract dynamic information of the transformation of individual anti-junctions in the structures, we used time-lapse imaging (alternating 638 nm and 532 nm excitation, 100 ms every 1 s per color) on the same area and extracted dual-color fluorescence transients of single structures.

Figure 2a shows an exemplary transient recorded during the transformation reaction (for additional transients, see Supplementary Fig. 3). The transient exhibits a single-step increase in fluorescence intensity occurring simultaneously for both FRET probes within the time resolution of 1 s of our measurement followed by single-step photobleaching. Such an increase was not observable when conducting the same measurement in the absence of the trigger DNA strands, excluding the possibility of it being caused by photobleaching of the quencher molecules (Supplementary Figs. 2j, k). We thus interpreted the single-step increase in fluorescence as the transformation reaction progressing through the corresponding anti-junction and defined the time between the addition of the trigger DNA staples and this increase as the transformation time of the corresponding anti-junction. The transformation times at the positions of the FRET probes were extracted separately for each structure from the transients (Fig. 2b).

To visualize the transformation behavior of different anti-junction combinations, we assembled four different DNA origami array structures bearing red and green FRET probes at different anti-junctions (Positions 1-4, Fig. 2c, Supplementary Fig. 4). We extracted the time differences Δt between the transformation occurring at the position of the green and of the red FRET probe for each single construct (Figs. 2d, g). For the FRET probes used for the transient in Fig. 2a, this Δt is, for example, 0 s which is the dominating value for the anti-junction combination surveilled by the FRET probes at position 2 and 4 (Fig. 2c, d). Transients and transformation times for the other FRET probe combinations are provided in Supplementary Figs. 3, 5–8).

Time difference distributions of the transformation reactions of DNA origami array structures bearing FRET probes at Position 2 and 4 and at Position 2 and 3 showed a narrow unimodal distribution (Fig. 2d, e). With the exception of a few outlier values, the transformation at the studied positions occurred simultaneously within our temporal resolution of 1 s. In contrast, a time delay between the transformation at Positions 1 and Position 3 was noticed (Fig. 2f). The

transformation occurred first at Position 1 and reached Position 3 after an average time of 198 s (see Supplementary Fig. 9 for controls). When the FRET probes were placed at Positions 1 and 2 (Fig. 2g), the transformation again first occurred at Position 1 before progressing to Position 2. In combination, this implies the transformation first occurring at Position 1 before progressing to Positions 2-4 which is in accordance with the intended asymmetric trigger DNA strand design (Supplementary Fig. 1).

Based on our single-molecule fluorescence measurements and previously reported AFM data[18], we propose a model for the energy landscape of the transformation reaction in our DNA origami array (Fig. 2h). Start and end points of the transformation reaction are the thermodynamically stable transformed and untransformed conformations in which all anti-junctions adopt the same conformation. In all transformation intermediates, some anti-junctions adapt an unstable open conformation. We estimate the energy of those intermediates based on their number of open anti-junctions. The more open anti-junctions a conformation has, the less stable it is. Hybridization of all five trigger DNA strands tilts the energy landscape of the transformation reaction strongly towards the transformed conformation. During the first and second steps of the diagonal transformation reaction, the number of anti-junctions that are forced into their thermodynamically unfavored open conformation increases. Thus, the corresponding steps are accompanied by higher activation energies, resulting in the measured time delay between the transformation occurring at Position 1 and all other positions. In consecutive steps, the number of unstable open anti-junctions remains the same and eventually decreases, which explains the observed quasi-simultaneous transformation at these positions. We then introduced an additional Position 5 which–following our model–transforms in the same step as Position 1. In our measurements, this position transformed at the same time as Position 1 but before Position 3, further confirming the proposed energy landscape (Supplementary Fig. 10).

Mechanochemical coupled and uncoupled transformation of anti-junctions in DNA origami array structures

To study the coupling between the transformation steps and how it can be influenced, we first reduced the driving force of the transformation reaction by reducing the number of added trigger DNA strands from all five to only the upper four. Figure 3a–f shows exemplary single-molecule fluorescence transients of structures with FRET probes placed at different positions. Upon addition of all five trigger DNA strands, over 90% of all transients showed only one irreversible transformation step–independent of the positions of the FRET probes (Figs. 3a, b, and Supplementary Fig. 3, 5–7).

When adding only the upper four trigger DNA strands, a significant fraction of transients showed intensity fluctuations between two well-defined levels for Positions 2–4 (Fig. 3a, Supplementary Fig. 11). In contrast, at Position 1, the fraction of transients exhibiting fluctuations remained at a similarly low level as when adding all five trigger DNA strands (Fig. 3a, Supplementary Fig. 9). We ascribe the emerging fluctuations to reversible transformations of the respective anti-junctions.

A comparison of the transformation times between the studied positions (Fig. 3c, Supplementary Fig. 12) shows the same trends as the transformation upon addition of all five trigger DNA strands. As such, the transformation reaction first irreversibly progresses through Position 1 followed by simultaneous time-delayed reversible transformations at Positions 2-4. However, the time between the transformation occurring at Position 1 and Positions 2-4 increased compared to the time upon addition of all five trigger DNA strands (Fig. 3c). While this indicates that the kinetics of the overall transformation reaction was slowed down by reducing the number of trigger DNA strands added, it did not affect the coupling between anti-junctions to the extent that we could visualize their separate transformations. Further reduction of the number of trigger DNA strands to three or less led to the transformation reaction being either incomplete or not initiated at all (Supplementary Fig. 13).

To further investigate the fluctuating behavior of the anti-junctions upon addition of the upper four trigger DNA strands, we quantified the percentage of fluctuating structures 24 h after addition of the trigger DNA strands. While in many cases, the reversible fluctuations ceased and the fully transformed conformation was adapted in the first 25 min after addition of the trigger DNA strands (Fig. 3a), 24 h after addition of the upper four trigger DNA strands, still a substantial fraction of 30% of fluctuating structures was observed. This shows that structures can return from a fully transformed to a fluctuating state (Supplementary Fig. 13).

Interestingly, for Positions 2-4, the reversible transformations seemed to occur quasi-simultaneously at the different anti-junctions (Fig. 3a, and Supplementary Fig. 11). To quantify the extent of this correlated behavior, we introduced the coupling parameter C (Supplementary Fig. 14) that reports on the time two anti-junctions spend in the same conformation (untransformed or transformed) compared to the time they spend in differing conformations. A maximum value of $C = 1$ corresponds to a DNA origami array with maximally coupled junctions in which only fully correlated fluctuations occur. The closer the value is to $C = 0$, the larger is the time the studied junctions spend in differing conformations and the smaller is the extent of coupling. Systems with $C > 0.95$ are considered fully coupled.

Figure 3d-g show the coupling distributions for the transformation of DNA origami arrays with FRET probes at the strongly coupled Positions 2 and 4, and at the less coupled Positions 1 and 3 upon addition of all five and only the upper four trigger DNA strands. In the coupled system, 67% and 56% of all structures exhibited perfect coupling for the transformation upon addition of five and four trigger DNA strands, respectively, indicating that in many structures also all fluctuations are fully correlated. The coupling distribution of the less coupled systems also feature a small distinct peak at $C > 0.95$ (highlighted by the orange bar, 8% and 23% for the addition of five and four trigger DNA strands, respectively) and an additional larger left-skewed distribution close to $C = 0$. Thus, the majority of all systems exhibit largely uncoupled behavior. The coupling distributions of all other studied systems are shown in Supplementary Fig. 15 and are in good agreement with the proposed transformation reaction cascade starting at Position 1 and progressing to Positions 2-4 at which strongly coupled behavior was observed.

By reducing the number of added trigger DNA strands from five to the upper four, the untransformed conformation was destabilized less, resulting in a slower transformation reaction (Fig. 3c). The destabilization of the transformed conformations yielded reversible transformations at 37 °C (Figs. 3h, i) as described by the energy landscape in Fig. 3j.

To further study the extent of the coupling between the transformation steps, we additionally recorded the fluctuations occurring upon the addition of only the upper four trigger DNA strands at Position 2 and Position 4 with a higher temporal resolution of 200 ms. Even with this fivefold improvement in resolution, the transformations at the studied positions still occurred simultaneously, reinforcing the assumption of a strongly coupled system across distal sites (Supplementary Fig. 16).

Decoupling of anti-junctions in DNA origami array structures by introduction of artificial activation energy barriers

With a deeper understanding on the transformation mechanism, we then aimed for modulating the transformation reaction via selective decoupling of anti-junctions. First, we weakened the coupling between individual positions, i.e., between Positions 2 and 3, by engineering the energy landscape at the corresponding step to introduce a heightened activation energy barrier (Fig. 4a). In addition to an unmodified

https://doi.org/10.1038/s41467-024-51721-y

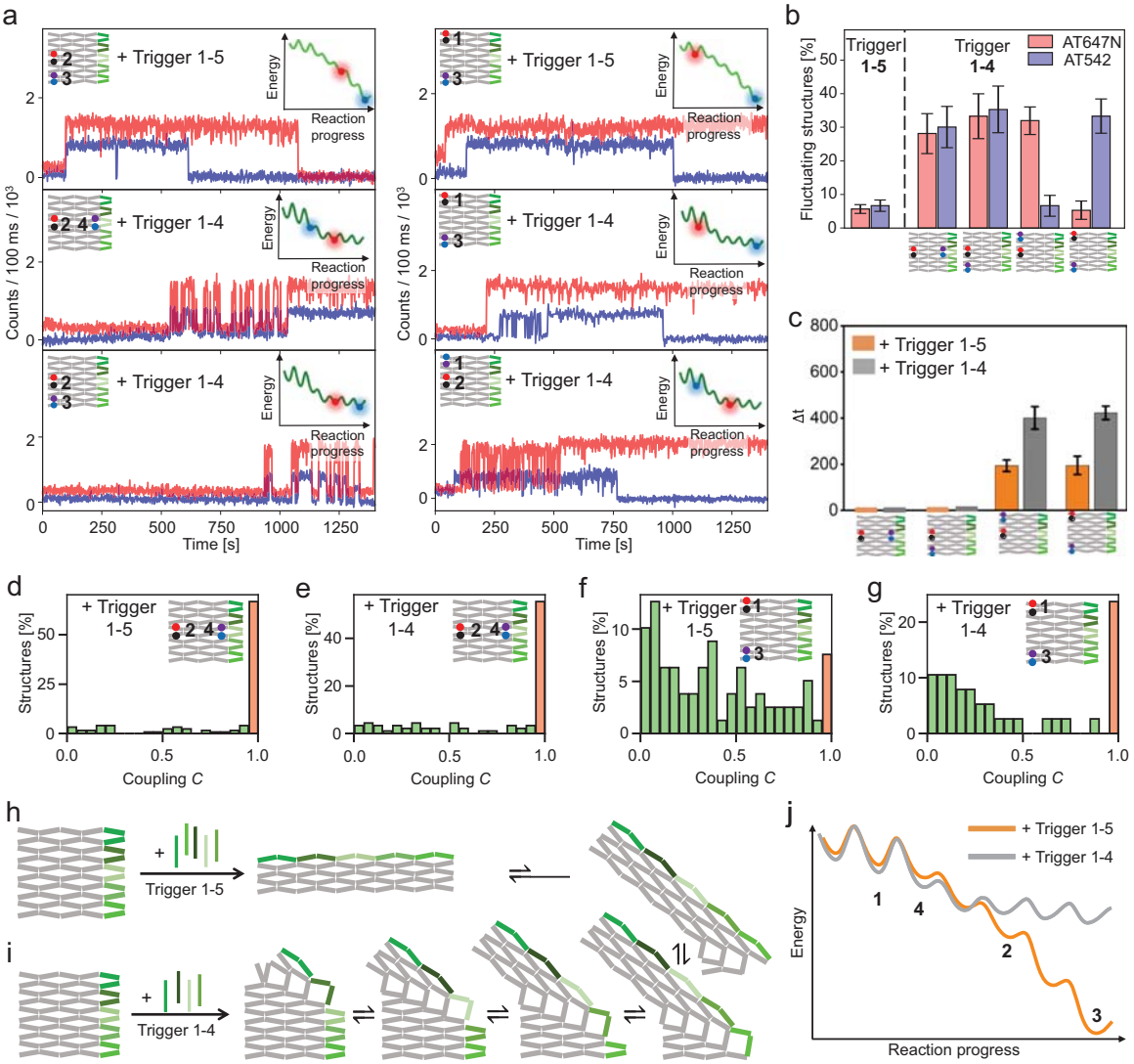

Fig. 3 | Reversibility and coupling in the transformation reaction upon addition of different numbers of trigger DNA strands. a Representative single-molecule fluorescence intensity transients of DNA origami arrays with FRET probes placed at different positions upon the addition of all five trigger DNA strands (upper row) and only the upper four trigger strands (middle and lower row) at 0 s. Fluorescence of ATTO647N and ATTO542 is shown in red and blue, respectively. **b** Fraction of structures exhibiting fluctuations between the untransformed and transformed conformation at the different positions of the FRET probes upon addition of all five or the upper four trigger strands. Error bars represent the standard error of at least 80 structures. **c** Mean absolute time differences for the transformation occurring at the different positions upon addition of five trigger strands and upon the addition of the upper four trigger DNA strands. For designs in which the majority of structures exhibited a time delay between the transformation at the different positions, only non-perfectly coupled structures with $\triangle t \neq 0$ s were considered. All plots show the mean values and standard errors of Gaussian fits to the corresponding time difference distributions. **d**–**g** Coupling histograms for DNA origami array structures with the FRET probes at different positions. The fraction of structures exhibiting full coupling is indicated by an orange bar. **h**, **i** Scheme of the transformation reaction upon addition of five and the upper four trigger strands. **j** Proposed, simplified energy landscape of the transformation reaction with four and five trigger strands. The potential wells at which the studied positions switch their conformation are marked with numbers.

reference (Design 1), three DNA origami arrays bearing FRET probes at Positions 2 and 3 were assembled (Fig. 4b, Supplementary Data 1). In the second array, a locking mechanism was introduced. The mechanism consists of two complementary DNA strands protruding from the origami surface which are in close proximity in the untransformed and further apart in the transformed conformation. Hybridization of the two strands thus stabilizes the untransformed conformation and increases the energy necessary to induce the transformation at the corresponding position (Design 2). For the third and fourth array (Designs 3 and 4), staple strands around positions of central anti-junctions in the structure were left out during assembly of the structures (Supplementary Data 1).

The time lags between the transformation occurring at Positions 2 and 3 upon addition of all five trigger DNA strands are shown in Fig. 4c for all four designs (Supplementary Fig. 17 for time difference histograms). The corresponding coupling distributions are shown in Figs. 4d–f. In Design 1, the transformation at Positions 2 and 3 was strongly coupled (Fig. 4d) with $C > 0.95$ for 73% of all structures. In Design 2, the extent of coupling was reduced and only 40% of all structures exhibited a coupling of $C > 0.95$ (Fig. 4e). This tendency

https://doi.org/10.1038/s41467-024-51721-y

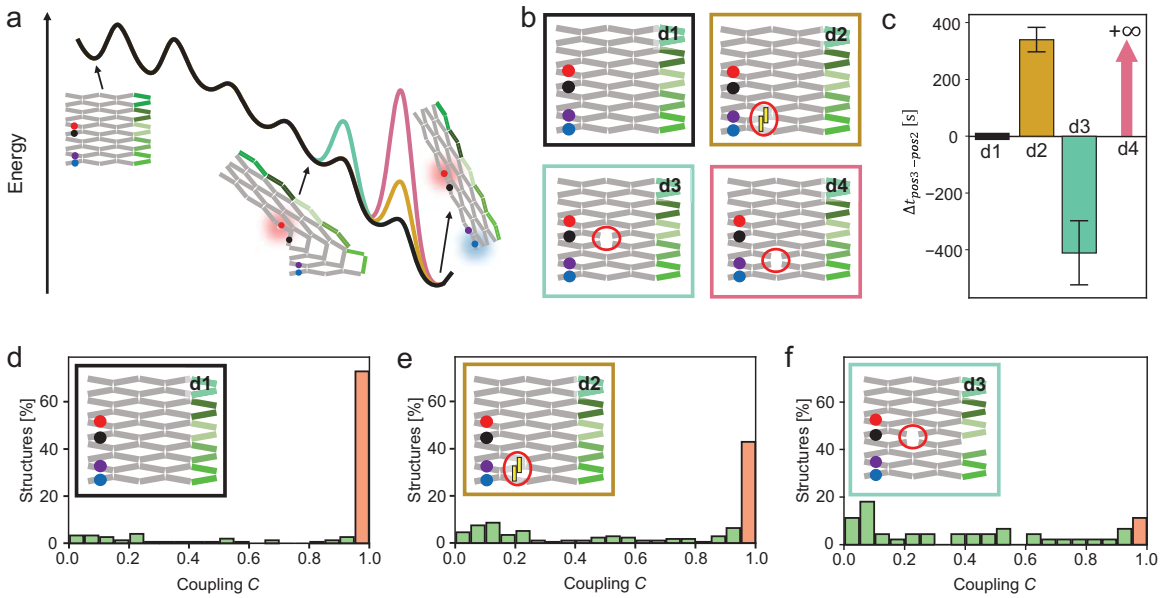

Fig. 4 | Temporal decoupling of different steps in the transformation reaction by artificially introducing energy barriers. a, **b** Mechanisms used to engineer the energy landscape. d1 corresponds to the unmodified reference, d2 to a system with a locking unit incorporated and d3 and d4 to systems with missing central anti-junctions. **c** Lag times for the transformation to progress from Position 2 to Position 3 upon addition of all five trigger DNA strands in the systems shown in (**b**). Error bars represent the standard deviation of the Gaussian fit of the corresponding time difference histograms. For designs in which the majority of structures exhibited a time delay between the transformation at the different positions, only non-perfectly coupled structures with $\triangle t \neq 0$ s were considered. All plots show the mean values and standard errors of Gaussian fits to the corresponding time difference distributions. **d**–**f** Corresponding coupling histograms. The fraction of structures exhibiting full coupling ($C > 0.95$) is indicated by an orange bar.

became even more pronounced for Design 3, for which only 12% of structures exhibited a coupling of $C > 0.95$. In the uncoupled structures of Design 2, the transformation preferentially occurred first at Position 2 before progressing to Position 3. In Design 3, the order of events was reversed, and the transformation occurred at Position 3 before progressing to Position 2. For Design 4, the transformation stopped after Position 2 such that it did not progress to Position 3 at all, rendering the global transformation incomplete.

The data shows that the energy landscape of the transformation reaction could be specifically tailored to selectively weaken the coupling between Position 2 and 3 to different extents in Designs 2-4. We concluded that the incorporation of locking units (Design 2) and leaving out staple strands (Design 3, 4) at positions transforming at different steps in the transformation reaction cascade form efficient tools to engineer different extents of coupling and time delays within cascade systems.

Using Design 2, we additionally studied the energy transport efficiency of the transformation reaction at the position of the locking unit. By stepwise increasing the number of hybridizing base pairs of the locking unit (Supplementary Data 1), we systematically varied the hybridization energy of the unit. Quantification of the number of structures transforming at Position 3 within 25 min revealed a 50% transport efficiency for hybridization energy of 16.0 ± 0.5 kcal/ mol (not considering possible effects of binding the locking unit to the DNA origami scaffold, Supplementary Fig. 18).

Besides quantifying how much energy is transferable at a specific step in the transformation reaction, we also demonstrated the transfer of a cargo DNA strand to the environment. Based on the principle of allosteric inhibition, we designed a cargo release unit to which a cargo DNA strand binds in the untransformed conformation. Upon binding of the trigger DNA strands to the transformation origami and the subsequent transformation of the cargo release unit, the binding of the cargo DNA strand to the unit is weakened, resulting in its release. In this process, the mechanical energy of the conformational change is reconverted to chemical energy to dehybridize the cargo DNA strand from the structure–tens of nanometers away from the initial activation site (Supplementary Figs. 19, 20, Supplementary Note 1).

Discussion

In conclusion, we established a double-FRET single molecule assay to reveal insights into the allosteric transformation reaction cascade of reconfigurable DNA origami arrays. The assay allowed zooming in into single steps of the cascade process, making it possible to characterize the transformation reaction cascade, including intermediates. For our DNA origami array model structure, the energy landscape predominantly depends on the number of open anti-junctions of the intermediates. As such, the first few steps are accompanied by comparably high activation energies, whereas all the following steps occur quasi-simultaneously. Our assay allowed us to define strategies to tailor the transformation reaction cascade both globally and at predefined steps. The incorporation of different locking elements into the structure introduces artificial energy barriers, resulting in weakened coupling between selected intermediates, which, in the extreme, leads to altered transformation pathways or incomplete transformations.

The principal findings should be applicable to more complex DNA origami array systems. Such systems could feature different proximity-induced operations. Exemplarily, we demonstrated a cargo DNA strand released at a predefined step in the transformation reaction cascade. Combining the transformation reaction cascade with its intrinsic allosteric control, the addressability of the DNA origami approach, and the findings revealed by our double-FRET single molecule assay highlights the potential of DNA origami arrays as a universal platform to engineer spatially controlled reactions for information and energy transfer. In addition to the prototypical allosteric transfer of

spatial information, we added the dimension of temporal control as timing between certain elements could be engineered. Overall, we envision that further developing these approaches will pave the way for DNA origami array systems being used as a platform for programmable, artificial reaction networks containing elements such as cooperativity and anti-cooperativity[28], rows of logical gating[29,30] as well as signal amplification[31] and transduction over several tens of nanometers.

Methods

Synthesis of DNA origami arrays

DNA origami structures were designed using the open-source software caDNAno2[32] and assembled and purified using published protocols[33]. For the exact sequences of all unmodified and modified DNA staple strands used to fold the DNA origami structures see Supplementary Data 1. DNA staple strands were purchased from Eurofins Genomics GmbH (Germany) and Integrated DNA Technologies (USA).

For DNA origami folding, 25.0 µL of in house produced p1800 scaffold at 100 nM were mixed with 3.4 µL of unmodified staples and 8.6 µL of modified staples pooled from 100 µM original concentration. Briefly, 5.0 µL of 10 × TAE buffer (400 mM Tris, 400 mM acetic acid, 10 mM EDTA, pH 8), 6.0 µL of 100 mM $MgCl_2$ and 7.0 µL water were added and the mixture was heated to 65 °C in a thermocycler. The solution was kept at this temperature for 15 min before being cooled down to 25 °C with a temperature gradient of −1 °C min^{-1}. Folded DNA origamis were purified from excessive staple strands by gel electrophoresis. All gels were ran using a 1.5% agarose gel, 1 × TAE (40 mM Tris, 40 mM acetic acid, 1 mM EDTA, pH 8) containing 12.5 mM $MgCl_2$ for 2 hours at 6 V/cm. The target band containing DNA origami was cut from the gel and DNA origami solution extracted from the band via squeezing.

Atomic force microscopy (AFM) measurements

The AFM imaging was carried out on the Multimode VIII system (Bruker). 2 µL of the sample was deposited onto freshly cleaved mica surface. The sample area was filled with 80 µL 1 × TE buffer with 10 mM $MgCl_2$. The sample was imaged in liquid mode using commercial tips (SNL-10, Bruker). The imaging results were analyzed with Nanoscope analysis (Bruker).

Sample preparation on the coverslip for single-molecule wide-field measurements

Adhesive SecureSeal™ Hybridization Chambers (2.6 mm depth, Grace Bio-Labs, USA) were glued on microscope coverslips (24 mm × 60 mm, 170 µm thickness, Carl Roth GmbH, Germany). 1 M KOH was added to the chambers, incubated for 1 h and washed with 1 × PBS buffer three times. The chambers then were incubated with BSA-Biotin (0.5 mg/mL in 1 × PBS, Sigma Aldrich, USA) for 10 min to passivate the surface and washed with 150 µL 1 × PBS buffer three times. The surfaces were then incubated with NeutrAvidin (0.25 mg/mL in 1 × PBS, Thermo Fisher, USA) for 10 min and then washed three times with 150 µL 1 × PBS buffer. DNA origami structures were then immobilized onto the surfaces of the chambers via biotin-neutrAvidin interactions using a biotinylated DNA staple incorporated in the unused scaffold loop of the structures during folding. For this, 150 µL of the DNA origami sample solution diluted to ~10 pM in 1 × TE buffer containing 750 mM NaCl was incubated in the chambers for 5 min and the chambers then washed with 150 µL 1 × TE buffer containing 750 mM NaCl for three times to remove residual unbound DNA origami. In order to minimize photo bleaching and photoblinking, a reducing and oxidizing buffer system (1 × TAE, 2 mM Trolox/Troloxquinone, 12.5 mM $MgCl_2$)[34] in combination with an oxygen scavenging system (12 mM protocatechuic acid (PCA), 56 µM protocatechuate 3,4-dioxygenase (PCD), 1% glycerol, 2 mM Tris-HCl, 1 mM KCl, 20 µM $Na_2EDTA{\cdot}2H_2O$) was added prior the measurement.

Loading of the cargo release unit

The cargo release unit was loaded with an ATTO542 labeled cargo DNA strand by incubating surface immobilized origami structures with 100 nM cargo strand in 1 × TAE containing 12.5 mM $MgCl_2$ for 10 min. To remove excess cargo DNA strands, samples were washed three times with 150 µL 1 × TE buffer containing 750 mM NaCl and then prepared for imaging.

DNA origami transformation procedure

For the transformation of DNA origami structures, an excess of trigger DNA strands (50 nM) were added to photostabilized DNA origami sample chambers at 37 °C. Immediately after addition of the trigger strands, the sample chambers were sealed and the DNA origami imaged.

Wide-field measurements

The data acquisition of single molecule trajectories was realized with the commercial Nanoimager from Oxford Nanoimaging Ltd. At 532 nm, a 1000 mW laser was used to excite the ATTO542 dye, with a relative power-level set to 9%. At 638 nm, a 1100 mW was used to excite the ATTO647N dye with a relative power-level set to 18%. In order to improve the signal-to-background ratio, the wide field illumination was set to TIRF-illumination. In the emission, spectral filtering is applied to separate the fluorescence from scattered excitation light (685/40 filter for the red detection channel and 585/70 filter for the green detection channel). Data acquisition was initialized by activating the lasers and taking a frame of 100 ms every second separately for both excitation lasers (with a time lag of 0.5 s between them) over a measurement period of 25 min. Measurements were carried out at 37 °C.

Data analysis

Data processing and analysis of time-lapse movies was realized using custom-written Python scripts. Briefly, the acquired movies were first drift corrected using DNA origami structures carrying fluorophores which were in their fluorescent state throughout the whole measurement as fiducial markers. Spots appearing during the measurement were detected from the drift-corrected movies, and dual-color background-subtracted fluorescence intensity transients of those spots were extracted. To determine transformation times and coupling of single structures, the corresponding transients were fitted using a Hidden Markov model (HMM). Two levels corresponding to the untransformed and transformed state of the structure were defined. Transformation times were defined as the time a structure switches from its untransformed state to its transformed state and subsequently remains in its transformed state for at least 10 s for the first time. They were extracted from the fitted HMM transients. For the calculation of the Coupling between different positions in a structure, transformations state occupancy density plots were created from the dual-color HMM transients. As the ATTO647N and the ATTO542 fluorescence transients were recorded with a time lag of 0.5 sec between them, data points measured in the frame directly before and directly after intensity jumps as determined by the HMM fits were excluded to not artificially weaken the Coupling. The further workflow for calculating the Coupling is given in Supplementary Fig. 11.

For determining the fraction of fluorophores experiencing photobleaching over the 25 min measurement period, all transients were considered. For all further transient analyses, only transients in which both fluorophores turned into their fluorescent state were considered.

Data availability

The experimental data generated in this study have been deposited in the zenodo database under accession code https://doi.org/10.5281/zenodo.12155916. Data supporting the findings of this manuscript are also available from the authors upon request.

Code availability

Custom code used for analysis in this study has been deposited in the zenodo database under accession code https://doi.org/10.5281/zenodo.12155916.

References

1. MONOD, J. & JACOB, F. Teleonomic mechanisms in cellular metabolism, growth, and differentiation. *Cold Spring Harb. symposia Quant. Biol.* **26**, 389–401 (1961).
2. Monod, J., Changeux, J.-P. & Jacob, F. Allosteric proteins and cellular control systems. *J. Mol. Biol.* **6**, 306–329 (1963).
3. Monod, J., Wyman, J. & Changeux, J.-P. On the nature of allosteric transitions: a plausible model. *J. Mol. Biol.* **12**, 88–118 (1965).
4. Koshland, D. E., Némethy, G. & Filmer, D. Comparison of experimental binding data and theoretical models in proteins containing subunits. *Biochemistry* **5**, 365–385 (1966).
5. Changeux, J.-P. & Edelstein, S. J. Allosteric mechanisms of signal transduction. *Sci. (N. Y., N. Y.)* **308**, 1424–1428 (2005).
6. Buddingh', B. C., Elzinga, J. & van Hest, J. C. M. Intercellular communication between artificial cells by allosteric amplification of a molecular signal. *Nat. Commun.* **11**, 1652 (2020).
7. Ma, B. & Nussinov, R. Amplification of signaling via cellular allosteric relay and protein disorder. *Proc. Natl Acad. Sci. USA* **106**, 6887–6888 (2009).
8. Zhu, L. & Anslyn, E. V. Signal amplification by allosteric catalysis. *Angew. Chem. (Int. ed. Engl.)* **45**, 1190–1196 (2006).
9. Galstyan, V., Funk, L., Einav, T. & Phillips, R. Combinatorial control through allostery. *J. Phys. Chem. B* **123**, 2792–2800 (2019).
10. Lim, W. A. The modular logic of signaling proteins: building allosteric switches from simple binding domains. *Curr. Opin. Struct. Biol.* **12**, 61–68 (2002).
11. Gruber, R. & Horovitz, A. Allosteric mechanisms in chaperonin machines. *Chem. Rev.* **116**, 6588–6606 (2016).
12. Yuan, Y., Tam, M. F., Simplaceanu, V. & Ho, C. New look at hemoglobin allostery. *Chem. Rev.* **115**, 1702–1724 (2015).
13. Zhang, C. et al. Programmable allosteric DNA regulations for molecular networks and nanomachines. *Sci. Adv.* **8**, eabl4589 (2022).
14. Kholodenko, B., Yaffe, M. B. & Kolch, W. Computational approaches for analyzing information flow in biological networks. *Sci. Signal.* **5**, re1 (2012).
15. Yan, Q., Wang, Y., Shi, J. & Wei, B. Allostery of DNA nanostructures controlled by enzymatic modifications. *Nucleic Acids Res* **48**, 7595–7600 (2020).
16. Pfeiffer, M. et al. Single antibody detection in a DNA origami nanoantenna. *iScience* **24**, 103072 (2021).
17. Cui, Y. et al. Versatile DNA origami nanostructures in simplified and modular designing framework. *ACS nano* **11**, 8199–8206 (2017). Published Online: Jul. 6, 2017.
18. Song, J.; *et al* Reconfiguration of DNA molecular arrays driven by information relay. *Science* **357**, eaan3377 *(New York, N.Y.)* 2017.
19. Gerling, T., Wagenbauer, K. F., Neuner, A. M. & Dietz, H. Dynamic DNA devices and assemblies formed by shape-complementary, non-base pairing 3D components. *Sci. (N. Y., N. Y.)* **347**, 1446–1452 (2015).
20. Wang, D. et al. Design and operation of reconfigurable two-dimensional DNA molecular arrays. *Nat. Protoc.* **13**, 2312–2329 (2018).
21. Wang, D. et al. Programmable transformations of DNA origami made of small modular dynamic units. *J. Am. Chem. Soc.* **143**, 2256–2263 (2021).
22. Wang, D. et al. Programming the curvatures in reconfigurable DNA domino origami by using asymmetric units. *Nano Lett.* **20**, 8236–8241 (2020).
23. Liu, Y. et al. Modular Reconfigurable DNA origami: from two-dimensional to three-dimensional structures. *Angew. Chem. (Int. ed. Engl.)* **59**, 23277–23282 (2020).
24. Fan, S. et al. Information coding in a reconfigurable DNA origami domino array. *Angew. Chem. (Int. ed. Engl.)* **59**, 12991–12997 (2020).
25. Fan, S. et al. Proximity-induced pattern operations in reconfigurable DNA origami domino array. *J. Am. Chem. Soc.* **142**, 14566–14573 (2020).
26. Fan, S. et al. Spatiotemporal control of molecular cascade reactions by a reconfigurable DNA origami domino array. *Angew. Chem. (Int. ed. Engl.)* **61**, e202116324 (2022).
27. Liu, Y.; et al *Multistep Transformations of DNA Origami Domino Array via Mechanical Forces*. *Small Structures* **4**, 2200167 (2022).
28. Simon, A. J., Vallée-Bélisle, A., Ricci, F. & Plaxco, K. W. Intrinsic disorder as a generalizable strategy for the rational design of highly responsive, allosterically cooperative receptors. *Proc. Natl Acad. Sci. USA* **111**, 15048–15053 (2014).
29. Chatterjee, G., Dalchau, N., Muscat, R. A., Phillips, A. & Seelig, G. A spatially localized architecture for fast and modular DNA computing. *Nat. Nanotech* **12**, 920–927 (2017).
30. Shah, S. et al. Using strand displacing polymerase to program chemical reaction networks. *J. Am. Chem. Soc.* **142**, 9587–9593 (2020).
31. Wang, B., Barahona, M. & Buck, M. Engineering modular and tunable genetic amplifiers for scaling transcriptional signals in cascaded gene networks. *Nucleic Acids Res.* **42**, 9484–9492 (2014).
32. Douglas, S. M. et al. Self-assembly of DNA into nanoscale three-dimensional shapes. *Nature* **459**, 414–418 (2009).
33. Wagenbauer, K. F. et al. How we make DNA origami. *ChemBioChem* **18**, 1873–1885 (2017).
34. Cordes, T., Vogelsang, J. & Tinnefeld, P. On the mechanism of Trolox as antiblinking and antibleaching reagent. *J. Am. Chem. Soc.* **131**, 5018–5019 (2009).

Acknowledgements

P.T. gratefully acknowledges financial support from the Federal Ministry of Education and Research (BMBF) and the Free State of Bavaria under the Excellence Strategy of the Federal Government and the Länder through the ONE MUNICH Project 'Munich Multiscale Biofabrication' and the BMBF in the framework of the Cluster4Future program (Cluster for Nucleic Acid Therapeutics Munich, CNATM) (Project ID: 03ZU1201AA). Y.K. acknowledges the support by the Department of Energy grant DE-SC0020996, the National Science Foundation grants CCF-2227399 and ECCS-2328217, and the National Institute of Health grants 1R35GM153472 and 1RM1GM145394. The AFM images of DNA origami were collected on an atomic force microscope supported by Grants GM084070 and 3R01GM084070-07S1. M.P. acknowledges support by Studienstiftung des Deutschen Volkes. The authors thank P. Luna, P. Xaverl, and T. Charly for their support with measurements and data analysis, and A. Kardinal, H. Lipfert, S. Steger, and M. Ehrl for laboratory upkeep.

Author contributions

M.P., D.W., F.C., T.S., Y.K., and P.T. conceived and developed the concept. M.P., D.W., and F.C. prepared samples and performed and analyzed the measurements. Y.K. and P.T. supervised the project. M.P., D.W., F.C., T.S., Y.K., and P.T. have written, read, and approved the final manuscript.

Funding

Open Access funding enabled and organized by Projekt DEAL.

Competing interests

The authors declare no competing interests.

Additional information

Supplementary information The online version contains supplementary material available at https://doi.org/10.1038/s41467-024-51721-y.

Correspondence and requests for materials should be addressed to Yonggang Ke or Philip Tinnefeld.

Peer review information *Nature Communications* thanks Eitan Lerner and the other, anonymous, reviewer(s) for their contribution to the peer review of this work. A peer review file is available.

Supplementary Information

Controlled mechanochemical coupling of anti-junctions in DNA origami arrays

Fiona Cole [1,2,7], Martina Pfeiffer [1,2,7], Dongfang Wang [3,4,5,6,7], Tim Schröder [1,2], Yonggang Ke [3,4*] and Philip Tinnefeld [1,2*]

[1] Department of Chemistry, Ludwig-Maximilians-Universität München, Butenandtstr. 5-13, 81377 München, Germany

[2] Center for NanoScience, Ludwig-Maximilians-Universität München, Schellingstraße 4, 80799 München, Germany

[3] Wallace H. Coulter Department of Biomedical Engineering, Emory University, Atlanta, GA 30322, USA

[4] Georgia Institute of Technology, Atlanta, GA 30322, USA

[5] School of Biomedical Engineering, University of Science and Technology of China, , Suzhou 215123, China

[6] Suzhou Institute for Advanced Research, University of Science and Technology of China, Suzhou 215123, China

[7] These authors contributed equally

[*] Correspondence: philip.tinnefeld@cup.uni-muenchen.de, yonggang.ke@emory.edu

Supplementary Figures

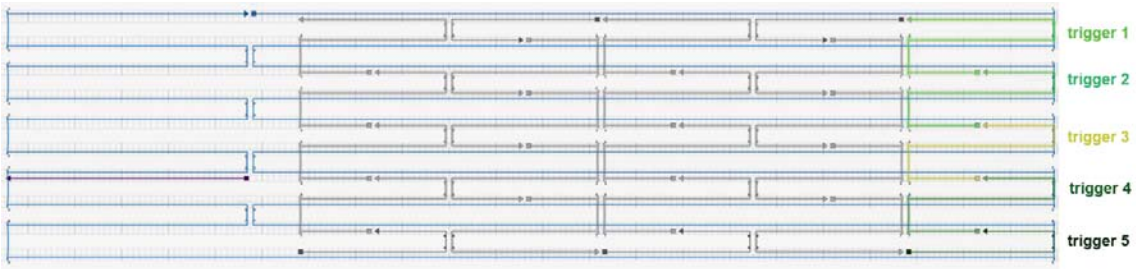

Supplementary Figure 1. Design of the 5 × 2.5 reconfigurable DNA origami array model structure in its untransformed conformation. Blue, gray, purple and green lines represent the scaffold strand, core DNA staple strands of the structure, biotin staple strands and trigger DNA strands, respectively. By labeling one of the staple strands with biotin, we use it as anker point for surface immobilization via biotin-neutravidin interactions. This allows us to avoid directly tethering the core structure (gray staples) to the surface which could possibly affect the transformation process. Trigger DNA strand 1 has a length of 65 base pairs and trigger DNA strands 2-4 all have the same length of 52 base pairs. Trigger DNA strand 5 is shorter, consisting of only 39 base pairs. As the transformation process starts either at the upper right (trigger 1) or lower right corner (trigger 5), this asymmetry induces a preferential transformation starting point. The longer length of trigger 1 compared to trigger 5 results in the transformation preferentially starting from the upper right corner.

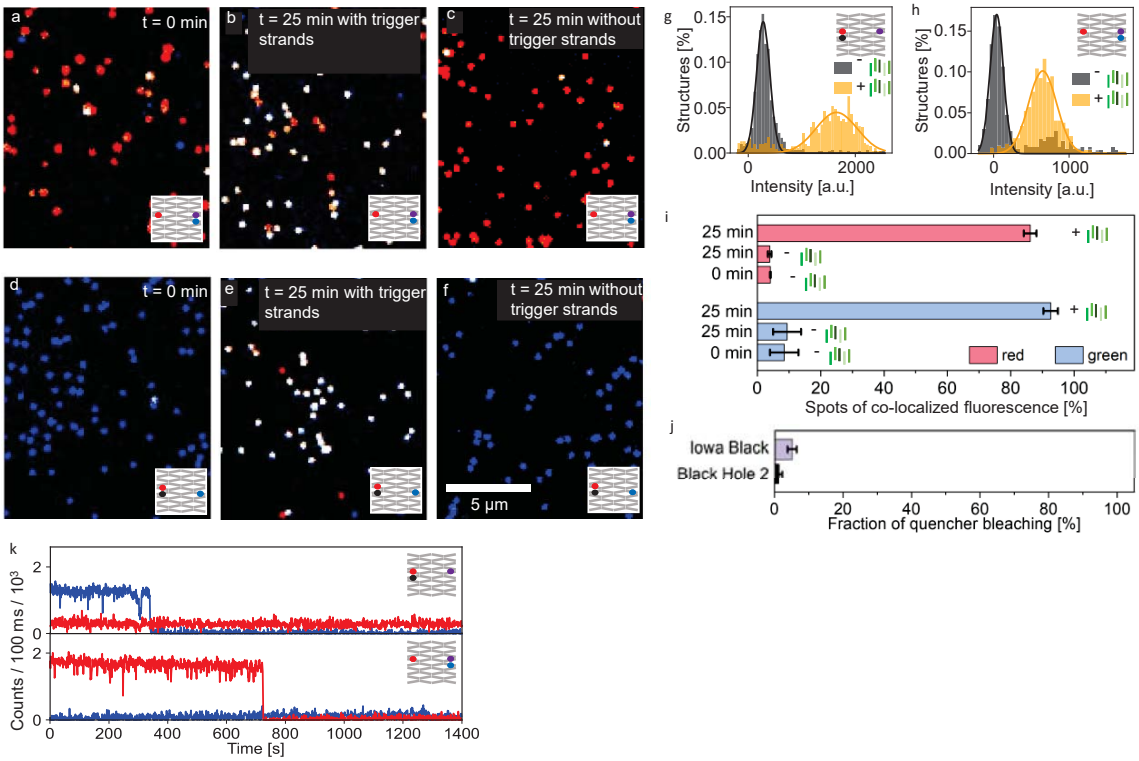

Supplementary Figure 2. Transformation of reconfigurable DNA origami array structures on the single-molecule level. (a-f) Exemplary TIRF images of DNA origami array with (a) the green dye-quencher pair and a red co-localization dye and (b) the red dye-quencher pair and a green co-localization dye incorporated after 0 min incubation, after 25 min incubation (b,e) with all five trigger DNA strands and (c,f) without trigger DNA strands. (g,h) Intensities of the FRET probe in DNA origami arrays prior (grey) and after 25 min (orange) incubation with all five trigger DNA strands for both FRET probes. (i) Fraction of spots of co-localized red and green fluorescence obtained for TIRF images of structures with the red and the green dye-quencher pair as well as a co-localization dye incorporated after 0 min and 25 min of incubation with and without of all five trigger DNA strands. The fraction of spots of co-localized red and green fluorescence indicates the transformation yield as determined with the FRET probes. (j) Fraction of quencher molecules photobleached during the measurement period of 25 min. The fractions were extracted from the intensity transients recorded from the images shown in (a) and (d). (k) Exemplary intensity transients recorded from the images shown in (a) and (d) indicating the absence of quencher blinking. Error bars in (i,j) represent the standard error of at least 200 structures.

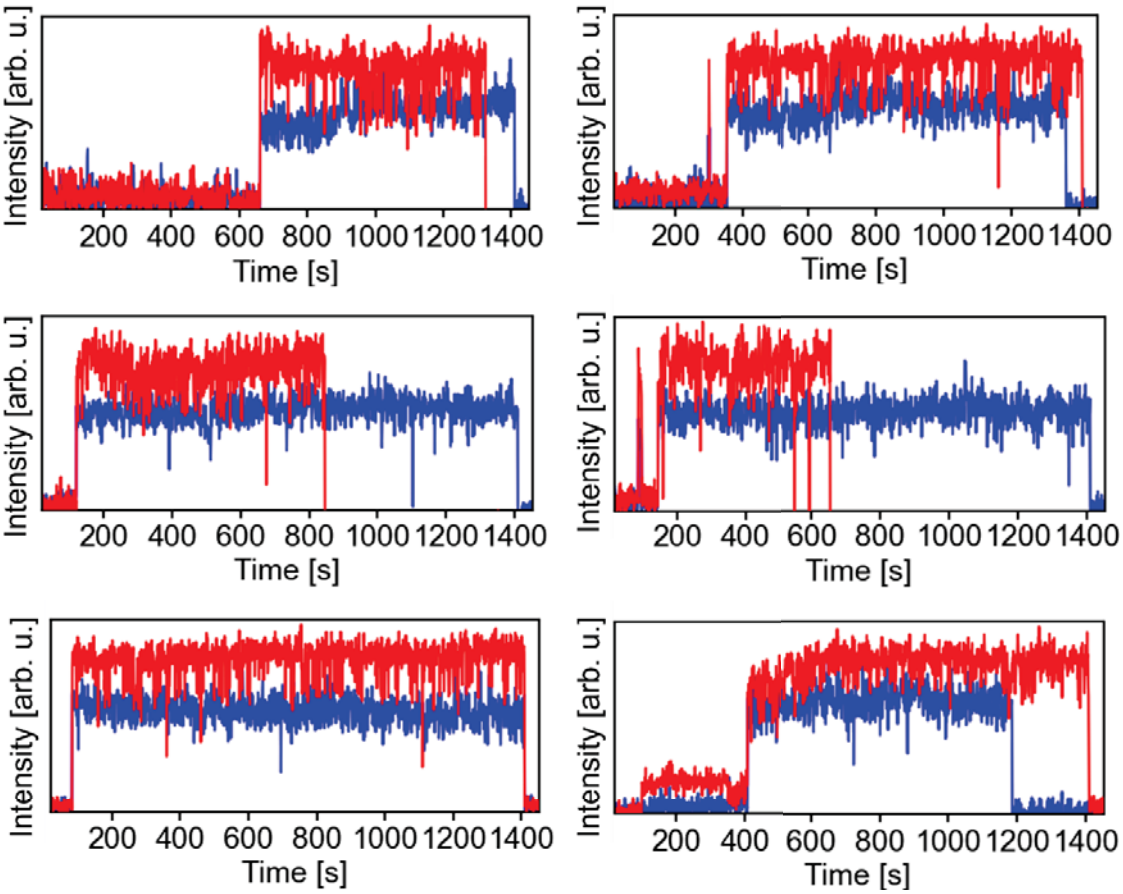

Supplementary Figure 3. Representative single-molecule fluorescence intensity transients of DNA origami array structures with the red and the green FRET probe at Position 4 and Position 2, respectively, recorded after addition of all five trigger DNA strands at 0 s. Fluorescence of ATTO647N is shown in red, fluorescence of ATTO542 in blue. In addition to a sudden jump in fluorescence intensity corresponding to the transformation of the studied position also short dips in fluorescence intensity are observed in the raw data exemplified in Figure S3-S11. While uncorrelated fluctuations can be easily explained by photophysics of the used fluorophores and quenchers, some aspects such as correlated intensity jumps of both dyes simultaneously (e.g. Figure S5 upper left) are sometimes more difficult to interpret. Such effects however occur too infrequently to be included in the statistical analysis.

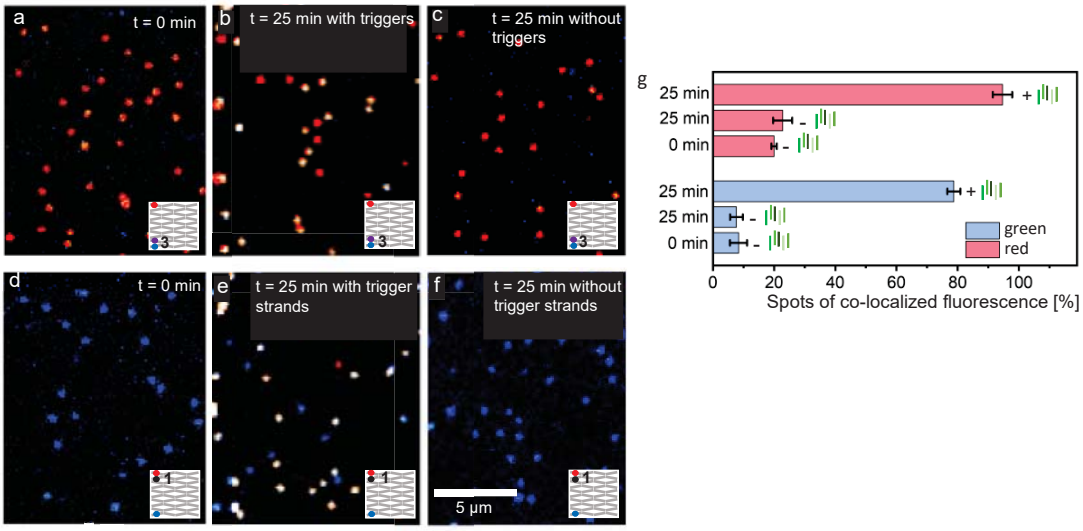

Supplementary Figure 4. Additional FRET probes at Position 1 and Position 3. (a-f) Exemplary TIRF images of DNA origami array with (a) the green dye-quencher pair at Position 3 and a red co-localization dye and (b) the red dye-quencher pair at Position 1and a green co-localization dye incorporated after 0 min incubation, after 25 min incubation (b,e) with all five trigger DNA strands and (c,f) without trigger DNA strands. (g) Fraction of spots of co-localized red and green fluorescence obtained for TIRF images of structures with the red and the green dye-quencher pair as well as a co-localization dye incorporated after 0 min and 25 min of incubation with and without of all five trigger DNA strands. The fraction of spots of co-localized red and green fluorescence indicates the transformation yield as determined with the FRET probes. Error bars in (g) represent the standard error of at least 200 structures.

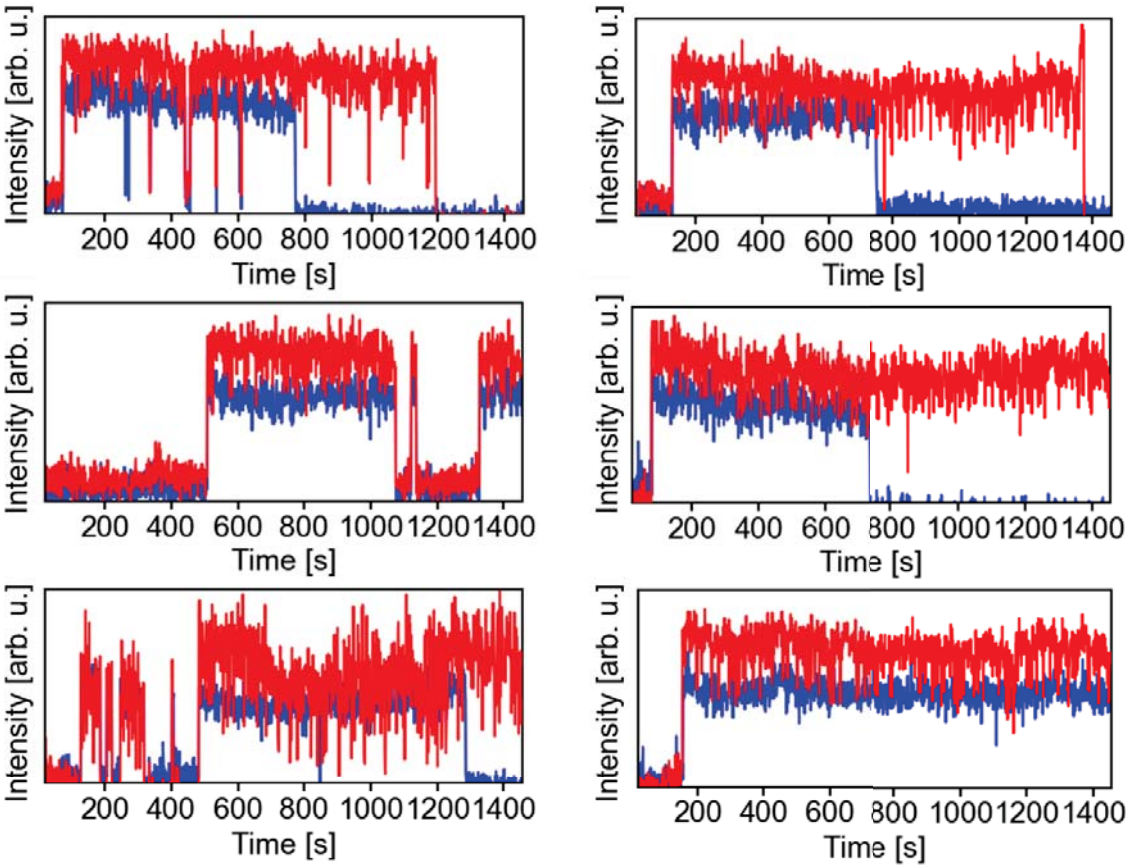

Supplementary Figure 5. Representative single-molecule fluorescence intensity transients of DNA origami array structures with the red and the green FRET probe at Position 2 and Position 3, respectively, recorded after addition of all five trigger DNA strands at 0 s. Fluorescence of ATTO647N is shown in red, fluorescence of ATTO542 in blue.

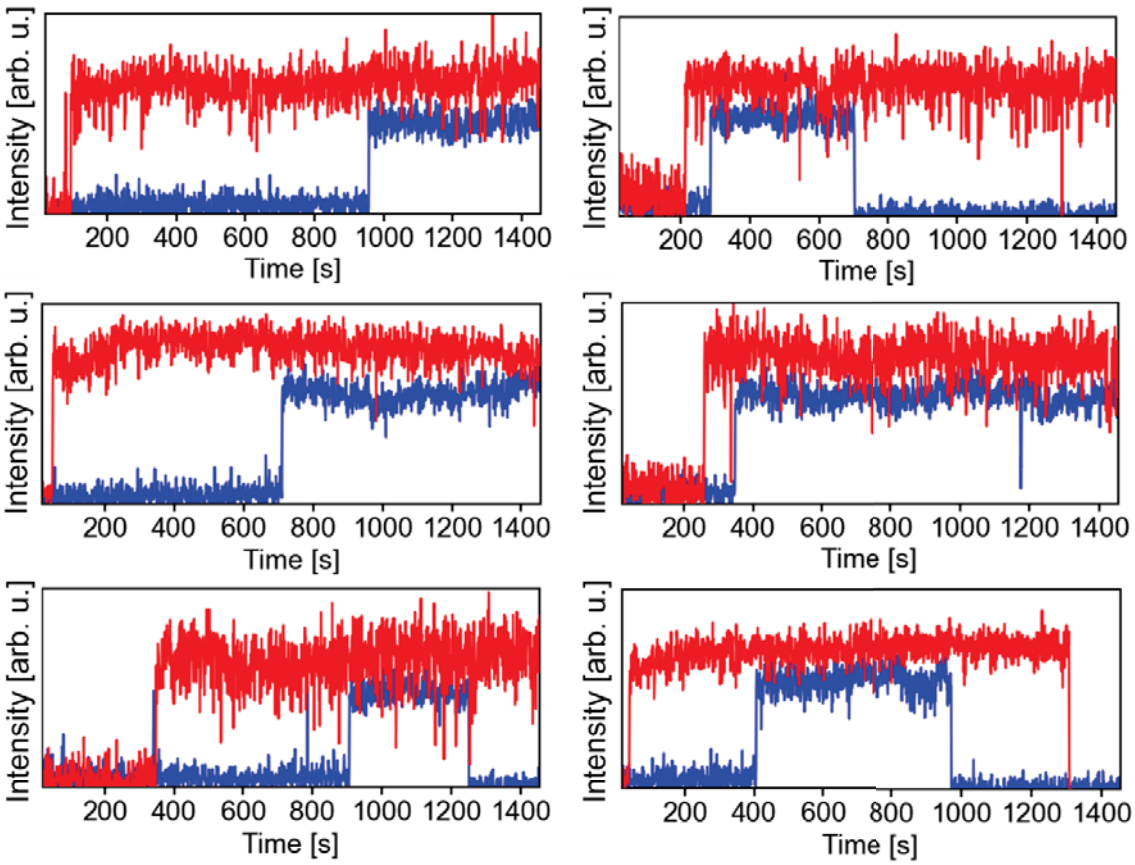

Supplementary Figure 6. Representative single-molecule fluorescence intensity transients of DNA origami array structures with the red and the green FRET probe at Position 1 and Position 3, respectively, recorded after addition of all five trigger DNA strands at 0 s. Fluorescence of ATTO647N is shown in red, fluorescence of ATTO542 in blue.

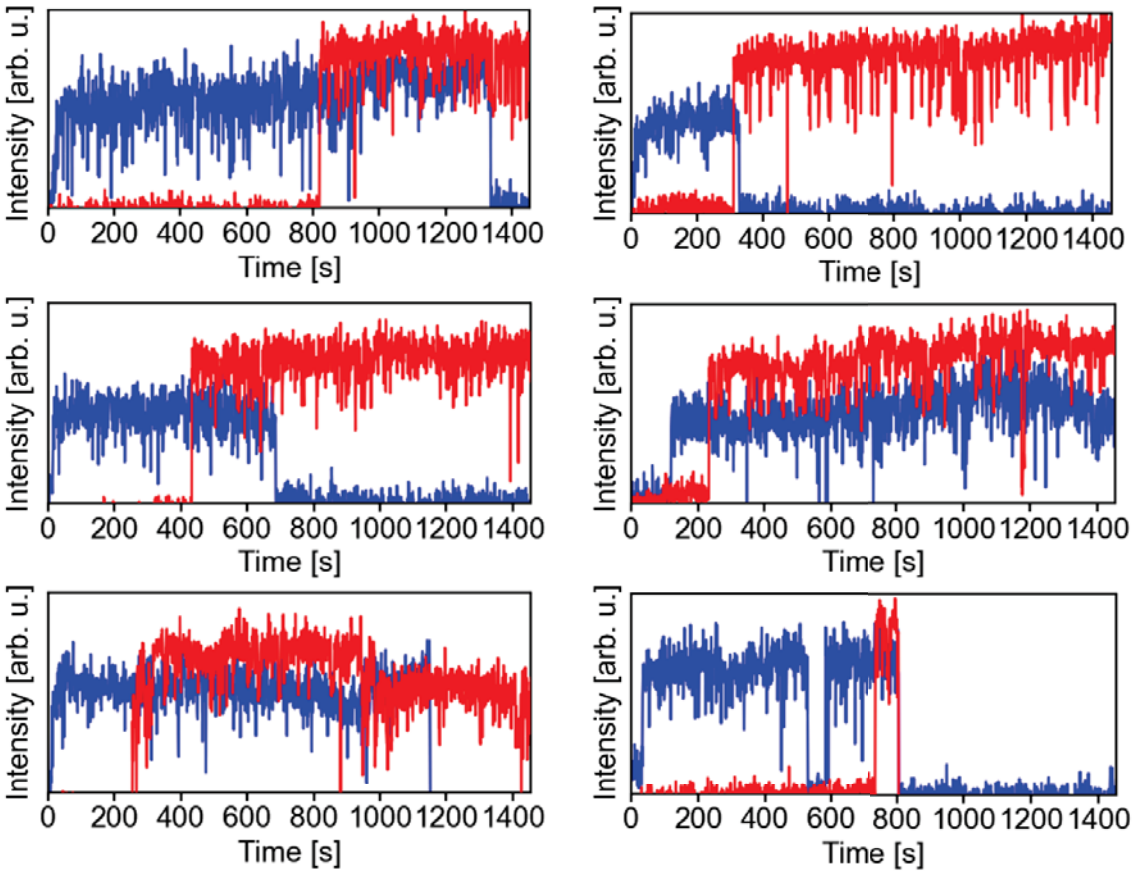

Supplementary Figure 7. Representative single-molecule fluorescence intensity transients of DNA origami array structures with the red and the green FRET probe at Position 2 and Position 1, respectively, recorded after addition of all five trigger DNA strands at 0 s. Fluorescence of ATTO647N is shown in red, fluorescence of ATTO542 in blue.

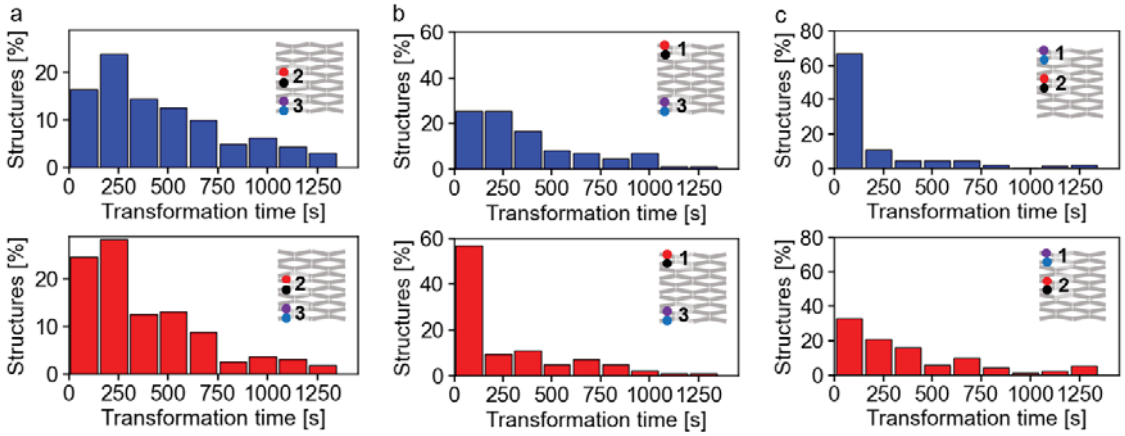

Supplementary Figure 8. Transformation times at the position of the green dye-quencher pair (upper row) and at the position of the red dye-quencher pair (lower row) after addition of all five trigger DNA strands for DNA origami array structures with the dye-quencher incorporated at different positions. (a) Position 2 and 3, (b) Position 1 and 3 and (c) Position 1 and 2.

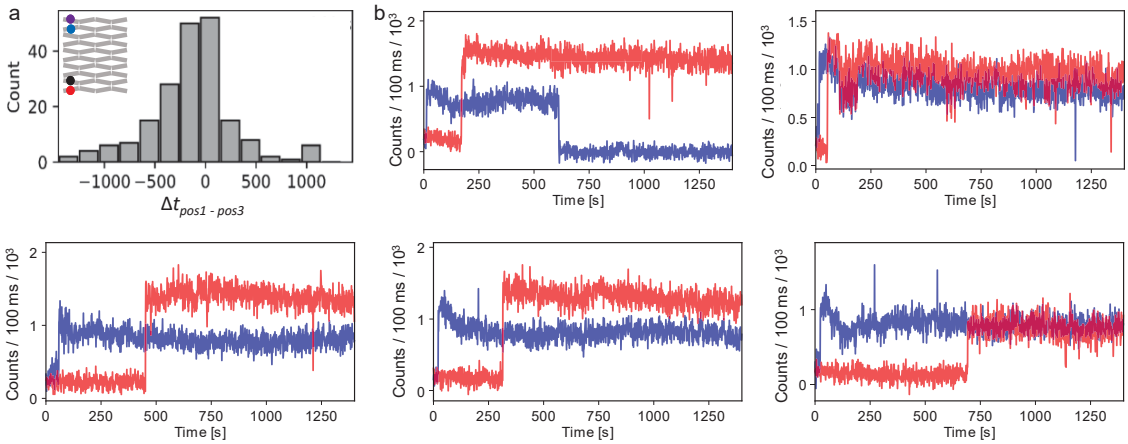

Supplementary Figure 9. Transformation process of DNA origami array with the green and red FRET probes at switched positions in comparison to Figure 2f. The green dye-quencher pair was placed at Position 1 and the red dye-quencher pair at Position 3. (a) Time difference between the transformation occurring at the positions of the green and red dye-quencher pairs positioned at Position 1 and Position 3, respectively. As for the design with the FRET probes placed at the switched positions in Figure 2f, the transformation preferentially first occurs at Position 1, confirming that this tendency was caused by the structure itself and not by differing interactions of the red and green FRET probes with DNA (e.g. stickiness).[1] (b) Representative single-molecule fluorescence intensity transients of a surface-immobilized DNA origami array structures recorded after addition of all five trigger DNA strands at 0 s. Fluorescence of ATTO647N is shown in red, fluorescence of ATTO542 in blue.

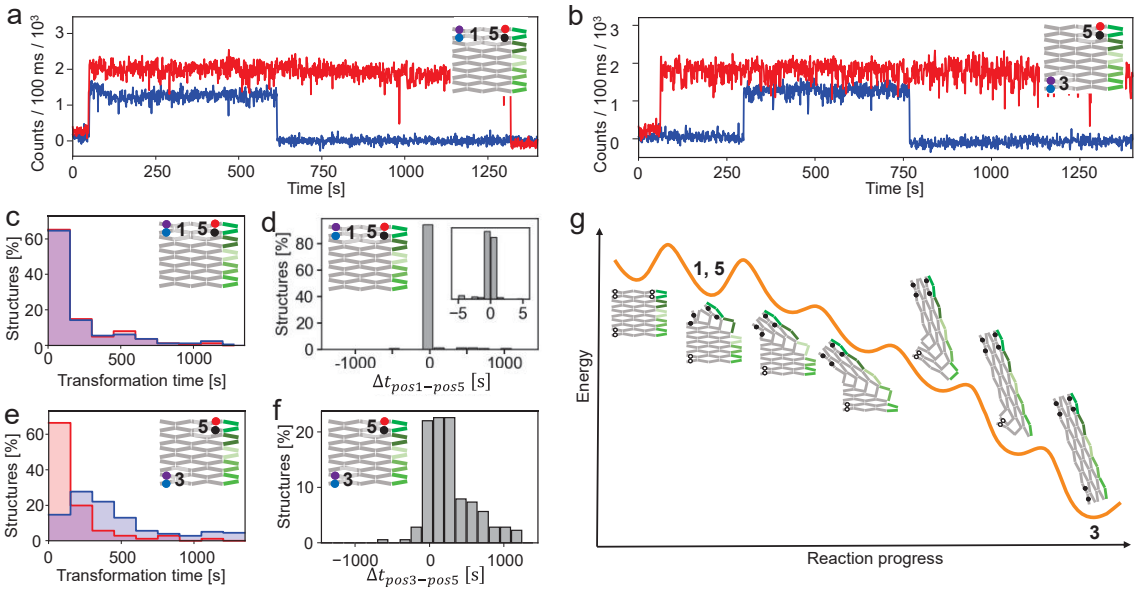

Supplementary Figure 10. Transformation at Position 5 after addition of all five trigger DNA strands at 0s. (a-b) Representative single-molecule fluorescence intensity transients of DNA origami array structures with the red and green FRET probe at (a) the newly introduced Position 5 and Position 1 and (b) Position 5 and Position 3, respectively. (c-f) Analysis of the transformation times. (c,e) Transformation times after addition of five trigger DNA strands at the positions of the red and the green FRET probe. (d,f) Time differences between the transformation occurring at the positions of the green and red FRET probes. The transformation occurs simultaneously at Position 1 and Position 5 and time-delayed at Position 3. (g) Proposed, simplified sketch of the energy landscape of the transformation reaction which is in agreement with the measured time difference distributions. The intermediates at which the studied positions first transform are marked with numbers.

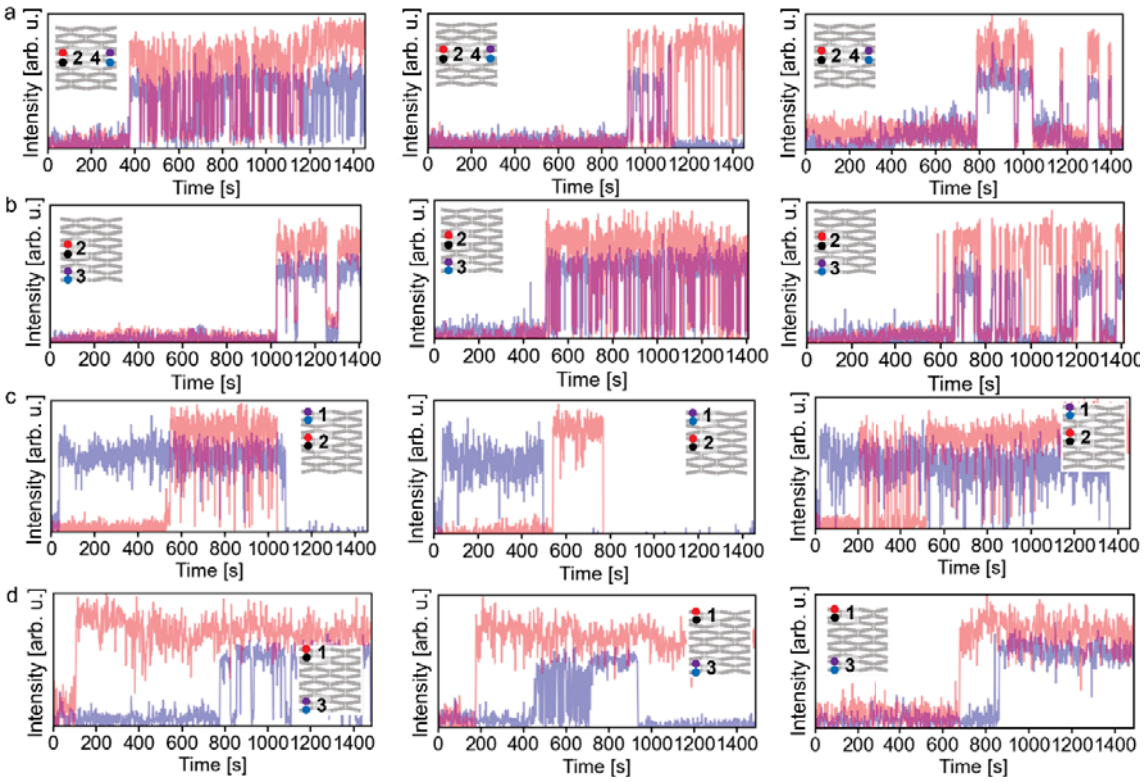

Supplementary Figure 11. Representative single-molecule fluorescence intensity transients of surface-immobilized DNA origami arrays with the red and the green dye-quencher pair incorporated at different positions. (a) Position 4 and Position 2, (b) Position 3 and Position 2, (c) Position 1 and Position 2, (d) Position 1 and Position 3 recorded after addition of the upper four trigger DNA strands at 0 s. Fluorescence of ATTO647N is shown in red, fluorescence of ATTO542 in blue.

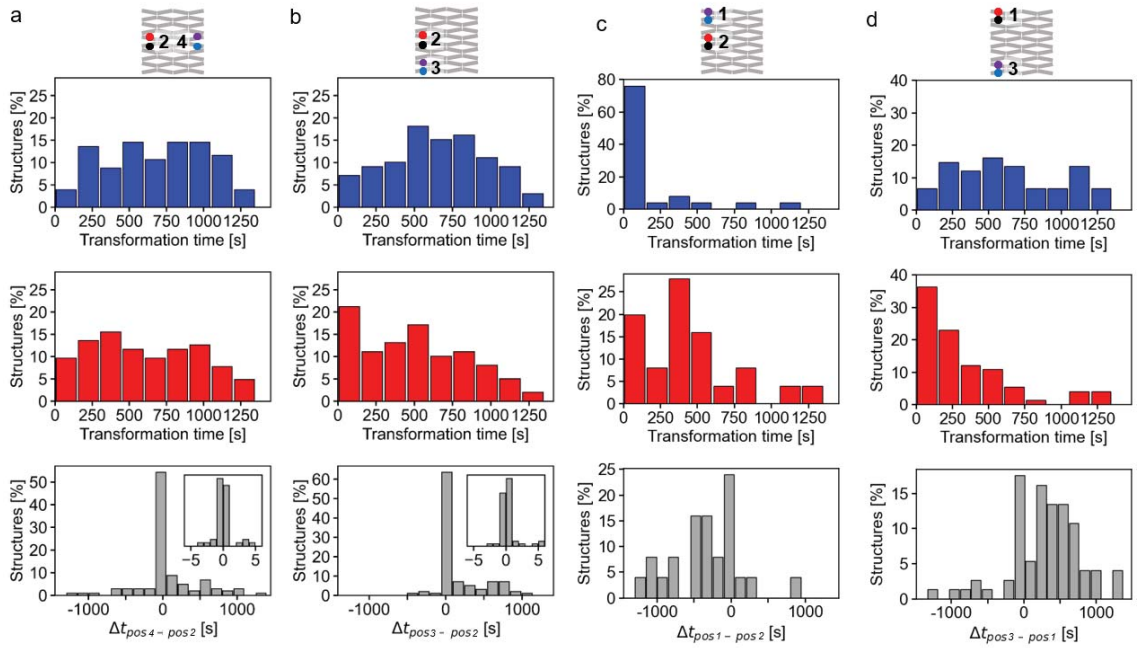

Supplementary Figure 12. Transformation times at the position of the green dye-quencher pair (upper row) and at the position of the red dye-quencher pair (middle row) and time differences between the transformation at the position of the green dye-quencher pair and the position of the red-dye quencher pair after addition of the upper four trigger DNA strands with the dye-quencher incorporated at different positions. (a) Position 4 and 2, (b) Position 3 and 2, (c) Position 1 and 2, (d) Position 3 and 1.

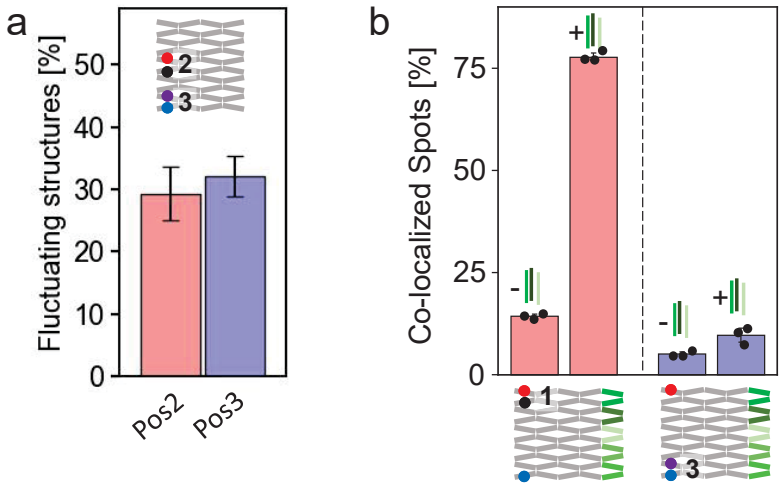

Supplementary Figure 13. Continuous fluctuations and incomplete transformation when reducing the number of trigger DNA strands. (a) Fraction of structures showing intensity fluctuations after 24 h incubation with four trigger DNA strands. Error bars represent the standard error of 82 structures. (b) Fraction of co-localized spots of red and green fluorescence in TIRF images of DNA origami arrays (left) with the red dye-quencher pair incorporated at Position 1 and a green co-localization dye incorporated at Position 3 and (right) with the green dye-quencher pair incorporated at Position 3 and a red co-localization dye incorporated at Position 1 prior and after incubation with the upper three trigger DNA strands for 25 min. For the second origami array, only a small increase in the number of co-localized structures upon incubation with the trigger DNA strands was observed. This indicates incomplete transformation not progressing through Position 3 upon addition of only the upper three trigger DNA strands. Error bars represent the standard deviation in the fractions calculated from three TIFR images (at least 250 single nanostructures per image).

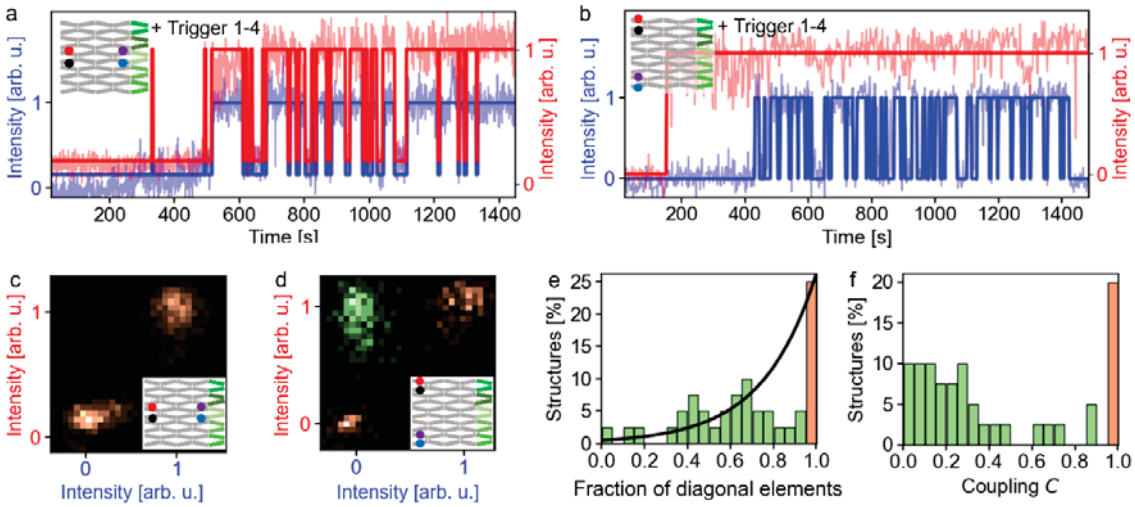

Supplementary Figure 14. Determination of the Coupling C. (a, b) Representative single-molecule fluorescence intensity transients of DNA origami arrays with the red and the green FRET probe incorporated at (a) Position 2 and 4 and (b) Position 1 and 3 of ATTO542 fluorescence (blue transients) and ATTO647N fluorescence (red transient) after addition of the upper four trigger DNA strands. The Coupling of the transformation between two positions in a DNA origami structure is calculated using the transformation state occupancy density plots of the corresponding positions in the structure. (c,d) transformation state occupancy density plots for a system exhibiting (c) $C = 1$ and (d) with $C < 0.95$. In these density plots, the fraction of diagonal elements with respect to the total number of both diagonal and off-diagonal elements is determined. (e) Exemplary distribution of the fractions of diagonal elements calculated for the structures shown in (b). The Coupling between two positions in a system is calculated by weighing the fraction of diagonal elements with the exponential distribution $C = \exp\left(-4\,(1 - \text{fraction})\right)$ shown by the black line. This separates perfectly coupled systems ($C = 1$) from slightly uncoupled systems. (f) Resulting Coupling distribution for the data shown in (e). The fraction of structures exhibiting full coupling is indicated by an orange bar.

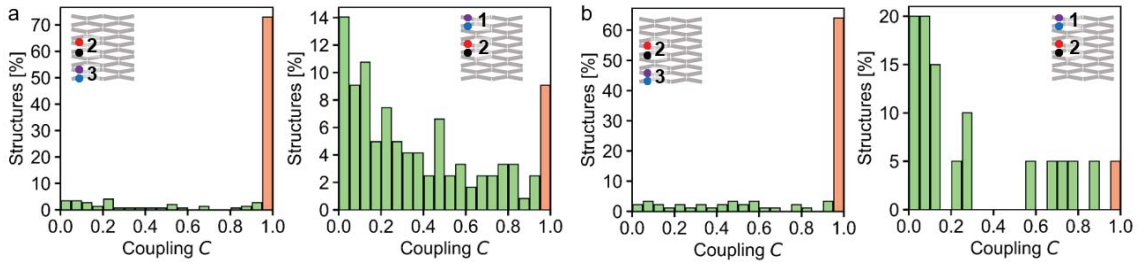

Supplementary Figure 15. Coupling histograms for the dye quencher pairs at different positions upon the addition of different numbers of trigger DNA strands. (a) all five trigger DNA strands and (b) only the upper four trigger DNA strands.

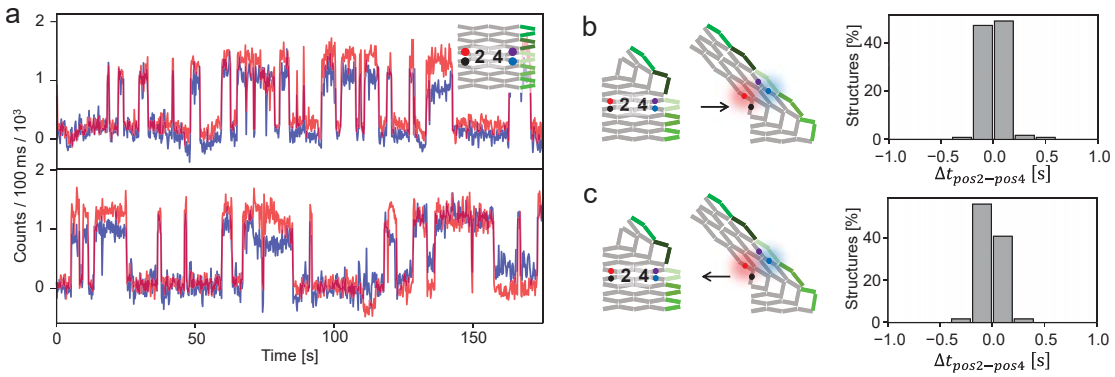

Supplementary Figure 16. Transformation time differences between Position 2 and Position 4 measured with an improved temporal resolution of 200 ms. (a) Representative single-molecule fluorescence intensity transients of DNA origami array structures with the red and green FRET probe at Position 2 and Position 4, respectively. The transients were recorded 10 min after addition of the upper four trigger DNA strands with alternating laser excitation (ALEX) of the green and the red laser (100 ms per frame), resulting in an improved temporal resolution of 200 ms. (b, c) Sketch of (a) the forward and (b) the reverse reaction of the transformation process occurring at both Position 2 and Position 4 (left) and the corresponding time differences between the reactions occurring at the corresponding positions (right). The time difference distributions are binned according to the experimental temporal resolution. They show that both the forward and the reverse transformation occurs in consecutive frames of the ALEX illumination scheme at the studied positions in > 96% of all cases, indicating that the studied transformation steps occur (quasi)simultaneous also at an improved temporal resolution of 200 ms. For calculation of the time difference histograms more than 100 forward and more than 100 reverse fluctuations were analyzed.

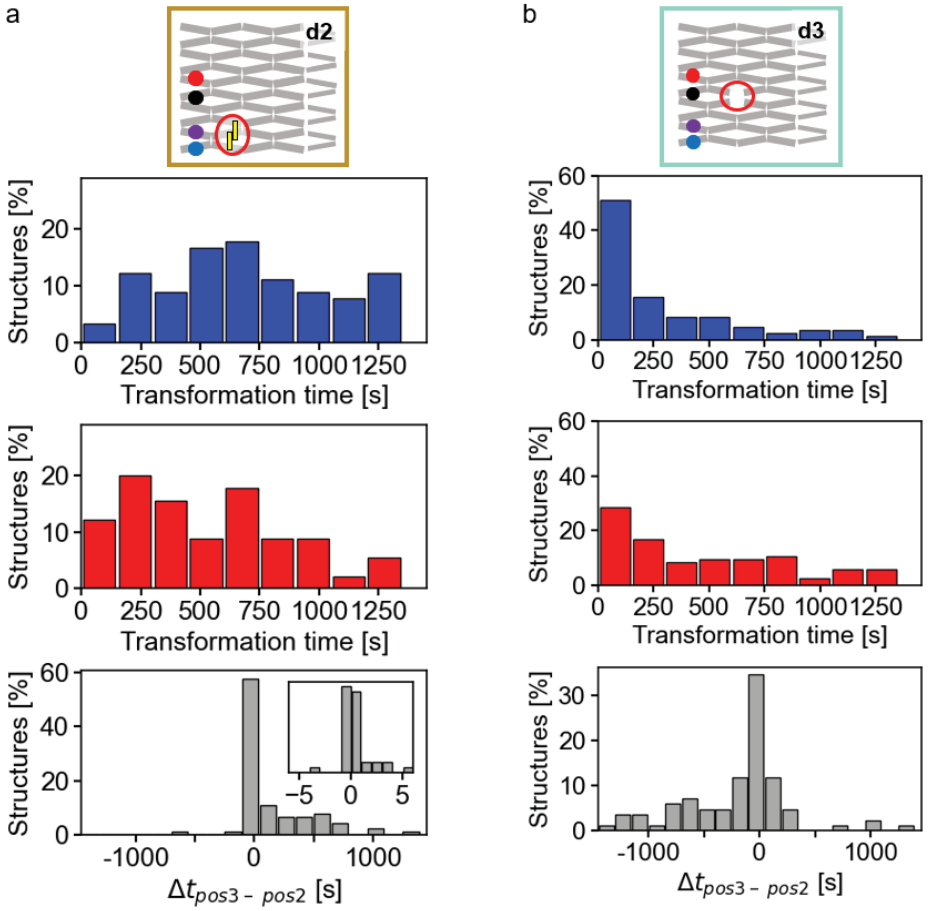

Supplementary Figure 17. Transformation times at the position of the green dye-quencher pair (upper row) and at the position of the red dye-quencher pair (middle row) and time differences between the transformation at the position of the green dye-quencher pair and the position of the red-dye quencher pair after addition of all five trigger DNA strands with the dye-quencher pairs incorporated Position 3 and Position 2 to different DNA origami array constructs. (a) DNA origami arrays with a locking unit incorporated and (b) DNA origami arrays with missing staples at an anti-junction (red circle). For determination of the mean time differences shown in Figure 4c only non-perfectly coupled structures with $\Delta t \neq 0$ s were considered.

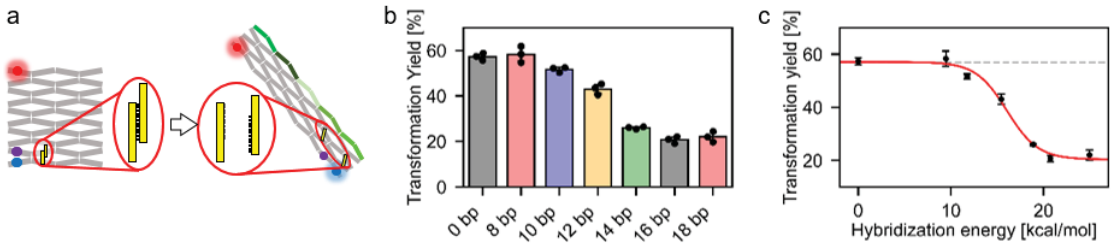

Supplementary Figure 18. Energy transport efficiency at the position of the locking unit. (a) Origami design for determining the energy transport efficiency. We systematically varied the number of hybridizing base pairs of the locking unit and thus its hybridization energy and then determined the transformation yield at the lower left position (Position 3). For colocalization, we additionally placed an AT647N dye at Position 1. (b) Transformation yields after 25 min incubation with five trigger DNA strands at the lower left position (Position 3) for different numbers of hybridizing base pairs in the locking unit. Transformation yields were determined from TIRF images by dividing the number of colocalized red-green spots by the total number of red spots. (c) Transformation yield as a function of the hybridization energy of the locking unit. The data points were fitted by a logistic function (red curve) to determine the hybridization energy at which 50% energy transfer occurs within 25 min as 16.0±0.5 kcal/mol. The grey dashed line represents the fraction of co-localized spots in an origami with a 0 bp locking unit folded in its transformed state. Hybridization energies were estimated using NUPACK without considering possible effects of binding the locking unit to the DNA origami array scaffold.[2] Error bars in (b,c) represent the standard deviation in transformation yield of three TIFR images (at least 300 single nanostructures per image).

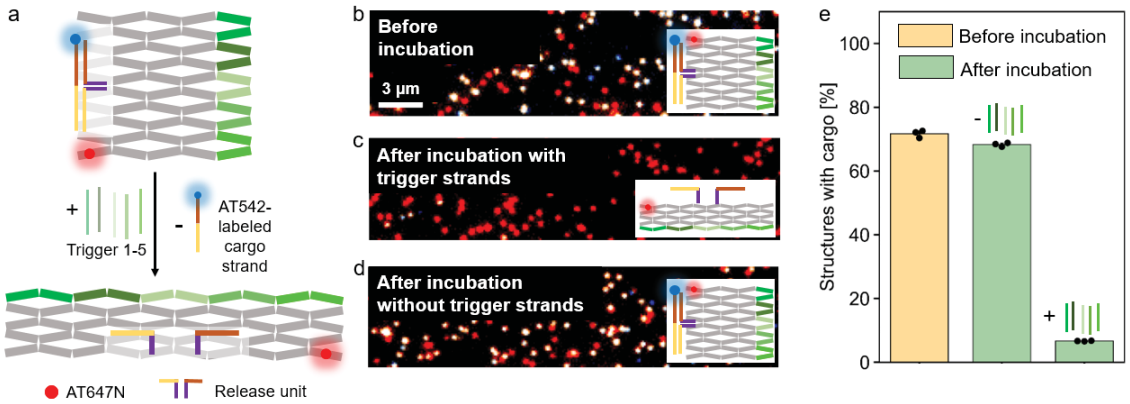

Supplementary Figure 19. Cargo release. (a) Scheme of the procedure of cargo release. (b) TIRF image of the DNA origami array bearing a catching unit after incubation with an ATTO542 labeled cargo strand. (c, d) TIRF images of DNA origami arrays carrying ATTO542 labeled cargo strand after 25 min incubation (c) without and (d) with all five trigger DNA strands. (e) Corresponding fractions of DNA origami array structures carrying a cargo DNA strand. Error bars represent the standard deviation in the fractions calculated from three TIFR images (at least 300 single nanostructures per image).

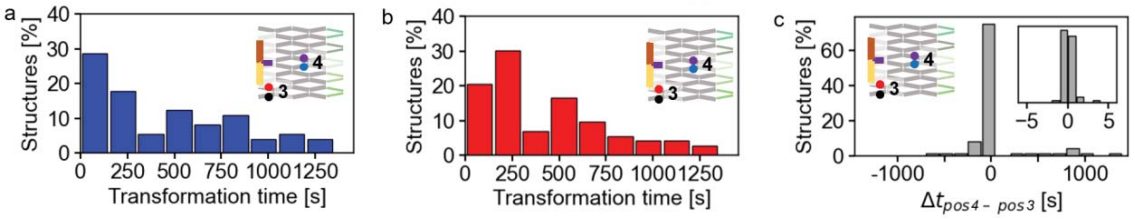

Supplementary Figure 20. Transformation of DNA origami arrays with an incorporated cargo release unit and the green dye-quencher pair incorporated at Position 4 and the red dye-quencher pair at position 3. (a, b) Transformation time at the position of (a) the green dye quencher pair and (b) the red dye-quencher pair. (c) Time difference between the transformation occurring at the positions of the green and red dye-quencher pairs.

Supplementary Notes

Supplementary Note 1. Temporal and spatial controlled proximity-induced reactions in DNA origami array structures. Temporally and spatially controlled proximity-induced reaction cascades could find exciting applications e.g. in a cargo release process. For this, a cargo release unit was positioned on the DNA origami array structure at Position 2.

The cargo release unit is formed by two DNA strands protruding from the DNA origami array on neighboring helices. They contain a 6-nt complementary sequence which forms a stem followed by a 10-nt non-complementary sequence on each strand to which an ATTO542-labelled single-stranded DNA strand containing a 20-nt complementary sequence can permanently hybridize (Supplementary Figure 19a). Due to the opening of the stem, the distance between the arms of the catching unit becomes too large to enable a permanent binding of the cargo strand to both arms and the cargo is released. Thus, the release of the cargo strand could be initiated by addition of trigger DNA strands and performed at the pre-programmed position in the transformation cascade. The unbinding of the cargo strand was detected in single-molecule TIRF images (Supplementary Figure 19b-d) where white spots of co-localized fluorescence of ATTO647N and ATTO542 are attributed to DNA origami structures with a bound cargo release strand while red spots of ATTO647N fluorescence indicate the presence of DNA origami array structures bearing no cargo strand. Blue spots of ATTO542 fluorescence were attributed to non-specific bound cargo strands or DNA origami array structures with a bound cargo and an unlabeled ATTO647N DNA strand. After 25 min incubation with trigger DNA strands the number of co-localized spots decreased drastically (see Supplementary Figure 19c) while only a slight drop in the number of co-localized spots was observed upon incubation without trigger strands (Supplementary Figure 19d). Quantification (Supplementary Figure 19e) confirmed the specific nature of cargo release strand unbinding initiated by the transformation process. Interestingly, the introduction of the cargo release process did not induce a time delay between the FRET probes framing the cargo release unit (see Supplementary Figure 20).

Sequence of the p1800 scaffold used to fold the DNA origami array structure from 5' to 3' end:

TACGAAGAGTTCCAGCAGGGATTCCAAGAAATGGCCAATGAAGATTGGATCAC
CTTTCGCACTAAGACCTACTTGTTTGAGGAGTGCCTGATGAATTGGCACGACCG
CCTCAGGAAAGTGGAGGAGCATTCTGTGATGACTGTCAAGCTCCAATCTGAGG
TGGGCAAATATAAGATTGTTATCCCTATCTAGAAGTACGTCCGCGGAGAACACC
TGCCACCCGATCACTGGCTGGATCTGTTACGCTTGCTGGGTCTGCCTCGCGGC
ACATCTCTGGAGAAACTGCTGTTCGGTGACCTGCTGAGAGTTGCCGATACCATC
GTGGCCAAGGCTGCTAACCTGAAAGATCTGAACTCACGCGGCCAGGGTGAAGT
GACCATCCGCGAATAACTCAGGGAACTGGATTTGTGGGGCGTGGGTGCTGTGT
TCACACTGATCGGCTATGAGGACTCCCAGAGCCGCACCTAGAAGCTGATCAAG
GATTGGAAGGAGCTCGTCAACCAGGTGGGCGACAATATATGCCTCCTGCAGTC
CTTGAAGGACTCACCATACTATAAAGGCTTTGAAGACAAGGTCAGCATCTGGGC
AAGGAAACTCGCCGAACTGGACGATAATTTGCAGAACCTCAACCATATTCGCAG
AAAGTGGGTTTACCTCGAACCATACTTTGGTCGCGGAGCCCTGCCCAAAGAGC
AGACCAGATTCAACAGGGTGGGCGAAGATTTCCGCAGCATCATGACATATATCA
AGAAGGACAATCGCGTCACGCCCTTGACTACCCACGCAGGCATTCTAAACTCA
CTGCTGACCATCCTGGACCAATTGCAGAGATGCCAGCGCAGCCTCAACGAGTT
CCTGGAGGCGAAGCGCAGCGCCTTCCCTCGCTTTAACTTCATCGGAGACGATG
ACCTGCGCGAGATCTTGGGCCAGTCAACCAATTAATCCGTGATTCAGTCTCACC
TCAAGAAGCTGTTTGCTGGTATCAACTCTGGCTGTTTCGATGAGAAGTCTAAGC
ACTATACTGCAATGAAGTCCTTGGAGGGGCAAGTTGTGCCATTCAAGAATAACG
TACCCTTGTCCAATAACGTCGAAACCTGGCTGAACGATCTGGCCCTGGAGATG
AAGAAGACCCTGGAGGCGCTGCTGAAGGAGTGCGTGACAACTAGACGCAGCT
CTCAGGGAGCTGTGGGCCCTTCTCTGTTCCCATCACAGATCTAGTGCTTGGCC
GAACAGATCAAGTTTACCGAAGATGTGGAGAACGCAATTAAAGATCACTCCCTG
CACCAGATTGAGTAACAGCTGGTGAACAAATTGGAGCAGTATACTAACATCGAC
ACATCTTCCGTAGACCCAGGTAACACAGAGTCCGGTATTCTGGAGCTGAAACTG
AAAGCACTGATTCTCGACGGATCCACGCGCCCTGTAGCGGCGCATTAAGCGCG
GCGGGTGTGGTGGTTACGCGCAGCGTGACCGCTACACTTGCCAGCGCCCTAG
CGCCCGCTCCTTTCGCTTTCTTCCCTTCCTTTCTCGCCACGTTCGCCGGCTTTC
CCCGTCAAGCTCTAAATCGGGGGCTCCCTTTAGGGTTCCGATTTAGTGCTTTAC
GGCACCTCGACCCCAAAAAACTTGATTTGGGTGATGGTTCACGTAGTGGGCCA
TCGCCCTGATAGACGGTTTTTCGCCCTTTGACGTTGGAGTCCACGTTCTTTAAT
AGTGGACTCTTGTTCCAAACTGGAACAACACTCAACCCTATCTCGGGCTATTCT
TTTGATTTATAAGGGATTTTGCCGATTTCGGGGTACC

Supplementary References

(1) Jahnke, K.; Grubmüller, H.; Igaev, M.; Göpfrich, K. Choice of fluorophore affects dynamic DNA nanostructures. *Nucleic Acids Res* **2021**, *49* (7), 4186–4195. DOI: 10.1093/nar/gkab201.

(2) Zadeh, J. N.; Steenberg, C. D.; Bois, J. S.; Wolfe, B. R.; Pierce, M. B.; Khan, A. R.; Dirks, R. M.; Pierce, N. A. NUPACK: Analysis and design of nucleic acid systems. *Journal of computational chemistry* **2011**, *32* (1), 170–173. DOI: 10.1002/jcc.21596.

8.3 Associated Publication P3

Spring-loaded DNA origami arrays as energy-supplied hardware for modular nanorobots

by

Martina Pfeiffer[1], **Fiona Cole[1]**, Dongfang Wang[1], Yonggang Ke[*] and Philip Tinnefeld[*]
([1] These authors contributed equally, [*] Correspondence)

Submitted to Science Robotics

Preprint available on BioRxiv
DOI: 10.1101/2024.09.30.615428

Author contributions:
I proposed the initial idea of the project together with Martina Pfeiffer. The initial origami design and scaffold were provided by Dongfang Wang. Martina Pfeiffer designed the input responsive units and the output units, performed the corresponding measurements and analyzed the data. I designed the Boolean logic gates and the signal amplification, performed the corresponding measurements and analyzed the data. I designed, measured and analyzed the combination of multiple inputs with logic gating and multiple temporally controlled outputs together with Martina Pfeiffer. I wrote the manuscript together with Martina Pfeiffer and Philiip Tinnefeld. The project was supervised by Philip Tinnefeld and Yonggang Ke.

Spring-loaded DNA origami arrays as energy-supplied hardware for modular nanorobots

Martina Pfeiffer[1,4], Fiona Cole [1,4], Dongfang Wang [2,3,4], Yonggang Ke [2*] and Philip Tinnefeld [1*]

[1] Department of Chemistry and Center for NanoScience, Ludwig-Maximilians-Universität München, Butenandtstr. 5-13, 81377 München, Germany

[2] Wallace H. Coulter Department of Biomedical Engineering, Emory University and Georgia Institute of Technology, Atlanta, GA 30322, USA

[3] School of Biomedical Engineering and Suzhou Institute for Advanced Research, University of Science and Technology of China, Suzhou 215123, China

[4] These authors contributed equally

* Correspondence: philip.tinnefeld@cup.uni-muenchen.de, yonggang.ke@emory.edu

Summary

DNA origami nanorobots allow for the rational design of nanomachines that respond to environmental stimuli with preprogrammed tasks. To date, this mostly is achieved by constructing conformational two-state switches which upon activation change their conformation resulting in the performance of an operation. Their applicability however is often limited to a single, specific stimuli – output combination due to their intrinsic properties as two-state systems only. This makes expanding them further challenging. Here, we address this limitation by introducing reconfigurable DNA origami arrays as networks of coupled two-state systems. This universal design strategy enables the integration of various operational units into any two-state system within the nanorobot, allowing it to process multiple stimuli, compute responses using multi-level Boolean logic and execute a range of operations with controlled order, timing, and spatial position. We anticipate this strategy will be instrumental in further developing DNA origami nanorobots for applications in various technological fields.

Introduction

Over the last decades, the DNA origami technique[1,2] has emerged as an indispensable tool for designing devices capable of emulating functions and properties of naturally occurring machines on the nanoscale and beyond that, increasingly perform robotic tasks such as sensing, computing and actuating.[3–8]

DNA origami involves the folding of a long single-stranded scaffold strand into a custom shape by up to hundreds of oligonucleotide “staple” strands. Most current DNA origami nanodevices are designed and optimized to perform a specific operation such as cargo release[4,7–9], a rotational motion[3,10,11] or a chemical reaction[5,12] after sensing chemical or physical stimuli[13]. This is often achieved by inducing a single, relatively simple conformational change in the nanodevice, causing it to act as a two-state switch whose operation may optionally include simple AND or OR[6,7] gate logics. The conformational change alters the proximity of interacting players of the operational parts of the nanodevice, resulting in the performance of a defined operation. However, the fact that this concept is based on a single conformational change makes expanding it further challenging. For the realization of more sophisticated nanodevices capable of autonomously performing a series of operations in response to different combinations of environmental stimuli, so far no general concept exists.

Here, we present the DNA origami nanorobot platform SEPP (for **S**erial **E**xecution of **P**rogrammable **P**rocesses) that uses a reconfigurable DNA origami array system composed of multiple, structurally similar blocks – so-called antijunctions as basis for multistep operations (Fig. 1a,b).[14–16] Antijunctions are small symmetric constructs containing four DNA duplex domains of equal length which are pairwise stacked as well as four dynamic nicking points. They exist in two stable conformations with reversed stacking order between which they can switch via an instable open conformation.[14] In reconfigurable DNA origami arrays, multiple antijunctions are coupled to each other by the scaffold strand which threads through the whole system. It interconnects the individual antijunctions and forces them to all adapt the same conformation. Induced by the hybridization of fuel DNA strands to certain antijunctions at the edge of the structure, the conformation of the whole system can be reconfigured in a diagonal stepwise manner (Fig. 1b). In each of the steps, a row of antijunctions in the system undergoes a conformational change, ultimately resulting in the reconfiguration of the whole structure. Full reconfiguration of DNA origami arrays generally was used to activate different proximity-induced operations[17,18] such as the onset of catalytic activity[19], the performance of different pattern operations involving writing, erasing and shifting[20], the generation of an optical output signal[17], or the release of cargo DNA strands[21]. However, these stimuli did not target the conformation of a specific antijunction in the system. They rather targeted the overall conformation of the system itself disregarding the potential of its intermediates and reducing it to a simple two-state switch.

In contrast, SEPP interprets reconfigurable DNA origami arrays as two-dimensional networks of coupled two-state switches represented by their individual antijunctions.

SEPP builds on previous studies that uncovered the energy landscape of the reconfiguration process (Fig. 1c)[14,15,21] and showed how – by incorporation of energy barriers – the coupling between different antijunctions is rationally altered to retard or even fully stop the reconfiguration at a specified intermediate step.[21] In our approach, a reconfigurable DNA origami array constitutes the "hardware" of a DNA nanorobot which can be programmed by a software framework described in this work (Fig. 1d).

With its individual antijunctions, the hardware provides a set of nodes with known connectivity given by the network's energy landscape as well as a defined starting point. With the fuel DNA strands, the hardware also provides an energy source to create a spring-loaded allosteric driving force for the nanorobot's autonomous action. In our software framework, each antijunction within the system is considered as a potential input, output or timing node. By subscribing them with a functionality, the energy landscape of the transformation process is altered at the position where the corresponding node changes its conformation.

The universal and rational approach of the combined hardware and software package is demonstrated with different inputs, such as enzyme activities, proteins, DNA and light. The inputs are modularly combined with a range of operations, including cargo release, fluorescence on- and offset and signal amplification to achieve arbitrary input – output combinations on demand (Fig. 1d). Additionally, we highlight how our understanding of both the pathway and energy landscape of the reconfiguration process enables us to implement order dependencies, timing control and multi-level logic gating as well as simplicity of designing antagonistic operations by exploiting the antijunction's symmetric nature (Fig. 1a). As such, this merge of hardware and software promises a new era of versatile nanoscale devices.

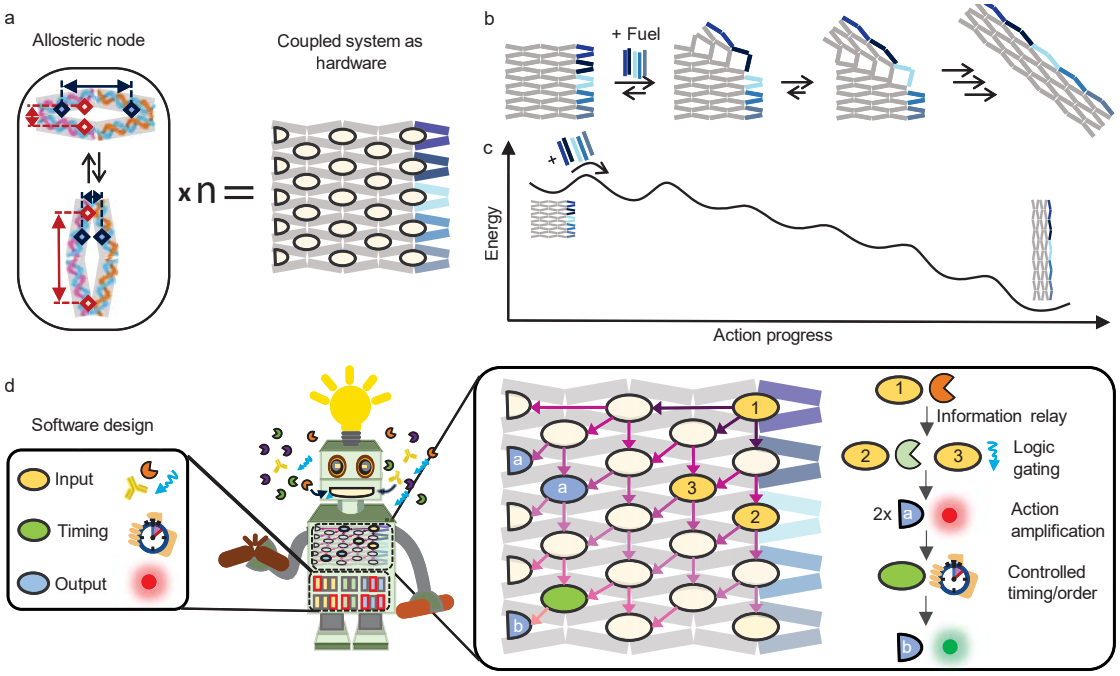

Figure 1: Concept of a modular reconfigurable DNA origami nanorobot. (a) Sketch of multiple allosteric nodes coupled together in a reconfigurable DNA origami array forming the hardware of the design of the nanorobot. The nodes are indicated by ellipses at the corresponding positions in the DNA origami array. The basis unit of an allosteric node is a so-called anti-junction which switches between two conformational states (left). Due to the symmetric nature of the antijunction, the switching can be used to both increase (red) and decrease (dark blue) the distance between markers placed on the antijunction depending on which domains they are placed on. (b) Sketch of the reconfiguration process of the unmodified DNA origami array structure upon hybridization of fuel DNA strands (blue lines) to the right side of the structure. (c) Simplified sketch of the energy landscape of the multistep reconfiguration process.[21] (d) The software of the designed nanorobot is formed by developing generalized strategies to encode environmental responsiveness to different target, timing, and output operations into single allosteric nodes (left panel). The nanorobot is then formed by programming different nodes of the DNA origami array hardware with the software (middle panel). The arrows hereby represent the connectivity between the different units given by the energy landscape of the hardware. This enables the robot to respond autonomously to targets in its environment in a pre-programmed, multistep manner (right panel).

Results

SEPP is based on a small reconfigurable DNA origami array structure composed of 5 x 2.5 antijunctions[14] that can be transformed by hybridizing five fuel DNA strands to the right side of the structure (Fig. 1a, b).[21] The transformation process is characterized by five intermediates (Fig. 1c). Our software framework targets the energy barriers between these intermediates and the start and the end point of the transformation. To characterize SEPP at the single-molecule level with fluorescence microscopy, we additionally incorporate dye-quencher pairs for reporting on the state of individual antijunctions and a biotinylated ssDNA for surface-immobilization on BSA-biotin/Neutravidin coated cover slips (Supplementary Fig. 1).

Design of environmental-responsive input nodes

Environmental responsiveness is encoded into the antijunction nodes by the introduction of locking units which stabilize one conformation of the targeted node over the other. This results in an energetic bias either hindering or favoring the transformation of the whole array (Fig. 2a). By varying the number of added fuel DNA strands, we spring-load the array system with varying degrees of tension and adjust the energy levels of the untransformed and transformed state of the array to lie close together such that presence of (multiple) locking units becomes the decisive factor for the transformation to occur. In presence of the corresponding environmental input, the units are unlocked and the energetic bias is removed, resulting in the release of the stored tension and an activation or inhibition of the transformation process, respectively. Based on this principle, we design locking units responsive to single-stranded DNA (ssDNA), restriction enzyme activity, light and antibodies (Fig. 2, Supplementary Fig. 2-4).

For ssDNA as an input, locking units are formed by two ssDNA strands protruding from two domains of the targeted antijunction nodes. The ssDNA strands contain a complementary section which hybridizes when both domains are in close proximity. Depending on which domains they are placed on, hybridization of the strands occurs either in the untransformed or transformed conformation of the nodes (Fig. 2b, upper and lower panel), resulting in their energetic stabilization. To enable unlocking, one of the protruding ssDNA strands is designed with a toehold overhang. This allows for unlocking by toehold-mediated strand displacement with a ssDNA input.

The successful implementation of the ssDNA locking units is verified using a fluorescence onset unit placed on an antijunction node transforming downstream in the transformation process. The fluorescence onset unit reports on the conformational state of the node it is placed on (Fig. 2b). It is based on a red dye-quencher probe (ATTO647N – IowaBlackRQ) positioned on two different domains of an antijunction node which are in close proximity in the untransformed state of the antijunction node. The increase in distance between these domains caused by the transformation of the corresponding node results in an increased fluorescence signal of the dye molecule. This allows to distinguish the

untransformed from the transformed state of the node. We additionally incorporate an ATTO542 dye into the arrays and quantified the fraction of arrays in their transformed state (transformation yield) from dual-color single-molecule TIRF images of surface-immobilized array structures collected in absence and presence of the ssDNA input (Fig. 2c, Materials and Methods).

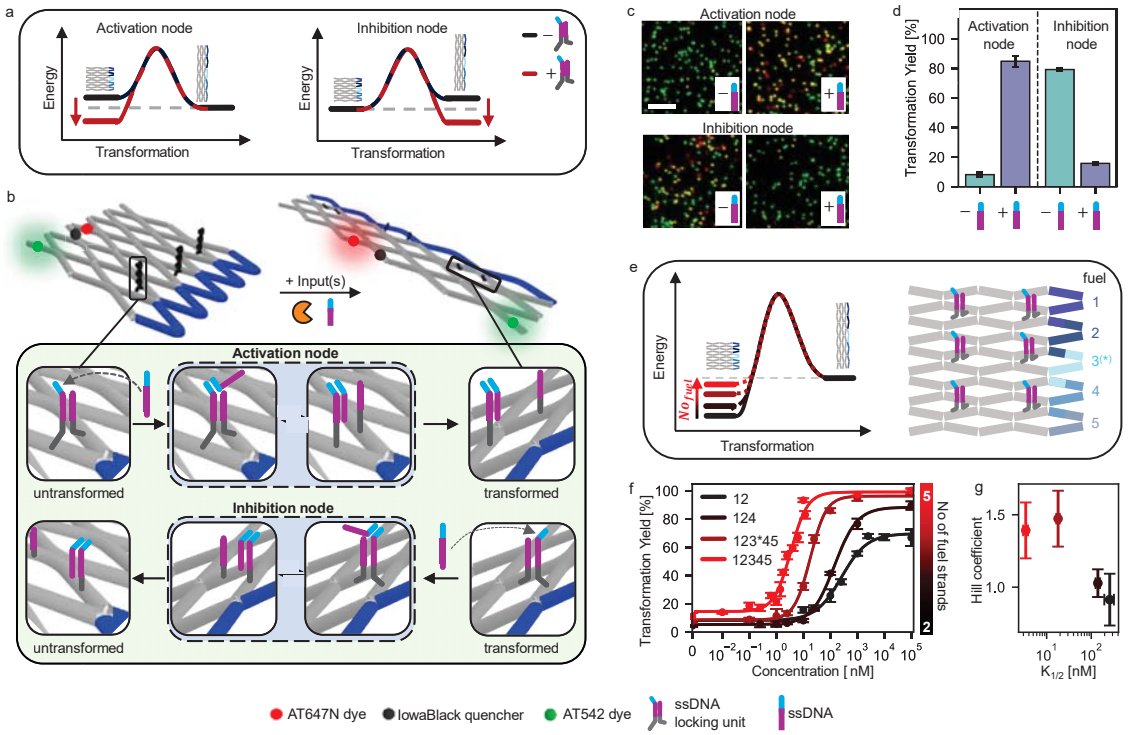

Figure 2. Environmentally responsive activation and inhibition nodes. (a) Energy schemes showing the influence of a locking unit in activation and inhibition nodes on the transformation process. In presence of their inputs, this effect is nullified. The energy schemes in absence of the locking units are programmed priorly by adding different combinations of fuel DNA strands. (b) Sketch of the DNA origami nanorobot bearing environmentally responsive nodes, a red dye-quencher FRET pair (ATTO647N-IowaBlackRQ) reporting on the state of the nanorobot and a green dye (ATTO542) for co-localization (upper panel). Nodes responsive to ssDNA activating and inhibiting the transformation are based on a reversible dsDNA lock which is unlocked via a toehold-mediated strand displacement reaction with a ssDNA input (lower panel). (c) Exemplary TIRF images of DNA origami nanorobots bearing ssDNA-responsive activation and inhibition nodes after incubation with fuel DNA strands 1,2 and 1,3* respectively and without and with the ssDNA input. (d) Corresponding transformation yields. (e) Strategy for tuning the responsive concentration window of the ssDNA input. (left) Increasing the number of added fuel DNA strands increases the tension in the spring-loaded system, resulting in a destabilization of the untransformed state of the array. (right) Employed DNA array system with six ssDNA locking units incorporated. The hybridization positions of fuel strands 1-5 are marked with color. Fuel strand 3* represents a shortened version of fuel strand 3. (f) Increasing the number of added fuel DNA strands from strands 1,2 over 1,2,4 and 1,2,3*,4,5 to 1,2,3,4,5, shifts the responsive window. (g)

Impact of the number of added fuel DNA strands on $K_{1/2}$ and the Hill coefficient. Error bars in (d,f) represent the standard deviation in the transformation yields calculated from at least three TIRF images. Error bars in (g) represent the fit error to the curves fitted in (f). Scalebar: 4 µm.

With a transformation yield of 10%, arrays with three ssDNA activation nodes incorporated and fuel DNA strands 1-2 are predominantly in their untransformed state in absence of ssDNA input. Upon addition of ssDNA input, the arrays transform, resulting in an increased transformation yield of 83%. In contrast, arrays with three ssDNA inhibition nodes incorporated and fuel DNA strand 1,3* show transformation yields of 80% and 16% in absence and presence of ssDNA input, demonstrating the antagonistic usability of the same DNA locking unit with near quantitative responses (Fig. 2d). As this process is reversible (Supplementary Fig. 5), our control over the energy landscape of the system provides additional access to tune the location ($K_{1/2}$) and width of the responsive concentration window towards the ssDNA input without modifying the ssDNA locking unit itself. When incorporating six ssDNA activation units into the array, increasing the number of added fuel DNA strands from two to five leads to an increased mechanical strain exerted on the untransformed conformation of the array (Fig. 2e). This results in an over 75-fold decrease in $K_{1/2}$ (from 260±60 nM to 3.4±0.4 nM) while simultaneously increasing the Hill coefficient from 0.9±0.2 to 1.4±0.2 and thus narrowing the responsive concentration window (Fig. 2f-g). Reducing the number of incorporated ssDNA activation units and replacing one of the ssDNA activation units with different units, introduces additional tuning strategies for the responsive window and allows shifting $K_{1/2}$ down to 0.08±0.02 nM (Supplementary Fig. 6). In combination, all strategies allow shifting $K_{1/2}$ over 3000-fold without modifying the ssDNA locking unit itself.[6] This promises a good adaptability of these tuning strategies towards other inputs without the need for re-engineering the input-responsive locking units to create different affinities towards the inputs.

We then demonstrate the simple adaptability of our universal design approach towards other inputs. The designs of input nodes responsive to restriction enzyme activity and light are based on ssDNA locking units containing an enzyme-specific restriction site and a photocleavable linker, respectively. The locks are cleaved in presence of active restriction enzyme or light of a specified wavelength, effectively unlocking them (Supplementary Fig. 2, 3). When implemented as activation nodes in DNA array systems, they responded specifically to their respective inputs (XhoI, StuI and BamHI restriction enzyme and light of 365 nm) by transforming quantitatively only in their presence (Supplementary Fig. 2, 3) after addition of fuel DNA strands which can also be pre-loaded onto the structure (Supplementary Fig. 7). We further extend SEPP's spectrum of inputs to proteins which do not directly interact with DNA by designing an input unit responsive to IgG antibodies and demonstrating its application in inhibition nodes (Supplementary Fig. 4).

Computation based on Boolean logics

In the design of our locking units, the presence of a single unit alone does not suffice to quantitatively initiate or inhibit the transformation process when the arrays are spring-loaded with all five fuel DNA strands (Supplementary Note 1, Supplementary Fig. 8). This design anticipates the rational creation of computation schemes, thus providing the ability to respond to diverse input combinations in a pre-programmed manner. We systematically characterize the impact of restriction enzyme locking units positioned at different nodes, both individually and in combinations (Fig. 3a, Supplementary Fig. 8). Notably, when comparing the effects of the same locking unit positioned at two different nodes in an otherwise identical design, we observe significant differences in the obtained transformation yields (Fig. 3a). When the locking unit is positioned at a node transforming during the first step of the transformation process, the transformation is inhibited. In contrast, placing the unit at a node transforming during the fourth step results in an increased transformation yield of 70%. This finding aligns with the profile of the energy landscape of the transformation process and is also consistent with all other studied locking unit combinations (Supplementary Note 1, Supplementary Fig. 8). The tilted profile of the energy landscape indicates a weakened effect of an incorporated locking unit the further downstream the corresponding antijunction node is in the transformation cascade. Using this dependence and placing multiple locking units specific to various inputs at predefined antijunction nodes on the same structure, we establish a computation framework to program responses to diverse input combinations based on Boolean logic gates.

We first implement basic Boolean AND and OR gates responsive to combinations of the restriction enzymes XhoI and StuI. We again use a fluorescence onset unit to confirm the designed responsiveness of the system. For the AND gate, only upon addition of both restriction enzymes a near quantitative transformation of all structures occurs (Fig. 3b, Supplementary Fig. 9) whereas for the OR gate already the addition of one restriction enzyme results in transformation yields of above 80% (Fig. 3c, Supplementary Fig. 9). The applicability of these gates is not limited to inputs of the same molecular class. Our modular design strategy of locking units for example allows the simple exchange of the XhoI locking unit with a light locking unit in the OR gate design while maintaining the functionality of the gate (Fig. 3d, Supplementary Fig. 9). This demonstrates how inputs of different molecular classes can be processed on the same structure in DNA origami arrays using SEPP.

Both the AND and the OR gate designs demonstrate low leakages in all logical FALSE conditions, with the TRUE state providing at least fourfold higher transformation yields in all cases. The low leakages of these basic gates allow expanding the concept further to also include multi-level logic gates. We use the multistep nature of the transformation cascade to – figuratively speaking – create cascades of multiple logic gates and connect them in series. Using the prior characterization of the effect of restriction enzyme locking units at different position as a basis, we design two multi-level logic gates of different complexity: A 3x AND gate which is comprised of two logic AND gates connected in series (Fig. 3e, Supplementary Fig. 10) as well as a gate which only gives a positive response

if at least two of its three inputs are present (Supplementary Fig. 11). We find that both systems provide low leakages in all logical FALSE conditions that were statistically distinguishable from the transformation yields obtained for the TRUE states, demonstrating the successful implementation of the designed gates. Besides logic gating, the modularity offered by SEPP enables multiplexing as an additional pathway to process multiple inputs in parallel (Supplementary Fig. 12).

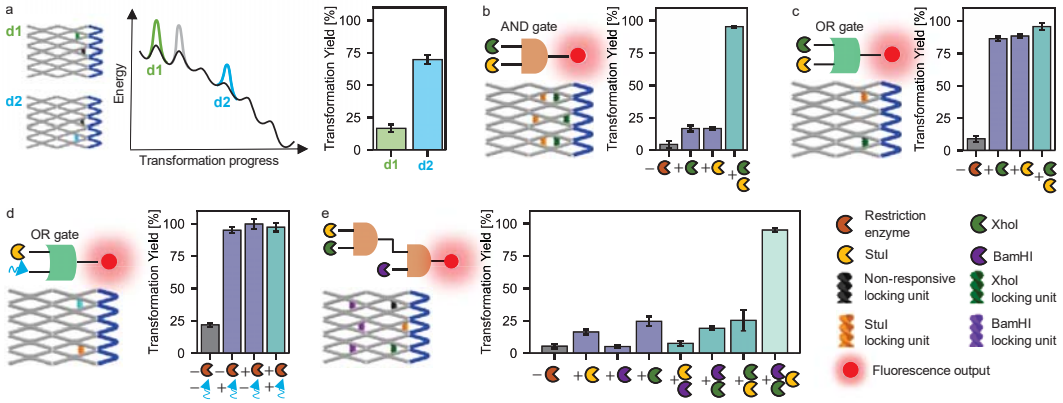

Figure 3. DNA origami array nanorobot processing one- and multi-level Boolean logic gates. One- level and multi-level Boolean logic gates responsive to combinations of restriction enzymes and light are implemented by combining different restriction enzyme/ light locking units and stabilization units. The molecular logic is programmed by the number and position of the incorporated units. Additionally, a red fluorescence onset unit is incorporated for reading out the state of the robot. (a) Comparison of the transformation yields of two array designs. The designs differ only in the position of one locking unit stabilizing the untransformed conformation marked in green (d1) and blue (d2) that target different positions in the energy landscape of the transformation process. The gray locking unit/ energy barrier is present in both designs. (b) Schematic design of a basic logic AND gate responsive to combinations of XhoI and StuI and obtained transformation yields. (c) Schematic design of a basic logic OR gate responsive to combinations of XhoI and StuI and obtained transformation yields. (d) Schematic design of a basic logic OR gate responsive to combinations of StuI and light and obtained transformation yields. (e) Schematic design of a 3xAND gate and obtained transformation yields. Error bars show the standard deviation from the mean. In addition to possible inputs, all DNA origami arrays are incubated with fuel DNA strands 1-5. Error bars represent the standard deviation in the transformation yields calculated from three TIRF images.

Combining logical gated input operations with output operations

The aim of smart nanorobots not only includes programming responses to different input combinations but also the conduction of these responses if the required conditions are met. Beyond simple fluorescence onset units to generate output signals, we next demonstrate different output operations and combine input-responsive locking units with a more complex output operation. As an example, we choose a cargo release unit, which

upon activation releases a fluorescently labelled (ATTO542) cargo DNA strand from the system (Fig. 4a, Supplementary Note 2).[21]

First, we combine the cargo release unit with restriction enzyme locking units specific to the activity of BamHI. Here, the fraction of structures carrying a DNA cargo strand is determined from the colocalization yield with an ATTO647N dye additionally incorporated in the DNA origami.

After assembly, DNA origami arrays near quantitatively carry the cargo DNA strand (Supplementary Fig. 13). Upon incubation with and without enzyme, the fraction of structures carrying the cargo drops from 98% to 75% and 20%, respectively (Fig. 4b-d). While this indicates some unspecific cargo release, the majority of all cargo is only released in presence of the restriction enzyme. We attribute the unspecific loss of the cargo strand to the decreased stability at the incubation temperature of 37 °C (Supplementary Note 2, Supplementary Fig. 13). As we achieved both the implementation of logic gates and variable input-output combinations, we then use the modularity of our system to combine all of the above. We design structures which compute the controlled release of cargo in response to combinations of XhoI and BamHI activity. In both AND and OR logic configuration, a high fraction of cargo is released only when the gate gives a positive response (Fig. 4e,f, Supplementary Fig. 14, 15).

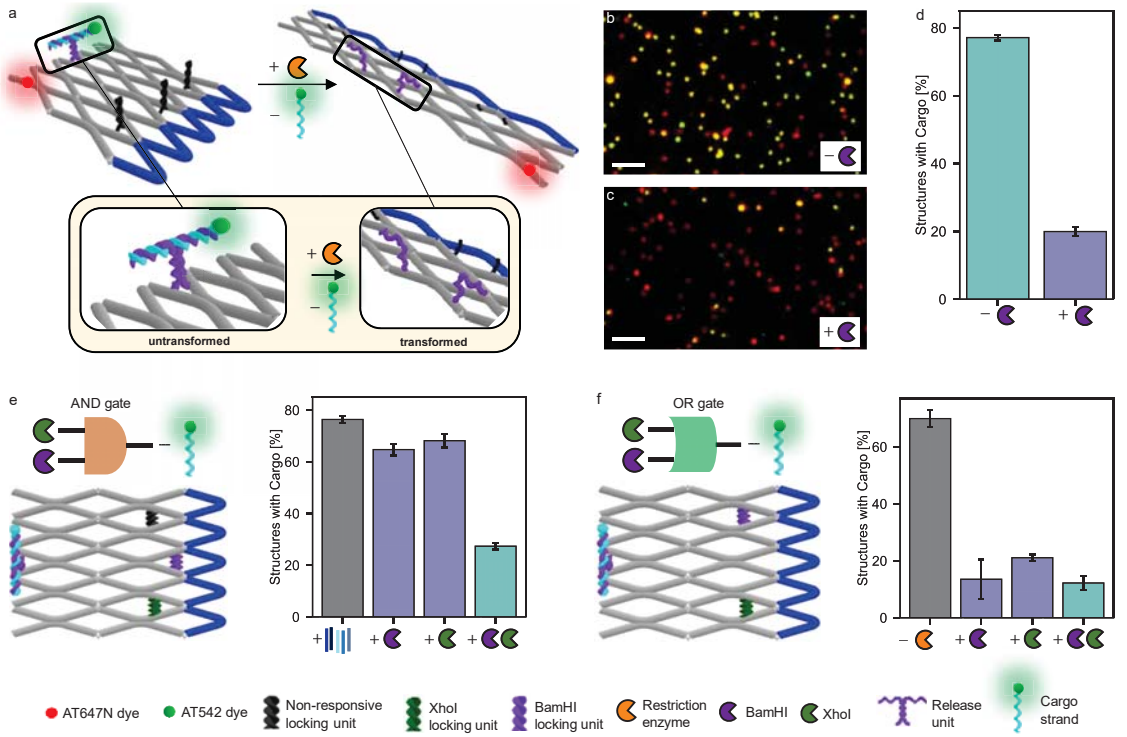

Figure 4. Proximity-induced output operation generated upon molecular inputs by DNA origami array nanorobot. (a) Schematic representation of DNA origami array structures which

release a cargo DNA strand in response to the activity of BamHI. (b,c) TIRF images of the DNA origami array nanodevice after incubation (b) without and (c) with BamHI. (d) Corresponding fractions of DNA origami array nanodevices with a bound cargo DNA strand. (e,f) Schematic representation of DNA origami array nanodevices computing the controlled release of a cargo in response to the presence of combinations of XhoI and BamHI and corresponding fractions of DNA origami array nanodevices with a bound cargo DNA strand for an AND (e) and an OR (f) logic gate. In addition to possible inputs, all DNA origami arrays are incubated with fuel DNA strands 1-5. Error bars represent the standard deviation of the fractions calculated from three TIRF images. Scalebar: 3 μm.

Constructing networks of multiple inputs and outputs

Analogously to the input units, SEPP also enables incorporating multiple output units. This can be used to amplify these outputs as we demonstrate exemplarily for the fluorescence onset unit (Supplementary Fig. 16) or to perform different events consecutively (Supplementary Fig. 17). Here, we use timing units based on a DNA lock to control order and timing between different events.[21,22] Timing units slightly heighten the activation barrier at a certain intermediate step in the transformation cascade, and thus introduce a time lag between operations placed on antijunctions transforming before and after them. We demonstrate this exemplarily by positioning a timing unit between two fluorescence onset units. In absence of the timing unit, the fluorescence onset units light up simultaneously upon activation by restriction enzyme activity. If a timing unit is incorporated, a time lag between both fluorescence onsets is achieved for the majority of all structures. The order in which the fluorescence onset units light up can be reversed by switching the antijunction nodes they are incorporated in (Supplementary Fig. 17).

We then set out to make full use of our designed software framework and combine all developed unit types in a single system, using ssDNA and restriction enzyme input units, fluorescence on- and offset output units (Supplementary Fig. 18) as well as a timing unit (Fig. 5a). In the absence of inputs, SEPP shows only a red fluorescence signal (Fig. 5b,c). Upon activation by a ssDNA input and XhoI restriction enzyme activity combined to a logic AND gate, SEPP switches off the red fluorescent signal (Fig. 5b,c). Depending on whether an additional timing unit is incorporated or not, a green fluorescent signal lights up either after the red fluorescence offset occurs or simultaneous to it (Fig. 5b-g). This good agreement between programmed function and execution exemplifies the control achievable in programmed systems using SEPP.

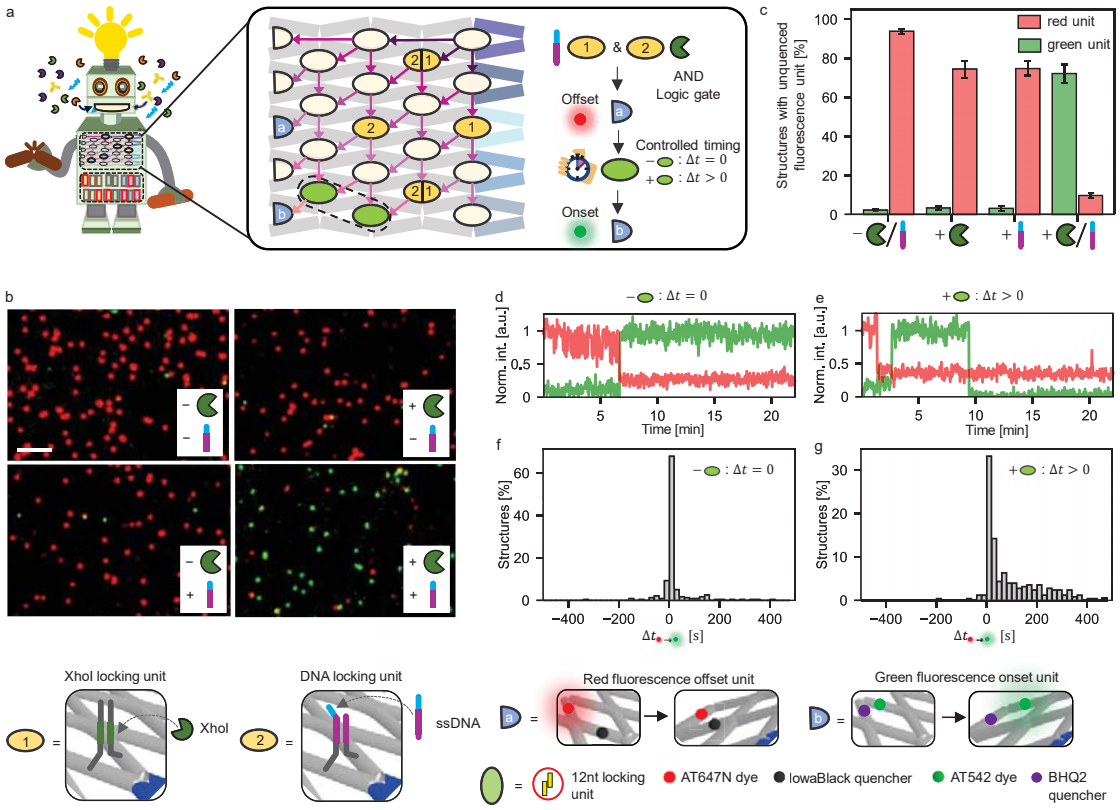

Figure 5. DNA origami array nanorobot performing output operations under temporal control after processing a Boolean logic AND gate based on restriction enzyme activity and ssDNA binding. (a) Schematic design of a DNA origami array nanorobot programmed to perform a series of operations with the corresponding plan of action. (b) TIRF images of the DNA origami array nanorobot after incubation with different combinations of restriction enzyme and/or ssDNA (c) Corresponding fraction of structures with unquenched green and red fluorescence units. Error bars represent the standard deviation in the fractions calculated from three TIRF images. (d,e) Exemplary single-molecule transients for structures without (d) and with (e) a timing unit incorporated. (f,g) Time between the occurrence of the red fluorescence offset and the green fluorescence onset for structures without (f) and with (g) a timing unit incorporated. In addition to possible inputs, all DNA origami arrays are incubated with fuel DNA strands 1-5. Scalebar: 3 μm.

Conclusion

We demonstrate the rational development of DNA origami nanorobots using the network of coupled two-state systems offered by DNA origami arrays as a programmable hardware and fuel DNA strands as energy source which spring-load the system with varying degrees of tension. By designing a software package which defines different units, we show how a wide range of functionalities can be encoded into any of the

network's two-state systems and coupled together through the network's energy landscape. We design input units responsive to ssDNA, light, restriction enzyme activity and antibodies that either activate and/ or inhibit the DNA origami array transformation. By combining multiple units on a single DNA array structure, we develop strategies to tune the responsive input concentration window, shifting $K_{1/2}$ over 3000-fold while evolving cooperativity. We use the same strategy to incorporate Boolean logic gating, creating specific responses for different input combinations, both with inputs of the same and different molecular classes. Subsequently, we demonstrate the potential of the modularity of this software-hardware combination. We program a nanorobot that combines activation by different inputs with Boolean logic gating and a sequence of output operations such as (amplified) fluorescence output or cargo release conducted in a predefined order and under temporal control and demonstrate its proper functionality.

Overall, we expect that expanding our hardware by using different DNA origami arrays and software packages by including further proximity-based operations will be straightforward. Including further input and output software units that – besides the demonstrated cargo release and fluorescence on-/offset – enable e.g. the on-demand onset of catalysis or cargo uptake,[19] will pave the way for a broad range of applications in the fields of clinical diagnosis and – by implementation of arising DNA origami stabilization strategies[23–25] – also therapeutics.

Resource availability

Lead contact

Philip Tinnefeld: Department of Chemistry and Center for NanoScience, Ludwig-Maximilians-Universität München, Butenandtstr. 5-13, 81377 München, Germany. Philip.tinnefeld@cup.uni-muenchen.de

Materials and Methods

Synthesis of DNA origami arrays

DNA origami structures are designed using the open-source software caDNAno2 [26] and assembled and purified using published protocols [27] For the exact sequences of all unmodified and modified DNA staple strands used to fold the DNA origami structures see Supplementary Tables 1-10. DNA staple strands are purchased from Eurofins Genomics GmbH (Germany) and Integrated DNA Technologies (USA).

For DNA origami folding, 10 nM of in house produced p1800 scaffold (Supplementary Note 3) in 1xTAE (400 mM Tris, 400 mM acetic acid, 10 mM EDTA, pH 8) containing 12.5 mM is mixed with a 10-fold excess of all unmodified and a 30-fold excess of all modified

oligonucleotides, respectively. The mixture is heated to 65 °C in a thermocycler and kept at this temperature for 15 min before being cooled down to 25 °C with a temperature gradient of – 1 °C min^{-1}. Folded DNA origamis are purified from excessive staple strands by gel electrophoresis. All gels are ran using a 1.5% agarose gel, 1xTAE containing 12.5 mM $MgCl_2$ for 2 hours at 6 V/cm. The target band containing DNA origami is cut from the gel and DNA origami solution extracted from the band via squeezing.

Sample preparation on the coverslip for single-molecule widefield measurements

For chamber preparation, adhesive SecureSeal™ Hybridization Chambers (2.6 mm depth, Grace Bio-Labs, USA) are glued on microscope coverslips of 24 mm × 60 mm size and 170 µm thickness (Carl Roth GmbH, Germany). The created wells are incubated with 1 M KOH for 1 h and washed three times with 1×PBS buffer. After surface passivation by incubation with BSA-Biotin (0.5 mg/mL, Sigma Aldrich, USA) for 10 min, the surface is washed with 200 µL 1× PBS buffer. 150 µL neutravidin (0.25 mg/mL, Thermo Fisher, USA) is incubated for 10 min and then washed three times with 150 µL 1× PBS buffer. Surface immobilization is achieved via biotin-neutravidin interactions. For this, we incorporate one biotinylated DNA staple strand in the loop of the DNA origami structure during folding. The DNA origami solution is diluted with 1× TE buffer containing 750 mM NaCl to a concentration of ~10 pM and then immobilized on the biotin-neutravidin surface via biotin-neutravidin interactions. For this, 150 µL of the DNA origami sample solution is added and incubated for 5 min. Residual unbound DNA origami is removed by washing the chambers with 150 µL 1x TE buffer containing 750 mM NaCl. The density of DNA origami on the surface suitable for single-molecule measurements is checked on a TIRF microscope. For acquisition of single-molecule fluorescence movies, an oxidizing and reducing buffer system (1x TAE, 12.5 mM $MgCl_2$, 2 mM Trolox/Troloxquinone)[28] is used in combination with an oxygen scavenging system (12 mM protocatechuic acid, 56 µM protocatechuate 3,4-dioxygenase from pseudomonas sp., 1% glycerol, 1 mM KCl, 2 mM Tris HCl, 20 µM EDTA-Na_2*$2H_2O$) to suppress blinking and photobleaching. If not stated otherwise, for acquisition of single TIRF images, no oxidizing and reducing buffer system was added.

Reconfiguration of DNA origami array structures in response to different molecular inputs

ssDNA detection assay

For the detection of ssDNA, DNA origami array structures are folded with ssDNA locking units. After surface-immobilization, 50 nM fuel DNA strands in 1xTE buffer containing 750 mM NaCl and if not stated otherwise 2 uM ssDNA input are added. The samples are incubated at 37 °C for 15 min and dual-color TIRF images recorded. For titration curve measurements, samples are incubated overnight to ensure equilibrium conditions.

Restriction enzyme activity assay

For the detection of restriction enzyme activity, DNA origami array structures are folded with restriction enzyme locking units. 50 nM of all five fuel DNA strands in 1xTAE buffer containing 12.5 mM $MgCl_2$ and 2 µL of XhoI (20,000 units/ml, New England BioLabs, USA), StuI (10,000 units/ml, New England BioLabs, USA) or BamHI (100,000 units/ml, New England BioLabs, USA) are added to surface-immobilized DNA origami samples. To determine transformation yields, the structures are incubated for 15 min at 37 °C and dual-color TIRF images recorded. To measure transformation time distributions (e.g. for the incorporation of timing units), sample chambers are sealed immediately after addition of the enzymes and the photostabilization system and dual-color movies of the DNA origami arrays acquired for 20 min at 37 °C.

Light detection assay

For the detection of light of 365 nm, DNA origami structures are folded with a light-responsive locking unit. 50 nM of all five fuel DNA strands in 1xTAE buffer containing 12.5 mM $MgCl_2$ are added to surface-immobilized DNA origami samples and the samples illuminated with light of 365 nm for 5 min. After subsequent incubation at 37 °C for 15 min, dual-color TIRF images are recorded.

Anti-Dig antibody detection assay

For the detection of anti-Dig antibodies, DNA origami array structures are folded with two Dig recognition elements. 50 nM of fuel DNA strands 1 and 2 in 1xTE buffer containing 750 mM NaCl and 100 nM anti-Dig antibodies (Rb Monoclonal, Thermo Fisher Scientific, cat#: 700772, PRID: AB_2532342) are added to surface-immobilized DNA origami samples. Samples are incubated at 37 °C for 15 min and dual-color TIRF images recorded.

Boolean logic gating and cargo release assays

For the measurement of Boolean logic gates and cargo release, surface-immobilized DNA origami structures are incubated with 50 nM fuel DNA strands 1-5 in 1xTAE buffer containing 12.5 mM $MgCl_2$ and the different restriction enzyme/ light inputs at 37 °C as described above and dual-color TIRF images recorded.

Nanorobot measurement combining multiple inputs with multiple outputs

For the nanorobot measurement which combines multiple inputs with multiple outputs (Fig. 5), surface-immobilized DNA origami array structures are incubated with 50 nM fuel DNA strands 1-5 in 1xTAE buffer containing 12.5 mM $MgCl_2$ and different combinations of 2 uL BamHI/ 2 uM ssDNA at 37 °C as described above. For determining the fraction of structures with unquenched fluorescent units, dual-color TIRF images are recorded after 15 min incubation time. For determining the time delay between the red fluorescence offset and the green fluorescence onset, sample chambers are sealed immediately after addition of both inputs and the photostabilization system and dual-color movies of the DNA origami arrays acquired for 20 min at 37 °C.

Wide-field measurements

For detection of single-molecule fluorescence, a commercial wide-field/TIRF microscope Nanoimager from Oxford Nanoimaging Ltd. is used. Red excitation at 638 nm is realized with a 1100 mW laser, green excitation at 532 nm with a 1000 mW laser, respectively. The relative laser intensities are set to 9% for green and to 18% for red excitation. The microscope is set to TIRF illumination. Measurements are carried out at 37 °C. For quantifying transformation yields and the percentage of structures carrying cargo, dual-color fluorescence images are acquired. For recording fluorescence movies, the lasers are activated and a frame of 100 ms is taken every second separately for both excitation lasers (with a time lag of 0.5 s between them) over a measurement period of 20 min.

Data analysis

We quantify the percentage of transformed structures by dividing the number of green (ATTO 542) and red (ATTO647N) co-localized spots by the total number of green spots from dual-color TIRF images. To account for a labelling efficiency < 100%, the percentage of co-localized spots is normalized by the percentage of co-localized spots of a DNA origami array folded with all five fuel DNA strands to calculate transformation yields. In the normalization sample, AFM imaging confirmed the full transformation of all structures in previous work.[21] For structures with a cargo release unit incorporated, the percentage of structures carrying cargo is determined analogously.

Data processing and analysis of time-lapse movies is realized using custom-written Python scripts. Briefly, the acquired movies are first drift corrected using DNA origami structures carrying fluorophores which are in their fluorescent state throughout the whole measurement as fiducial markers. Spots appearing during the measurement are detected from the drift-corrected movies and dual-color background-subtracted fluorescence intensity transients of those spots extracted. To determine transformation times of single structures, the corresponding transients were fitted using a Hidden Markov model (HMM). Two levels corresponding to the quenched and unquenched state of the corresponding fluorescence unit are defined. For fluorescence onset (offset) units, transformation times

are defined as the time a structure switches from its quenched (unquenched) state to its unquenched (quenched) state and subsequently remains in it for at least 10 s for the first time. To determine transformation time distributions, only structures showing an intensity change in both colors are considered.

For titration curve measurements, the transformation yields obtained upon incubation with different concentrations of ssDNA input [*DNA*] are calculated from dual-color TIRF images as described above. $K_{1/2}$ and the Hill coefficient n_H are subsequently determined by fitting the calculated transformation yields Y to the modified Hill equation.

$$Y([DNA]) = Y(0) + \big(Y(\infty) - Y(0)\big) \cdot \frac{[DNA]^{n_H}}{K_{1/2}^{n_H} + [DNA]^{n_H}}$$

where $Y(0)$ and $Y(\infty)$ give the start and the end points of the titration.

For determining the fraction of structures with unquenched fluorescence unit in Fig. 5, we quantify the total number of structures in a TIRF image by counting the number of both weak (quenched) and bright (unquenched) red fluorescent spots. The fraction of red unquenched fluorescence units is then calculated as the fraction of the bright red spots of the total number of red spots. As green quenched fluorescence units are not visible in TIRF images, the fraction of green unquenched fluorescence units is calculated by dividing the number of green spots by the total number of red spots and subsequently normalizing them by the fraction of colocalized red and green spots in fully transformed DNA origami arrays.

Acknowledgments

P.T. gratefully acknowledges financial support from the Federal Ministry of Education and Research (BMBF) in the framework of the Cluster4Future program (Cluster for Nucleic Acid Therapeutics Munich, CNATM) (Project ID: 03ZU1201AA) as well as the Free State of Bavaria under the Excellence Strategy of the Federal Government and the Länder through the ONE MUNICH Project Munich Multiscale Biofabrication. Y.K. acknowledges the support by the Department of Energy grant DESC0020996, the National Science Foundation grants CCF-2227399 and ECCS-2328217, and the National Institute of Health grants 1R35GM153472 and 1RM1GM145394. M.P. acknowledges the support by Studienstiftung des Deutschen Volkes. The authors thank Luna, Charly and Xaverl for their support with the measurements and Angelika, Frau Steger and Herr Ehrl for lab upkeep.

Author contributions

All authors conceived and developed the concept. M.P., F.C. and D.W. prepared samples, performed and analyzed the measurements. Y.K. and P.T. supervised the project. All authors have written, read and approved the final manuscript.

Declaration of interests

The authors declare no conflict of interest.

Data availability

All experimental data supporting the findings of this work will be made available from a public repository.

References

(1) Rothemund, P. W. K. Folding DNA to create nanoscale shapes and patterns. *Nature* **2006**, *440* (7082), 297–302. DOI: 10.1038/nature04586.

(2) Dey, S.; Fan, C.; Gothelf, K. V.; Li, J.; Lin, C.; Liu, L.; Liu, N.; Nijenhuis, M. A. D.; Saccà, B.; Simmel, F. C.; Yan, H.; Zhan, P. DNA origami. *Nat Rev Methods Primers* **2021**, *1* (1). DOI: 10.1038/s43586-020-00009-8.

(3) Pumm, A.-K.; Engelen, W.; Kopperger, E.; Isensee, J.; Vogt, M.; Kozina, V.; Kube, M.; Honemann, M. N.; Bertosin, E.; Langecker, M.; Golestanian, R.; Simmel, F. C.; Dietz, H. A DNA origami rotary ratchet motor. *Nature* **2022**, *607* (7919), 492–498. DOI: 10.1038/s41586-022-04910-y. Published Online: Jul. 20, 2022.

(4) Li, S.; Jiang, Q.; Liu, S.; Zhang, Y.; Tian, Y.; Song, C.; Wang, J.; Zou, Y.; Anderson, G. J.; Han, J.-Y.; Chang, Y.; Liu, Y.; Zhang, C.; Chen, L.; Zhou, G.; Nie, G.; Yan, H.; Ding, B.; Zhao, Y. A DNA nanorobot functions as a cancer therapeutic in response to a molecular trigger in vivo. *Nat Biotechnol* **2018**, *36* (3), 258–264. DOI: 10.1038/nbt.4071. Published Online: Feb. 12, 2018.

(5) Fu, J.; Yang, Y. R.; Johnson-Buck, A.; Liu, M.; Liu, Y.; Walter, N. G.; Woodbury, N. W.; Yan, H. Multi-enzyme complexes on DNA scaffolds capable of substrate channelling with an artificial swinging arm. *Nature nanotechnology* **2014**, *9* (7), 531–536. DOI: 10.1038/nnano.2014.100. Published Online: May. 25, 2014.

(6) Grabenhorst, L.; Pfeiffer, M.; Schinkel, T.; Kümmerlin, M.; Maglic, J. B.; Brüggenthies, G. A.; Selbach, F.; Murr, A. T.; Tinnefeld, P.; Glembockyte, V. Engineering Modular and Tunable Single Molecule Sensors by Decoupling Sensing from Signal Output. *bioRxiv* **2023**, 2023.11.06.565795. DOI: 10.1101/2023.11.06.565795.

(7) Douglas, S. M.; Bachelet, I.; Church, G. M. A logic-gated nanorobot for targeted transport of molecular payloads. *Science (New York, N.Y.)* **2012**, *335* (6070), 831–834. DOI: 10.1126/science.1214081.

(8) Engelen, W.; Sigl, C.; Kadletz, K.; Willner, E. M.; Dietz, H. Antigen-Triggered Logic-Gating of DNA Nanodevices. *Journal of the American Chemical Society* **2021**, *143* (51), 21630–21636. DOI: 10.1021/jacs.1c09967. Published Online: Dec. 20, 2021.
(9) Burns, J. R.; Lamarre, B.; Pyne, A. L. B.; Noble, J. E.; Ryadnov, M. G. DNA Origami Inside-Out Viruses. *ACS synthetic biology* **2018**, *7* (3), 767–773. DOI: 10.1021/acssynbio.7b00278. Published Online: Feb. 9, 2018.
(10) Marras, A. E.; Shi, Z.; Lindell, M. G.; Patton, R. A.; Huang, C.-M.; Zhou, L.; Su, H.-J.; Arya, G.; Castro, C. E. Cation-Activated Avidity for Rapid Reconfiguration of DNA Nanodevices. *ACS nano* **2018**, *12* (9), 9484–9494. DOI: 10.1021/acsnano.8b04817. Published Online: Sep. 4, 2018.
(11) Andersen, E. S.; Dong, M.; Nielsen, M. M.; Jahn, K.; Subramani, R.; Mamdouh, W.; Golas, M. M.; Sander, B.; Stark, H.; Oliveira, C. L. P.; Pedersen, J. S.; Birkedal, V.; Besenbacher, F.; Gothelf, K. V.; Kjems, J. Self-assembly of a nanoscale DNA box with a controllable lid. *Nature* **2009**, *459* (7243), 73–76. DOI: 10.1038/nature07971.
(12) Voigt, N. V.; Tørring, T.; Rotaru, A.; Jacobsen, M. F.; Ravnsbaek, J. B.; Subramani, R.; Mamdouh, W.; Kjems, J.; Mokhir, A.; Besenbacher, F.; Gothelf, K. V. Single-molecule chemical reactions on DNA origami. *Nature nanotechnology* **2010**, *5* (3), 200–203. DOI: 10.1038/nnano.2010.5. Published Online: Feb. 28, 2010.
(13) Wang, Y.; Baars, I.; Berzina, I.; Rocamonde-Lago, I.; Shen, B.; Yang, Y.; Lolaico, M.; Waldvogel, J.; Smyrlaki, I.; Zhu, K.; Harris, R. A.; Högberg, B. A DNA robotic switch with regulated autonomous display of cytotoxic ligand nanopatterns. *Nat. Nanotechnol.* **2024**, 1–9. DOI: 10.1038/s41565-024-01676-4. Published Online: Jul. 1, 2024.
(14) Song, J.; Li, Z.; Wang, P.; Meyer, T.; Mao, C.; Ke, Y. Reconfiguration of DNA molecular arrays driven by information relay. *Science (New York, N.Y.)* **2017**, *357* (6349). DOI: 10.1126/science.aan3377. Published Online: Jun. 22, 2017.
(15) Wang, D.; Song, J.; Wang, P.; Pan, V.; Zhang, Y.; Cui, D.; Ke, Y. Design and operation of reconfigurable two-dimensional DNA molecular arrays. *Nature protocols* **2018**, *13* (10), 2312–2329. DOI: 10.1038/s41596-018-0039-0.
(16) Cui, Y.; Chen, R.; Kai, M.; Wang, Y.; Mi, Y.; Wei, B. Versatile DNA Origami Nanostructures in Simplified and Modular Designing Framework. *ACS nano* **2017**, *11* (8), 8199–8206. DOI: 10.1021/acsnano.7b03187. Published Online: Jul. 6, 2017.
(17) Liu, Y.; Ge, H.; Wang, Y.; Tang, L.; Pei, Y.; Fan, S.; Song, Y.; Zhang, C.; Song, J. Multistep Transformations of DNA Origami Domino Array via Mechanical Forces. *Small Structures* **2023**, *4* (2), 2200167. DOI: 10.1002/sstr.202200167.
(18) Yan, Q.; Wang, Y.; Shi, J.; Wei, B. Allostery of DNA nanostructures controlled by enzymatic modifications. *Nucleic acids research* **2020**, *48* (13), 7595–7600. DOI: 10.1093/nar/gkaa488.
(19) Fan, S.; Ji, B.; Liu, Y.; Zou, K.; Tian, Z.; Dai, B.; Cui, D.; Zhang, P.; Ke, Y.; Song, J. Spatiotemporal Control of Molecular Cascade Reactions by a Reconfigurable DNA Origami Domino Array. *Angewandte Chemie (International ed. in English)* **2022**, *61* (9), e202116324. DOI: 10.1002/anie.202116324. Published Online: Jan. 11, 2022.
(20) Fan, S.; Cheng, J.; Liu, Y.; Wang, D.; Luo, T.; Dai, B.; Zhang, C.; Cui, D.; Ke, Y.; Song, J. Proximity-Induced Pattern Operations in Reconfigurable DNA Origami Domino

Array. *Journal of the American Chemical Society* **2020**, *142* (34), 14566–14573. DOI: 10.1021/jacs.0c06061. Published Online: Aug. 12, 2020.
(21) Cole, F.; Pfeiffer, M.; Wang, D.; Schröder, T.; Ke, Y.; Tinnefeld, P. Controlled mechanochemical coupling of anti-junctions in DNA origami arrays. *Nat Commun* **2024**, *15* (1), 7894. DOI: 10.1038/s41467-024-51721-y. Published Online: Sep. 10, 2024.
(22) Bucci, J.; Irmisch, P.; Del Grosso, E.; Seidel, R.; Ricci, F. Timed Pulses in DNA Strand Displacement Reactions. *Journal of the American Chemical Society* **2023**, *145* (38), 20968–20974. DOI: 10.1021/jacs.3c06664. Published Online: Sep. 14, 2023.
(23) Wassermann, L. M.; Scheckenbach, M.; Baptist, A. V.; Glembockyte, V.; Heuer-Jungemann, A. Full Site-Specific Addressability in DNA Origami-Templated Silica Nanostructures. *Advanced materials (Deerfield Beach, Fla.)* **2023**, *35* (23), e2212024. DOI: 10.1002/adma.202212024. Published Online: Apr. 25, 2023.
(24) Scheckenbach, M.; Schubert, T.; Forthmann, C.; Glembockyte, V.; Tinnefeld, P. Self-Regeneration and Self-Healing in DNA Origami Nanostructures. *Angewandte Chemie (International ed. in English)* **2021**, *60* (9), 4931–4938. DOI: 10.1002/anie.202012986. Published Online: Jan. 28, 2021.
(25) Chandrasekaran, A. R. Nuclease resistance of DNA nanostructures. *Nat Rev Chem* **2021**, *5* (4), 225–239. DOI: 10.1038/s41570-021-00251-y.
(26) Douglas, S. M.; Dietz, H.; Liedl, T.; Högberg, B.; Graf, F.; Shih, W. M. Self-assembly of DNA into nanoscale three-dimensional shapes. *Nature* **2009**, *459* (7245), 414–418. DOI: 10.1038/nature08016.
(27) Wagenbauer, K. F.; Engelhardt, F. A. S.; Stahl, E.; Hechtl, V. K.; Stömmer, P.; Seebacher, F.; Meregalli, L.; Ketterer, P.; Gerling, T.; Dietz, H. How We Make DNA Origami. *Chembiochem : a European journal of chemical biology* **2017**, *18* (19), 1873–1885. DOI: 10.1002/cbic.201700377. Published Online: Aug. 10, 2017.
(28) Cordes, T.; Vogelsang, J.; Tinnefeld, P. On the mechanism of Trolox as antiblinking and antibleaching reagent. *Journal of the American Chemical Society* **2009**, *131* (14), 5018–5019. DOI: 10.1021/ja809117z.

Supplementary Information

Spring-loaded DNA origami arrays as energy-supplied hardware for modular nanorobots

Martina Pfeiffer[1,4], Fiona Cole [1,4], Dongfang Wang [2,3,4], Yonggang Ke [2*] and Philip Tinnefeld [1*]

[1] Department of Chemistry and Center for NanoScience, Ludwig-Maximilians-Universität München, Butenandtstr. 5-13, 81377 München, Germany

[2] Wallace H. Coulter Department of Biomedical Engineering, Emory University and Georgia Institute of Technology, Atlanta, GA 30322, USA

[3] School of Biomedical Engineering and Suzhou Institute for Advanced Research, University of Science and Technology of China, Suzhou 215123, China

[4] These authors contributed equally

* Correspondence: philip.tinnefeld@cup.uni-muenchen.de, yonggang.ke@emory.edu

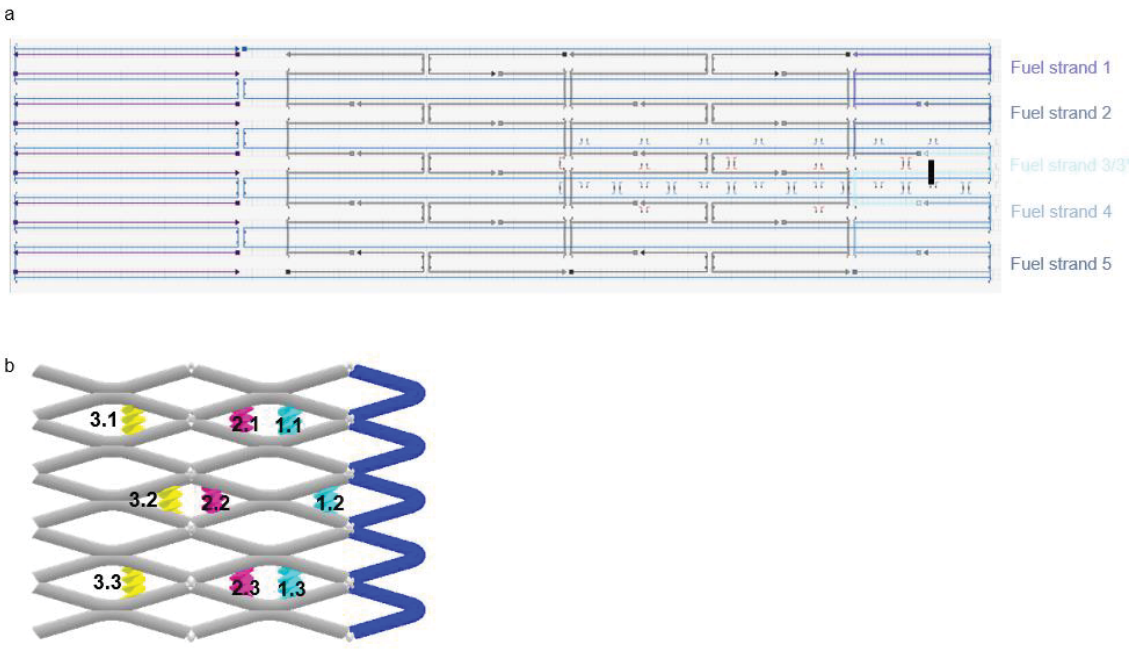

Supplementary Figure 1. Design of the 5 × 2.5 reconfigurable DNA origami array structure in its untransformed conformation. (a) Blue, gray, purple and blue lines represent the scaffold strand, core DNA staple strands of the structure, loop staple strands and fuel DNA strands, respectively. The DNA loop spans the structure from one end to the other but does not participate in the transformation process. By labeling one of the staple strands with biotin, we use it as an anchor point for surface immobilization via biotin-neutravidin interactions. Fuel DNA strands 1-4 all have the same length of 65 base pairs. Fuel DNA strand 5 is shorter, consisting of only 39 base pairs. Fuel strand 3* is shortened version of fuel strand 3 consisting of only 25 base pairs. The position of its 5-prime end is marked with a black line. As the transformation process is starts either at the upper right or lower right corner, this asymmetry induces a preferential transformation starting point. The longer length of fuel DNA strand 1 compared to fuel DNA strand 5 results in the transformation preferentially starting from the upper right corner. (b) Sketch illustrating the positions of the activation locking units specific to ssDNA, restriction enzyme activity and light at different anti-junctions of the DNA origami array structure.

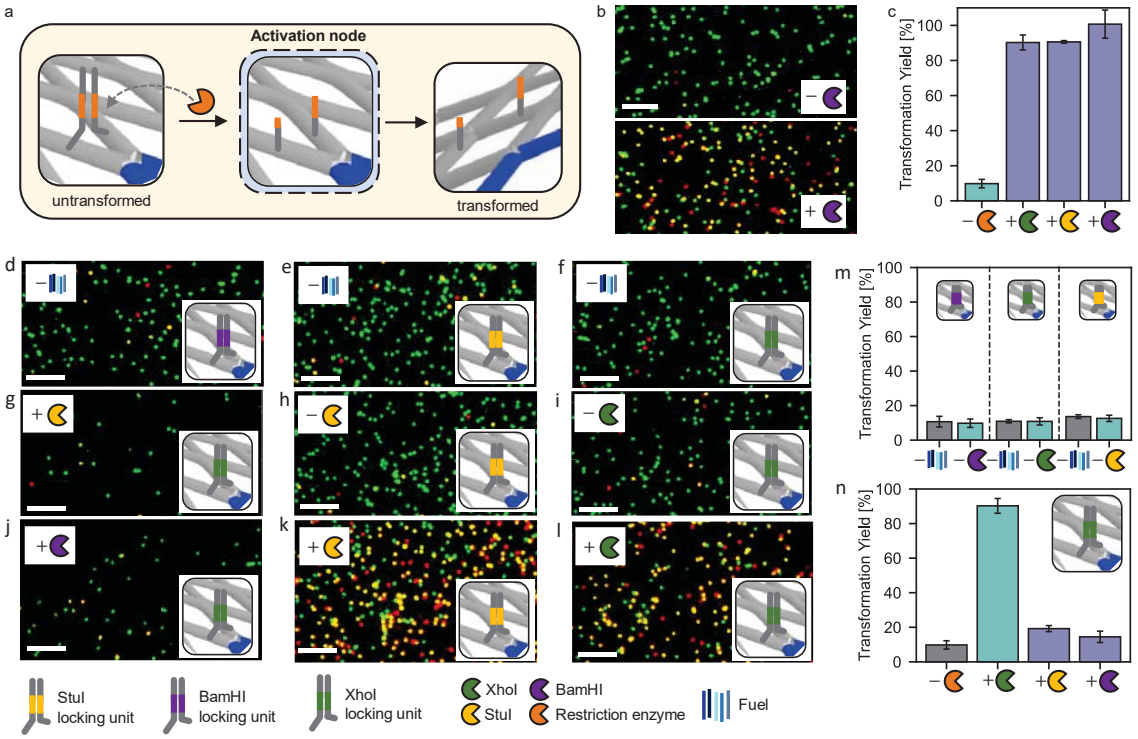

Supplementary Figure 2. Restriction enzyme activity as input. (a) Sketch of nodes responsive to restriction enzyme activity. Their design is based on a dsDNA lock containing the restriction enzyme-specific cleavage and binding site. The lock is cleaved in presence of active restriction enzyme. (b) Exemplary TIRF images of DNA origami array structures with three restriction enzyme locking units (positions 1.1, 1.2 and 1.3) containing the binding and cleavage site for BamHI before and after incubation with DNA fuel strands and after incubation with fuel strands and BamHI. (c) Transformation yields of DNA origami array structures with three restriction enzyme locking units containing the binding and cleavage site for BamHI, StuI and XhoI, respectively, before and after incubation with DNA fuel strands and BamHI, StuI and XhoI, respectively. (d-l) Exemplary TIRF images of DNA origami array structures with three restriction enzyme locking units before and after incubation with DNA fuel strands and after incubation with fuel strands and restriction enzymes. (m,n) Corresponding transformation yields. (m) When adding the fuel DNA strands (-Enzyme) no significant increase in transformation yield is observed, indicating that by introduction of the restriction enzyme locking units, the transformation process cannot be induced by the fuel DNA strands alone. (n) Only in presence of XhoI, DNA origami array structures with three XhoI locking units show a high transformation yield, indicating good specificity. In addition to possible inputs, all DNA origami arrays are incubated with fuel DNA strands 1-5. Error bars represent the standard deviation in the transformation yields calculated from three TIRF images. Scalebar: 4 µm.

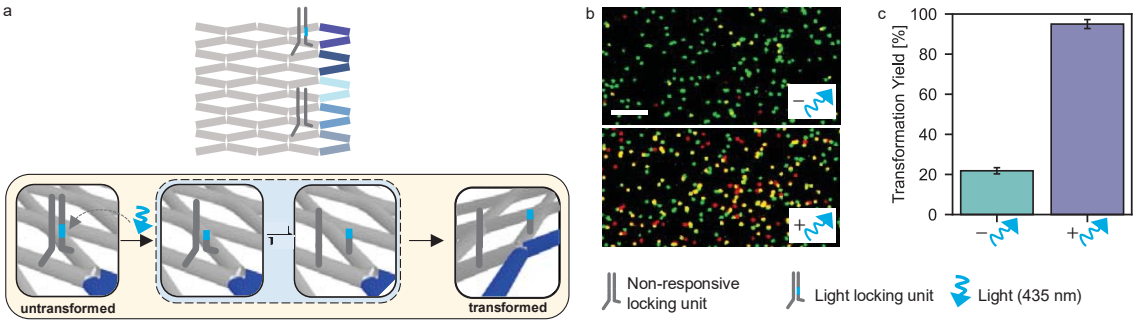

Supplementary Figure 3. Light as input. (a) Sketch of nodes responsive to light. The design is based on a dsDNA lock containing a light-cleavable linker which is cleaved in presence of light). (b) Exemplary TIRF images of DNA origami array structures with a light-cleavable locking unit (position 1.1) and an additional stabilization unit which stabilizes the untransformed state of the array and does not interact with any inputs (position 1.3) incubated with fuel DNA strands 1-5 in the presence and absence of light. (c) Corresponding transformation yields. Error bars represent the standard deviation in the transformation yields calculated from three TIRF images. Scalebar: 4 µm.

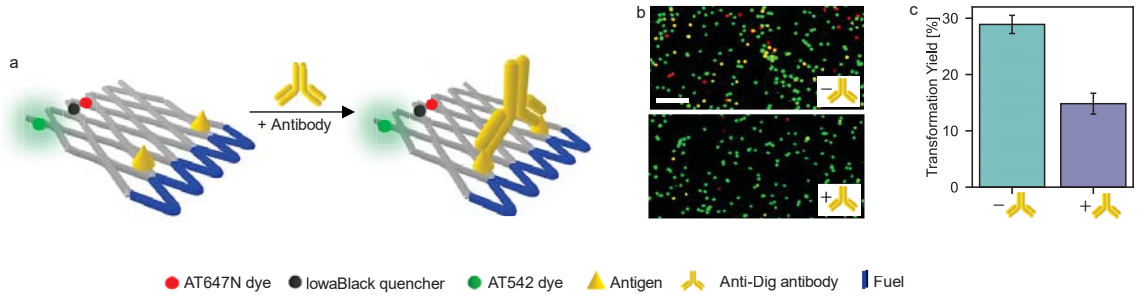

Supplementary Figure 4. Antibody as input. (a) Sketch of DNA origami array structure bearing two antigens as binding elements for an antibody. Bivalent binding of an antibody inhibits the transformation process. (b) Exemplary TIRF images of DNA origami array structures with Dig antigen input units before (upper) and after (middle) incubation with fuel DNA strands 1,2 and after incubation with anti-Dig antibodies and fuel DNA strands 1,2 (lower). (b) Corresponding transformation yields. Error bars represent the standard deviation in the transformation yields calculated from three TIRF images. Scalebar: 4 µm.

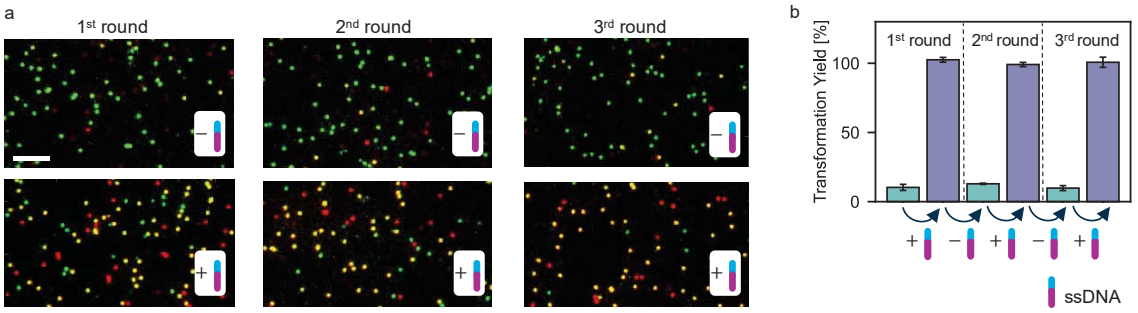

Supplementary Figure 5. Reversibility of the transformation process activated by ssDNA input. (a) Exemplary TIRF images of DNA origami array structures with six ssDNA activation units (positions 1.1-1.3, 3.1-3.3) incorporated throughout three rounds of incubation with ssDNA input, washing and incubation without ssDNA inputs. The measurements are carried out in the presence of fuel DNA strands 1,2,4. (b) Corresponding transformation yields. In addition to ssDNA as a possible input, the DNA origami arrays are incubated with fuel DNA strands 1-5 throughout all steps. Error bars represent the standard deviation in the transformation yields calculated from three TIRF images. Scalebar: 4 µm.

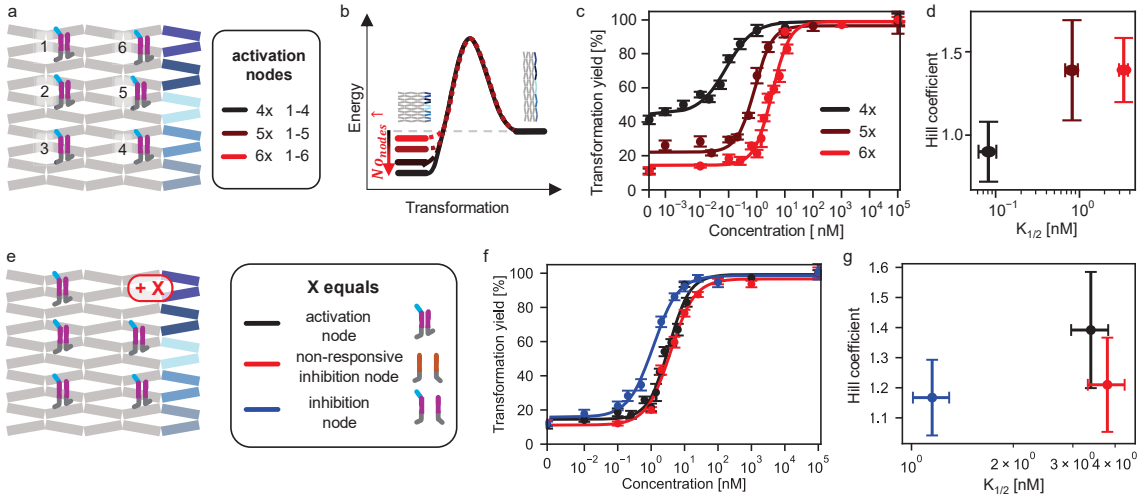

Supplementary Figure 6. Further parameters to tune the responsive concentration window of the ssDNA input. (a-d) Effect of the number of incorporated ssDNA activation units. (a) Design of the DNA origami array carrying different numbers of ssDNA activation units. (b) When increasing the number of ssDNA activation units, the untransformed state of the DNA origami system is stabilized, decreasing the tension in the spring-loaded system. (c-d) This shifts the responsive window to higher concentrations while simultaneously increasing the Hill coefficient. (c) (e-g) Effect of the additional incorporation of different units to a DNA array carrying five ssDNA activation units. (e) Design of the DNA origami array carrying five ssDNA activation units and additionally a variable unit X. Activation and inhibition units stabilize the untransformed and the transformed conformation of the antijunction node they are placed on, respectively. Their stabilizing effect is removed by binding of the ssDNA input to the unit. In contrast, non-responsive inhibition units stabilize the transformed conformation of the antijunction node they are placed on but do not interact with the ssDNA input. (f) Varying the unit X shifts the responsive window. (g) As expected, the addition of a non-responsive inhibition unit and an inhibition unit results in lower Hill coefficients than the addition of another activation unit. Also, the introduction of these units shifted $K_{1/2}$ to different extents. In addition to ssDNA as a possible input, all DNA origami arrays are incubated with fuel DNA strands 1-5. Error bars in (c,f) represent the standard deviation in the transformation yields calculated from at least three TIRF images. Error bars in (d,g) represent the fit error to the curves fitted in (c,f).

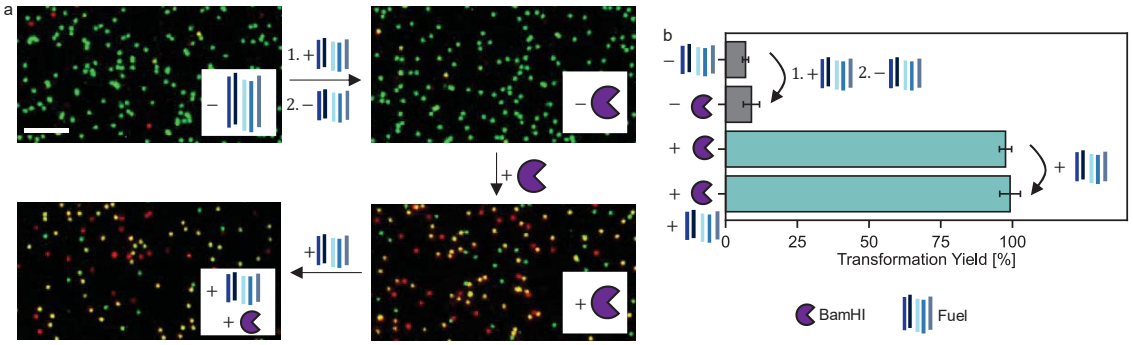

Supplementary Figure 7. Pre-loading DNA origami array structures with fuel DNA strands. We first incubate a DNA origami array structures with three BamHI locking units (positions 1.1, 1.2 and 1.3) with the fuel DNA strands before removing unbound fuels in solution by five washing steps. Subsequent addition of BamHI results in a near quantitative transformation of all structures, demonstrating the successful pre-loading with fuel strands and creation of the pre-tensioned state. The near quantitative transformation is confirmed by again adding the fuel DNA strands at the end of the assay which does not result in a significant increase in transformation yield. Thus, we conclude that pre-loading the fuel DNA strands and their attached energy in a quantitative manner is possible (a) Exemplary TIRF images of the DNA origami arrays before incubation with fuel DNA strands (upper left), after incubation with fuel DNA strands 1-5 which then are removed from solution (upper right), after incubation with BamHI (lower right) and again adding the fuel DNA strands 1-5 (lower left). (b) Corresponding transformation yields. Error bars represent the standard deviation in the transformation yields calculated from three TIRF images. Scalebar: 4 µm.

Supplementary Note 1. Effect of restriction enzyme input units specific for XhoI placed at different positions as well as combinations of these units.

For studying the inhibition effect of locking units on the overall transformation process, we place different numbers of locking units specific for XhoI at different antijunctions nodes in the system (see Fig. S8a, S8b). Depending on which antijunction the locking units are placed on, we observe different efficiencies in its inhibition of the reconfiguration process. We find that the position-dependency is directly linked to the energy landscape of the reconfiguration process: the further right the antijunction of the input unit is positioned in the DNA array, the earlier it reconfigures its conformation in the transformation process and the larger is the effect of the corresponding locking unit on the overall transformation yield. This is in good agreement with the proposed energy landscape which is tilted more strongly downwards towards the end of the transformation. Thus, in the beginning, an additional energy barrier of the same size has a larger effect than in a downhill tilt. Due to the identical design of the developed restriction enzyme locking units specific for XhoI, StuI, BamHI we expect that the obtained position-dependencies to be transferable to StuI and BamHI. We use the position-dependency to define design strategies for Boolean logic AND and OR gates (see Fig. S8c-f).

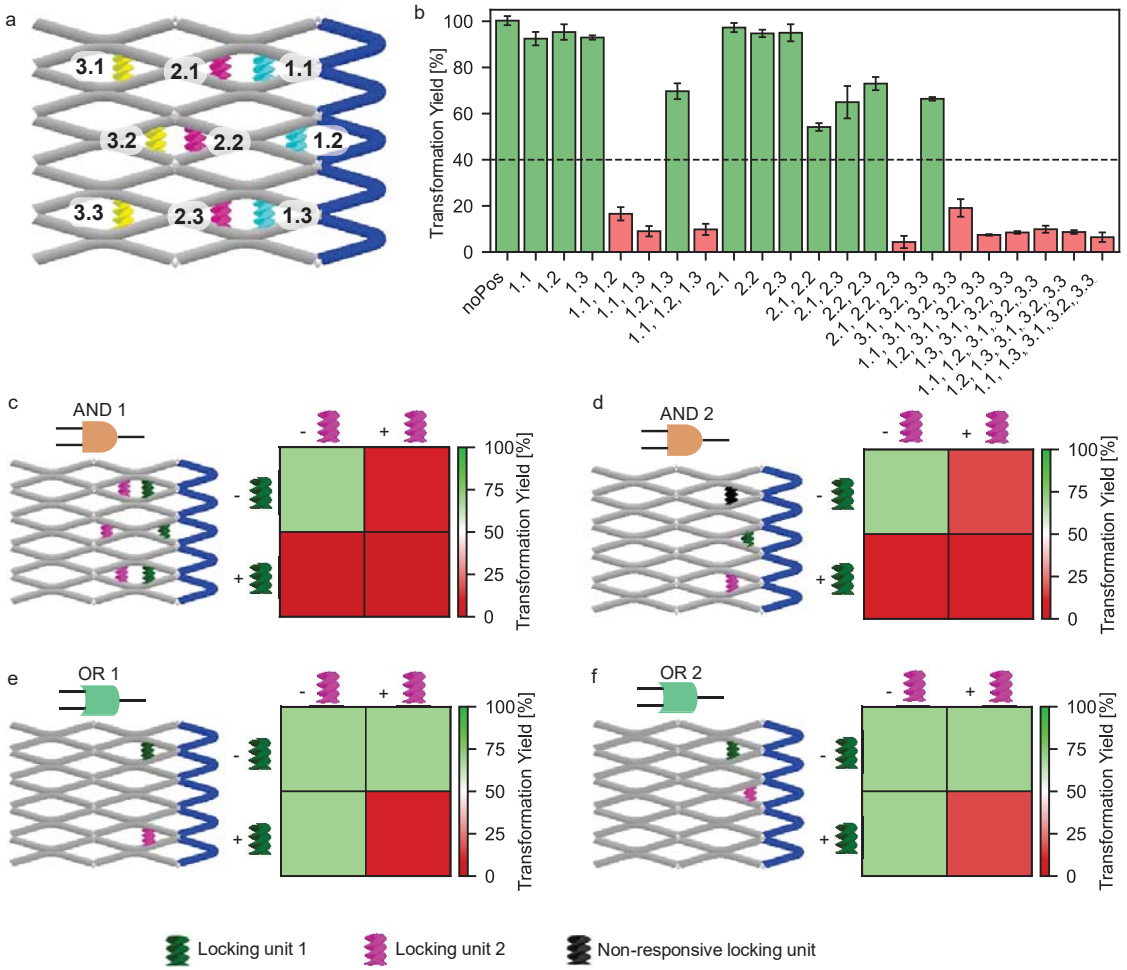

Supplementary Figure 8. Effect of locking units specific for XhoI placed at different positions as well as combinations of these units. (a) Sketch illustrating the nomenclature of the XhoI locking units positioned at different anti-junctions of the DNA origami array structure. (b) Transformation yields of DNA origami array structures with different combinations of XhoI locking units incorporated. The yields are obtained after incubation with the fuel DNA strands but in absence of restriction enzyme. DNA origami arrays with transformation yields above 40% (dashed line) are considered successfully transformed and marked in green. DNA origami arrays exhibiting lower transformation yields are marked in red. (c-f) Two possible DNA origami array configurations for Boolean logic AND (c,d) and OR (e,f) gates using two types of restriction enzyme as inputs. The corresponding restriction enzyme locking units are marked in the designs in pink and forest green (left sketches). Non-responsive locking units which stabilize the untransformed state of the antijunction node they are placed on and are inactive towards either of the restriction enzymes are marked in black. The transformation yields obtained for DNA origami arrays with (+) and without (-) the locking units 1/ 2 incorporated indicate the possibility of implementing Boolean logic gates based on restriction enzyme activity (right plots). Transformation yields are the same as in (b). When applying the designs to restriction enzyme activities, the absence (presence) of a locking unit corresponds to the presence (absence) of a restriction enzyme which cleaves the unit. As such, the configurations are expected to correspond to AND (c,d) gates and OR (e,f) gates with respect to the activity of restriction enzymes. The designs of (c) and (e) are used in Figure 3 of the main paper. Multi-level Boolean logic gates are designed analogously. All DNA origami arrays are incubated with fuel DNA strands 1-5. Error bars represent the standard deviation in the transformation yields calculated from three TIRF images.

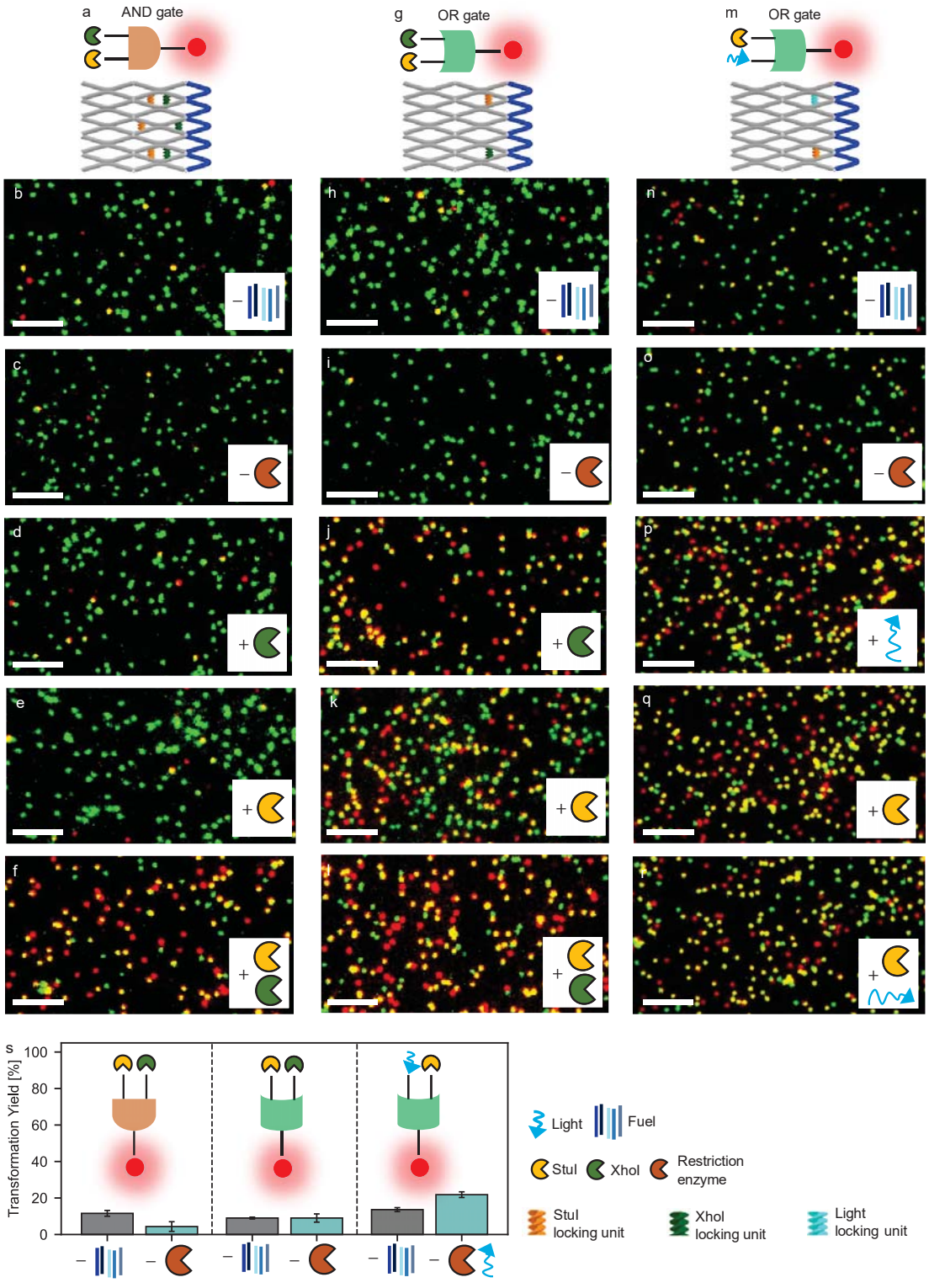

Supplementary Figure 9. Processing one-level Boolean logic gates. (a-f) Schematic representation of DNA origami array structures with (a) an AND logic gate responsive to combinations of StuI and XhoI and (b-f) exemplary TIRF images before and upon addition of different inputs. (g-l) Schematic representation of DNA origami array structures with (g) an OR logic gate responsive to combinations of StuI and XhoI and (h-l) exemplary TIRF images before and upon addition of different inputs. (m-q) Schematic representation of DNA origami array structures with (m) an AND logic gate responsive to combinations of StuI and light and (m-q) exemplary TIRF images before and upon addition of different

inputs. (s) Corresponding transformation yields. In addition to possible inputs, all DNA origami arrays are incubated with fuel DNA strands 1-5. Error bars represent the standard deviation in the transformation yields calculated from three TIRF images. Scalebar: 4 μm.

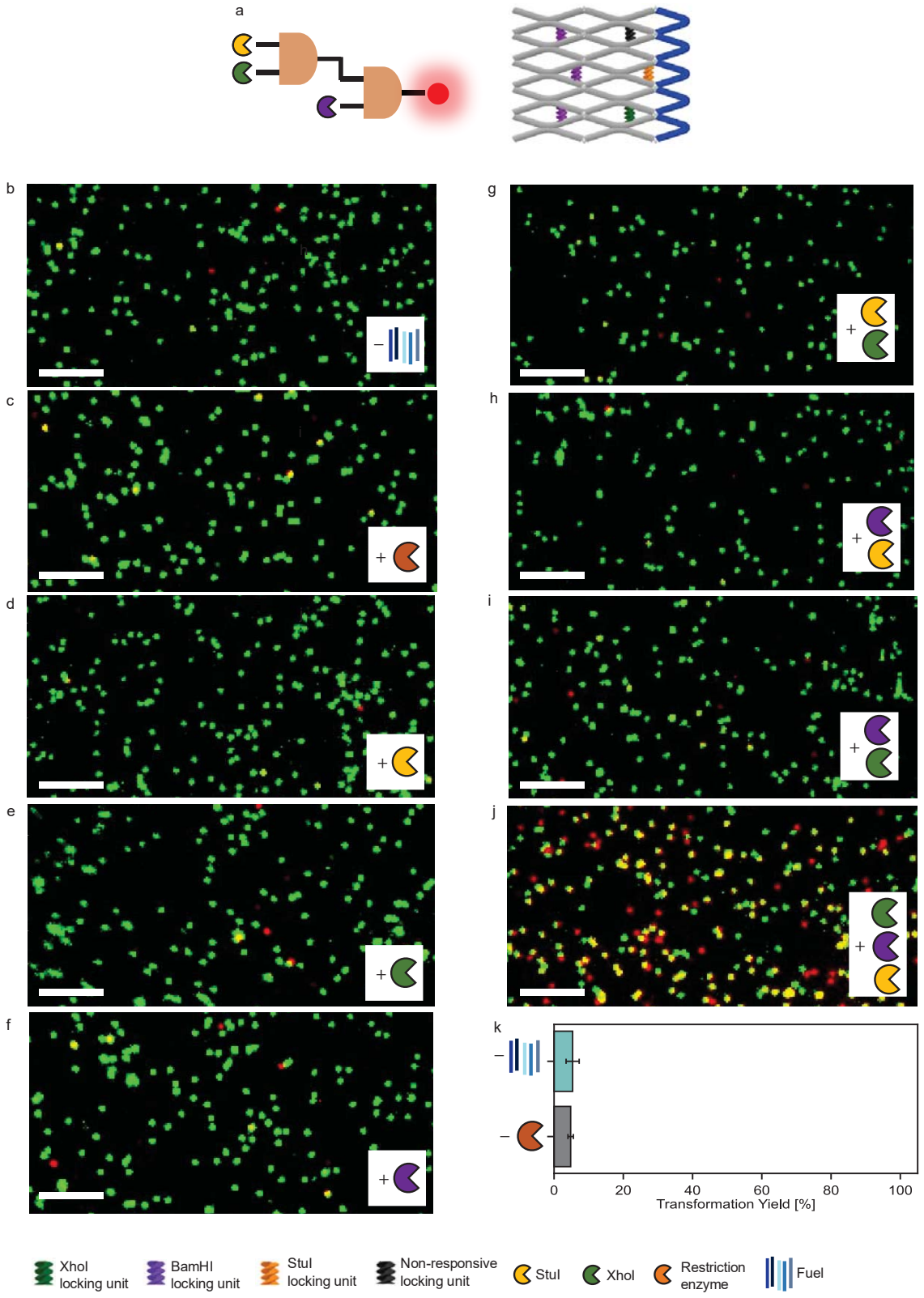

Supplementary Figure 10. DNA origami array nanodevices processing a 3xAND gate. (a-j) Schematic representation of DNA origami array structures with a 3xAND logic gate responsive to combinations of StuI, XhoI and BamHI and (b-j) exemplary TIRF images before and upon addition of different inputs. (k) Transformation yields obtained before and after incubation with fuel DNA strands but without restriction enzymes. In addition to possible inputs, all DNA origami arrays are incubated with

fuel DNA strands 1-5. Error bars represent the standard deviation in the transformation yields calculated from three TIRF images. Scalebar: 4 μm.

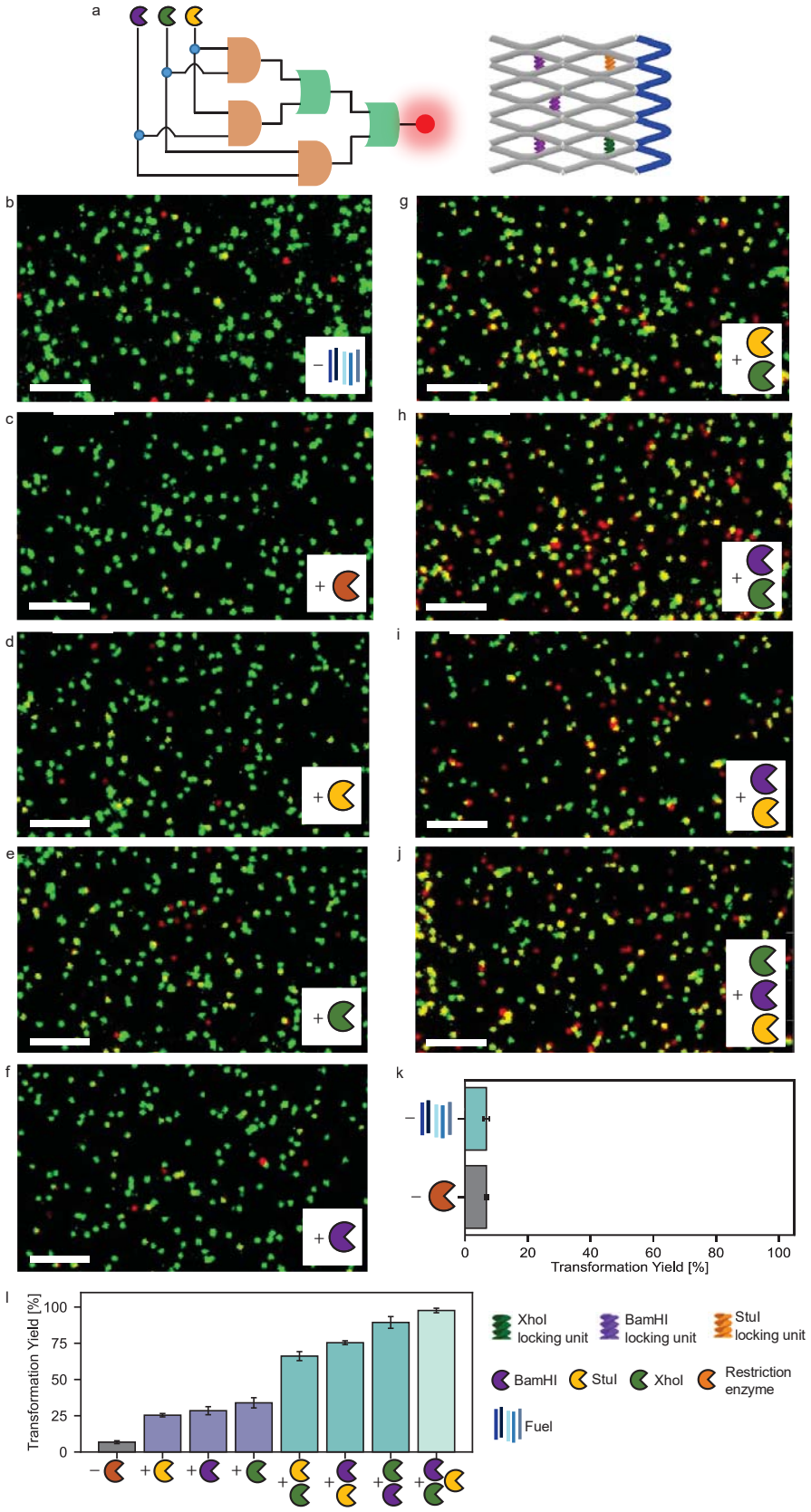

Supplementary Figure 11. DNA origami array nanodevices processing a multi-level logic gate consisting of a series of three AND gates and two OR gates. (a) Schematic representation of DNA

origami array structures with a multi-level logic gate responsive to combinations of StuI, XhoI and BamHI and (b-j) exemplary TIRF images before and upon addition of different inputs. (k) Transformation yields obtained before and after incubation with fuel DNA strands but without restriction enzymes. (l) Transformation yields before and after incubation with fuel DNA strands and restriction enzymes. In addition to possible inputs, all DNA origami arrays are incubated with fuel DNA strands 1-5. Error bars represent the standard deviation in the transformation yields calculated from three TIRF images. Scalebar: 4 µm.

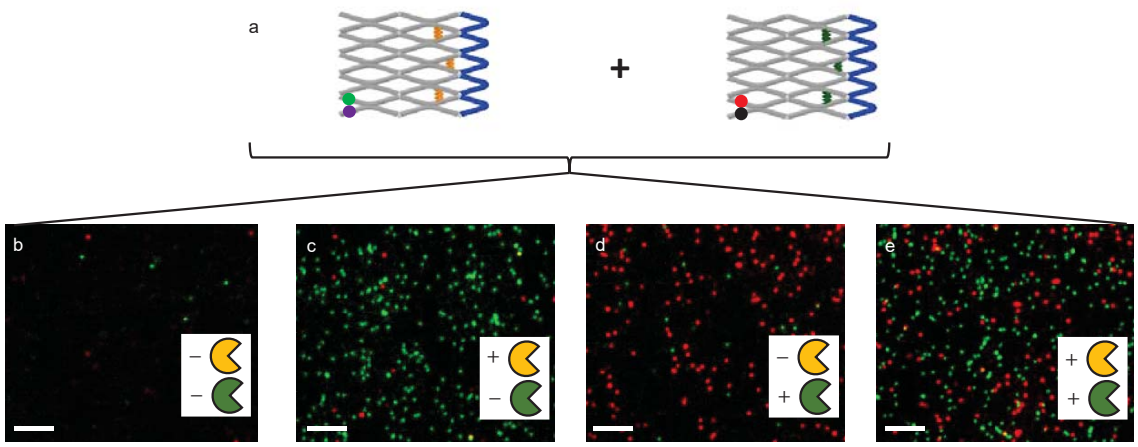

Supplementary Figure 12. Multiplexing with DNA origami arrays. (a) Sketch of the two different DNA origami array designs used for multiplexing. The DNA origami array responsive to StuI restriction enzyme activity (left panel) carries a green fluorescence onset unit whereas the DNA origami array responsive to XhoI restriction enzyme activity (right panel) carries a red fluorescence onset unit. By immobilizing both DNA origami arrays on the same surface, multiplexing is achieved by spectral separation. (b-e) Exemplary TIRF images of surfaces bearing both DNA origami array structures upon incubation with and without StuI (yellow) and XhoI (green) restriction enzymes. Only in the presence of the corresponding enzymes, green and/ or red spots appear. In addition to possible inputs, all DNA origami arrays are incubated with fuel DNA strands 1-5. Scalebar: 4 µm.

Supplementary Note 2. Cargo Release Unit

The cargo release unit is formed by two ssDNA strands protruding from domains of two neighboring antijunctions. The ssDNA strands are placed on the antijunction domains such that they are in close proximity in the untransformed conformation of the DNA array and further apart in its transformed conformation. They each contain a 10 nt non-complementary linker sequence followed by a 9 nt complementary sequence which – if both strands are in close proximity – forms a stem. The stem is followed by a 10 nt non-complementary sequence on each strand to which an ATTO542-labelled ssDNA strand containing a 20-nt complementary sequence is hybridized during DNA origami array folding.

Transformation of the antijunctions carrying the cargo release unit then results in the spatial separation of the two ssDNA strands forming the cargo release unit. The stem dehybridizes resulting in a weakened affinity of the cargo strand to the release unit and subsequently to its release.

During measurements also a certain degree of unspecific cargo release is observed. Both upon incubation with and without fuel DNA strands but without restriction enzyme, we note a decrease in the fraction of structures carrying cargo. As this decrease occurs both upon incubation with and without fuel DNA strands, we do not attribute the unspecific cargo release mainly to the addition of fuel DNA strands but to the heightened incubation temperature of 37 °C (Supplementary Fig. 13)

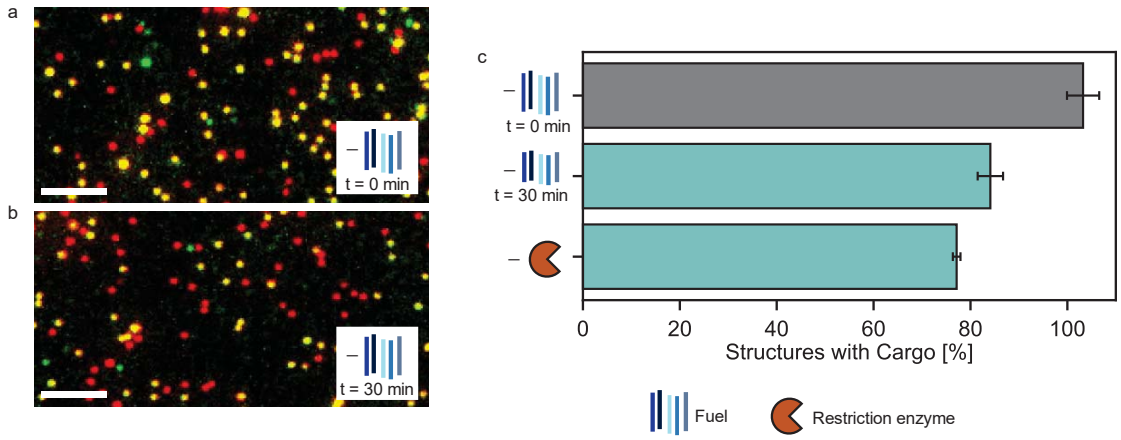

Supplementary Figure 13. Unspecific release of a cargo DNA strand from DNA origami array structures upon incubation at 37°C and upon incubation without restriction enzyme. (a) Exemplary TIRF images of DNA origami array structures (a) before and (b) after 30 min incubation without fuel DNA strands at 37°C. (c) Corresponding fraction of structures with cargo DNA strand before and upon incubation without and with fuel DNA strands but without restriction enzyme. After incubation, we note a decrease in the fraction of structures carrying cargo both without and with fuel DNA strands but without restriction enzyme. Thus, we do not attribute the unspecific cargo release mainly to the addition of the fuel DNA strands but to the heightened incubation temperature of 37 °C. In addition to possible inputs, all DNA origami arrays are incubated with fuel DNA strands 1-5. Error bars represent the standard deviation in the fractions calculated from three TIRF images. Scalebar: 4 µm.

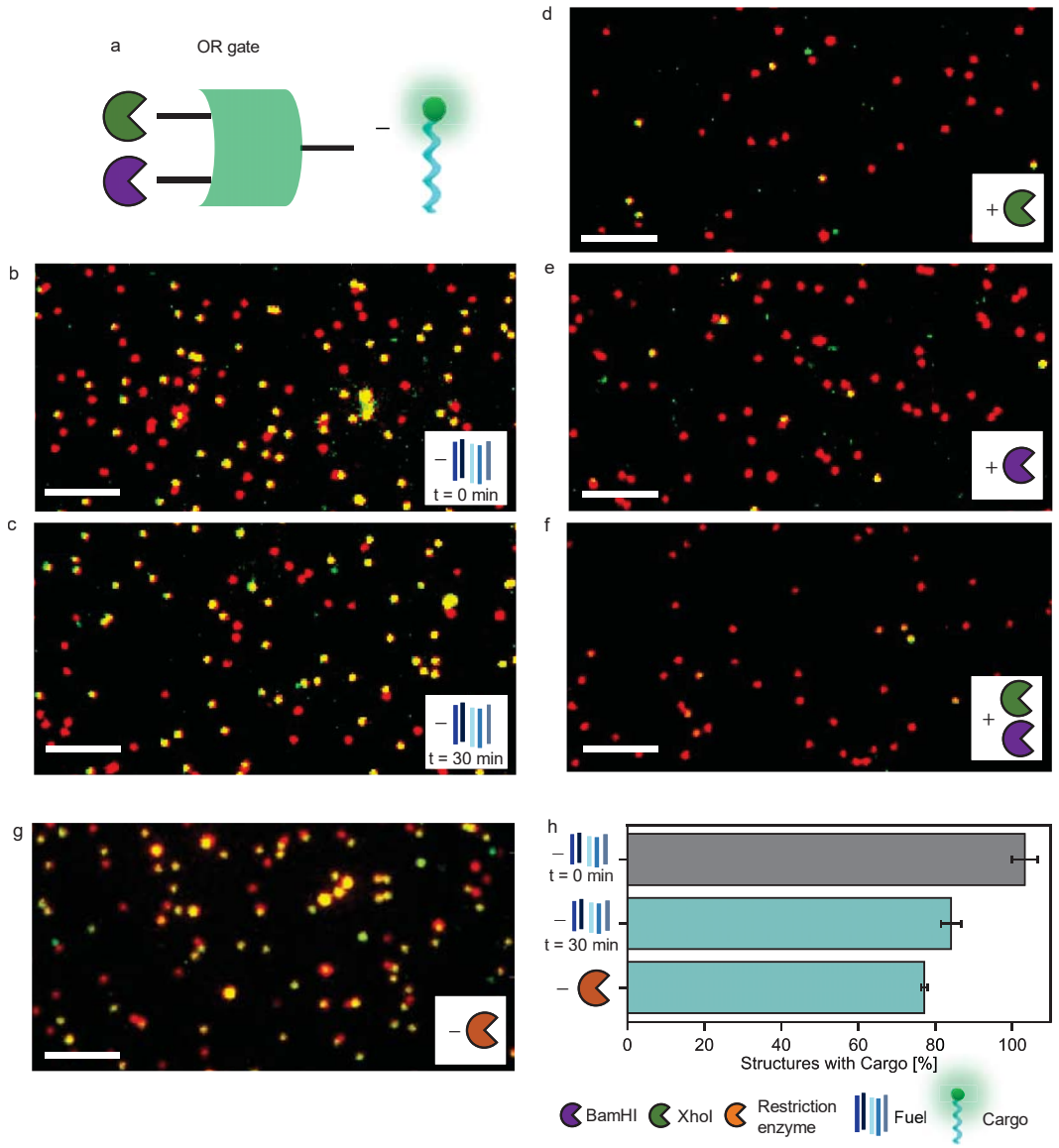

Supplementary Figure 14. DNA origami arrays with OR logic gate releasing a cargo DNA strand in response to the combination of different restriction enzymes. (a) Schematic representation of a OR logic gate which releases a cargo DNA strand in response to the activity of BamHI and XhoI. (b-g) Exemplary TIRF images of DNA origami array structures before and after incubation with different inputs. (h) Fraction of structures with cargo before and after incubation without and with fuel DNA strand but without restriction enzymes. In addition to possible inputs, all DNA origami arrays are incubated with fuel DNA strands 1-5. Error bars represent the standard deviation in the fractions calculated from three TIRF images. Scalebar: 4 µm.

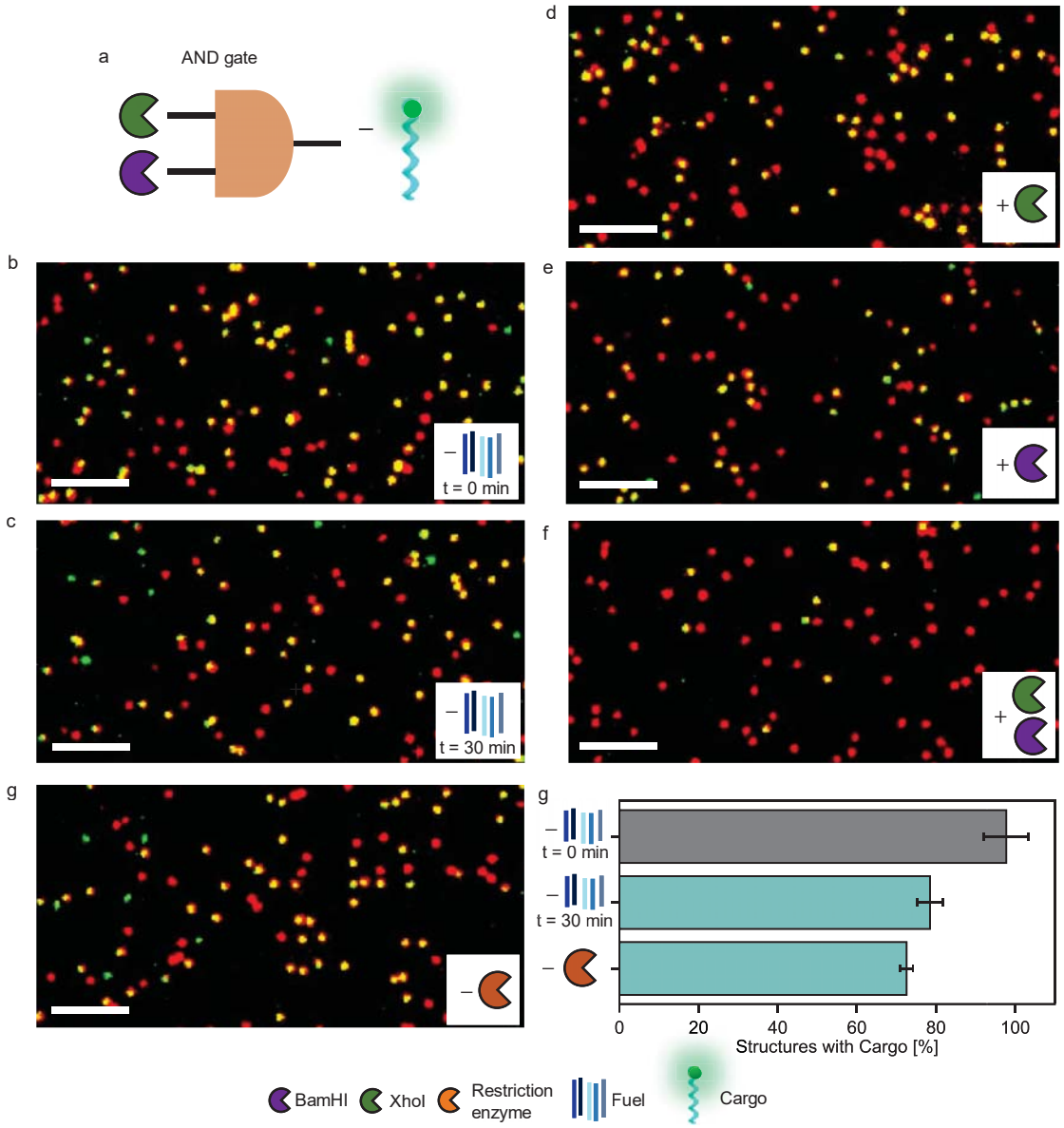

Supplementary Figure 15. DNA origami arrays with AND logic gate releasing a cargo DNA strand in response to the combination of different restriction enzymes. (a) Schematic representation of an AND logic gate which releases a cargo DNA strand in response to the activity of BamHI and XhoI. (b-f) Exemplary TIRF images of DNA origami array structures before and after incubation with different inputs. (g) Fraction of structures with cargo before and after incubation with and without fuel DNA strand but without restriction enzymes. In addition to possible inputs, all DNA origami arrays are incubated with fuel DNA strands 1-5. Error bars represent the standard deviation in the fractions calculated from three TIRF images. Scalebar: 4 µm.

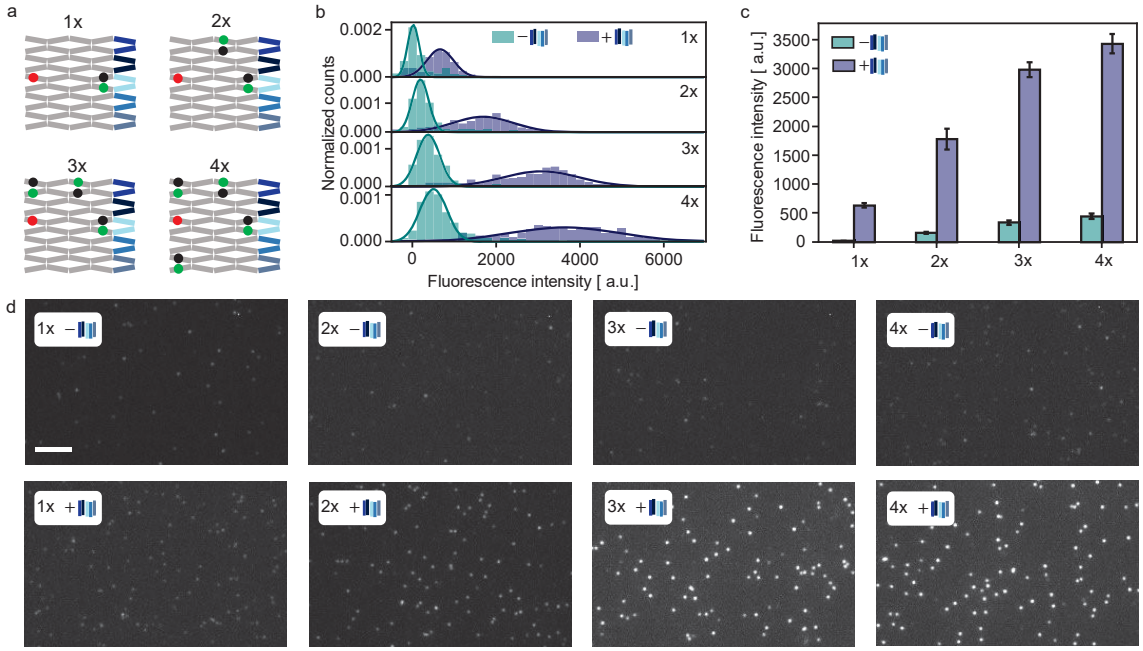

Supplementary Figure 16. Signal amplification by incorporating multiple fluorescence onset output units into different antijunction nodes. (a) DNA array designs for incorporating one, two, three and four green fluorescence onset units. Additionally, an ATTO647N dye is incorporated for locating the DNA array positions. ATTO542, BHQ2 (green onset unit) and ATTO647N are shown as green, black and red dots. (b) Fluorescence intensity distributions of ATTO542 for the different structures prior and after incubation with fuel DNA strands. When increasing the number of incorporated fluorescence onset units, the intensity contrast between the two states increases. Fluorescence intensities are calculated from dual-color TIRF images using ATTO647N fluorescence to locate the positions of the structures. The distributions are fitted with a Gaussian. (c) Mean values of the fluorescence intensity distributions for the different structures. Error bars represent the standard deviation in the mean values calculated from at least three TIRF images. (d) Exemplary TIRF images (ATTO542 excitation) for the DNA origami array structures shown in (a) before (upper row) and after (lower row) incubation with fuel DNA strands 1-5. Scalebar: 4 µm.

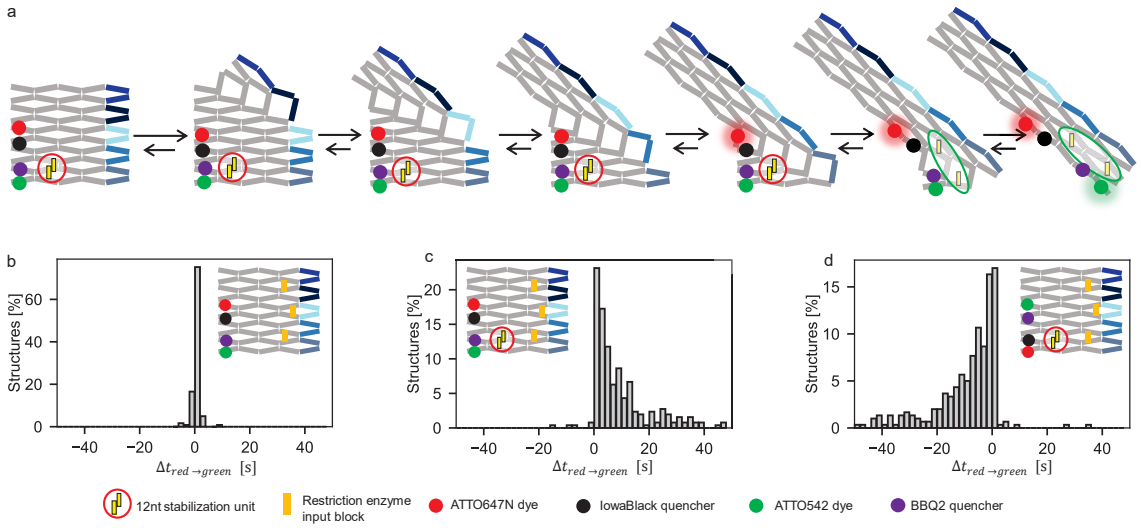

Supplementary Figure 17. Controlling the timing and the order between output operations. (a) A timing unit consisting of a 12 nt DNA lock is placed on antijunctions transforming before two red and green fluorescence onset units. (b-d) Distributions of the time difference between the fluorescence onset at the studied positions for a DNA origami array with BamHI-responsive input units (positions 1.1, 1.2, 1.3) obtained upon incubation with BamHI for DNA origamis (b) without and (c,d) with a timing unit incorporated. (b) Without the timing unit the red and green fluorescence onsets occur simultaneously. (c,d) with the timing unit, the red and green fluorescence onsets occur with a time delay between them. The order of fluorescence onsets hereby is controlled by the placement of the onset units with respect to the timing unit. In addition to BamHI, all DNA origami arrays are incubated with fuel DNA strands 1-5.

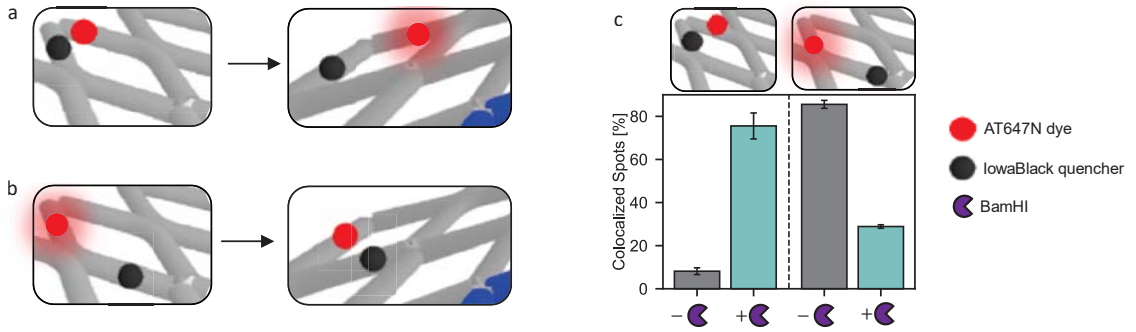

Supplementary Figure 18. Concept of fluorescence onset and offset unit. (a,b) Sketch demonstrating the principle of a fluorescence onset (a) and a fluorescent offset (b) unit. (c) Fraction of red-green colocalized spots on dual-color TIRF images of DNA origami arrays with a fluorescence on-/offset unit and three restriction enzyme locking units responsive to BamHI incorporated before and upon incubation with BamHI. In addition to BamHI, all DNA origami arrays are incubated with fuel DNA strands 1-5. Error bars represent the standard deviation in the fractions calculated from three TIRF images.

Supplementary Note 3. Sequence of the p1800 scaffold used to fold the DNA origami array structure from 5' to 3' end:

TACGAAGAGTTCCAGCAGGGATTCCAAGAAATGGCCAATGAAGATTGGATCACC
TTTCGCACTAAGACCTACTTGTTTGAGGAGTGCCTGATGAATTGGCACGACCGC
CTCAGGAAAGTGGAGGAGCATTCTGTGATGACTGTCAAGCTCCAATCTGAGGTG
GGCAAATATAAGATTGTTATCCCTATCTAGAAGTACGTCCGCGGAGAACACCTG
CCACCCGATCACTGGCTGGATCTGTTACGCTTGCTGGGTCTGCCTCGCGGCAC
ATCTCTGGAGAAACTGCTGTTCGGTGACCTGCTGAGAGTTGCCGATACCATCGT
GGCCAAGGCTGCTAACCTGAAAGATCTGAACTCACGCGGCCAGGGTGAAGTGA
CCATCCGCGAATAACTCAGGGAACTGGATTTGTGGGGCGTGGGTGCTGTGTTC
ACACTGATCGGCTATGAGGACTCCCAGAGCCGCACCTAGAAGCTGATCAAGGA
TTGGAAGGAGCTCGTCAACCAGGTGGGCGACAATATATGCCTCCTGCAGTCCTT
GAAGGACTCACCATACTATAAAGGCTTTGAAGACAAGGTCAGCATCTGGGCAAG
GAAACTCGCCGAACTGGACGATAATTTGCAGAACCTCAACCATATTCGCAGAAA
GTGGGTTTACCTCGAACCATACTTTGGTCGCGGAGCCCTGCCCAAAGAGCAGA
CCAGATTCAACAGGGTGGGCGAAGATTTCCGCAGCATCATGACATATATCAAGA
AGGACAATCGCGTCACGCCCTTGACTACCCACGCAGGCATTCTAAACTCACTGC
TGACCATCCTGGACCAATTGCAGAGATGCCAGCGCAGCCTCAACGAGTTCCTG
GAGGCGAAGCGCAGCGCCTTCCCTCGCTTTAACTTCATCGGAGACGATGACCT
GCGCGAGATCTTGGGCCAGTCAACCAATTAATCCGTGATTCAGTCTCACCTCAA
GAAGCTGTTTGCTGGTATCAACTCTGGCTGTTTCGATGAGAAGTCTAAGCACTAT
ACTGCAATGAAGTCCTTGGAGGGGCAAGTTGTGCCATTCAAGAATAACGTACCC
TTGTCCAATAACGTCGAAACCTGGCTGAACGATCTGGCCCTGGAGATGAAGAAG
ACCCTGGAGGCGCTGCTGAAGGAGTGCGTGACAACTAGACGCAGCTCTCAGGG
AGCTGTGGGCCCTTCTCTGTTCCCATCACAGATCTAGTGCTTGGCCGAACAGAT
CAAGTTTACCGAAGATGTGGAGAACGCAATTAAAGATCACTCCCTGCACCAGAT
TGAGTAACAGCTGGTGAACAAATTGGAGCAGTATACTAACATCGACACATCTTC
CGTAGACCCAGGTAACACAGAGTCCGGTATTCTGGAGCTGAAACTGAAAGCACT
GATTCTCGACGGATCCACGCGCCCTGTAGCGGCGCATTAAGCGCGGCGGGTGT
GGTGGTTACGCGCAGCGTGACCGCTACACTTGCCAGCGCCCTAGCGCCCGCTC
CTTTCGCTTTCTTCCCTTCCTTTCTCGCCACGTTCGCCGGCTTTCCCCGTCAAGC
TCTAAATCGGGGGCTCCCTTTAGGGTTCCGATTTAGTGCTTTACGGCACCTCGA
CCCCAAAAAACTTGATTTGGGTGATGGTTCACGTAGTGGGCCATCGCCCTGATA
GACGGTTTTTCGCCCTTTGACGTTGGAGTCCACGTTCTTTAATAGTGGACTCTTG
TTCCAAACTGGAACAACACTCAACCCTATCTCGGGCTATTCTTTTGATTTATAAG
GGATTTTGCCGATTTCGGGGTACC

Table 1. Core staples from the 5‘ to the 3’ end for the DNA origami array structure.

ID	Sequence (5‘ to 3‘)	Function
C1	GGAGTCCTCATAGATGGTTCGAGGTAAACCCACTTTCTGATGT CATGATGCT	core
C2	GCGGAAATCTTCGAATTGGTTGACTGG CCCAAGATCTCGAGTGCTTAGACTT	core
C3	GTTGAGGCTGCGCGGTCCAGGATGGTCAGCAGTGAGTTTCCC AGATGCTGAC	core
C4	CTTGTCTTCAAAGAGTCCTTCAAGGACTGCAGGAGGCATCAAC TCTCAGCAG	core
C5	AATCTTATATTTGATTCGCGGATGGTCACTTCACCCTGGAGGT GCGGCTCTG	core
C6	GAGAGCTGCGTCTCCCCTCCAAG GACTTCATTGCAGTATCGCAGGT CATCGT	core
C7	AGTGATCGGGTGGAGCAGCCTTGGCCACGATGGTATCGGATA TTGTCGCCCA	core
C8	CCTGGTTGACGAGATCGTCCAGTTCGGCGAGTTTCCTTGAGA ATGCCTGCGT	core
C9	CTCATCGAAACAGAGATCTGTGATGGGAACAGAGAAGGGACT CAATCTGGTGCAGGGAGTGATCTTTTTT	core
C10	TTTTTGCGAAAGGTGATCCAATCTTCATTGGAACAGATCCAGC C	core
C11	ATGGCACAACTTGAGTTGTCACGCACTCCTTCAGCAGCGACG GAAGATGTGTCGATGTTAGTATATTTTT	core
C12	CTTCATCTCCAGGAGGTTTCGACGTTATTGGACAAGGGTCCTC CAGGAACTC	core
C13	GTCACCGAACAGCTGCCGCGAGGCAGACCCAGCAAGCGTCC ATTTCTTGGAATCCCTGCTGGAAC	core
C14	GGTTCTGCAAATTCTCCTTCCAATCCTTGATCAGCTTCTCCGC GTGAGTTCA	core
C15	GATCTTTCAGGTTCAGGTGTTCTCCGCGGACGTACTTCTCACT CCTCAAACAAGTAGGTCTTAGTTTTTT	core
C16	TTTTTTGAGGCGGTCGTGCCAATTCATCAGGAGATAGGGATAA C	core
C17	TACCGGACTCTGTGTTACCTGGGTCTCCTCCAGGGTCTT	core
C18	TTTTTCTGCTCCAATTTGTTCACCAGCTGTTCCCACAGCTCCCT	core
C19	CTCCGATGAAGTTCGTGACGCGATTGTCCTTCTTGATATCGAA TATGGTTGA	core
C20	GGGTAGTCAAGGGAAAGCGAGGGAAGGCGCTGCGCTTCGAC GTTATTCTTGA	core
X1	CCAAATCAAGTTTTTTGGGGTCGAGGTGCCGTAAAGCACTAA	loop
X2	AAACCGTCTATCAGGGCGATGGCCCACTACGTGAACCATCAC	loop
X3	GTCCACTATTAAAGAACGTGGACTCCAACGTCAAAGGGCGAA	loop
X4	GGTACCCCGAAATCGGCAAAATCCCTTATAAATCAAAAGAAT	loop
X5	AAGGAGCGGGCGCTAGGGCGCTGGCAAGTGTAGCGGTCACG C	loop
X6	AGCCCGAGATAGGGTTGAGTGTTGTTCCAGTTTGGAACAAGA	loop

X7	ATCGGAACCCTAAAGGGAGCCCCCGATTTAGAGCTTGACGGG	loop
X8	TGCGCGTAACCACCACACCCGCCGCGCTTAATGCGCCGCTAC	loop
X9	AGGGCGCGTGGATCCGTCGAGAATCAGTGCTTTCAGTTTCAG	loop
X10	GAAAGCCGGCGAACGTGGCGAGAAAGGAAGGGAAGAAAGCGA	loop

Table 2. Fuel staples from the 5‘ to the 3’ end used to transform the DNA origami array structure. Fuel staples are labelled according to the position they can bind to the DNA origami array structure, starting from the upper right corner to the lower right corner.

ID	**Sequence (5‘ to 3‘)**	**Function**
T1	AGTTCCCTGAGTTCCCACCTCAGATTGGAGCTTGACAGTCATCACAGAAGCTCCTCCACTTTCCTTTTT	fuel 1
T2	CCGCGACCAAAGTCCGATCAGTGTGAACACAGCACCCACGCCCCACAAACC	fuel 2
T3	TGAATCACGGATTCCCACCCTGTTGAATCTGGTCTGCTCTTTGGGCAGGGT	fuel 3
T4	TCGGCCAAGCACTCCAGAGTTGATACCAGCAAACAGCTTCTTGAGGTGAGAC	fuel 4
T5	TTTTTTTAATTGCGTTCTCCACATCTTCGGTAAACTTGATCTGT	fuel 5
T3*	TCTGGTCTGCTCTTTGGGCAGGGCT	fuel 3 - 25nt

Table 3. Staples from the 5‘ to the 3’ end for labelling the DNA origami array structure with biotin and fluorescent dye – quencher pairs. B1 is included in all DNA array structures for surface immobilization. For the upper and lower fluorescence onset units (U and D staples) either the green or the red dye-quencher pair is used. The staples of the lower fluorescence onset unit (D1-D6) are used to incorporate AT542 and AT647N dyes for co-localization in the DNA arrays. Here, the corresponding quencher-labeled oligonucleotides (D4/ D6) are replaced by their unlabeled alternatives. For the red fluorescence offset unit O2 is used in combination with the staples of the left fluorescence onset unit (L1-L4). Here, the quencher labelled oligonucleotide L4 is replaced by the corresponding unlabeled strand.

ID	Sequence (5‘ to 3‘)	Function	Replaces
B1	**Biotin-**GAAAGCCGGCGAACGTGGCGAGAAAGGAAGGGAAGAAAGCGA	biotin	X10
L1	CTGCAGGAGGCATCAACTCTCAGCAG	onset/ offset Left replacement	C3, C4
L2	CAGTGAGTTTCCCAGATGCT	onset/ offset Left replacement	
L3	GTTGAGGCTGCGCGGTCCAGGATGGTCAG**-ATTO647N**	onset/ offset Left red AT647N	
L4	**IowaBlack-**GACCTTGTCTTCAAAGAGTCCTTCAAGGA	onset Left red Iowa Black	
U1	CAGCAAGCGTCCATTTCTTG	onset Up replacement	C13
U2	**ATTO647N**-GAATCCCTGCTGGAAC	onset Up red AT647N	
U3	GTCACCGAACAGCTGCCGCGAGGCAGACC**-IowaBlack**	onset Up red Iowa Black	
U4	**ATTO542**-GAATCCCTGCTGGAAC	onset Up green AT542	
U5	GTCACCGAACAGCTGCCGCGAGGCAGACC**-BHQ2**	onset Up green BHQ2	
D1	ATTGGACAAGGGTCCTCCAGGAACTC	onset Low replacement	C12, C17
D2	ACCTGGGTCTCCTCCAGGGT	onset Low replacement	
D3	**ATTO647N-**CTTCTTCATCTCCAGGAGGTTTCGACGTT	onset Low red AT647N	
D4	TACCGGACTCTGTGTT-**IowaBlack**	onset Low red Iowa Black	
D5	**ATTO542-**CTTCTTCATCTCCAGGAGGTTTCGACGTT	onset Low green AT542	
D6	TACCGGACTCTGTGTT-**BHQ2**	onset Low green BHQ2	
O1	CCTGGTTGACGAGATCGTCCAGTTCGGCGAGTTTCCTTGAGAATGCCTG-**IowaBlack**	offset Left red Iowa Black	C8
Ri1	GCCCAAGATCTCGAGTGCTTAGACTT	onset Right replacement	C1, C2
Ri2	CCACTTTCTGATGTCATGAT	onset Right replacement	
Ri3	**ATTO542-**GCTGCGGAAATCTTCGAATTGGTTGACTG	onset Right green AT542	
Ri4	GGAGTCCTCATAGATGGTTCGAGGTAAAC-**BHQ2**	onset Right green BHQ2	
URi 1	CGTACTTCTCACTCCTCA	onset UpRight replacement	C15
URi 2	**ATTO542**-AACAAGTAGGTCTTAGT	onset UpRight green AT542	
URi 3	GATCTTTCAGGTTCAGGTGTTCTCCGCGGA**-BHQ2**	onset UpRight green BHQ2	

Table 4. Staples from the 5‘ to the 3’ end for incorporation of activation input units responsive to restriction enzyme activity and light. Staples used to form locking units responsive to restriction enzyme activity (E-staples) and light of 300-350 nm (Li-staples). The part of the staples which is used to anchor them into the core structure is shown in black whereas linker sections added for flexibility and the stems which form the DNA locks are shown in blue and red, respectively. For E-staples, the part of the stem which is designed to be responsive to restriction enzyme activity is highlighted with six bold red Xs. This section is to be replaced by the cutting sequence of the restriction enzyme the corresponding input unit is designed to be responsive to (see Table 5). In Li-1, a spacer photocleavable by light of 300-350 nm is included after the linker sequence as denoted in the sequence by PC in purple.

ID	Sequence (5‘ to 3‘)	Function	Replaces
E1	TGAGGCGGTCGTGCCAATTCATCAGGAGATAGGGATAA TTTT GCCT **XXXXXX** GTGATGTAGGTGGTAGAGG	1.1 Enzyme Unit 3'	C1, C2, C5, C9, C16
E2	CCTCTACCACCTACATCAC **XXXXXX** AGGC TTTT CACCCTGGAGGTGCGGCTCT	1.1 Enzyme Unit 5'	
E3	GGGAGTCCTCATAGATGGTTCGAG TTTT GCCT **XXXXXX** GTGATGTAGGTGGTAGAGG	1.2 Enzyme Unit 3'	
E4	CCTCTACCACCTACATCAC **XXXXXX** AGGC TTTT GCGGAAATCTTCGAATTGGTTGACTGGC	1.2 Enzyme Unit 5'	
E5	CCAAGATCTCGAGTGCTTAGACT TTTT GCCT **XXXXXX** GTGATGTAGGTGGTAGAGG	1.3 Enzyme Unit 3'	
E6	CCTCTACCACCTACATCAC **XXXXXX** AGGC TTTT GAGAAGGGACTCAATCTGGTGCAGGGAGTGATCT	1.3 Enzyme Unit 5'	
E7	TCTCATCGAAACAGAGATCTGTGATGGGAACA	1.1-3 Enzyme Units Replacement	
E8	GTAAACCCACTTTCTGATGTCATGATGCT	1.1-3 Enzyme Units Replacement	
E9	CAATCTTATATTTGATTCGCGGATGGTCACTT	1.1-3 Enzyme Units Replacement	
E10	TTGATCAGCTTCTCCGCGTGAGTTCAG TTTT GCCT **XXXXXX** GTGATGTAGGTGGTAGAGG	2.1 Enzyme Unit 3'	C6, C14, C15, C18, C19
E11	CCTCTACCACCTACATCAC **XXXXXX** AGGC TTTT GACGTACTTCTCACTCCTCAAACAAGTAGGTCTTAGT	2.1 Enzyme Unit 5'	
E12	CTCCGATGAAGTTCGTGACGCGATTGTCCTTT TTTT GCCT **XXXXXX** GTGATGTAGGTGGTAGAGG	2.2 Enzyme Unit 3'	

E13	CCTCTACCACCTACATCAC **XXXXXX** AGGC TTTT TTTTCTGCAAATTCTCCTTCCAATCC	2.2 Enzyme Unit 5'	
E14	CTGCTCCAATTTGTTCACCAGCTGTTCCCACAGCTC CCTG TTTT GCCT **XXXXXX** GTGATGTAGGTGGTAGAGG	2.3 Enzyme Unit 3'	
E15	CCTCTACCACCTACATCAC **XXXXXX** AGGC TTTT CATTGCAGTATCGCAGGTCATCGT	2.3 Enzyme Unit 5'	
E16	AGAGCTGCGTCTCCCCTCCAAGGACTT	2.1-3 Enzyme Units Replacement	
E17	TCTTGATATCGAATATGGTTGAGG	2.1-3 Enzyme Units Replacement	
E18	ATCTTTCAGGTTCAGGTGTTCTCCGCG	2.1-3 Enzyme Units Replacement	
E19	GCGAAAGGTGATCCAATCTTCATTGGAACAGATCCA G TTTTTT GCCT **XXXXXX** GTGATGTAGGTGGTAGAGG	3.1 Enzyme Unit 3'	C7, C8, C10, C11, C20
E20	CCTCTACCACCTACATCAC **XXXXXX** AGGC TTTTTT GCCACGATGGTATCGGATATTGTCGCC	3.1 Enzyme Unit 5'	
E21	CACCTGGTTGACGAGATCGTCCAGTT TTTTTT GCCT **XXXXXX** GTGATGTAGGTGGTAGAGG	3.2 Enzyme Unit 3'	
E22	CCTCTACCACCTACATCAC **XXXXXX** AGGC TTTTTT CGTGGGTAGTCAAGGGAAAGCGAGGGAAG	3.2 Enzyme Unit 5'	
E23	GCGCTGCGCTTCGACGTTATTCTT TTTTTT GCCT **XXXXXX** GTGATGTAGGTGGTAGAGG	3.3 Enzyme Unit 3'	
E24	CCTCTACCACCTACATCAC **XXXXXX** AGGC TTTTTT CACTCCTTCAGCAGCGACGGAAGATGTGTCGATGTT AGTATA	3.3 Enzyme Unit 5'	
E25	CCAGTGATCGGGTGGAGCAGCCTTG	3.1-3 Enzyme Units Replacement	
E26	CGGCGAGTTTCCTTGAGAATGCCTG	3.1-3 Enzyme Units Replacement	
E27	GAATGGCACAACTTGAGTTGTCACG	3.1-3 Enzyme	

		Units Replacement	
Li1	TGAGGCGGTCGTGCCAATTCATCAGGAGATAGGGATAA TTTT **PC** GCCTAAGCTTGTGATGTAGGTGGTAGAGG	1.1 Light Unit 3'	E1, E2
Li2	CCTCTACCACCTACATCACAAGCTTAGGC TTTT CACCCTGGAGGTGCGGCTCT	1.1 Light Unit 5'	

Table 5. Cutting sites of the used restriction enzymes from the 5‘ to the 3’ end. Sequences for the cut sites of the restriction enzymes BamHI, XhoI and StuI. Additionally, a fourth sequence is shown which is not cleavable by any of the aforementioned enzymes. Depending on which enzyme an input unit is designed to be responsive to, the sequences replace the red Xs for the corresponding E-staples in Table 4.

Restriction enzyme	Cut site (5‘ to 3‘)
BamHI	GGATCC
XhoI	CTCGAG
StuI	AGGCCT
not activatable	AAGCTT

Table 6. Staples from the 5‘ to the 3’ end for incorporation of an inhibition input units responsive to the anti-Dig antibody.

ID	Sequence (5‘ to 3‘)	Function	Replaces
A1	TGAGGCGGTCGTGCCAATTCATCAGGAGATAGGGATAA C-**Dig**	Antibody Unit - Antigen 1	C16
A2	TAACATTCCTAACTTCTCATACTCATCGAAACAGAGATCT GTG	Antibody Unit - Antigen 2 site	C9
A3	ATGGGAACAGAGAAGGGACTCAATCTGGTG	Antibody Unit - Antigen 2 Replacement	
A4	**Dig**-TTATGAGAAGTTAGGAATGTTA	Antibody Unit - Antigen 2	

Table 7. Staples from the 5‘ to the 3’ end for incorporation of activation and inhibition input units responsive to a 20 nt ssDNA input. The part of the staples which is used to anchor them into the core structure is shown in black. Linker sections added for flexibility and the ssDNA binding sites with toehold at the 5’ are shown in blue and red, respectively.

ID	Sequence (5‘ to 3‘)	Function	Replaces
DNA1	TGAGGCGGTCGTGCCAATTCATCAGGAGA TAGGGATAA TTT GCTCGACTGATG	1.1 DNA Activation/Inhibition Unit 3'	C1, C2, C5, C9, C16
DNA2	TGCAGTCG CATCAGTCGAGC TTT CACCCTGGAGGTGCGGCTCT	1.1 DNA Activation Unit 5'	
DNA3	GGGAGTCCTCATAGATGGTTCGAG TTT GCTCGACTGATG	1.2 DNA Activation/ Inhibition Unit 3'	
DNA4	TGCAGTCG CATCAGTCGAGC TTT GCGGAAATCTTCGAATTGGTTGACTGGC	1.2 DNA Activation Unit 5'	
DNA5	CCAAGATCTCGAGTGCTTAGACT TTT GCTCGACTGATG	1.3 DNA Activation/ Inhibition Unit 3'	
DNA6	TGCAGTCG CATCAGTCGAGC TTT GAGAAGGGACTCAATCTGGTGCAGGGAGT GATCT	1.3 DNA Activation Unit 5'	
DNA7	AACCCACTTTCTGATGTCATGAT	1.1-3 DNA Units Replacement	
DNA8	TCTTATATTTGATTCGCGGATGGTCA	1.1-3 DNA Units Replacement	
DNA9	CATCGAAACAGAGATCTGTGATGGGA	1.1-3 DNA Units Replacement	
DNA10	GCGAAAGGTGATCCAATCTTCATTGGAACA GATCCAG TTT GCTCGACTGATG	3.1 DNA Activation Unit 3'	C7, C8, C10, C11, C20
DNA11	TGCAGTCG CATCAGTCGAGC TTT GTATCGGATATTGTCGCC	3.1 DNA Activation Unit 5'	
DNA12	CACCTGGTTGACGAGATCGTCCAGTT TTT GCTCGACTGATG	3.2 DNA Activation Unit 3'	
DNA13	TGCAGTCG CATCAGTCGAGC TTT TGGGTAGTCAAGGGAAAGCGAGGGAAG	3.2 DNA Activation Unit 5'	
DNA14	GCGCTGCGCTTCGACGTTATTCTT TTT GCTCGACTGATG	3.3 DNA Activation Unit 3'	
DNA15	TGCAGTCG CATCAGTCGAGC TTT AGCAGCGACGGAAGATGTGTCGATGTTAG TATA	3.3 DNA Activation Unit 5'	
DNA16	GTGATCGGGTGGAGCAGCCTTGGCCACG	3.1-3 DNA Units Replacement	
DNA17	TGGCACAACTTGAGTTGTCACGCACTCC	3.1-3 DNA Units Replacement	
DNA18	CGAGTTTCCTTGAGAATGCCT	3.1-3 DNA Units Replacement	
DNA19	TGCAGTCG CATCAGTCGAGC TTT GACGTACTTCTCACTCCTCAAACAAGTAGG TCTTAGT	1.1 DNA Inhibition Unit 5'	E11, E13, E15
DNA20	TGCAGTCG CATCAGTCGAGC TTT TTTTCTGCAAATTCTCCTTCCAATCC	1.2 DNA Inhibition Unit 5'	

DNA21	TGCAGTCG CATCAGTCGAGC TTT CATTGCAGTATCGCAGGTCATCGT	1.3 DNA Inhibition Unit 5'	
DNA22	TGAGGCGGTCGTGCCAATTCATCAGGAGA TAGGGATAA TTT GTGATGTAGGTG	1.1 DNA Destabilization Unit 3'	DNA1
DNA23	CACCTACATCAC TTT GACGTACTTCTCACTCCTCAAACAAGTAGG TCTTAGT	1.2 DNA Destabilization Unit 5'	DNA19
DNA24	GACTGATG CGACTG	14nt ssDNA input	-

Table 8. Staples from the 5‘ to the 3’ end for incorporation of a cargo release output operation unit. The part of the staples which is used to anchor them into the core structure is shown in black whereas linker sections added for flexibility and the stems which form the DNA locks are shown in blue and red, respectively. The part of the sequence to which the ATTO542-labelled cargo ssDNA strand which is to be released is hybridized is shown in purple.

ID	Sequence (5‘ to 3‘)	Function	Replaces
R1	TCCTCTACCA GTATCGTAG TTTTTTTTTT AGCAGTGAGTTTCCCAGATGCTGACCT	Cargo release - Catching unit 5'	C3, C4
R2	TGTCTTCAAAGAGTCCTTCAAGGACTGC TTTTTTTTTT CTACGATAC CCTACATCAC	Cargo release - Catching unit 3'	
R3	AGGAGGCATCAACTCTCAGCAG	Cargo release - Replacement	
R4	GTTGAGGCTGCGCGGTCCAGGATGGTC	Cargo release - Replacement	
R5	GTGATGTAGGTGGTAGAGGAT-**ATTO542**	Cargo strand	-

Table 9. Staples from the 5‘ to the 3’ end for incorporation of the timing unit used to retard the transformation at a specific position. The part of the staples which is used to anker them into the core structure is shown in black. Linker sections added for flexibility and the 12 nt long locking unit which forms a stem are shown in blue and red, respectively.

ID	Sequence (5‘ to 3‘)	Function	Replaces
T1	GGGTAGTCAAGGGAAAGCGAGGGAAGGCGCTG CGCTTCGACGTTATTCTTGAATG TTT CGACTACGATAC	Timing Unit - Locking unit 12bp	C11, C20
T2	GCACAACTTGAGTTGTCACGCACTCCTTCAGCA GCGACGGAAGATGTGTCGA T GTATCGTAGTCG	Timing Unit - Locking unit 12bp	

Table 10. DNA origami array designs used in this work. For each DNA origami design, the modified staples are listed. Staples which are used as given in Tables 3-9 are listed without additional notation. Staples which are used without their corresponding modification (either highlighted in color or in bold in Tables 3-9) are listed with the addition _um. For E-staples, the included cutting site of the corresponding enzyme (Table 5) is highlighted by the addition _Enzyme or _nonAct for the corresponding enzyme cutting site and the non-cleavable sequence, respectively. The modified staples replace staples of the core mix (C- and L-staples as highlighted in Tables 3-9). For DNA origami folding, in addition to the modified staples, all unreplaced core staples are added.

No	Modified Staples	Description
1	B1, L1-4, D1-2, D5, D6_um, DNA1-9	DNA Activation Block Introduction (3x Block in Col1, Fig. 2)
2	B1, L1-4, D1-2, D5, D6_um, DNA1, DNA3, DNA5, DNA 7-9, DNA19-21, DNA2_um, DNA4_um, DNA6_um, E10_um, E12_um, E14_um, E16-18	DNA Inhibition Block Introduction (3x Block in Col1,2, Fig. 2)
3	B1, L1-4, D1-2, D5, D6_um, DNA1-18	6x DNA Activation Block (Fig. 2)
4	B1, L1-4, D1-2, D5, D6_um, E1-4_XhoI, E5-6_um, E7-9	XhoI Block Col1 Up, Mid (design 1, Fig. 3)
5	B1, L1-4, D1-2, D5, D6_um, E1-2_um, E3-6_XhoI, E7-9	XhoI Block Col1 Mid, Low (design 2, Fig. 3)
6	B1, L1-4, D1-2, D5, D6_um, E1-6_StuI, E7-9, E10-15_XhoI, E16-18	AND gate (XhoI, StuI, Fig. 3)
7	B1, L1-4, D1-2, D5, D6_um, E1-2_StuI, E3-4_um, E5-6_XhoI, E7-9	OR gate (XhoI, StuI, Fig. 3)
8	B1, L1-4, D1-2, D5, D6_um, Li1-2, E3-4_um, E5-6_XhoI, E7-9	OR gate (XhoI, Light, Fig. 3)
9	B1, L1-4, D1-2, D5, D6_um, E1-2_nonAct, E3-4_StuI, E5-6_XhoI, E7-9, E19-24_BamHI, E25-27	3xAND gate (XhoI, StuI, BamHI, Fig. 3)
10	B1, D1-3, D4_um, E1-6_BamHI, E7-9, R1-5	Cargo release by BamHI activity (Fig. 4)
11	B1, D1-3, D4_um, E1-2_nonAct, E3-4_BamHI, E5-6_XhoI, E7-9, R1-5	Cargo release by AND gate (BamHI, XhoI, Fig. 4)
12	B1, D1-3, D4_um, E1-2_BamHI, E3-4_um, E5-6_XhoI, E7-9, R1-5	Cargo release by OR gate (BamHI, XhoI, Fig. 4)
13	B1, L1-3, L4_um, O1, D1-2, D5-6, DNA1-6, E7-9, E10-15_XhoI, E16-18	full nanorobot with $\Delta t = 0$ (Fig. 5)
14	B1, L1-3, L4_um, O1, D1-2, D5-6, DNA1-6, E7-9, E10-15_XhoI, E16-18, Ti1-2	full nanorobot with $\Delta t > 0$ (Fig. 5)
15	B1, L1-4, D1-2, D5, D6_um, E1-6_BamHI, E7-9	BamHI Block Introduction (Fig. S2)
16	B1, L1-4, D1-2, D5, D6_um, E1-6_XhoI, E7-9	XhoI Block Introduction (Fig. S2)
17	B1, L1-4, D1-2, D5, D6_um, E1-6_StuI, E7-9	StuI Block Introduction (Fig. S2)
18	B1, L1-4, D1-2, D5, D6_um, Li1-2, E3-4_um, E5-6_nonAct, E7-9	Light Block Introduction (Fig. S3)
19	B1, L1-4, D1-2, D5, D6_um, A1-4	Dig Block Introduction (Fig. S4)
20	B1, L1-4, D1-2, D5, D6_um, DNA3-18, DNA1-2_um	5x DNA Activation Block (Fig. S6)

21	B1, L1-4, D1-2, D5, D6_um, DNA5-18, DNA1-4_um	4x DNA Activation Block (Fig. S6)
22	B1, L1-4, D1-2, D5, D6_um, DNA1, DNA3-19, DNA2_um, E11-15_um, E16-18	5x DNA Activation Block + 1x Inhibition Block (Fig. S6)
23	B1, L1-4, D1-2, D5, D6_um, DNA3-18, DNA22-23, DNA2_um, E11-15_um, E16-18	5x DNA Activation Block + 1x Destabilization Block (Fig. S6)
24	B1, L1-4, D1-2, D5, D6_um, E1-2_XhoI, E3-6_um, E7-9	XhoI Block Col1 Up (Fig. S8)
25	B1, L1-4, D1-2, D5, D6_um, E1-2_um, E3-4_XhoI, E5-6_um, E7-9	XhoI Block Col1 Mid (Fig. S8)
26	B1, L1-4, D1-2, D5, D6_um, E1-4_um, E5-6_XhoI, E7-9	XhoI Block Col1 Low (Fig. S8)
27	B1, L1-4, D1-2, D5, D6_um, E1-2_XhoI, E4-5_um, E5-6_XhoI, E7-9	XhoI Block Col1 Up, Low (Fig. S8)
28	B1, L1-4, D1-2, D5, D6_um, E1-6_XhoI, E7-9	XhoI Block Col1 Up, Mid, Low (Fig. S8)
29	B1, L1-4, D1-2, D5, D6_um, E10-11_XhoI, E12-15_um, E16-18	XhoI Block Col2 Up (Fig. S8)
30	B1, L1-4, D1-2, D5, D6_um, E10-11_um, E12-13_XhoI, E14-15_um, E16-18	XhoI Block Col2 Mid (Fig. S8)
31	B1, L1-4, D1-2, D5, D6_um, E10-13_um, E14-15_XhoI, E16-18	XhoI Block Col2 Low (Fig. S8)
32	B1, L1-4, D1-2, D5, D6_um, E10-13_XhoI, E14-15_um, E16-18	XhoI Block Col2 Up, Mid (Fig. S8)
33	B1, L1-4, D1-2, D5, D6_um, E10-11_XhoI, E12-13_um, E14-15_XhoI, E16-18	XhoI Block Col2 Up, Low (Fig. S8)
34	B1, L1-4, D1-2, D5, D6_um, E10-11_um, E12-15_XhoI, E16-18	XhoI Block Col2 Mid, Low (Fig. S8)
35	B1, L1-4, D1-2, D5, D6_um, E10-15_XhoI, E16-18	XhoI Block Col2 Up, Mid, Low (Fig. S8)
36	B1, L1-4, D1-2, D5, D6_um, E19-24_XhoI, E25-27	XhoI Block Col3 Up, Mid, Low (Fig. S8)
37	B1, L1-4, D1-2, D5, D6_um, E1-2_XhoI, E3-6_um, E7-9, E19-24_XhoI, E25-27	XhoI Block Col1 Up; Col3 Up, Mid, Low (Fig. S8)
38	B1, L1-4, D1-2, D5, D6_um, E1-2_um, E3-4_XhoI, E5-6_um, E7-9, E19-24_XhoI, E25-27	XhoI Block Col1 Mid; Col3 Up, Mid, Low (Fig. S8)
39	B1, L1-4, D1-2, D5, D6_um, E1-4_um, E5-6_XhoI, E7-9, E19-24_XhoI, E25-27	XhoI Block Col1 Low; Col3 Up, Mid, Low (Fig. S8)
40	B1, L1-4, D1-2, D5, D6_um, E1-4_XhoI, E5-6_um, E7-9, E19-24_XhoI, E25-27	XhoI Block Col1 Up, Mid; Col3 Up, Mid, Low (Fig. S8)
41	B1, L1-4, D1-2, D5, D6_um, E1-2_um, E3-6_XhoI, E7-9, E19-24_XhoI, E25-27	XhoI Block Col1 Mid, Low; Col3 Up, Mid, Low (Fig. S8)
42	B1, L1-4, D1-2, D5, D6_um, E1-2_XhoI, E4-5_um, E5-6_XhoI, E7-9, E19-24_XhoI, E25-27	XhoI Block Col1 Up, Low; Col3 Up, Mid, Low (Fig. S8)
43	B1, L1-4, D1-2, D5, D6_um, E1-2_StuI, E3-4_um, E5-6_XhoI, E7-9, E19-24_BamHI, E25-27	2outOf3 gate (XhoI, StuI, BamHI, Fig. S11)

44	B1, D1-2, D5-6, E1-6_StuI, E7-9	StuI Block + green Onset Block (Multiplexing, Fig. S12)
45	B1, D1-4, E1-6_XhoI, E7-9	XhoI Block + red Onset Block (Multiplexing, Fig. S12)
46	B1, L1-3, L4_um, Ri1-4	1x green Onset Block (Fig. S16)
47	B1, L1-3, L4_um, Ri1-4, URi1-3	2x green Onset Block (Fig. S16)
48	B1, L1-3, L4_um, Ri1-4, URi1-3, U1, U4-5	3x green Onset Block (Fig. S16)
49	B1, L1-3, L4_um, Ri1-4, URi1-3, U1, U4-5, D1-2, D5-6	4x green Onset Block (Fig. S16)
50	B1, L1-4, D1-2, D5-6, E1-6_BamHI, E7-9	red Onset, green Onset simultaneous (Fig. S17)
51	B1, L1-4, D1-2, D5-6, E1-6_BamHI, E7-9, Ti1-2	red Onset, green Onset delayed (Fig. S17)
52	B1, L1-2, L5-6, D1-4, E1-6_BamHI, E7-9, Ti1-2	green Onset, red Onset delayed (Fig. S17)
53	B1, L1-3, L4_um, O1 D1-2, D5, D6_um, E1-6_BamHI, E7-9	red Offset Block Introduction (+BamHI, Fig. S18)

8.4 Associated Publication P4

Super-resolved FRET and co-tracking in pMINFLUX

by

Fiona Cole[1], Jonas Zähringer[1], Johann Bohlen, Tim Schröder, Florian Steiner, Martina Pfeiffer, Patrick Schüler, Fernando D. Stefani and Philip Tinnefeld[*]
([1] These authors contributed equally, [*] Correspondence)

Nature Photonics, volume 18, pages 478-484 (**2024**)
DOI: 10.1038/s41566-024-01384-4

Author contributions:
Jonas Zähringer and I developed and conceptualized the project. Jonas Zähringer designed, performed and analyzed the FRET-MINFLUX experiments and helped with the design and analysis of the pMINFLUX multiplexing experiments. I designed, performed and analyzed the pMINFLUX multiplexing experiments and helped with the design and analysis of the FRET-MINFLUX experiments. I wrote parts of the manuscript.

nature photonics

Article

https://doi.org/10.1038/s41566-024-01384-4

Super-resolved FRET and co-tracking in pMINFLUX

Received: 10 February 2023

Accepted: 8 January 2024

Published online: 9 February 2024

Check for updates

Fiona Cole[1,4], Jonas Zähringer[1,4], Johann Bohlen[1], Tim Schröder[1], Florian Steiner[1], Martina Pfeiffer[1], Patrick Schüler[1], Fernando D. Stefani[2,3] & Philip Tinnefeld[1]

Single-molecule fluorescence resonance energy transfer (smFRET) is widely used to investigate dynamic (bio)molecular interactions occurring over distances of up to 10 nm. Recent advances in super-resolution methods have brought their spatiotemporal resolution closer towards the smFRET regime. Although these methods do not suffer from the spatial restrictions of FRET, they only visualize one emitter at a time, thus making it difficult to capture fast dynamics of the interactions. Here we describe two approaches to overcome this limitation in pulsed-interleaved MINFLUX (pMINFLUX) microscopy by using its intrinsic fluorescence lifetime information. First we combine pMINFLUX with smFRET, which enables tracking a FRET donor with nanometre precision while simultaneously determining its distance to a FRET acceptor, yielding the acceptor position by multilateration. Second, we developed pMINFLUX lifetime multiplexing—a method that simultaneously tracks two fluorophores with similar spectral properties but distinct fluorescence lifetimes—to extend co-localized tracking beyond the FRET range. We demonstrate applications on DNA origami systems as well as by imaging the paratopes of an antibody with precision better than 2 nm, paving the way for nanometre precise co-localized tracking for inter-dye distances between 4 nm and 100 nm, and closing the resolution gap between smFRET and co-tracking.

Molecular interactions and changes of conformational states are revealed using single-molecule FRET (smFRET)[1]. With its high sensitivity to small distance changes, smFRET has provided unique insight into the molecular mechanisms of life, including DNA replication[2,3], transcription[2,4], translation[5,6] and repair[3], protein folding[7,8] and various enzymatic functions[9,10]. However, its working range being limited to distances smaller than 10 nm impedes the observation of many relevant biomolecular interactions occurring at longer distances, such as protein–protein interactions in supramolecular multicomponent assemblies. Here, the co-tracking of multiple molecules of interest with nanometre precision may offer a viable alternative. However, experimental limitations such as chromatic aberrations in multicolour experiments and photon-inefficient single-molecule localizations by camera-based systems have restricted widespread applications, and in turn combined single-molecule tracking and FRET visualizations have been rare (see, for example, refs. 11–14).

In recent years, new conceptual advances such as MINFLUX[15–17]—and later MINSTED[18] and RASTMIN[19]—have demonstrated the routine localization of single-molecules with nanometre precision, thus reaching the working range of FRET. Particularly in MINFLUX, emitters are

[1]Department of Chemistry and Center for NanoScience, Ludwig-Maximilians-Universität München, Munich, Germany. [2]Centro de Investigaciones en Bionanociencias (CIBION), Consejo Nacional de Investigaciones Científicas y Técnicas (CONICET), Buenos Aires, Argentina. [3]Departamento de Física, Facultad de Ciencias Exactas y Naturales, Universidad de Buenos Aires, Buenos Aires, Argentina. [4]These authors contributed equally: Fiona Cole, Jonas Zähringer. e-mail: philip.tinnefeld@cup.uni-muenchen.de

localized by sequentially interrogating their position with spatially displaced excitation beams comprising a minimum of intensity[20]. The absolute position of emitters is estimated by comparing the number of photons emitted upon excitation with different beams of known beam profiles. MINFLUX can reach submillisecond temporal resolution ideal for tracking applications with strikingly optimized photon budgets[21,22]. So far, all MINFLUX implementations have used single-colour excitation, presumably due to the substantial increase in instrumental complexity required for multicolour excitation. Although MINFLUX multiplexing was achieved for imaging by spectral splitting[17] and exchange DNA-PAINT[23], multiplexed MINFLUX tracking experiments have not been reported.

Here, using pulsed-interleaved MINFLUX (pMINFLUX)[16,24] in a series of experiments on DNA origami model nanostructures, we demonstrate multiplexed single-molecule tracking down to the FRET range. pMINFLUX provides fast localization rates by performing the excitation sequence at the repetition rate of the laser and direct access to the fluorescence lifetime[16]. The fluorescence lifetime information enables FRET efficiency determination within the FRET range or serves as a distinguishable characteristic to separate the photons from different molecules, as previously demonstrated in fluorescence lifetime imaging microscopy and stimulated emission depletion microscopy[25–27].

First we tracked a FRET-donor-labelled DNA sequence that transitions between the vertices of a triangular structure with side lengths of 6 nm. pMINFLUX provides the donor position and simultaneously detects the proximity of a FRET acceptor by the shortened fluorescence lifetime of the donor. Calculation of the FRET efficiency enables the estimation of the inter-dye distance at the different donor positions, which, in turn, enables determining the position of the acceptor. We next introduce a concept to localize two dye molecules with similar spectra but distinct fluorescence lifetimes at distances beyond the FRET range without photoswitching. We simultaneously localized ATTO647N and AlexaFluor647 (separated by 15 nm) at a precision only slightly reduced compared with individual localizations. We then continued to use this concept to simultaneously track the position of two dye molecules that independently jump between different sites on a DNA origami, the translational and rotational motion of a DNA origami raft, and to image antibody paratopes. With a combined phasor–microtime gating approach, we extend the concept to dye molecules positioned at distances within the FRET range. These experiments altogether exemplify how MINFLUX in combination with the fluorescence lifetime information provides new insights into molecular interactions and dynamics occurring in the FRET range and beyond.

Results

Super-resolved FRET in pMINFLUX

We used a DNA origami molecular balance[28] for simultaneous pMINFLUX and FRET tracking experiments (Fig. 1a). The molecular balance features a 19-nucleotides-long (19-nt-long) single-stranded DNA pointer labelled with ATTO542 (FRET donor). The position of the donor was tracked by pMINFLUX using green excitation (Supplementary Fig. 1). The pointer transiently hybridizes to three single-stranded protrusions placed in a nearly equilateral triangle with side lengths of ~6 nm via an 8 nt complementary sequence. Cy5 (FRET acceptor) was placed at a fixed position in proximity to the protrusions on the DNA origami structure (see Supplementary Tables 2–4 for details).

To monitor FRET, the detection was spectrally split into two channels for donor and acceptor emission. The fluorescence transients recorded for ATTO542 and Cy5 show anticorrelated fluctuations between three intensity levels that are correlated with fluctuations of the donor's fluorescence lifetime (Fig. 1b), representing the DNA pointer transitioning between the three positions. Calculation of the FRET efficiency from the fluorescence lifetime of ATTO542 (Fig. 1c) reveals that the donor–acceptor distances for the three pointer positions are 5.3 nm, 6.7 nm and 9.5 nm (R_0 = 7.1 nm; Fig. 1d and Supplementary Section 2).

Localization analysis of the same pMINFLUX transient (Fig. 1b) yields the binding positions of the donor with ~1–2 nm precision at 100 ms temporal resolution. The 2D localization histogram (Fig. 1e) confirms that the DNA pointer visited the three protruding strand positions separated ~6 nm from each other.

To synergistically combine MINFLUX with FRET, each MINFLUX localization was assigned to its corresponding fluorescence lifetime. The resulting super-resolved fluorescence lifetime image (Fig. 1f) shows that ATTO542 decays with different lifetimes depending on the pointer position, confirming that both FRET and MINFLUX describe the DNA pointer dynamics well. Next, both the position of ATTO542 and its separation distance to Cy5 were determined from each pMINFLUX localization (the latter was determined by using the fluorescence lifetime information). A circle centred at the ATTO542 position with a radius of the assigned FRET distance was then defined. Doing this repeatedly as the DNA pointer explores the three positions delivered three sets of circles (Fig. 1g and Supplementary Video 1). From these circles, a multiplicative probability density map for the location of Cy5 was created (Fig. 1h and Supplementary Fig. 2). This density map featured a single peak with a full-width at half-maximum of 0.17 nm, determining the position of Cy5 in close proximity to two of the three DNA pointer locations by multilateration[29–32].

Besides multilateration, the combination of pMINFLUX localizations with their intrinsic FRET information can generally be used to track the absolute position of a molecule with pMINFLUX while simultaneously tracking the distance of a second molecule to the first molecule. Due to the simplicity of the implementation of FRET measurements on pMINFLUX set-ups, we believe that this combination has the potential to become a powerful tool for studying biological interactions; however, due to the use of FRET, the approach probes interactions that occur at distances shorter than ~12 nm. Structural information is lost if molecular interactions occur with the dyes being further apart. Thus, other methods that exploit the optical distinguishability of different emitters are required for MINFLUX.

Fluorescence lifetime multiplexing in pMINFLUX

We developed fluorescence lifetime-based pMINFLUX multiplexing to localize more than one emitter simultaneously without photoswitching. Therefore, the fluorescence intensities necessary for position estimation of each dye are obtained from fits to the fluorescence decays of the four excitation beams (Supplementary Section 3). To test the suitability of this approach, we compared pMINFLUX localizations of single AlexaFluor647 (AF647) molecules obtained from intensity counts and monoexponential fits. Localizations with both approaches exhibit negligible differences in AF647 position and localization precision (Supplementary Fig. 3).

Next we set out to localize two emitters simultaneously using lifetime multiplexing. We designed a static DNA origami with two fluorophores (AF647 and ATTO647N) placed at fixed positions with a nominal separation distance of 14.6 nm (Fig. 2a). AF647 and ATTO647N have similar spectral properties (Supplementary Fig. 4), but distinct fluorescence lifetimes of 1.1 ns and 4.3 ns, respectively. Figure 2b shows a fluorescence intensity transient with two photobleaching steps recorded for a single DNA origami structure in a pMINFLUX measurement. The fluorescence lifetime decay before the first bleaching step exhibits biexponential behaviour, indicating the presence of both dyes (time window I in Fig. 2b). After the first photobleaching event, the decay shows a monoexponential profile with a fluorescence lifetime of 4.3 ns corresponding to ATTO647N (time window II in Fig. 2b). Time window I, where both fluorophores were in their emissive state (Supplementary Fig. 5), was analysed using a biexponential fit with fixed fluorescence lifetimes. The separate fluorescence decays of AF647 and ATTO647N were extracted from the fit (Fig. 2c). The area below each decay (blue

https://doi.org/10.1038/s41566-024-01384-4

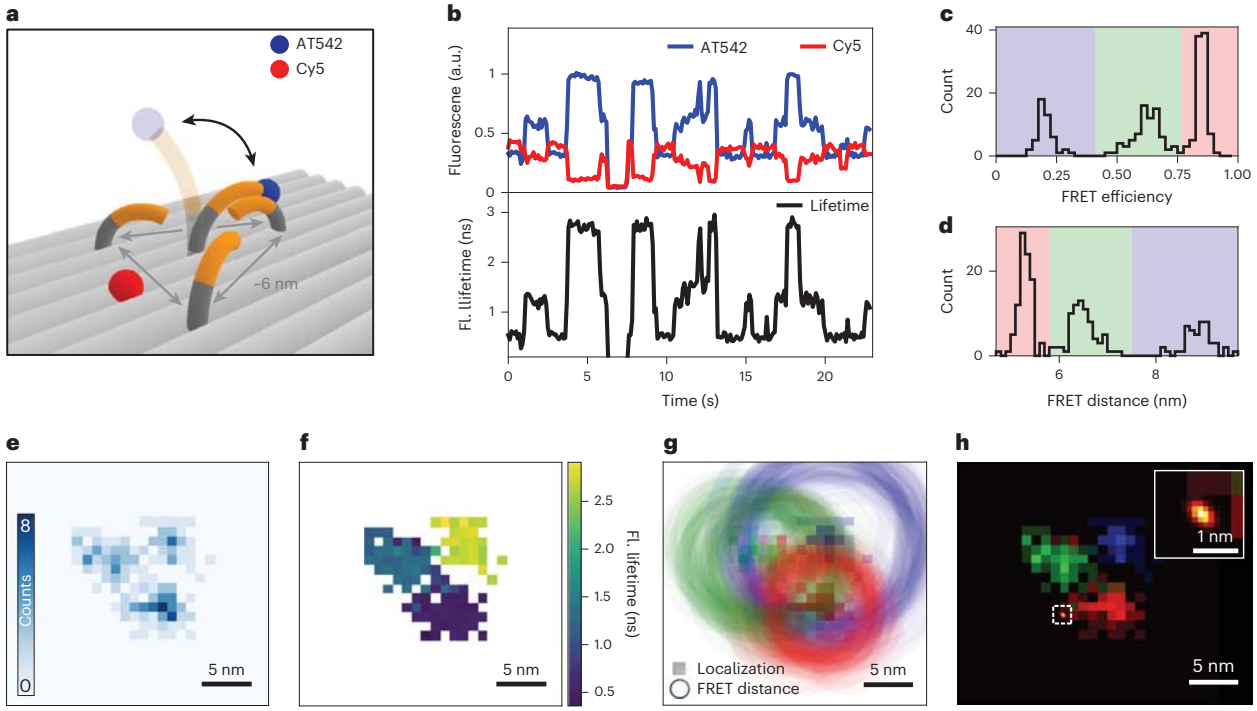

Fig. 1 | Super-resolved FRET in pMINFLUX. a, Schematic of the dynamic DNA origami with three protruding strands at distances of ~6 nm to each other, to which an ATTO542 (AT542)-labelled DNA pointer transiently hybridizes. **b**, Anticorrelated fluctuations in ATTO542 (blue) and Cy5 (red) fluorescence between three intensity levels that are correlated with fluctuations in the fluorescence lifetime of ATTO542, indicating transitions of the DNA pointer between the three positions. **c**,**d**, FRET efficiency (**c**) and distance (**d**) distributions calculated from the fluorescence lifetimes of ATTO542, featuring three distinct populations highlighted in blue, green and red. **e**, 2D histogram of the pMINFLUX localizations of the DNA pointer. **f**, Spatially resolved fluorescence lifetimes of the ATTO542 dye on the DNA pointer. **g**,**h**, Multilateration of the position of the Cy5 dye. By combining each MINFLUX localization of the DNA pointer (squares) with a FRET distance (circles) (**g**), a multiplicative probability density map of the position of the Cy5 molecule is constructed (**h**). The inset is a magnification of the area around the multilaterated Cy5 position, as highlighted by the dashed white box. The corresponding maximum in the probability density map has a full-width at half-maximum of only 0.17 nm.

and red overlays in Fig. 2c) corresponds to the fluorescence intensities obtained for AF647 and ATTO647N upon excitation with each of the four beams (Fig. 2d). Using the standard MINFLUX position estimation algorithm, both fluorophores were localized separately. The resulting 2D localization histogram features two distinct populations describing the positions of AF647 and ATTO647N, with a distance of 15.0 nm in agreement with the DNA origami design (Fig. 2e).

We tested the accuracy of lifetime multiplexing by comparing its results with localizations obtained using the so-called bleach analysis. Analogous to similar approaches in wide-field imaging[33–35], we performed measurements until both molecules photobleached. We then first localized the lasting molecule (ATTO647N) using the data in time window II. The position of the other molecule (AF647) was estimated by subtracting the average fluorescence intensity of ATTO647N from the fluorescence of both dyes in time window I (Fig. 2f and Supplementary Fig. 6). The resulting positions of both dyes match the positions obtained by lifetime multiplexing (Fig. 2g); however, in contrast to lifetime multiplexing, bleach analysis can only be applied to static systems. The localization precisions obtained with lifetime multiplexing are only about 40% worse compared with the precisions attained for MINFLUX nanoscopy of individual molecules (Supplementary Sections 8 and 9).

In contrast to conventional MINFLUX nanoscopy, lifetime-multiplexed pMINFLUX offers the possibility to track multiple emitters simultaneously on the nanoscale. For demonstration, we designed a DNA origami structure featuring two independent DNA pointers, one labelled with AF647 and the other with ATTO647N (Fig. 3a). Each DNA pointer transiently hybridizes to two single-stranded protrusions on the DNA origami distanced ~12 nm from each other.

Lifetime-multiplexed pMINFLUX enabled the simultaneous tracking of both fluorophores as they jump between the two binding positions in agreement with the designed geometrical arrangement (Fig. 3b,c and Supplementary Video 2). The kinetics of the transitions was extracted from the spatial trajectories of the DNA pointers, separately for each dye. The AF647 DNA pointer system—which features an 8 nt sequence that is complementary to the docking site—shows a mean dwell time of 1.5 s at each protrusion, whereas the ATTO647N system, with a shorter complementary sequence of 7 nt, exhibited a dwell time of 0.5 s. Due to the differing kinetics, the data were reanalysed with different temporal resolutions individually for both DNA pointers to achieve the best trade-off between temporal resolution and localization precision (Supplementary Fig. 10).

We then imaged the two paratopes of an IgG antibody simultaneously to further explore the potential of lifetime multiplexing. Inspired by an antibody detection assay[36], we bound an IgG antibody to a DNA origami structure via antigen-labelled DNA strands and positioned AF647 and ATTO647N in close proximity to the antigens to enable their imaging (Fig. 3d). Two-dimensional localization histograms of four exemplary lifetime-multiplexed pMINFLUX measurements of the construct feature two distinct populations distanced ~11 nm from each other (Fig. 3e and Supplementary Fig. 11) aligning with the range of the optimal binding distance of IgG antibodies[37,38]. The measurements indicated negligible fluctuations in the angular orientation

https://doi.org/10.1038/s41566-024-01384-4

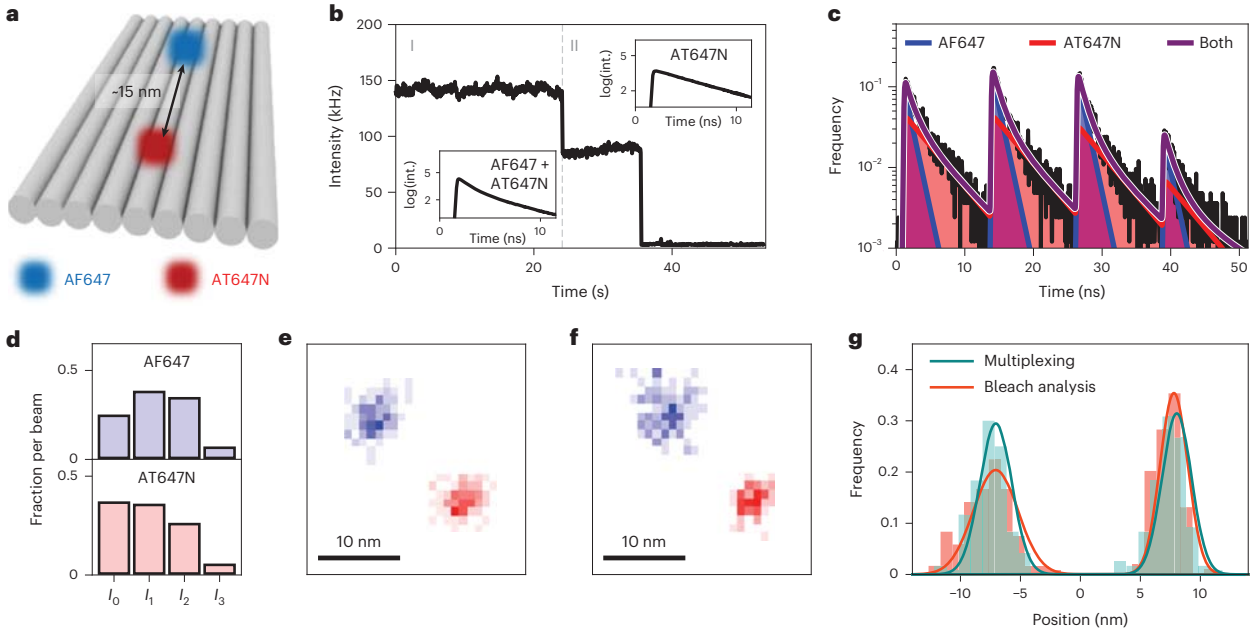

Fig. 2 | pMINFLUX lifetime multiplexing principle and accuracy. a, Schematic of a static DNA origami with AF647 and ATTO647N (AT647N) placed in a fixed distance of 14.6 nm from each other. **b**, Fluorescence intensity transient recorded for a single DNA origami structure shown in **a** during a pMINFLUX measurement. The insets show the fluorescence lifetime decays before and after the photobleaching of AF647 (dashed grey line). **c**, Fluorescence microtime decays for time window I in **b**. Biexponential fitting (purple) reveals the fluorescence decay profiles of AF647 (blue) and ATTO647N (red) separately. **d**, Relative fluorescence intensities recorded upon excitation from the four pulsed-interleaved beams for both dyes. The intensity values were extracted from the biexponential fit model shown in **c**. **e**, 2D histogram of the lifetime-multiplexed pMINFLUX localizations recorded while both dyes were simultaneously in their fluorescent state. The localizations of AF647 and ATTO647N are shown in blue and red, respectively. **f**, 2D histogram of pMINFLUX localizations of the same trace obtained by bleach analysis (Supplementary Fig. 6). **g**, Line profiles of the localizations shown in **e** and **f**, projected along the axis of both localizations. The two maxima found with both approaches correspond to the localizations of AF647 (left) and ATTO647N (right).

of the two paratopes occurring within our temporal resolution of 100 ms (Fig. 3f).

Finally, lifetime multiplexing enables the simultaneous tracking of multiple markers positioned on the same particle. This enabled the separation of the rotational and translational motion of a DNA origami raft labelled with AF647 and ATTO647N on a lipid bilayer (Fig. 3g,h and Supplementary Video 3). The motion of the raft exhibited both translational and rotational components (Fig. 3h,i) that were not observable when immobilizing the same raft on a glass surface (Supplementary Fig. 12). The orientation of the raft, as described by the angle between both fluorophores, remained relatively constant at the beginning and an onset of rotational motion was observed after 5 s (Fig. 3i).

pMINFLUX lifetime multiplexing within the FRET range

At distances compatible with FRET, fluorophores such as AF647 and ATTO647N interact and cannot be considered independent from each other. Due to the mutual overlap of excitation and emission spectra of both fluorophores, FRET occurs both from AF647 to ATTO647N and vice versa. Consequently, a detected photon cannot accurately be assigned to the excitation of a specific fluorophore, as needed for MINFLUX localizations (Fig. 4a). Instead, as the distance shortens and FRET becomes stronger, the fluorescence decay shows an increasingly monoexponential profile (Fig. 4b and Supplementary Fig. 13). Naturally, this affects the accuracy of lifetime multiplexing. Monte Carlo simulations for AF647 and ATTO647N at different distances to each other show deviations from the estimated distances to the ground truth at inter-dye distances smaller than ~10 nm (Fig. 4c). To achieve accurate localizations with pMINFLUX in the FRET range, we complemented the lifetime multiplexing with phasor analysis[39] and microtime-gated detection[28,40]. The idea is that, although the positions of the fluorophores cannot be determined directly, they can be deduced from their separation distance, the direction of the connecting vector, and the centre of mass of the two positions.

The separation distance can be obtained using the phasor approach[39]. Under this framework, emitting species with a pure monoexponential decay have a phasor lying along a so-called universal circle. As the coordinates of the phasor plot are additive, the phasor of systems of two fluorophores in which no FRET occurs lie on the line joining the individual phasors—in our case the AF647 and ATTO647N phasors (Fig. 4d). In such systems, lifetime-multiplexed pMINFLUX works well as described above. By contrast, if FRET occurs, the resulting phasor deviates from this line. In our case of mutual FRET, as the separation shortens, the coupling between the two fluorophores increases, which shows in the phasor analysis as a deviation from the AF647–ATTO647N lines towards the universal circle (Fig. 4d and Supplementary Section 13). Using a calibration with DNA origami structures containing AF647 and ATTO647N at different fixed distances, this deviation is used to estimate the separation distance between AF647 and ATTO647N in the FRET range (Fig. 4d and Supplementary Fig. 14).

The direction defined by the actual positions of AF647 and ATTO647N is then determined by combining the standard pMINFLUX localization algorithm with microtime-gated detection[28,40] (Fig. 4e). Due to the different fluorescence lifetimes of AF647 and ATTO647N, photons arriving shortly after each excitation pulse are predominantly due to AF647 emission, whereas photons with late microtimes are mainly emitted from ATTO647N. Thus, performing pMINFLUX using

https://doi.org/10.1038/s41566-024-01384-4

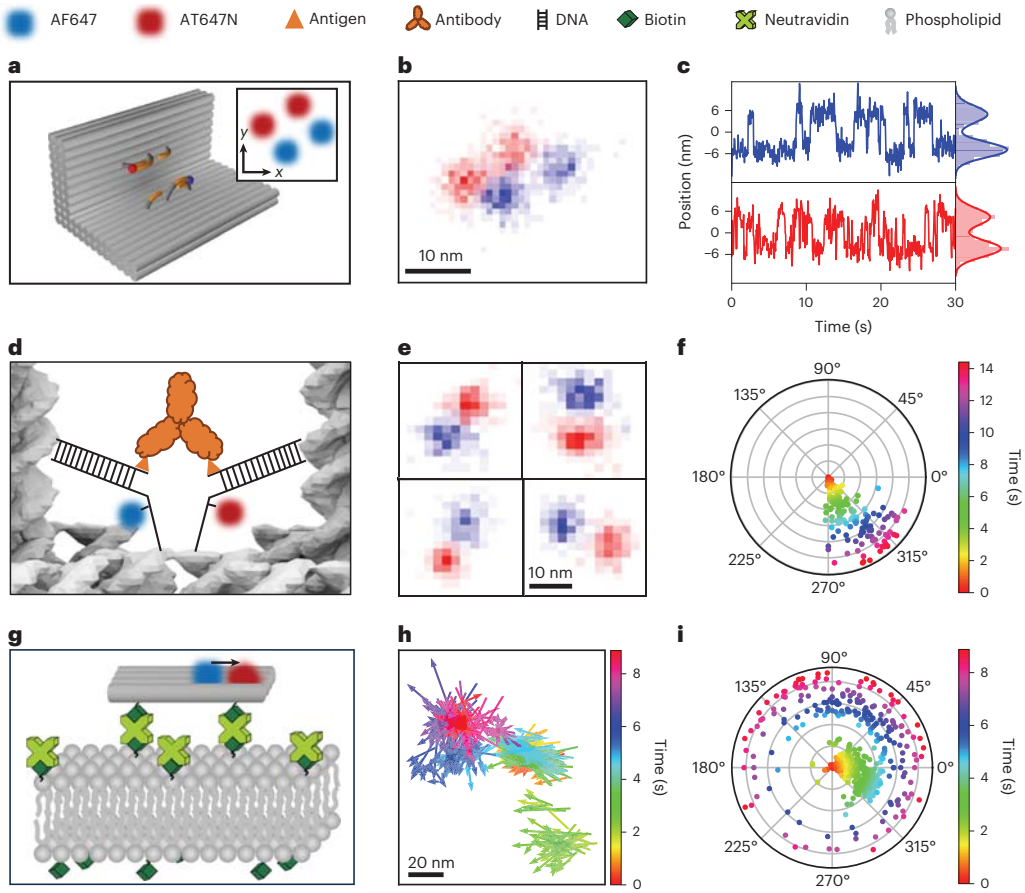

Fig. 3 | Applying pMINFLUX lifetime multiplexing to investigate molecular interactions. a, Schematic of the DNA origami with an AF647- (blue) and ATTO647N-labelled (red) DNA pointers, which independently and transiently hybridize to two protruding strands distanced ~12 nm from each other. The inset shows the *xy*-projection of the protruding strands to which AF647 (blue) and ATTO647N (red) can bind. **b**, 2D histogram of the lifetime-multiplexed pMINFLUX localizations of AF647 and ATTO647N, with each featuring two distinct positions. **c**, Localization trajectory of the AF647 (blue) and ATTO647N (red) DNA pointers, revealing uncorrelated fluctuations between two positions with different kinetics for both DNA pointers. **d**, Schematic of the DNA origami structure used to measure the distance between the paratopes of an IgG antibody. Each paratope binds to an antigen positioned on a DNA strand. These strands are hybridized to AF647/ATTO647N-labelled DNA strands protruding from the origami surface. **e**, 2D histograms of the lifetime-multiplexed pMINFLUX localizations of four DNA origami structures featuring two maxima at ~11 nm distance. Localizations of AF647 and ATTO647N are shown in blue and red, respectively. **f**, Angular distribution of the antibody orientation over time for the measurement shown in the lower right panel in **e**. The time coordinate is given by the radius. Binding to the DNA origami restricts the antibody in its rotation, thus locking it into a fixed orientation. **g**, Schematic of a DNA origami raft labelled with AF647 and ATTO647N diffusing onto a glass-supported lipid-bilayer. Biotin moieties were incorporated in the membrane and the DNA origami to mediate the attachment and diffusion through biotin–neutravidin interactions. **h**, Arrow plot of the lifetime-multiplexed pMINFLUX localizations of a single DNA origami raft over time (temporal resolution = 20 ms). The positions of AF647 and ATTO647N are indicated by the start and end points of the arrows, respectively. The plot highlights both translational and rotational movements of the raft, which are separated by pMINFLUX lifetime multiplexing. **i**, Angular distribution of the raft orientation over time. After remaining in a similar orientation for ~ 5 s, the raft begins to rotate. Dimensions are not to scale.

microtime gates at the beginning and at the end of each excitation window leads to inaccurate localizations at intermediate positions between the two molecules. Gradually increasing the size of the microtime gates gives a sequence of localizations along the line defined by the positions of the two target molecules.

Finally, performing a localization using all detected photons (no microtime gating) delivers the centre of mass of the coupled system of both fluorophores. Combining this centre of mass with the separation distance between both fluorophores as determined by phasor analysis and the direction defined by their positions extracted from microtime gating yields two absolute positions for AF647 and ATTO647N (Fig. 4f), extending the applicability of pMINFLUX lifetime multiplexing to the FRET range.

We also validated the accuracy of the phasor/microtime-gating-based localization approach in the FRET range by Monte Carlo simulations for systems with AF647 and ATTO647N placed at different distances. At distances above ~4 nm, the approach localizes both fluorophores accurately. At lower distances, high-FRET values reduce the distinguishability of both fluorophores, resulting in a lower co-localization bound of about 4–5 nm (Supplementary Figs. 13–15).

In analogy to pMINFLUX lifetime multiplexing in the fluorescence lifetime domain, we propose a multiplexing approach based on differing spectral properties of emitters that exploits small shifts in the emission spectra of different emitters (Supplementary Fig. 16). In the future, combining both approaches can be used to robustly apply multiplexing in more complex environments such as cells.

https://doi.org/10.1038/s41566-024-01384-4

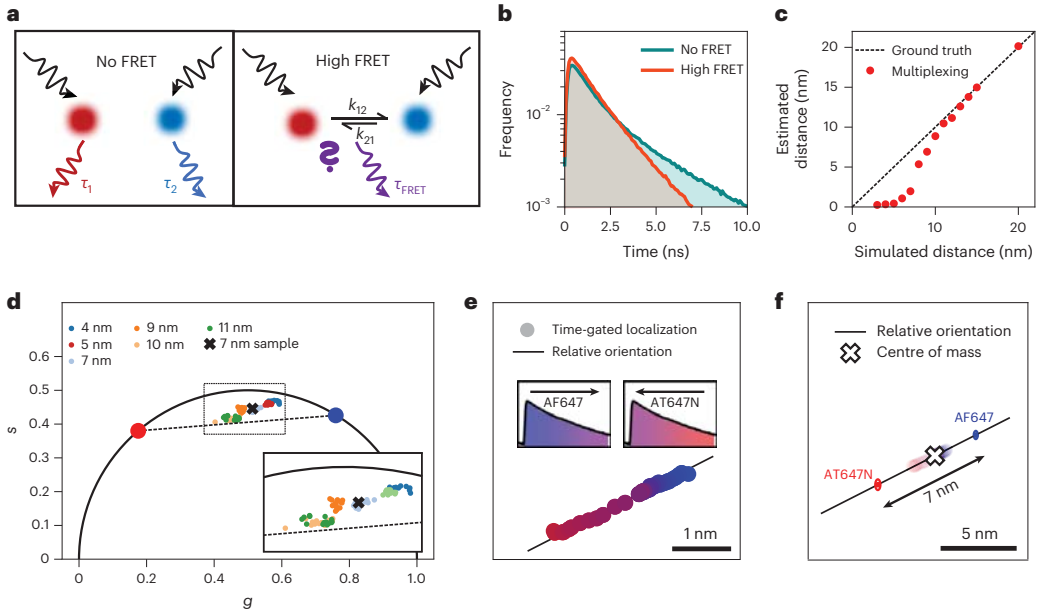

Fig. 4 | pMINFLUX lifetime multiplexing within the FRET range. a, At large distances when no FRET occurs, photon absorption and emission take place at the same emitter (fluorescence lifetimes τ_1 and τ_2). At short distances, FRET occurs in both directions (k_{12}, k_{21}) and photons are not necessarily emitted from the emitter that absorbed (fluorescence lifetime τ_{FRET}). **b**, Fluorescence lifetime decays measured for AF647 and ATTO647N at distances of 14 nm (no FRET) and 4 nm (high FRET). **c**, Accuracy of pMINFLUX lifetime multiplexing according to Monte Carlo simulations. The dashed black line indicates perfect accuracy. **d**, Phasor plots with phasor coordinates *s* and *g* for AF647 and ATTO647N placed at different distances. The red and blue dots represent pure ATTO647N and AF647, respectively. Data points on the dashed line indicate the presence of both dyes without interactions. The inset is a magnification of the boxed area. The black cross corresponds to the measurement used to demonstrate the phasor/microtime-gating-based localization approach in **e** and **f**. **e**, pMINFLUX microtime gating in the FRET range. The direction defined by the positions of AF647 and AT647N is determined by analysing subsets of photons selected in microtime windows. Increasing the size of the microtime gate from early (blue) to late detected photons (purple) after pulsed laser excitation (left inset) and from late (red) to early detected photons (right inset) yields a line of localizations along the line defined by the positions of the two target molecules (black line). The corresponding localizations are shown with a colour gradient from blue to purple for microtime gates of increasing size for the early photons and from red to purple for microtime gates of increasing size for the late photons. The colour code corresponds to the colour gradient used to visualize the gradual expansion of the microtime gates in the insets. **f**, pMINFLUX position estimation in the FRET range. Combining the distance information from the phasor plot (black arrow) with the direction from microtime gating (black line) and the centre of mass localization of the coupled system (white cross) yields an estimation of the absolute position of both dyes (blue and red ellipses).

Conclusion

In summary, we demonstrated how the fluorescence lifetime information intrinsic to pMINFLUX measurements is synergistically used to combine MINFLUX localizations with FRET. The combination allows tracking single emitters on the nanoscale while simultaneously scanning their immediate environment for the presence of acceptor molecules. We next established an approach to track multiple emitters simultaneously in pMINFLUX using only one excitation colour by assigning photons on the basis of their fluorescence lifetimes. At distances above 10 nm, the position of two emitters is estimated by implementing a biexponential fluorescence lifetime fit in the pMINFLUX localization algorithm. At lower distances, a combined phasor–microtime gating approach allows their simultaneous localization. As all developed algorithms are based solely on the microtime information of the emitters, both approaches can become generalized techniques for the simultaneous super-resolved tracking of two or more emitters. Their implementation is in principle possible by using techniques with fluorescence lifetime information such as RASTMIN[19], confocal fluorescence-lifetime single-molecule localization microscopy[41] and wide-field fluorescence lifetime imaging[42]. The findings are also not limited to 2D imaging, but should be extendable to 3D super-resolution microscopy.

Although lifetime multiplexing has the advantage of being based on a single-colour set-up, we note that multicolour excitation (p)MINFLUX measurements are possible. Here, chromatic aberrations, alignment of the beams on the sample, or coupling of multiple beams to a single fibre could become challenging aspects; however, lifetime multiplexing could be applied to each excitation colour, further expanding the multiplexing capabilities. Currently, FRET sets a lower limit for the resolution at an inter-dye distance of ~4 nm, below which photons originating from emitters become indistinguishable. An upper limit is given by the limited field of view of MINFLUX of up to ~100 nm, which could be further extended by the use of single-photon avalanche detector arrays[43]. Overall, we envision that further developing these approaches will pave the way for nanometre precise multicolour tracking experiments in living cells. They could directly visualize dynamic process such as the stepping mechanism of kinesin motor proteins[21,44] or diffusion through nuclear pore complexes on the nanoscale[45], giving direct insights into dynamic processes in interplay with their environment.

Online content

Any methods, additional references, Nature Portfolio reporting summaries, source data, extended data, supplementary information, acknowledgements, peer review information; details of author contributions and competing interests; and statements of data and code availability are available at https://doi.org/10.1038/s41566-024-01384-4.

References

1. Lerner, E. et al. Toward dynamic structural biology: two decades of single-molecule Förster resonance energy transfer. *Science* **359**, eaan1133 (2018).
2. Robinson, A. & van Oijen, A. M. Bacterial replication, transcription and translation: mechanistic insights from single-molecule biochemical studies. *Nat. Rev. Microbiol.* **11**, 303–315 (2013).
3. Stracy, M., Uphoff, S., Garza de Leon, F. & Kapanidis, A. N. In vivo single-molecule imaging of bacterial DNA replication, transcription, and repair. *FEBS Lett.* **588**, 3585–3594 (2014).
4. Alhadid, Y. et al. Studying transcription initiation by RNA polymerase with diffusion-based single-molecule fluorescence. *Protein Sci.* **26**, 1278–1290 (2017).
5. Blanchard, S. C. Single-molecule observations of ribosome function. *Curr. Opin. Struct. Biol.* **19**, 103–109 (2009).
6. Munro, J. B., Vaiana, A., Sanbonmatsu, K. Y. & Blanchard, S. C. A new view of protein synthesis: mapping the free energy landscape of the ribosome using single-molecule FRET. *Biopolymers* **89**, 565–577 (2008).
7. Gambin, Y. & Deniz, A. A. Multicolor single-molecule FRET to explore protein folding and binding. *Mol. Biosyst.* **6**, 1540–1547 (2010).
8. Schuler, B. & Eaton, W. A. Protein folding studied by single-molecule FRET. *Curr. Opin. Struct. Biol.* **18**, 16–26 (2008).
9. Sasmal, D. K., Pulido, L. E., Kasal, S. & Huang, J. Single-molecule fluorescence resonance energy transfer in molecular biology. *Nanoscale* **8**, 19928–19944 (2016).
10. Weikl, T. R. & Paul, F. Conformational selection in protein binding and function. *Protein Sci.* **23**, 1508–1518 (2014).
11. Sako, Y., Minoghchi, S. & Yanagida, T. Single-molecule imaging of EGFR signalling on the surface of living cells. *Nat. Cell Biol.* **2**, 168–172 (2000).
12. Winckler, P. et al. Identification and super-resolution imaging of ligand-activated receptor dimers in live cells. *Sci. Rep.* **3**, 2387 (2013).
13. Asher, W. B. et al. Single-molecule FRET imaging of GPCR dimers in living cells. *Nat. Methods* **18**, 397–405 (2021).
14. Mieskes, F., Ploetz, E., Wehnekamp, F., Rat, V. & Lamb, D. C. Multicolor 3D orbital tracking. *Small* **19**, e2204726 (2023).
15. Balzarotti, F. et al. Nanometer resolution imaging and tracking of fluorescent molecules with minimal photon fluxes. *Science* **355**, 606–612 (2017).
16. Masullo, L. A. et al. Pulsed Interleaved MINFLUX. *Nano Lett.* **21**, 840–846 (2021).
17. Gwosch, K. C. et al. MINFLUX nanoscopy delivers 3D multicolor nanometer resolution in cells. *Nat. Methods* **17**, 217–224 (2020).
18. Weber, M. et al. MINSTED fluorescence localization and nanoscopy. *Nat. Photonics* **15**, 361–366 (2021).
19. Masullo, L. A. et al. An alternative to MINFLUX that enables nanometer resolution in a confocal microscope. *Light Sci. Appl.* **11**, 199 (2022).
20. Stefani, F. D. Tracking nanoscopic motion with minima of light. *Nat. Photon.* **17**, 552–553 (2023).
21. Deguchi, T. et al. Direct observation of motor protein stepping in living cells using MINFLUX. *Science* **379**, 1010–1015 (2023).
22. Eilers, Y., Ta, H., Gwosch, K. C., Balzarotti, F. & Hell, S. W. MINFLUX monitors rapid molecular jumps with superior spatiotemporal resolution. *Proc. Natl Acad. Sci. USA* **115**, 6117–6122 (2018).
23. Ostersehlt, L. M. et al. DNA-PAINT MINFLUX nanoscopy. *Nat. Methods* **19**, 1072–1075 (2022).
24. Zähringer, J. et al. Combining pMINFLUX, graphene energy transfer and DNA-PAINT for nanometer precise 3D super-resolution microscopy. *Light Sci. Appl.* **12**, 70 (2023)
25. Betzig, E. Proposed method for molecular optical imaging. *Opt. Lett.* **20**, 237–239 (1995).
26. Heilemann, M. et al. High-resolution colocalization of single dye molecules by fluorescence lifetime imaging microscopy. *Anal. Chem.* **74**, 3511–3517 (2002).
27. Bückers, J., Wildanger, D., Vicidomini, G., Kastrup, L. & Hell, S. W. Simultaneous multi-lifetime multi-color STED imaging for colocalization analyses. *Opt. Express* **19**, 3130–3143 (2011).
28. Schröder, T. et al. Shrinking gate fluorescence correlation spectroscopy yields equilibrium constants and separates photophysics from structural dynamics. *Proc. Natl Acad. Sci. USA* **120**, e2211896120 (2023).
29. Mahalingam, M. et al. Structural mapping of divergent regions in the type 1 ryanodine receptor using fluorescence resonance energy transfer. *Structure* **22**, 1322–1332 (2014).
30. Svensson, B. et al. FRET-based trilateration of probes bound within functional ryanodine receptors. *Biophys. J.* **107**, 2037–2048 (2014).
31. Muschielok, A. et al. A nano-positioning system for macromolecular structural analysis. *Nat. Methods* **5**, 965–971 (2008).
32. Muschielok, A. & Michaelis, J. Application of the nano-positioning system to the analysis of fluorescence resonance energy transfer networks. *J. Phys. Chem. B* **115**, 11927–11937 (2011).
33. Qu, X., Wu, D., Mets, L. & Scherer, N. F. Nanometer-localized multiple single-molecule fluorescence microscopy. *Proc. Natl Acad. Sci. USA* **101**, 11298–11303 (2004).
34. Ram, S., Ward, E. S. & Ober, R. J. Beyond Rayleigh's criterion: a resolution measure with application to single-molecule microscopy. *Proc. Natl Acad. Sci. USA* **103**, 4457–4462 (2006).
35. Gordon, M. P., Ha, T. & Selvin, P. R. Single-molecule high-resolution imaging with photobleaching. *Proc. Natl Acad. Sci. USA* **101**, 6462–6465 (2004).
36. Pfeiffer, M. et al. Single antibody detection in a DNA origami nanoantenna. *iScience* **24**, 103072 (2021).
37. Shaw, A. et al. Binding to nanopatterned antigens is dominated by the spatial tolerance of antibodies. *Nat. Nanotechnol.* **14**, 184–190 (2019).
38. Zhang, P. et al. Capturing transient antibody conformations with DNA origami epitopes. *Nat. Commun.* **11**, 3114 (2020).
39. Digman, M. A., Caiolfa, V. R., Zamai, M. & Gratton, E. The phasor approach to fluorescence lifetime imaging analysis. *Biophys. J.* **94**, L14–L16 (2008).
40. Hedley, G. J. et al. Picosecond time-resolved photon antibunching measures nanoscale exciton motion and the true number of chromophores. *Nat. Commun.* **12**, 1327 (2021).
41. Thiele, J. C. et al. Confocal fluorescence-lifetime single-molecule localization microscopy. *ACS Nano* **14**, 14190–14200 (2020).
42. Oleksiievets, N. et al. Wide-field fluorescence lifetime imaging of single molecules. *J. Phys. Chem. A* **124**, 3494–3500 (2020).
43. Slenders, E. & Vicidomini, G. ISM-FLUX: MINFLUX with an array detector. *Phys. Rev. Res.* **5**, 023033 (2023).
44. Carter, N. J. & Cross, R. A. Mechanics of the kinesin step. *Nature* **435**, 308–312 (2005).
45. Timney, B. L. et al. Simple rules for passive diffusion through the nuclear pore complex. *J. Cell Biol.* **215**, 57–76 (2016).

Methods

Preparation of DNA origami structures

DNA origami structures were designed using the open-source software caDNAno2[46], and assembled and purified using published protocols[47]. Positions and distances of dyes in DNA origami structures were estimated assuming a distance of 0.34 nm between the nucleotides along the DNA double helix and 2.7 nm between the centres of adjacent helices[48,49]. See Supplementary Tables 2–9 for the exact sequences of all of the unmodified and modified DNA staple strands used to fold the DNA origami structures. DNA staple strands were purchased from Eurofins Genomics GmbH and Integrated DNA Technologies. The p8064 scaffold used for the dynamic pointer and the antibody-binding origami, and the p7049 used for the static two-colour origami, were produced in house (both were derived from M13mp18 bacteriophages).

For DNA origami folding of the dynamic pointer and static two-colour origami, 10 nM of scaffold in 1× TAE, diluted from a 50× TAE stock (Sigma-Aldrich, catalogue no. 1061741000; pH 8) containing 12.5 mM/20 mM $MgCl_2$ (Sigma-Aldrich, catalogue no. M8266; static/dynamic origami) was mixed with a tenfold (30-fold) excess of all unmodified (modified) oligonucleotides. The mixture was heated to 65 °C and kept at this temperature for 15 min before being cooled down to 25 °C either with a temperature gradient of −1 °C min^{-1} (static origami), or with a non-linear thermal annealing ramp over 16 h (ref. 50; dynamic origami). Folded DNA origami were purified from excessive staple strands by gel electrophoresis. Gels were ran using a 1.5% agarose gel, 1× TAE containing 12.5 mM $MgCl_2$ for 2 h at 6 V cm^{-1}. The target band containing DNA origami was cut from the gel and DNA origami solution extracted from the band via squeezing.

For the DNA origami structure used to bind antibodies, 25 µl of p8064 scaffold at 100 nM were mixed with 18 µl of unmodified staples pooled from 100 µM original concentration and 2 µl of modified staples pooled from 100 µM original concentration. For DNA origami folding, 5 µl of 10× FoB20 folding buffer (200 mM $MgCl_2$, 50 mM Tris (Sigma-Aldrich, catalogue no. 648314), 50 mM NaCl (Sigma-Aldrich, catalogue no. S9888) and 10 mM EDTA (Sigma-Aldrich, catalogue no. 03620)) were added and the mixture was subjected to a non-linear thermal annealing ramp over 16 h (ref. 50). Folded DNA origamis were purified from excessive staple strands using 100 kDa Amicon Ultra filters (Merck, catalogue no. MPUFC510024) with six washing steps with a lower ionic strength buffer (5 mM $MgCl_2$, 5 mM Tris, 5 mM NaCl, 1 mM EDTA) at 10 krcf for 5 min and 20 °C. To extract the purified origami, the filter was inverted in a new Eppendorf tube and the sample was recovered by spinning for 2 min at 1 krcf and 20 °C. Samples were stored at −20 °C until further use.

Preparation of small unilamellar vesicles

Small unilamellar vesicles (SUVs) were prepared from a 1 µmol mixture of 99% 1,2-dioleoyl-*sn*-glycero-3-phosphocholine (DOPC; Avanti Polar Lipids, catalogue no. 850375P) and 1% 1,2-dioleoyl-*sn*-glycero-3-phosphoethanolamine-*N*-(cap-biotinyl) (Biotinyl Cap PE; Avanti Polar Lipids, catalogue no. 870273P) dissolved in chloroform. The mixture was added to a glass vial; the solvent was dried under nitrogen stream and further for 4 h under vacuum. Lipid films were resuspended in 500 µl HBS-Mg buffer (20 mM Hepes (Sigma-Aldrich, catalogue no. H4034), 150 mM NaCl and 5 mM $MgCl_2$). For unilamellarity, seven freeze–thaw cycles were performed before extrusion through a 50 nm nuclepore PC membrane to get SUVs. The SUVs were then used to create glass-supported lipid-bilayers as described below.

Surface sample preparation for pMINFLUX measurements

Flow chambers, consisting of a glass coverslip glued onto an objective slide with double-sided scotch tape, were used as sample chambers. Before chamber assembly, coverslips were cleaned by incubation with 1% Hellmanex (Hellma, catalogue no. 9-307-011-4-507) for 20 min followed by two 15 min washing steps with MilliQ water. After surface passivation by incubation with BSA-Biotin (0.5 mg ml^{-1}, Sigma-Aldrich, catalogue no. A8549-10MG) for 10 min, the surface was washed with 200 µl 1× PBS buffer (137 mM NaCl, 2.7 mM KCl, 10 mM Na_2HPO_4, 1.8 mM KH_2PO_4; pH 8, Merck, catalogue no. 524650). For the glass-supported lipid-bilayer samples, the incubation step with BSA-Biotin was replaced by 10 min incubation of a 1:7 dilution of the SUV solution in HBS-Mg buffer; 150 µl neutrAvidin (0.25 mg ml^{-1}, Thermo Fisher Scientific, catalogue no. 31050) was incubated for 10 min and then washed with 200 µl 1× PBS buffer. DNA origami solution was diluted in 1× TE buffer (10 mM Tris, 1 mM EDTA) containing 750 mM NaCl, to a concentration of ~100 pM, and then immobilized on the biotin–neutravidin surface via biotin–neutravidin interactions. For this, 100 µl of the DNA origami sample solution was added and incubated for 5 min. Residual unbound DNA origami was removed by washing the chambers with 150 µl 1× TE buffer containing 750 mM NaCl. Next, gold nanorods with a longitudinal localized surface plasmon resonance peak at 900 nm (fabricated following established protocols)[51] were immobilized on the surface as fiducial markers for drift correction. Chambers were incubated with a diluted gold nanorod solution in 1× TAE containing 12.5 mM $MgCl_2$ for 2 min and flushed with 150 µl 1× TAE (12.5 mM $MgCl_2$). For the antibody measurements, the samples were then further incubated with 100 nM anti-Dig antibodies (Rb Monoclonal, Thermo Fisher Scientific, catalogue no. 700772, PRID: AB_2532342) in 1× TE buffer (10 mM Tris, 1 mM EDTA) containing 750 mM NaCl for 30 min at room temperature. Directly before MINFLUX measurements, an oxidizing and reducing buffer system (1× TAE, 12.5 mM $MgCl_2$, 2 mM Trolox/Troloxquinone; Merck, catalogue no. 238813)[52] was added to all samples in combination with an oxygen scavenging system (12 mM protocatechuic acid (Merck, catalogue no. 03930590), 56 µM protocatechuate 3,4-dioxygenase from Pseudomonas sp. (Merck, catalogue no. P8279-25UN), 1% glycerol (Merck, catalogue no. G5516), 1 mM KCl (Merck, catalogue no. 529552), 2 mM Tris and 20 µM EDTA) to suppress blinking and photobleaching. No blinking was observed under these conditions for AF647 and ATTO47N. Photostabilization chambers were then sealed with picodent twinsil and measured.

pMINFLUX set-up

A description of the pMINFLUX set-up is given in the first pMINFLUX implementation[16]. See Supplementary Section 1 for details.

Data analysis

Data processing and analysis of the MINFLUX experiments was realized using custom-written Python scripts. A description of the used algorithms is provided in the Supplementary Information. All Python scripts used for data analysis are available from the authors on request.

Data availability

All data are available from the corresponding author on reasonable request.

Code availability

Codes used in this study are available from the corresponding author on reasonable request.

References

46. Douglas, S. M. et al. Rapid prototyping of 3D DNA-origami shapes with caDNAno. *Nucleic Acids Res.* **37**, 5001–5006 (2009).
47. Wagenbauer, K. F. et al. How we make DNA origami. *Chembiochem* **18**, 1873–1885 (2017).
48. Fischer, S. et al. Shape and interhelical spacing of DNA origami nanostructures studied by small-angle X-ray scattering. *Nano Lett.* **16**, 4282–4287 (2016).
49. Ke, Y. et al. Multilayer DNA origami packed on a square lattice. *J. Am. Chem. Soc.* **131**, 15903–15908 (2009).
50. Nickels, P. C. et al. Molecular force spectroscopy with a DNA origami-based nanoscopic force clamp. *Science* **354**, 305–307 (2016).

51. Wang, S. et al. Three-photon luminescence of gold nanorods and its applications for high contrast tissue and deep in vivo brain imaging. *Theranostics* **5**, 251–266 (2015).
52. Cordes, T., Vogelsang, J. & Tinnefeld, P. On the mechanism of Trolox as antiblinking and antibleaching reagent. *J. Am. Chem. Soc.* **131**, 5018–5019 (2009).

Acknowledgements

P.T. is grateful for support from the Deutsche Forschungsgemeinschaft (DFG, German Research Foundation)—Project-ID 201269156—SFB 1032 Project A13 and funding by the Bavarian Ministry of Science and the Arts through the ONE MUNICH Project 'Munich Multiscale Biofabrication'. P.T. is indebted to the DFG for funding via grant nos. 470075523 and 459594986, and Germany's Excellence Strategy (grant no. EXC 2089/1-390776260). We thank P. Luna, P. Xaverl and T. Charly for their support with the measurements and data analysis, and A. Kardinal, H. Lipfert, S. Steger and M. Ehrl for laboratory upkeep.

Author contributions

F.C., J.Z., T.S., F.S., F.D.S. and P.T developed the concept. F.C., J.Z. and J.B. designed and prepared samples. M.P. designed and prepared antibody samples. P.S. designed and prepared lipid bilayer samples. F.C. and J.Z. performed and analysed measurements. P.T. supervised the project. All authors have written, read and approved the final manuscript.

Competing interests

The authors declare no competing interests.

Additional information

Supplementary information The online version contains supplementary material available at https://doi.org/10.1038/s41566-024-01384-4.

Correspondence and requests for materials should be addressed to Philip Tinnefeld.

Peer review information *Nature Photonics* thanks the anonymous reviewers for their contribution to the peer review of this work.

nature photonics

Article

https://doi.org/10.1038/s41566-024-01384-4

Super-resolved FRET and co-tracking in pMINFLUX

In the format provided by the authors and unedited

Table of Contents

Supplementary Section 1. pMINFLUX setup.

The pMINFLUX setup is described in the original pMINFLUX publication.[1] Depending on the excitation color, different optical elements such as filters, the vortex phase plate or polarization optics are used, however the beam path remains unchanged (see Supplementary Figure 1).

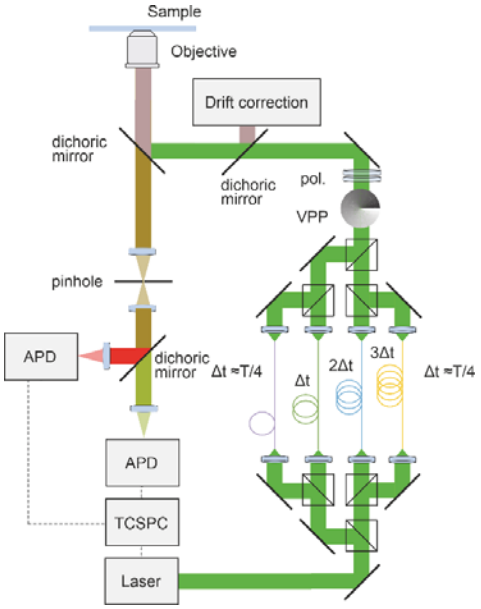

Supplementary Figure 1: pMINFLUX setup. A pulsed laser is split into four beams using beam splitters and coupled into optical fibers which delay the laser pulses as a function of the length of the fiber. The beams are recombined and doughnut-shaped beams are created with a vortex phase plate and polarization optics. The beams are focused onto the sample arranged in a triangular pattern with the fourth beam placed at the center of the triangle. For detection, APDs are used in combination with a TCSPC unit.

Excitation. A supercontinuum laser (SuperK Fianium FIU-15, NKT Photonics GmbH, Germany) is used at 19.5 MHz repetition rate as light source in combination with a tunable bandpass filter (SuperK VARIA, NKT Photonics GmbH, Germany) to select the desired wavelength range in the visible light spectrum. An additional clean-up filter (green: FLH532-10, Thorlabs GmbH, Germany, red: ZET 635/10, Chroma, USA) is used to further spectrally clean the excitation beam. Using a polarizing beam splitter cube (PBS251, Thorlabs GmbH, Germany), the light is split into two beams of orthogonal polarizations. Each of the beams is further split by a non-polarizing 50:50 beam splitter cube (BS013, Thorlabs GmbH, Germany). This beam splitting system generates two pairs of beams with each pair sharing the orthogonal linear polarization. The resulting four laser beams are coupled into polarization maintaining single-mode fibers (PM-S405-XP, Thorlabs GmbH, Germany) of lengths 2.0 m, 4.6 m, 7.1 m and 9.7 m such that the time delay between the beams after the fiber is ~12.5 ns (= T/4). The four beams are collimated after the fibers with an achromatic lens (AC254-035-A, Thorlabs GmbH, Germany) and recombined by using three 50:50 beam splitter cubes (BS013, Thorlabs GmbH, Germany). The overlay of the beams can be adjusted to

obtain the required arrangement of laser foci in the object plane. The axes of linear polarization are matched by turning the fiber out-couplers (Thorlabs GmbH, Germany). Subsequently, the linearly polarized laser beams pass a combination of a quarter- and a half-wave plate (green: WPQ05M-532 and WPH532M532, Thorlabs GmbH, Germany; red: additional linear polarizer: LPVISC100-MP2, Thorlabs GmbH, Germany, RAC 5.2.10, B. Halle, Germany, WPQ05M-633, Thorlabs GmbH, Germany) to make them circularly polarized. A vortex phase plate (green: VPP, V-532-20-1, Vortex Photonics, Germany; red: VPP, V-633-20-1, Vortex Photonics, Germany) is then used to introduce the phase modulation necessary to generate the doughnut-shaped foci. The beams are guided into the back entrance of the microscope body (IX83, Olympus Deutschland GmbH, Germany), reflected on a dichroic mirror (ZT532/640rpc flat– STED, Chroma Technology Corp., USA) and focused with an objective (UPLSAPO100XO/1.4, Olympus Deutschland GmbH, Germany) onto the sample plane.

Detection. The fluorescence light is collected with the same objective and transmitted through the dichroic mirror, focused via an Olympus tube lens onto a pinhole (120 µm, Owis, Germany), collimated with an achromatic lens (AC254-150-A, Thorlabs GmbH, Germany) and spectrally split with a dichroic mirror (640 RDC dichroic mirror, Chroma, USA). The beams then are focused with a second achromatic lens (AC127-025-A, Thorlabs GmbH, Germany) to the chip of an avalanche photodiode (SPCM-AQRH-16-TR, Excelitas Technologies GmbH & Co. KG, Germany) after filtering the remaining scattered light from the laser with suitable interference optical filters (785 SP EdgeBasic, Semrock Inc., USA, green: 582/75 Brightline HC, Semrock Inc. USA, red: 700/75 ET Bandpass, Chroma, USA). The digital signal from the APD is sent to a TCSPC unit (HydraHarp 400, PicoQuant GmbH, Germany).

Drift correction. To measure and correct for sample drift during the measurement, the IR output of the variable bandpass filter is used. A beam of wavelength between 850 and 900 nm is selected with optical filters (875/50 bandpass, Edmund Optics GmbH), coupled into a single-mode fiber (780HP, Thorlabs GmbH, Germany), outcoupled and collimated. This beam is then split with a 50:50 beam splitter cube (BS014, Thorlabs GmbH, Germany) and combined again after inserting a lens system (ACN254-040-B, AC254-150-B, Thorlabs GmbH, Germany) into one of the two paths that focuses the beam to the back focal plane of the objective (dotted line) to create a widefield illumination at the sample plane. This beam is used for xy drift correction where the position of fiducial markers is localized during the measurement. The collimated IR beam is focused onto the sample plane at an oblique angle to achieve a z position-dependent spot at the detector and use this for z drift correction. Both IR beams are coupled to the main beam path via a dichroic mirror (ZT 785 SPXXR, Chroma Technology Corp., USA) and fed into the microscope to illuminate a region close, but not overlapping with the field of view used for MINFLUX. The reflected and backscattered light is split with an additional 50:50 beam splitter cube (BS014,

Thorlabs GmbH, Germany) from the excitation IR beam and detected on a single CMOS camera (Zelux, Thorlabs GmbH, Germany) at different positions of the chip.

Setup control. The piezo stage (P733.3CD, Physik Instrumente (PI) GmbH &Co. KG, Germany) translates the sample in all three dimensions with a resolution of 0.3 nm when running in closed loop mode. All components of the setup including the piezo stage are controlled digitally and integrated via a custom version of the PyFLUX project. Further details and source-code of this control software version are available at https://github.com/zaehringer-Jonas/pyflux

Alignment. For measurement the four vortex beams were aligned in a fixed triangular excitation beam pattern (EBP), with L ≈ 100-150 nm.

Supplementary Section 2. FRET multilateration algorithm

Determination of FRET distances

The fluorescence lifetime of ATTO542 was determined via a fluorescence lifetime fit on the photons arriving at the green detection channel. The microtimes of these photons were extracted for each of the four excitation windows. They were then rebinned according to their maximal microtime bin in each excitation window and the resulting single histogram fitted with an IRF re-convoluted exponential fit. The fit model included an additional background component the weight of which was determined by a separate background measurement. By fitting each 'localization bin' in the time trace, the fluorescence lifetime of ATTO542 was extracted separately for each localization.

The FRET efficiency E_{FRET} between two molecules was then calculated from the following equation:

$$E_{FRET} = 1 - \frac{\tau_{FRET}}{\tau_0}$$

where τ_{FRET} and τ_0 are the fluorescence lifetimes of the FRET donor in presence and absence of the FRET acceptor, respectively. In the FRET pointer system, a fluorescence lifetime of τ_0 = 3.3 ns was measured for ATTO542 in absence of the Cy5 acceptor.

As the FRET efficiency between two dye molecules depends on the distance r between them with an inverse 6th-power law, it can also be described as a function of this distance.

$$E_{FRET} = \frac{1}{1 + \left(\frac{r}{R_0}\right)^6}$$

where R_0, the so-called Förster distance, defines the inter-dye distance at which 50% energy transfer occurs. For the donor-acceptor pair ATTO542/ Cy5 in the FRET pointer system, we assumed a Förster distance of R_0 = 7.06 nm.

By combining both equations, the distance between ATTO542 and Cy5 was calculated for each MINFLUX localization using the corresponding measured fluorescence lifetime τ_{FRET}.

$$r = R_0 \sqrt[6]{\frac{1}{\frac{\tau_0}{\tau_{FRET}} - 1}}$$

Multilateration of FRET acceptor position

The position of the red acceptor fluorophore in the FRET pointer measurement was multilaterated by combining each pMINFLUX localization with its respective FRET radius. For each localization of the ATTO542 donor fluorophore, a circle centered

around the localization with a radius corresponding to the FRET radius of the localization was drawn. These circles were convoluted with a Gaussian distribution with a standard deviation corresponding to the uncertainties in position and radius of the circle. The uncertainty in position of the circle center was estimated by the precision of the ATTO542 localizations. The uncertainty in radius was calculated in an error propagation of the error of the fluorescence lifetime fit. The resulting density maps describe the probability of the FRET acceptor to be found at different positions, individually for each localization.

To multilaterally localize the FRET acceptor, multiple of these density maps were combined in a multiplicative fashion. The Gauss-convoluted FRET circles of all localizations were multiplied, resulting in the multiplicative density map shown in Fig, 1H.

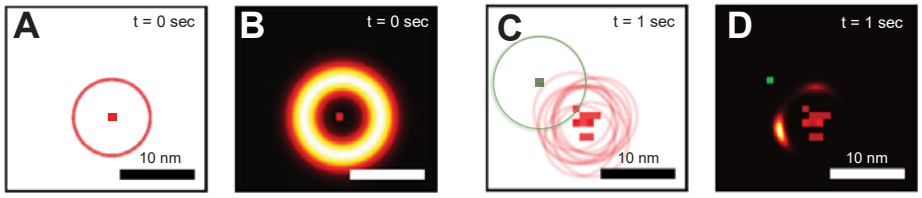

Supplementary Figure 2: Multilateration of a FRET acceptor position by pMINFLUX. By combining FRET donor (ATTO542) localizations (squares) with FRET distances (calculated through the corresponding fluorescence lifetimes of the FRET donor, circles), a probability density map for the location of the FRET acceptor (Cy5) was created. (A, C) FRET donor location and FRET distance combinations for (A) the first measurement point and (C) after 1 sec of measurement. (B,D) corresponding multiplicative probability density maps for the location of the FRET acceptor.

Supplementary Section 3. pMINFLUX lifetime multiplexing algorithm

Model fit function

The fluorescence decay of a single emitter $F(t)$ can be described by the probability density function (PDF) of an exponential distribution.

$$F(t) = \tau^{-1} \exp\left(-\frac{t}{\tau}\right) u(t)$$

where t is the emission time of a photon with respect to the preceding laser pulse, τ denotes the fluorescence lifetime of the corresponding emitter and $u(t)$ is the unit step function of t.

To correct for the instrument response function (IRF) and temporal crosstalk due to the finite repetition period T of pulsed lasers, the fluorescence decay is convolved with the IRF, and the fluorescence signal of the preceding excitation pulse added to the recorded fluorescence intensity.

$$I(t) = \sum_{i=0}^{1} F(t + iT, \tau) \star \mathrm{irf}$$

where $I(t)$ is the PDF of the measured fluorescence intensity, irf the normalized IRF and $\star$ the convolution operator.

In pMINFLUX, emitters are excited by four different, temporally delayed beam pulses per repetition period. The fit model thus is expanded to account for four beam pulses with the IRFs $\mathrm{irf_j}$.

$$I(t) = \sum_{j=0}^{3} a_j \sum_{i=0}^{1} F(t + iT, \tau) \star \mathrm{irf}_j$$

Here, a_j describes the integrated fluorescence intensity upon excitation by beam *j*. To maintain normalization of the PDF, a_j must be normalized to the accumulated integrated fluorescence intensity caused by all beams such that $\sum_j a_j = 1$.

To account for the fluorescence of multiple emitters, the fit model is expanded further to include the fluorescence decay of K emitters of different lifetimes τ_k.

$$\sum_{j=0}^{3} a_j \sum_{k=0}^{K} b_{jk} \sum_{i=0}^{1} F(t + iT, \tau_k) \star \mathrm{irf}_j$$

where b_{jk} describes the integrated fluorescence intensity of emitter k upon excitation with beam j. Similar to a_j, the ratios of b_{jk} must be normalized to the accumulated integrated fluorescence intensity of all emitters excited by beam k such that $\sum_k b_{jk} = 1$.

Contributions from background photons are included by adding a fraction γ of background signal $\mathrm{bg}(t)$ added to the model fit function. The final model fit function thus is described by the following equation.

$$I(t) = (1-\gamma)\left[\sum_{j=0}^{3} a_j \sum_{k=0}^{K} b_{jk} \sum_{i=0}^{1} F(t+iT, \tau_k) \star \mathrm{irf}_j\right] + \gamma \cdot \mathrm{bg}(t)$$

Both $\mathrm{bg}(t)$ and the fraction γ of $\mathrm{bg}(t)$ scatter as well as the fluorescence lifetimes τ_k were determined in separate background and calibration measurements. As a result, the fit function only depends on the parameter sets a_j and b_{jk}. Due to the normalization constraints placed on the parameter sets, only a total number of $(4 \cdot K - 1)$ parameters must be fitted when describing the fluorescence of K emitters in pMINFLUX measurements.

Parameter sets a_j and b_{jk}. are retrieved separately for each localization by fitting the model fit function to the corresponding pMINFLUX TCSPC data using maximum likelihood estimation.

Multiplying the parameter sets a_j and b_{jk} then gives a set of four parameters for each emitter k which describe the relative integrated fluorescence intensities of emitter k upon excitation with laser beam pulses j. These integrated fluorescence intensities correspond to the photon counts calculated for emitter k for the four beam pulses. They thus can be used as input parameters for the MINFLUX localisation algorithm, making the simultaneous localisation of multiple emitters possible.

Supplementary Section 4. Performance of the fluorescence fitting approach for the localization of single emitters

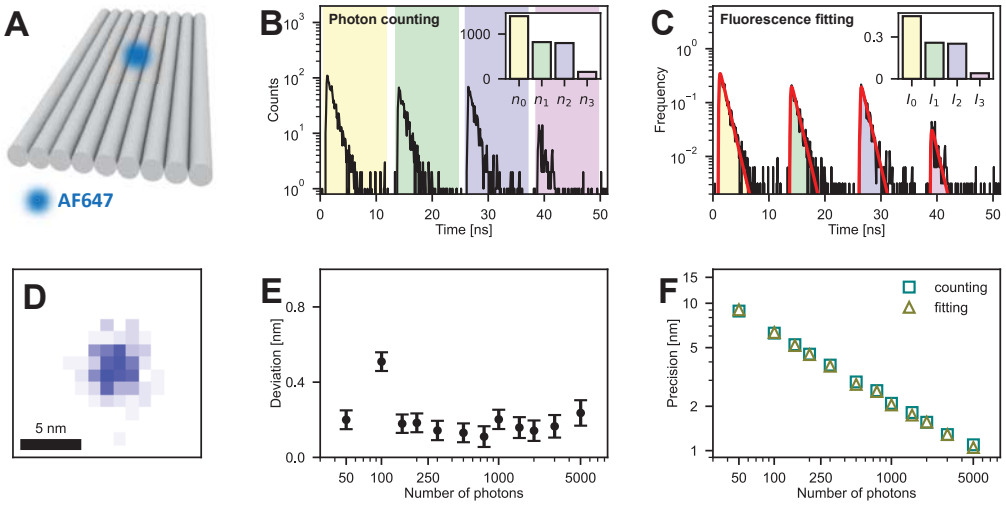

Supplementary Figure 3: Comparison of the localization of a single emitter via fluorescence fitting and photon counting. (A) Schematic of the static DNA origami carrying a single AF647 dye (τ = 1.1 ns) used in the pMINFLUX measurement to compare localizations obtained with the different approaches. (B, C) Fluorescence microtime decay of a pMINFLUX measurement of a single DNA origami as shown in (A). Colored areas mark (B) the detection microtime windows of the four different excitation beams and (C) the corresponding integrated fluorescence intensities extracted from the fitted fluorescence decay (red) used in the photon counting and the fluorescence fitting approach, respectively. The insets show (B) the photon numbers and (C) the relative fluorescence intensities upon excitation with the four different beams extracted from the pMINFLUX TCSPC data for both approaches. (D) 2D histogram of the pMINFLUX localizations of AF647 obtained by fluorescence fitting. (E) Deviation in position of localizations obtained by photon counting and fluorescence fitting as a function of the number of photons used for each localization. Deviations were calculated for the mean positions obtained from 2D Gaussian fits to 2D localization histograms as exemplarily shown in (D). (F) Localization precisions when using the fluorescence fitting and the photon counting approach as a function of the number of photons used for each localization.

Supplementary Section 5. Excitation and emission spectra of AF647 and ATTO647N

The absorption and emission spectra of AF647 and ATTO647N attached to DNA are shown in Supplementary Fig. 4. The absorption spectra of both dyes are similar, whereas the emission spectrum of ATTO647N features a small red shift compared to AF647. Both the absorption spectrum of AF647 and the emission spectrum of ATTO647N as well as the absorption spectrum of ATTO647N and the emission spectrum of AF647 have a substantial overlap.

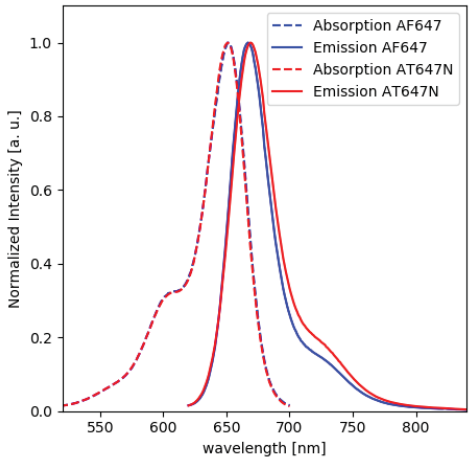

Supplementary Figure 4: Normalized absorption and emission spectra of AF647 and ATTO647N covalently bound to DNA.

Supplementary Section 6. Performance of pMINFLUX lifetime multiplexing in presence of two, one and zero emitters.

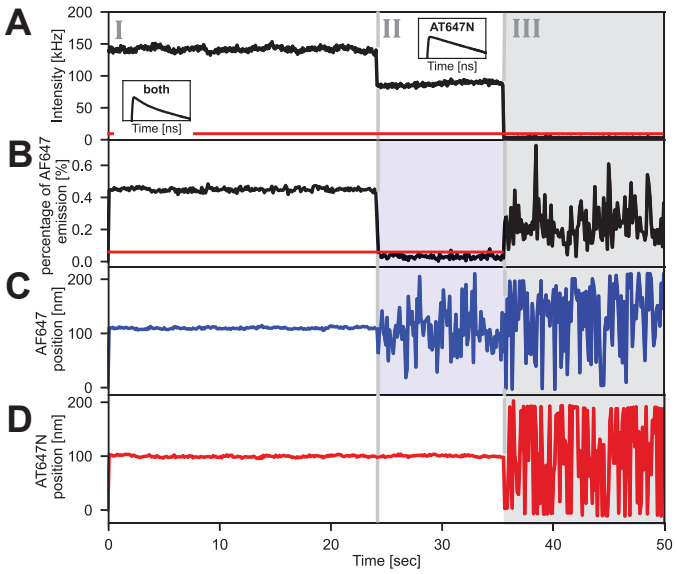

Supplementary Figure 5: pMINFLUX lifetime multiplexing in presence of two, one and zero emitters. Data analysis in this figure is based on the same measurement as in Fig. 2. (A) Fluorescence intensity transient recorded for a single DNA origami structure with AF647 and ATTO647N at a distance of 14.6 nm during a pMINFLUX measurement. Insets show the fluorescence lifetime decays before and after photobleaching of the first emitter, AF647 (first dashed gray line). Photobleaching of the second emitter, AT647N, and the subsequent drop of the fluorescence intensity to the background level is indicated by the second dashed gray line. The red line indicates a background threshold. Measurement points with a fluorescence intensity below this threshold are discarded (gray areas). (B) Percentage of AF647 emission of the total emission of both fluorophores as determined by the pMINFLUX lifetime multiplexing algorithm. In presence of both emitters, ~45% of the emitted photons are attributed to AF647 whereas the percentage drops close to zero after photobleaching of AF647. The red line indicates a percentage threshold for AF647. For measurement points with an AF647 emission percentage below this threshold, the localizations of AF647 are discarded as photobleaching of this emitter is assumed (blue areas). For AT647N, a threshold is defined analogously. (C) Position of AF647 as determined by pMINFLUX lifetime multiplexing. In presence of both emitters, AF647 is localized at a constant position. After photobleaching of AF647, its apparent localizations are distributed over the whole field of view (0-200 nm). However due to the priorly set thresholds, these false localizations are discarded. (D) Position of AT647N as determined by pMINFLUX lifetime multiplexing. Both in presence of both emitters and after photobleaching of AF647, the biexponential fitting approach of pMINFLUX lifetime multiplexing localizes AT647N at a constant position. Only after the second photobleaching step, the apparent localizations scatter. These false localizations however are discarded due to the priorly set background threshold.

Supplementary Section 7. Bleach analysis in pMINFLUX

The bleach analysis approach is based on similar concepts applied in wide-field super-resolution imaging.[2–4] Here, multiple emitters located within in a diffraction limited area are localized without photoswitching by imaging the same area multiple times. Ideally, during the imaging period the sequential photobleaching of all emitters occurs such that towards the end of the imaging period only one emitter is in its fluorescent state. This emitter can then be localized using standard procedures. For all images recorded prior to this, the fluorescence of the last emitter is then subtracted. This allows the localization of the emitter bleaching second-to-last. By again subtracting its fluorescence from all priorly recorded images, the next emitter can be localized. Repetition of this procedure eventually results in the full reconstruction of all emitter locations.

For its application in pMINFLUX, we adapted this concept to use the photon microtime information instead of recorded images. In the following, this adaption is described using the pMINFLUX measurement of AF647 and ATTO647N at a distance of 14.6 nm shown in Fig. 2 during which photobleaching of both emitters occurred (Supplementary Fig. 6A) as an example.

In a first step, we localized the emitter which photobleached last – in our case ATTO647N. For this, we applied the fluorescence fitting approach to the photon microtimes of photons detected after photobleaching of AF647 (time window II in Supplementary Fig. 6A) to extract the relative fluorescence intensities of ATTO647N upon excitation with the four different excitation beams (Supplementary Fig. 6B). We subsequently used these relative fluorescence intensities to determine the location of ATTO647N (red localization density map in Supplementary Fig. 6E) and calculated the number of photons emitted from ATTO647N by excitation with the different beams by multiplying the relative fluorescence intensities with the total number used for each localization.

We then applied the photon counting approach to the photon microtimes of photons detected while both AF647 and ATTO647N were in their fluorescent state (time window I in Supplementary Fig. 6A). The values extracted from this correspond to the number of photons emitted from both emitters upon excitation with the four different beams. To calculate the number of photons emitted from AF647 upon excitation with the different beams, we subtracted the number of photons emitted from ATTO647N as determined from time window II from the number of photons emitted from both emitters (see visualization in Supplementary Fig. 6C, Supplementary Fig. 6D). In a final step, the resulting photon numbers were used to determine the location of AF647 (blue localization density map in Supplementary Fig. 6E).

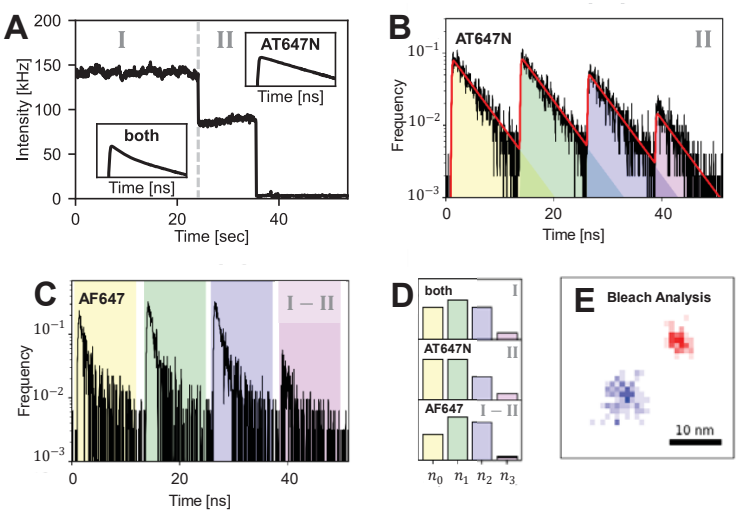

Supplementary Figure 6: Bleach analysis for the sequential localization of multiple emitters in pMINFLUX without photoswitching. The figure describes the bleach analysis used in Fig. 2 to validate the accuracy of the pMINFLUX multiplexing approach. Data analysis is based on the same measurement as in Fig. 2. (A) Fluorescence intensity transient recorded for a single DNA origami structure with AF647 and ATTO647N at a distance of 14.6 nm during a pMINFLUX measurement. Insets show the fluorescence lifetime decays before and after photobleaching of AF647 (dashed gray line). (B) Fluorescence microtime decay for ATTO647N in time window II in panel A. Colored areas mark the integrated fluorescence intensities for the different excitation beams extracted from the fluorescence fit (red line). The relative integrated fluorescence intensities then are used to localize ATTO647N. (C) Difference in the fluorescence microtime decays of time windows I and II, illustrating the sequential localization of AF647. Colored areas mark the detection microtime windows of the four different excitation beams in which the arriving photons are counted. (D) Retrieved normalized ratios of photon numbers/ fluorescence intensities of the four excitation beams for time window I (upper panel, fluorescence of both AF647 and ATTO647N), for time window II (middle panel, fluorescence of ATTO647N; used for the localization of ATTO647N) and for the difference between time windows I and II (lower panel, effective fluorescence of AF647; used for the localization of AF647). (E) 2D histogram of MINFLUX localizations obtained by bleach analysis. The localization of AF647 (blue) is less precise than the localization of ATTO647N (red) as it was not obtained directly.

Supplementary Section 8. Evaluation of the localization precision in pMINFLUX lifetime multiplexing

We evaluated the localization precision achievable in lifetime multiplexed pMINFLUX. Using the same measurement shown in Figure 2, we varied the number of photons used for each localization. Supplementary Figure 7A-F depicts two-dimensional histograms of lifetime multiplexed localizations of AF647 and ATTO647N performed with photon counts between 100 and 4000. The localization precision of both molecules follows the expected inverse dependency with √N, and with moderate photon counts of 2000 photons per emitter, both emitters were simultaneously localized with precisions better than 3 nm.

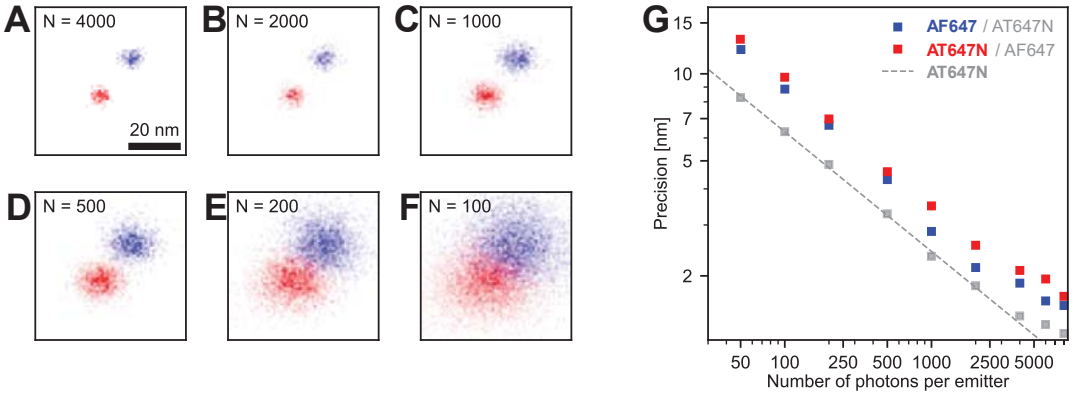

Supplementary Figure 7. Evaluation of the localization precision in pMINFLUX lifetime multiplexing. (A-F) 2D histograms of the lifetime multiplexed pMINFLUX localizations of an AF647 (blue) and an ATTO647N (red) dye in a fixed distance of 14.6 nm for different number of photons per emitter, N, used to estimate their positions. (G) localization precision as a function of collected photons per emitter for both AF647 (blue) and ATTO647N (red) localized simultaneously in pMINFLUX lifetime multiplexing. The localization precision of a single ATTO647N dye at the same position as in the multiplexing localized after photobleaching of AF647 is shown in gray.

Interestingly, the multiplexed simultaneous localizations have precisions about 40% worse compared to the localization precision attained for the individual ATTO647N molecule (time window II in Fig. 2B), (Supplementary Fig. 7G). These lower precisions are attributed to uncertainties of photon assignment. To investigate this, we performed numerical simulations (Supplementary Figure 8) varying the relative brightness ratios and lifetime contrasts of the two target fluorophores.

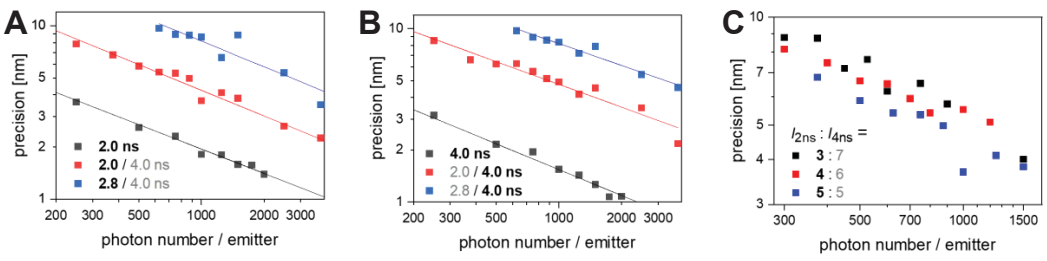

Supplementary Figure 8: Effect of fluorescence lifetime contrasts and brightness ratios of two

emitters on the performance of the pMINFLUX lifetime multiplexing approach in numerical simulations. (A,B) Localization precision as a function of the number of photons detected for the characterized emitter when simultaneously localizing two equally bright emitters of different fluorescence lifetimes by pMINFLUX lifetime multiplexing. The fluorescence lifetime of the characterized emitter is highlighted in black. For comparison, the localization precision when localizing a single emitter with the photon counting approach is given as reference. (C) localization precision of the emitter with a lifetime of τ_0 = 2.0 ns as a function of the number of detected for the emitter when simultaneously localizing two emitters (τ_1 = 4.0 ns) with different brightness ratios with pMINFLUX lifetime multiplexing. Numerical simulations were performed with a SBR of 10 and assuming a uniform background distribution.

We found that the brightness ratio of the emitters does not have a systematic influence on the attainable localization precision. By contrast, the localization precision reduces with lifetime contrast (Supplementary Fig. 8), which explains the reduction in localization precision observed in the experiments for the pair AF647-ATTO647N. Using the simulation framework, other suitable dye pairs for lifetime multiplexed pMINFLUX e.g. in the green spectral range are identified (Supplementary Fig. 9).

Supplementary Section 9. pMINFLUX lifetime multiplexing in the green spectral range

In the green spectral range, we identified ATTO542 and Alexa Fluor 555 (AF555) as a suitable emitter pair for pMINFLUX lifetime multiplexing. On reference DNA origami systems, ATTO542 exhibited a fluorescence lifetime of 3.3 ns whereas AF555 showed a biexponential decay profile with fluorescence lifetimes of 0.8 ns (85%) and 2.4 ns (15%), resulting in a high overall contrast in fluorescence lifetime of the emitter pair ideal for pMINFLUX lifetime multiplexing.

To account for the biexponential nature of the fluorescence of AF555, the model fit function of the multiplexing approach (see Supplementary Section 3) was extended to incorporate the biexponential decay of AF555 with fixed relative intensities.

We evaluated the performance of the pMINFLUX lifetime multiplexing approach when using AF555 and ATTO542 as an emitter pair by placing both emitters in a distance of ~18.7 nm from each other on a static DNA origami (Supplementary Fig. 9A) and performing a pMINFLUX measurement. The recorded fluorescence intensity/ fluorescence lifetime transient of the measurement (Supplementary Fig. 9B) featured time windows in which both fluorophores were in their fluorescent state (I), only AF555 was in its fluorescent state while ATTO542 was in a non-fluorescent state (II) and only ATTO542 was in its fluorescent state while AF555 was in a non-fluorescent state (III). This allowed localizing both AF555 and ATTO542 from time windows II and III using the standard photon counting approach (Supplementary Fig. 9C).

By applying the standard photon counting approach to photons arriving in time window I during which both fluorophores were in their fluorescent state, only the intensity-weighted average localization of both fluorophores was obtained (purple localizations in Supplementary Fig. 9C). In contrast, application of the pMINFLUX lifetime multiplexing approach to photons arriving in time window I revealed two separate locations for AF555 and ATTO542 (blue and red localizations in Supplementary Fig. 9D) which coincide with the positions for both fluorophores located via photon counting in Supplementary Fig. 9C, indicating a good accuracy of the pMINFLUX lifetime multiplexing approach when using AF555 and ATTO542 as an emitter pair.

When comparing the localization precisions achieved when simultaneously localizing both emitters using pMINFLUX lifetime multiplexing to those achieved when localizing single emitters using photon counting, localizations performed using pMINFLUX lifetime multiplexing are only less than two times less precise when using AF555 and ATTO542 as an emitter pair (Supplementary Fig. 9E,F).

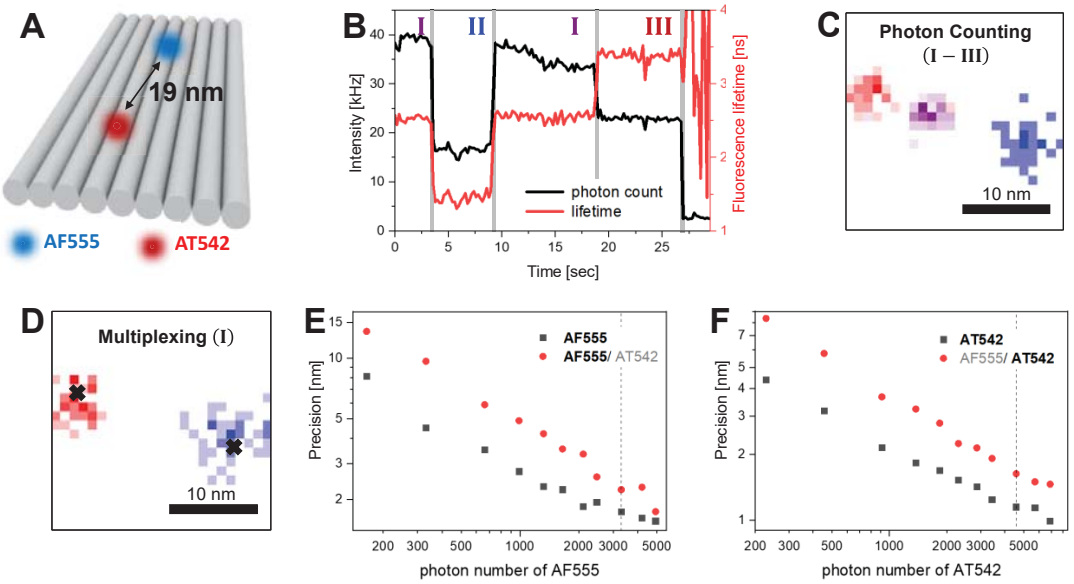

Supplementary Figure 9: pMINFLUX lifetime multiplexing in the green spectral range using AF555 and ATTO542 as an emitter pair. (A) Schematic of a static DNA origami on which both an AF555 dye and an ATTO542 dye are placed in a fixed distance of ~18.7 nm from each other. (B) Fluorescence intensity transient (black) recorded for a single DNA origami structure shown in panel A during a pMINFLUX measurement. The corresponding fluorescence lifetime transient as determined by a monoexponential fit model is shown in red. The dashed gray lines separate the transient into time windows during which both emitters (I) were in their fluorescent state and time windows during which only AF555 (II) or ATTO542 (III) were in their fluorescent state while the other emitter was in a non-fluorescent state. (C) 2D histogram of the pMINFLUX localizations in time windows I-III obtained by photon counting. Localizations of time window I corresponding to the combined fluorescence of both emitters are shown in purple, localizations of time window II corresponding to AF555 in blue and localizations of time window III corresponding to ATTO542 in red. (D) 2D histogram of the lifetime multiplexed pMINFLUX localizations in time window I. Localizations of AF555 are shown in blue, localizations of ATTO542 in red. The positions of the two emitters as determined by photon counting in panel C are indicated by black crosses. (E,F) Localization precision as a function of collected photons per emitter for both AF555 (E) and ATTO542 (F) localized simultaneously in time window I with pMINFLUX lifetime multiplexing (red). For comparison, the localization precision of the emitters localized during time windows II (E) and III (F) during which only the localized emitter was in its fluorescent state using the photon counting approach are shown in black. The dashed lines indicate the number of photons used per localization in the 2D histograms shown in panels C,D.

Supplementary Section 10. Adjustment of the temporal resolution of the separate emitters in pMINFLUX lifetime multiplexing

In pMINFLUX lifetime multiplexing, different temporal resolutions can be chosen for tracking the different emitters. If two processes with differing kinetics are studied, this allows separately optimizing the spatiotemporal resolution of both processes in a single, multiplexed measurement as demonstrated in Supplementary Fig. 10.

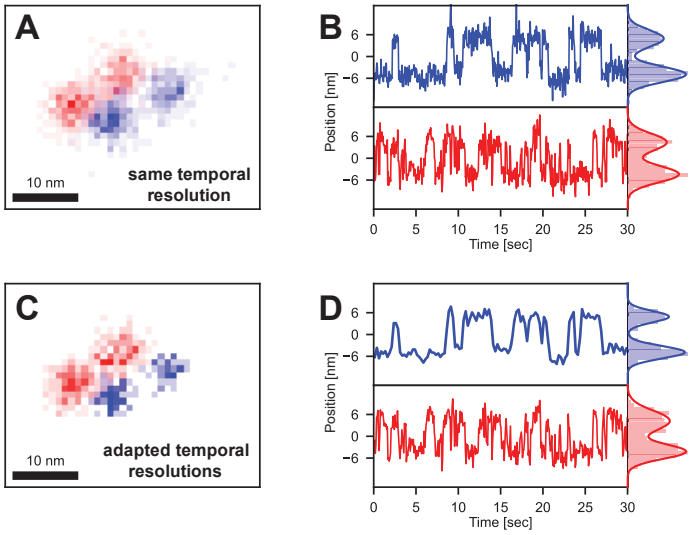

Supplementary Figure 10: Dual-color molecular scale tracking of the double pointer system using pMINFLUX lifetime multiplexing with individually adaptable temporal resolutions. (A,C) 2D histogram of the lifetime multiplexed pMINFLUX localizations of AF647 (blue) and ATTO647N (red), featuring each two distinct positions. (B,D) Localization trajectory of the AF647 (blue) and ATTO647N DNA pointer (red). In panels A and b, the temporal resolution is set to 60 ms for both colors. (C,D) The differing kinetics of the AF647 and the ATTO647N DNA pointer allows adjusting the temporal resolutions when tracking both pointer systems separately to 250 ms and 75 ms for the AF647 and the ATTO647N pointer, respectively, optimizing the spatiotemporal resolution separately for both tracked emitters.

Supplementary Section 11. Visualization of the antigen binding sites of an IgG antibody

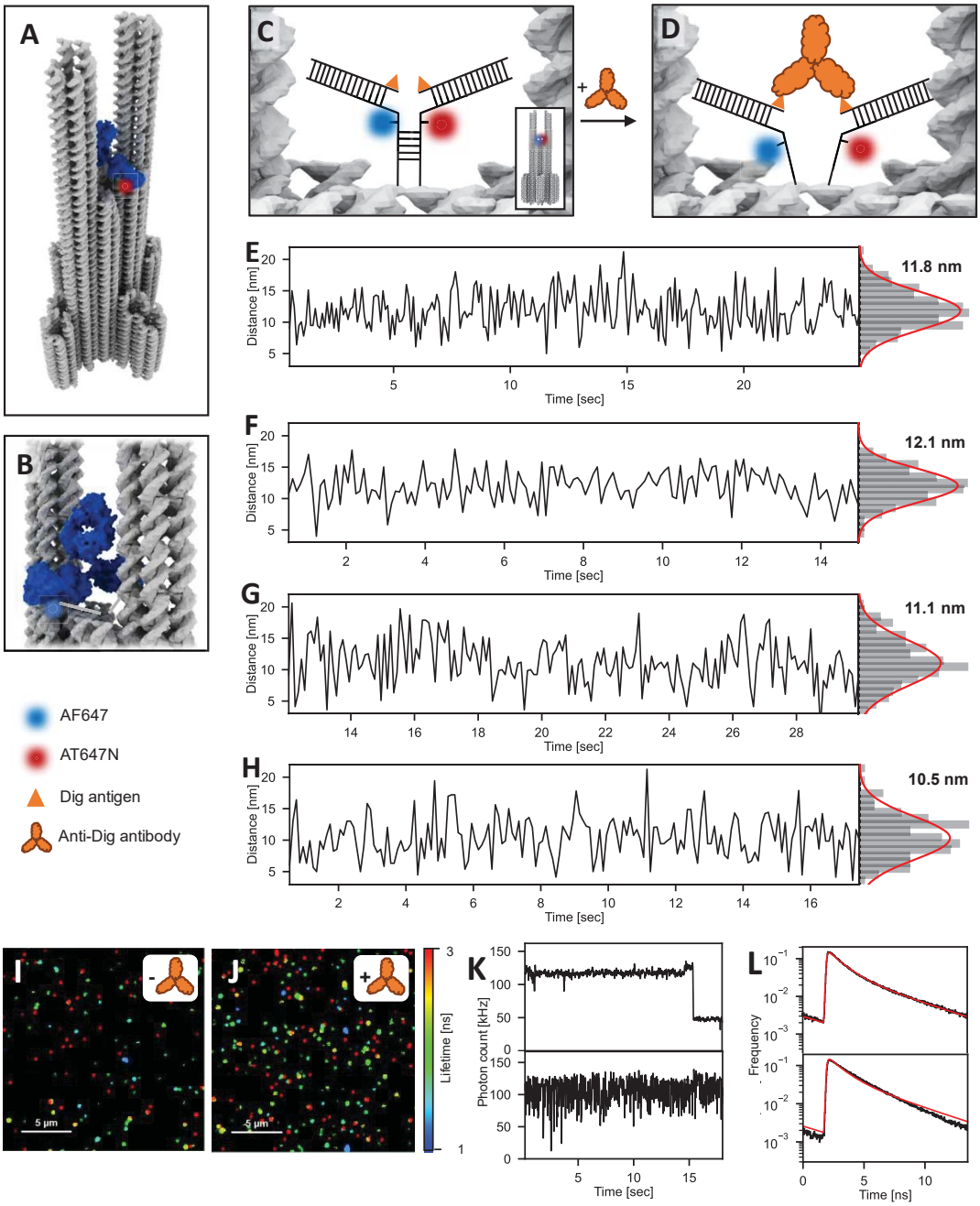

Supplementary Figure 11: Distance determination between the antigen binding sites of an IgG antibody. (A) Schematic of the DNA origami structure (grey) to which an exemplary IgG antibody (blue, Protein Data Bank (PDB) entry 1IGT) is bound via two antigen labelled DNA strands. (B) Zoom-in of panel (A). The antibody is bound between two DNA pillars which hinder its free rotation, restricting it in its orientation. (C, D) Nanoswitch assay for antibody binding adapted from *Pfeiffer* et al.[5] For antibody binding, the DNA origami structure is designed with two protruding DNA strands. These strands each include a 7 nt non-complementary linker followed by a 5 nt complementary stem. The stem is equipped

with AF647/ ATTO647N fluorophores as internal modifications and followed by a ssDNA anchor to which antigen modified DNA is hybridized. As a result of this design, the antigens are positioned in close proximity to the fluorophores. (C) In absence of antibodies, the complementary stem region of the DNA strands hybridizes and both fluorophores are in close proximity to each other. This causes contact quenching so that little fluorescence is detected. (D) Upon bivalent antibody binding to both antigens, the stem separates, and AF647 and ATTO647N spatially separate unleashing fluorescence. Their resulting positions offer insight into the positions of the antigen binding sites of the bound antibody. Dimensions are not to scale. (E-H) Distance between AF647 and ATTO647N over time as determined by pMINFLUX lifetime multiplexing for the four DNA origami – antibody constructs shown in Fig. 4E. The mean distance of each measurement is highlighted. (I, J) Confocal fluorescence lifetime scans of surface-immobilized DNA origami structures (I) before and (J) after antibody addition. Red and blue spots correspond to structures labelled only with ATTO647N and AF647, respectively. Green spots correspond to double-labelled structures. Upon addition of antibody, the number of green spots increases, indicating antibody binding. (K) Exemplary fluorescence intensity transient recorded for single DNA origami structures recorded upon antibody addition. Both transients with (lower panel) and without (upper panel) intensity fluctuations were observed. We attributed intensity fluctuations to structures without antibody bound in which contact quenching of both dyes occurs. Consequently, the absence of intensity fluctuations indicated the presence of bound antibody. (L) Corresponding fluorescence microtime decays of the transients shown in (K). Only in absence of intensity fluctuations, the decays show a biexponential behavior which can be fit with the fluorescence lifetimes of ATTO647N and AF647 (red line). For pMINFLUX analysis, only transients of double-labelled structures which did not show any intensity fluctuations were used.

Supplementary Section 12. Fixed orientation of a DNA origami raft immobilized on a glass surface

The DNA origami raft exhibiting both translational and rotational movements on a supported lipid-bilayer (see Fig. 4G-I) remains at a fixed position and a fixed orientation when immobilized on a glass surface via biotin-neutravidin interactions (see Supplementary Fig. 12).

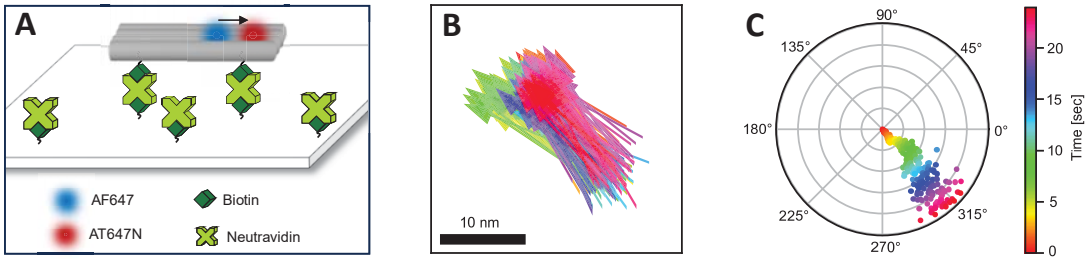

Supplementary Figure 12: Fixed position and orientation of a DNA origami raft immobilized on a glass surface. (A) Schematic of the DNA origami raft labelled with AF647 and ATTO647N immobilized on a glass surface. Biotins are incorporated into the structure for immobilization by biotin–neutravidin interactions onto glass surfaces. The DNA origami structure is the same as used in the supported lipid-bilayer experiments in Fig. 4G-I. (B) Arrow plot of the lifetime multiplexed pMINFLUX localizations of a single DNA origami raft over time. The positions of AF647 and AT647N are indicated by the start and end point of arrows. In contrast to the lipid-bilayer measurement, the plot shows no translational or rotational movement of the raft. (I) Angular distribution of the raft orientation over time. The raft remains at a constant orientation throughout the whole measurement. Dimensions not to scale.

Supplementary Section 13. Monte-Carlo simulations on pMINFLUX lifetime multiplexing in the FRET range and distance calibration

For pMINFLUX lifetime multiplexing, with AF647 and ATTO647N, two emitters with similar spectral properties are used. The resulting overlap in the absorption and emission spectra (see Supplementary Fig. 4) causes the occurrence of FRET, both from AF647 to ATTO647N and from ATTO647N to AF647 if the emitters are in close proximity to each other. To study the effect this has on the accuracy of the pMINFLUX lifetime multiplexing approach, we performed custom written kinetic Monte Carlo simulations simulating the fluorescence response of AF647 and ATTO647N placed at different distances from each other.

In these simulations, we assumed a gamma-shaped excitation pulse and an excitation probability p_{ex} corresponding to the extinction coefficient of each emitter. Once excited, the emitter has multiple pathways. It can return to its non-fluorescent ground state either by fluorescence, by FRET or by a non-radiative pathway in probabilities described by the rates k_f, k_{FRET} and k_{nr}, respectively.

The rates are coupled to photophysical properties such as the fluorescent lifetime τ, the quantum yield of the fluorescent state ϕ:

$$k_f = \tau_{noDNA}^{-1} \cdot \phi$$

where τ_{noDNA} is the fluorescence lifetime of the fluorophore without DNA modification. The modification with DNA only affects the non-radiative rate. The radiative rate remains the same thus can be calculated from manufacturer specifications. The non-radiative rate needs to be calculated from the experimental fluorescence lifetime with the corresponding buffer and DNA modification.

$$k_{nr} = \tau_{DNA}^{-1} - k_f$$

The FRET rate is strongly inter-dye distance r dependent as well as on the lifetime of the donor τ_D , as well as the Förster radius *R* characteristic for the dye pair:

$$k_{FRET} = \tau_D^{-1} \left(\frac{R_0}{r}\right)^6$$

As both dyes have similar spectral properties, both dyes can act as a donor hence, both FRET rates are needed.

Using the four rates for either dye (excitation, fluorescent emission, non-radiative relaxation and FRET), kinetic Monte-Carlo simulations[6] are performed for different distances. In the Monte-Carlo simulations we save where the photon is absorbed and where and when the photon is emitted. The kinetic Monte-Carlo framework is extended for pMINFLUX simulations. To this end, the excitation probability is modified according to the four vortex-beam excitation pattern and adding all four pMINFLUX excitations to one microtime window.

This framework is used to cross-check the experimental pMINFLUX lifetime multiplexing results with Monte-Carlo simulation for distances between 20 and 3 nm.

Rebinning the simulated photons according to their maximal microtime bin in each excitation window results in a single fluorescence decay (Supplementary Fig. 13A). The corresponding microtime decays show a distinct biexponential decay for large distances which becomes less distinct for smaller distances. In the simulations also the fraction of the photons absorbed and emitted by AF647 is determined (Supplementary Fig. 13B,C). As expected, the resulting fractions are strongly distance dependent and can be fitted by an adapted FRET relation:

$$E_{adapted} = E_{range} \cdot \left(1 + \left(\frac{d}{R_{50}}\right)^{6}\right)^{-1} + E_{low}$$

The fit results in $R_{50} = 7.8\,\mathrm{nm}$, $E_{range} = 19\%$ and $E_{low} = 48\%$ for the absorbed photons. This ratio is important to calculate the distance of the individual dyes to the center of mass of the MINFLUX measurement from the inter-dye distance. We then used photon packages of 2500 microtimes to calculate the phasor coordinates corresponding to the distances (Supplementary Fig. 13D,E). In simulations, the populations of AF647 and ATTO647N at distances of 10, 9, 8, 7, 6, 5 and 4 nm in the phasor plot can be easily differentiated. From of the phasor plot effective phasor coordinates can be calculated as the geometric mean of s and g.

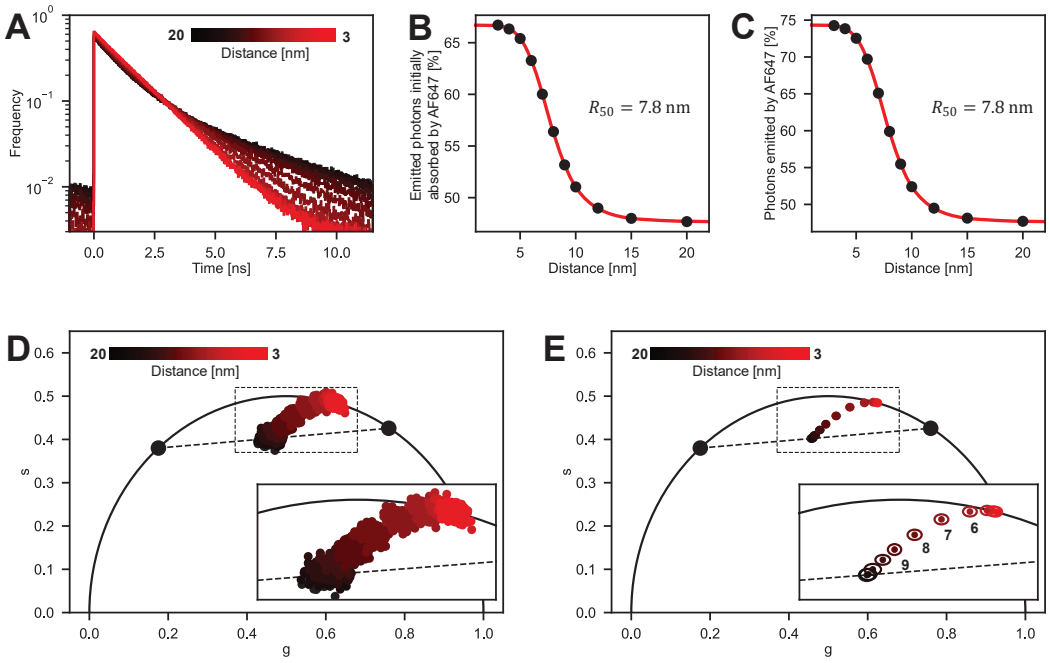

Supplementary Figure 13: Phasor approach for distance determination in the FRET range – Monte Carlo simulations. (A) Simulated fluorescence microtime decays of AF647 and ATTO647N placed at distances between 20 nm and 3 nm from each other in pMINFLUX experiments. The microtimes of the pMINFLUX simulations were extracted for each of the four excitation windows and then rebinned according to their maximal microtime bin in each excitation window, resulting in the shown single histogram (B,C) Fraction of photons absorbed (B) and emitted (C) by AF647 for different inter-fluorophore distances (black dots). Fitting with the adapted FRET equation revealed an apparent

Förster radius of $R_{50} = 7.8\,\mathrm{nm}$. (D, E) Simulated phasor plot of AF647 and ATTO647N placed at distances between 20 nm and 3 nm from each other in pMINFLUX experiments. The bold black dots correspond to the fluorescence of pure ATTO647N and AF647 (left and right dots), respectively. Datapoints on the dashed black line between them indicate inter-dye distances without interactions. The inset shows a zoom-in of the dashed box. Both a scatter plot of individual data points for all simulated distances (D) as well as a plot showing the mean phasor coordinates (dots) as well as the corresponding standard deviations (ellipses) for each simulated distance (E). The numbers in the inset of (E) correspond to the inter-dye distances in nanometer simulated for the respective data points. Simulations were carried out with a uniform background signal (overall SBR = 40) and using N = 2500 photons for calculating phasor data points in D,E.

The simulated data shows that the distance dependence of the phasor data follows the expected adapted FRET relation (Supplementary Fig. 14A). Using the same model for experimental data, also shows good agreement between fit and data. (Supplementary Fig. 14B). Thus, the fitted relation can be used as a calibration to calculate the distance out of the experimental phasor data used in Figure 4 (Supplementary Fig 14B black line).

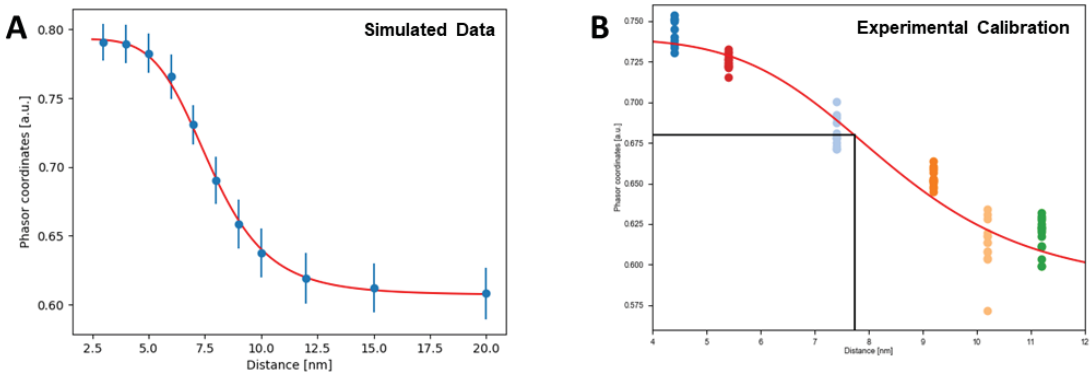

Supplementary Figure 14: Calibration curve for distance determination via the phasor approach in the FRET range. (A). The calibration curve of the simulated phasor coordinates and inter-dye distance. The red line represents the fit with the adapted FRET relation, used for calibration. (B). Color coded are the experimental phasor coordinates for samples of different inter-dye distances. The red line represents the fit with the adapted FRET relation, used for calibration. The black lines indicate the experimental measured phasor coordinate used in Figure 4 and its corresponding distance.

Microtime-Gating in pMINFLUX

For localizations in which AF647 and ATTO647N were in distances smaller than ~10 nm, we exploited the microtime information offered in pMINFLUX to determine the vector along which both fluorophores were located. In the following, the concept is illustrated using Monte Carlo simulations.

An easy approach to partially separate the fluorescence of AF647 and ATTO647N is the application of two small microtime gates, directly after each pulsed excitation beam and at the end of the corresponding microtime window. As the fluorescence lifetimes of AF647 (τ = 1.1 ns) and ATTO647N (τ = 4.3 ns) differ, the early photons can be predominantly attributed to AF647 whereas the late photons mainly are emitted from ATTO647N.

We thus performed the standard pMINFLUX localization algorithm using only photons arriving in the respective early and late microtime gates, yielding two separate localizations. We then gradually increased the length of both microtime gates in steps of 250 ps to include larger fractions of photons emitted from both fluorophores (Supplementary Fig. 15A,B). With increasing microtime gate length, the resulting localizations are displaced further towards the center of mass of both fluorophores. Fitting a linear function to the localizations of the different microtime gates revealed correctly the vector defined by the actual positions of the two fluorophores (Supplementary Fig. 15C). This vector can be used in combination with the phasor distance. However, with smaller distance FRET gets stronger, and more photons get emitted by the fluorophore with lower fluorescence lifetime. Thus, in the MINFLUX one fluorophore is weighted more, moving the center of mass towards the fluorophore with lower fluorescence lifetime. This is directly proportional to the intensity ratio of Supplementary Figure 13B, which can be used to recover the dye-center of mass distance.

By combining all three parts: the vector connecting both dyes, the previously fitted phasor distance calibration (Supplementary Figure 14A) and the dye-center of mass distance, the individual fluorophores can be localized. In simulations the localized positions are in good agreement with the true positions, thus confirming the validity of the approach.

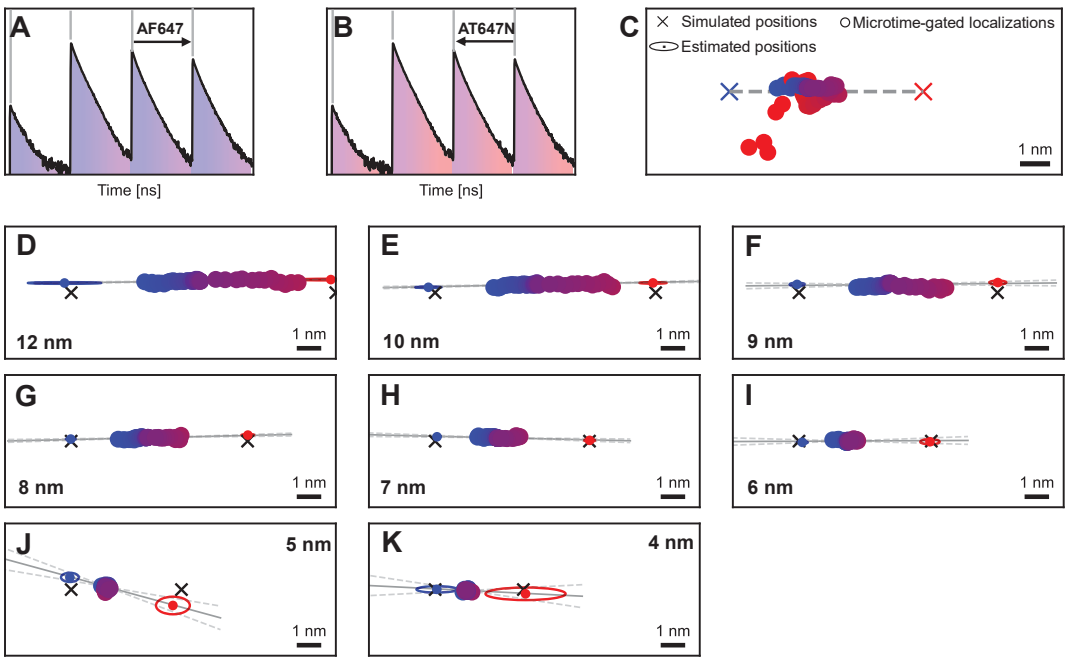

Supplementary Figure 15: Microtime-Gating in the FRET range in pMINFLUX – Monte Carlo simulations. (A, B) Simulated pMINFLUX microtime decays for AF647 and ATTO647N in a distance of 7 nm. For pMINFLUX localizations, only photons arriving in microtime gates right after each excitation pulse (A) or at the end of the corresponding microtime window (B) were considered. For determining the orientation of AF647 and ATTO647N to each other, the length of the microtime gates was gradually increased (color gradient to purple, black arrow). (C-K) Means of all localizations for the different gate lengths (circles) of the microtime decay shown in A,B (C) and AF647 and ATTO647N in distances between 12 nm and 4 nm. The color code corresponds to the different gate lengths illustrated in A,B. The large scattering in the mean localizations of late microtime gates in C (red circles) is caused by the increasingly shortened fluorescence lifetime of ATTO647N due to FRET and the resulting low number of photons/ high SBR in the late microtime gates. To circumvent this scattering, localizations performed with microtime gates filtering out more than 25% of the initial 8000 photons were discarded (D-K). The gray line indicates the fitted orientation vector. The dashed gray lines show the corresponding error margins. The blue and red dots and corresponding ellipses indicate the positions found for AF647 and AT647N with the phasor/ microtime-gating approach. Simulations were carried out with a uniform background signal (overall SBR = 40) and using N = 8000 photons for each localization. Initial microtime gate lengths were set to 0.25 ns and 3 ns for the early and the late photons, respectively. The gate lengths were increased in steps of 0.25 ns until they included the full microtime windows of the separate beam pulses. The SBR used for localizations was recalculated separately for each gate length to account for the different number of photons arriving in the different gates. For all distances, the microtimes of ~800 000 photons were simulated.

Due to the increasing indistinguishability of photons emitted from AF647 and ATTO647N due to FRET at small distances, the error of the determined vector direction; i.e. the slope of the linear fit, increases with decreasing distance (Supplementary Fig. 15D-K, Supplementary Tab. 1) The precision of the fit drops at distances of 5 nm and below, however still being accurate within 3 standard deviations.

Supplementary Table 1: Slope of the Microtime-Gating Fit corresponding to the vector along which AF647 and ATTO647N are determined to be orientated. The slope obtained from the ground truth of the simulations has a value of 0.

Distance [nm]	Slope
12	0.013 ± 0.005
10	0.019 ± 0.006
9	0.009 ± 0.019
8	0.022 ± 0.010
7	-0.02 ± 0.014
6	0.005 ± 0.03
5	-0.3 ± 0.10
4	-0.05 ± 0.10

Experimental data was analyzed accordingly.

Supplementary Section 14. Simulations on spectral multiplexing

An alternative approach to pMINFLUX multiplexing via the fluorescence lifetime utilizes the spectral information of the emitters. Here, emitters with similar absorption spectra but differences in their emission spectra are used. This allows exciting both emitters with the same excitation beam wavelength and still being able to partially separate their emission spectrally. It can also be applied to continuous-wave MINFLUX.

In spectral multiplexing, the fluorescence emission in MINFLUX experiments is spectrally split into two detection channels in each of which arriving photons are detected with an avalanche photon diode (APD0 and APD1, Supplementary Fig. 16A) using a dichroic mirror. The dichroic mirror optimally splits the fluorescence emission at a wavelength directly between the maxima in the emission spectra of the utilized emitters. This creates a contrast in the brightness with which both emitters are detected at the different APDs and allows their simultaneous localization.

In Supplementary Figure 16B the concept of spectral multiplexing is visualized using simulated pMINFLUX data of two emitters based on the fluorescent properties of ATTO542 and Cy3B which exhibit good photostability ideal for co-tracking. The results indicate that they could form a suitable emitter pair for spectral multiplexing in the green excitation range.

To extract the number of photons corresponding to each dye, the spectral splitting approach relies on knowing the fluorescent intensity fraction each dye has on each APD.

The total intensity on APD0 is the sum of the effective brightness of both dyes ($b_{dye,\#APD}$ with dye = 0,1 and # APD = 0,1), each multiplied with an intensity factor α_i:

$$I_{APD\,0} = \alpha_0\, b_{0,0} + \alpha_1\, b_{1,0}$$

Similar for APD1:

$$I_{APD\,1} = \alpha_0\, b_{0,1} + \alpha_1\, b_{1,1}$$

The intensity factor is dependent on the position hence for each excitation beam different, but not on the APD channel.

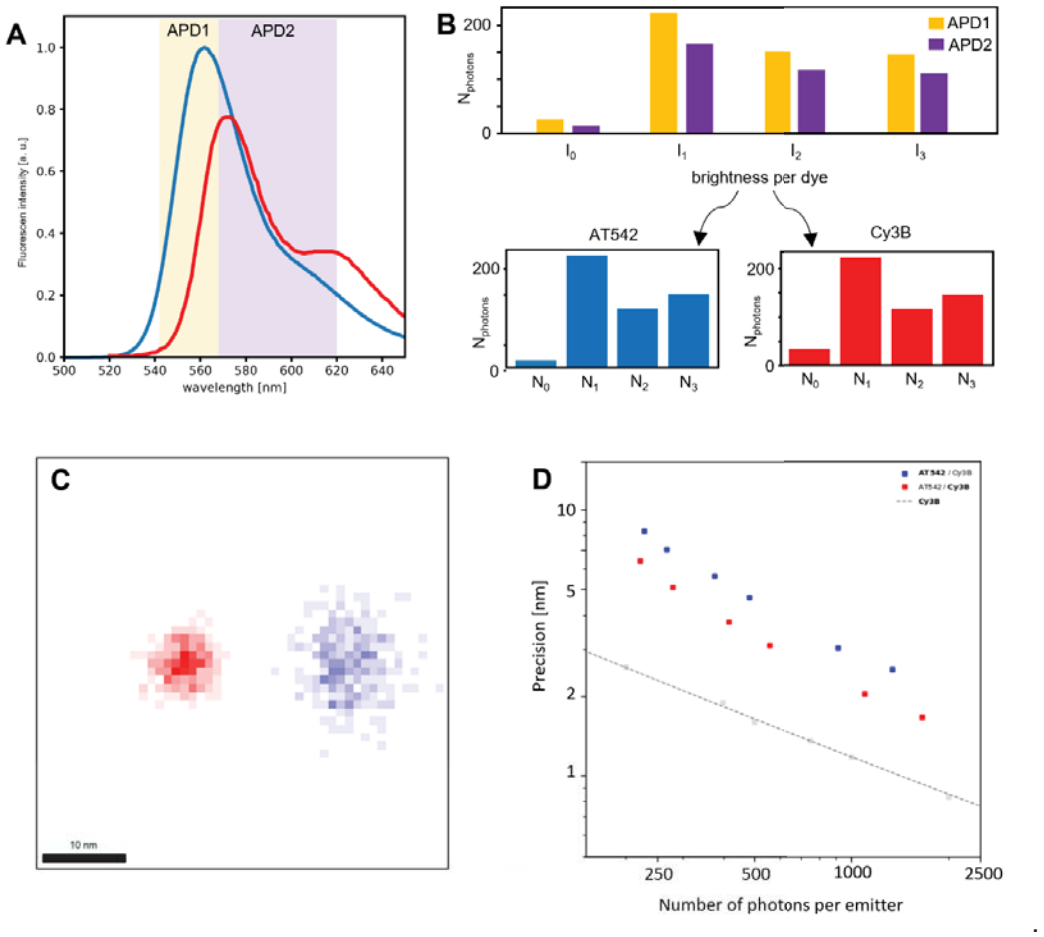

Supplementary Figure 16: MINFLUX multiplexing via Spectral Splitting. (A) Brightness normalized emission spectra of ATTO542 and Cy3b split with a dichroic mirror at 568 nm. The resulting spectral detection ranges of APD0 (yellow) and APD1 (purple) are marked. (B) Schematic of the spectral splitting workflow. For each localization, each excitation has detected photons on both APDs (yellow and purple). By knowing the brightness of each dye on each APD, the number of photons for each dye and each excitation can be extracted. (C) Simulated data of two dyes with spectral properties comparable to ATTO542 and Cy3B in a distance of 20 nm. Parameters for the simulations are 1000 localizations, with SBR = 50 and N = 2000 photons. Spectral splitting results in localizations of ATTO542 (blue) and Cy3B (blue) in a distance of 20 nm. (D) For simulations analogue to c, the precision of the spectral splitting localizations in dependence of the number of photons is comparable for both dyes (ATTO542: blue and Cy3B red). The precisions of a single dye (grey) at the same conditions outperforms the spectral splitting.

Our effective measurement is the intensity ratio of both APDs:

$$r = \frac{I_{APD\ 0}}{I_{APD\ 1}} = \frac{\alpha_0\ b_{0,0} + \alpha_1\ b_{1,0}}{\alpha_0\ b_{0,1} + \alpha_1\ b_{1,1}}$$

$$\left(\alpha_0\ b_{0,1} + \alpha_1\ b_{1,1}\right) * r = \alpha_0\ b_{0,0} + \alpha_1\ b_{1,0}$$

$$\alpha_0\left(r\ b_{0,0} - b_{0,1}\right) = \alpha_1\left(b_{1,0} - r\ b_{1,1}\right)$$

$$\frac{\alpha_0}{\alpha_1} = \frac{b_{1,0} - r\ b_{1,1}}{r\ b_{0,0} - \ b_{0,1}}$$

By introducing the intensity fraction of each dye in the APDs $f_0 = \frac{b_{0,0}}{b_{0,0}+b_{0,1}} = \frac{b_{0,0}}{b_0}$ and $f_1 = \frac{b_{1,0}}{b_{1,0}+b_{1,1}} = \frac{b_{1,0}}{b_1}$ it follows:

$$\frac{\alpha_0}{\alpha_1} = \frac{f_1 b_1 - r\ *(1-f_1)b_1}{r\ f_0 b_0 - (1-f_0) * b_0} = \frac{f_1 - r + r f_1}{r\ f_0 - 1 + f_0}\frac{b_1}{b_0}$$

$$x = \frac{\alpha_0\, b_0}{\alpha_1\, b_1} = \frac{f_1\ - r + r f_1}{r\ f_0 - 1 + f_0}$$

Here x is the absolute intensity ratio between both dyes.

$$x = \frac{N_0}{N_1}$$

It follows for the total number of photons for dye 0 (N_0):

$$N_0 = \ N - N_1 = N - \frac{N_0}{x} = \frac{x * N}{1 + x}$$

Using N_0 and N_1, the standard maximum likelihood approach of MINFLUX can be used. Hence only the expected fraction of a dye per APD needs to be known to calculate the number of photons corresponding to each dye out of the measured intensity ratio. This enables spectral multiplexing with a minimal number of parameters.

Next, we validated the spectral splitting approach in simulations. To this end two dyes spaced in a distance of 20.0 nm are simulated. Simulations parameter are a SBR of 50, 100 bins with each 2000 photons. The spectral splitting approach localized the dyes correctly in a distance of ~19.9 nm (Supplementary Fig. 16C). To characterize this method further simulations were performed, binning the localization with different number of photons. By measuring the precision for each of those simulation, the precision in dependence of the number of photons can be characterized analogue to Figure 3G (Supplementary Fig. 16D). The precision of the spectral splitting localizations is comparable for both dyes. The precision compared to simulations of a single dye with the same conditions shows a twofold reduction of the precision at the same number of photons. Compared to pMINFLUX multiplexing with a less than 1.5-fold reduction in precision at the same number of photons, spectral multiplexing is less photon efficient. However, spectral splitting is still considerably more photon efficient compared to widefield tracking methods. This makes spectral multiplexing attractive to implement in commercial continuous-wave MINFLUX setups.

References

(1) Masullo, L. A.; Steiner, F.; Zähringer, J.; Lopez, L. F.; Bohlen, J.; Richter, L.; Cole, F.; Tinnefeld, P.; Stefani, F. D. Pulsed Interleaved MINFLUX. *Nano letters* **2021**, *21* (1), 840–846. DOI: 10.1021/acs.nanolett.0c04600. Published Online: Dec. 18, 2020.

(2) Gordon, M. P.; Ha, T.; Selvin, P. R. Single-molecule high-resolution imaging with photobleaching. *Proceedings of the National Academy of Sciences of the United States of America* **2004**, *101* (17), 6462–6465. DOI: 10.1073/pnas.0401638101. Published Online: Apr. 19, 2004.

(3) Qu, X.; Wu, D.; Mets, L.; Scherer, N. F. Nanometer-localized multiple single-molecule fluorescence microscopy. *Proceedings of the National Academy of Sciences of the United States of America* **2004**, *101* (31), 11298–11303. DOI: 10.1073/pnas.0402155101. Published Online: Jul. 26, 2004.

(4) Ram, S.; Ward, E. S.; Ober, R. J. Beyond Rayleigh's criterion: a resolution measure with application to single-molecule microscopy. *Proceedings of the National Academy of Sciences of the United States of America* **2006**, *103* (12), 4457–4462. DOI: 10.1073/pnas.0508047103. Published Online: Mar. 1, 2006.

(5) Pfeiffer, M.; Trofymchuk, K.; Ranallo, S.; Ricci, F.; Steiner, F.; Cole, F.; Glembockyte, V.; Tinnefeld, P. Single antibody detection in a DNA origami nanoantenna. *iScience* **2021**, *24* (9), 103072. DOI: 10.1016/j.isci.2021.103072. Published Online: Sep. 1, 2021.

(6) Voter, A. F. INTRODUCTION TO THE KINETIC MONTE CARLO METHOD. In *Radiation Effects in Solids*; Springer, Dordrecht, 2007; pp 1–23. DOI: 10.1007/978-1-4020-5295-8_1.